Università degli Studi di Milano

Facoltà di Scienze Matematiche Fisiche e Naturali

Scuola di Dottorato in Scienze e Tecnologie Chimiche

Corso di dottorato in Chimica Industriale XXII ciclo

Dipartimento di Chimica Fisica ed Elettrochimica

Settore disciplinare: CHIM/02

MULTIPHASE, MULTIFUNCTIONAL MICRO- AND NANO-STRUCTURED ELECTROCATALYTIC MATERIALS FOR GREEN CHEMISTRY: APPLICATIONS TO ENERGY CONVERSION AND ENVIROMENTAL PROTECTION

Tutor: **Prof. Sandra Rondinini**

Co-tutor: **Prof. Silvia Ardizzone**

Dott. Alberto Vertova

Tesi di dottorato di

Cristina Locatelli

Matricola: R07276

Anno Accademico: 2008/2009

1-Introduction

At the beginning of the 21st century, the problem of global sustainability is widely recognized by world leaders, and is a common topic of discussion by journalists, scientists, teachers, students and citizens throughout the world. The idea of sustainability dates back more than 30 years and it was a key theme of the United Nations Conference on the Human Environment in Stockholm in 1972. The concept was coined explicitly to suggest that it was possible to achieve economic growth and industrialization without environmental damage. In the ensuing decades, mainstream sustainable development thinking was progressively developed through the World Conservation Strategy (1980), the Brundtland Report (1987) and the United Nations Conference on Environment and Development in Rio (1992), as well as in national government planning and wider engagement from business leaders and non-governmental organizations of all kinds. Over these decades, the definition of sustainable development evolved. The Brundtland Report defined sustainable as *'development that meets the needs of the present without compromising the ability of future generations to meet their own needs'*. This definition was vague but it cleverly captured two fundamental issues: the problem of the environmental degradation that so commonly accompanies economic growth and yet the need for such growth to alleviate poverty [1].

In recent years, the EU has demonstrated its clear commitment to sustainable development and has successfully mainstreamed this sustainability dimension into many policy fields. It has, in particular, taken the lead internationally in the fight against climate change and is committed to promoting a low carbon, knowledge-based, resource-efficient economy. The European Council on June 2006 adopted an ambitious and comprehensive renewed Sustainable Development Strategy (SDS). The overall aim of the EU Sustainable Development Strategy is to identify and develop actions to enable the EU to achieve a continuous long-term improvement of quality of life through the creation of sustainable communities able to manage and use resources efficiently, able to tap the ecological and social innovation potential of the economy and in the end able to ensure prosperity, environmental protection and social cohesion.

The strategy sets overall objectives and concrete actions for seven key priority challenges for the coming period until 2010, many of which are predominantly environmental [2]:

- climate change and clean energy;
- sustainable transport;
- sustainable consumption & production;
- conservation and management of natural resources;

- public health;
- social inclusion, demography and migration;
- global poverty and sustainable development challenges.

Within this frame and in direct relation with the key subjects of clean energy and sustainable consumption/production, the present work is aimed at the development of new materials for the exploitation of renewable energy sources and the treatment of wastes.

SUSTANAIBLE CONSUMPTION AND CLEAN ENERGY

Fossil fuels, coal, oil and natural gas are non-renewable sources of energy. It has been estimated that there are enough crude oil reserves to last the world about another 100 years (estimate based on current levels of consumption and estimated total reserve) [3]. Beside the limitations in the future projected availability there are the environmental aspects associated with the combustion by-products namely: SO_x, NO_x, CO, CO_2, volatile organic compounds (VOC), other micro-pollutants, fine particulates, noise.

Figure 1 compares the 1973 and 2007 regional shares and Figure 2 shows the evolution from 1971 to 2007 of the total final energy consumption by fuel [4].

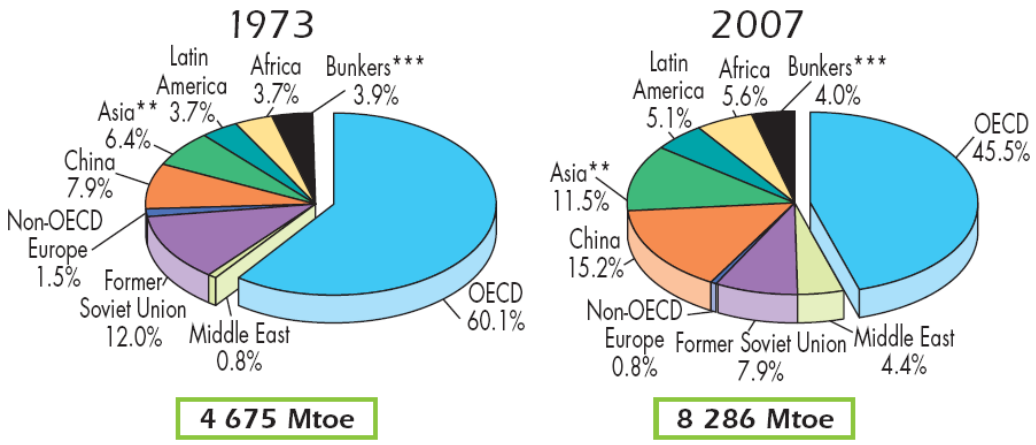

Asia excludes China.*Includes international aviation and international marine bunkers.

Figure 1: 1973 and 2007 total final energy consumption (Prior to 1994 combustible renewables & waste final consumption has been estimated) by country [4].

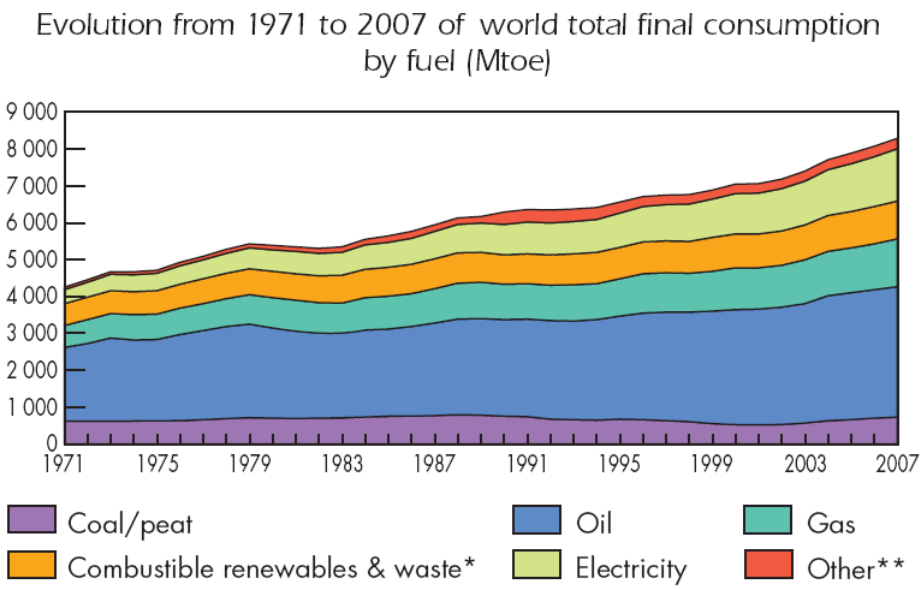

*Prior to 1994 combustible renewables & waste final consumption has been estimated.
**Other includes geothermal, solar, wind, heat, etc

Figure 2: Fuel share of total final energy consumption [4].

It is evident the drastic reduction in energy consumption of the OECD countries (OECD: Organisation for the Economic Co-operation and Development) and the modest increase of Latin America and Africa, while China, Asia and Middle East have cumulatively doubled their share. Parallelly, the continuous increase of the world energy consumption is globally dominated by the fossil sources. Nonetheless the share of renewable, electricity and others has steadily increased while oil, gas and coal have cumulatively decreased.

Figure 3 highlights the actual (2007) prevalent incidence of industry in coal consumption; of transport in oil; of agriculture, residential and public activity in electricity and gas demand.

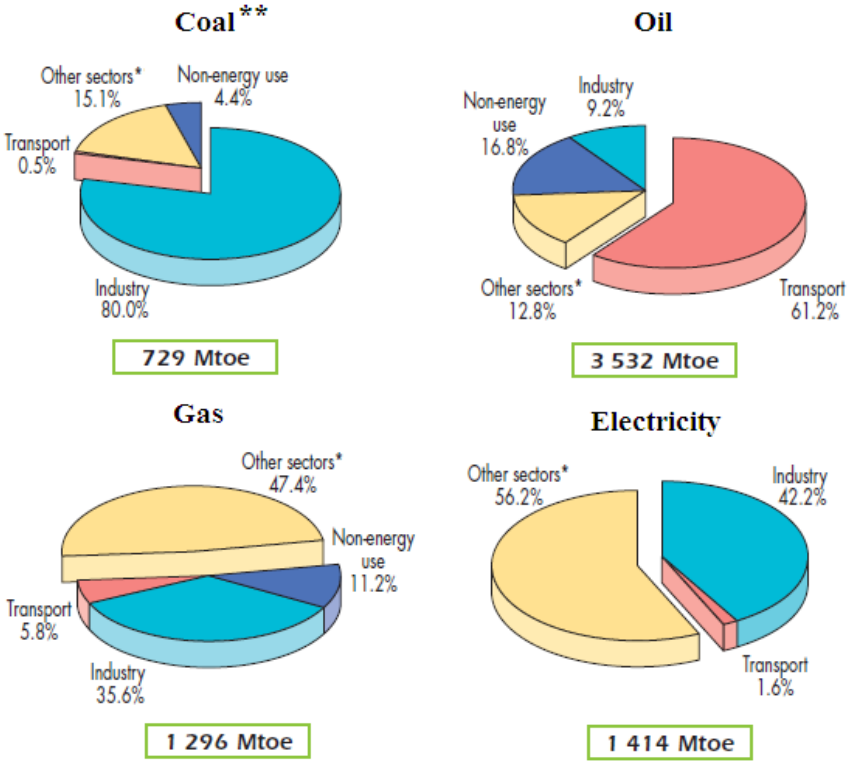

*Includes agriculture commercial & public services, residential and non-specified and non-specified other sectors. **Coal refers to coal/peat.

Figure 3: World total final consumption in 2007. [4].

Analogously, the Total Primary Energy Supply (TPES), *i.e.* the extraction of energy from natural sources, including the import-export balance, has roughly doubled in the last 30 years (see Figure 4).

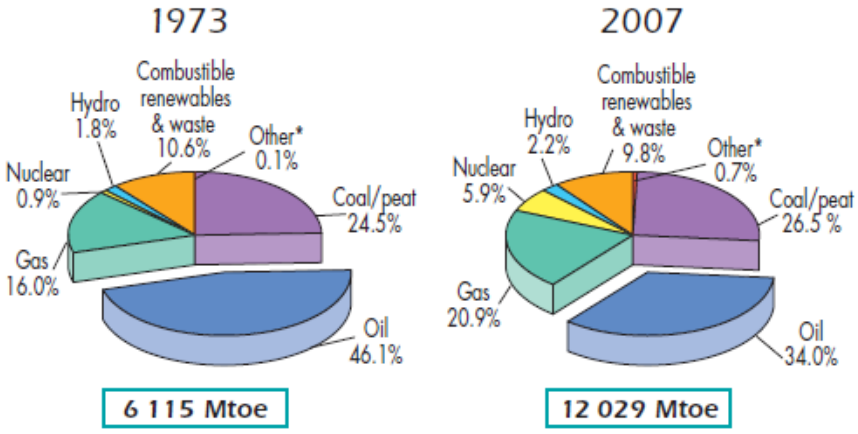

*Other includes geothermal, solar, wind, heat, etc.

Figure 4: 1973 and 2007 fuel shares of TPES. [4].

Fossil fuels currently account for more than 80% of the overall energy demand. Nevertheless, the fuel share is significantly decreased for oil and increased for nuclear energy. Unfortunately,

renewable and hydroelectric shares did not significantly change. Expectations for 2030, reported in the following figure, is not optimistic: renewable source would be still confined around 12%.

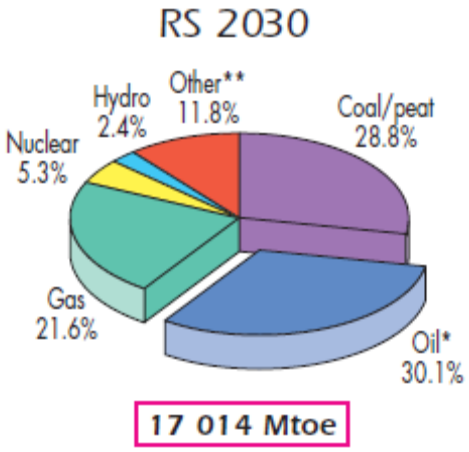

*Include international aviation and international marine bunkers. **Others includes combustible renewable & waste, geothermal solar, wind, tide, etc.

Figure 5: Fuel share of TPES in 2030 for the Reference Scenario [4].

Interestingly, OECD countries have effectively reduced their shares, while Middle East, China and Asia have greatly increased their primary energy supply, which in 2008 accounted for the 40.9% of the crude oil world production, 23.6% of natural gas, and the 61.3% of coal, as summarized in the following Figures.

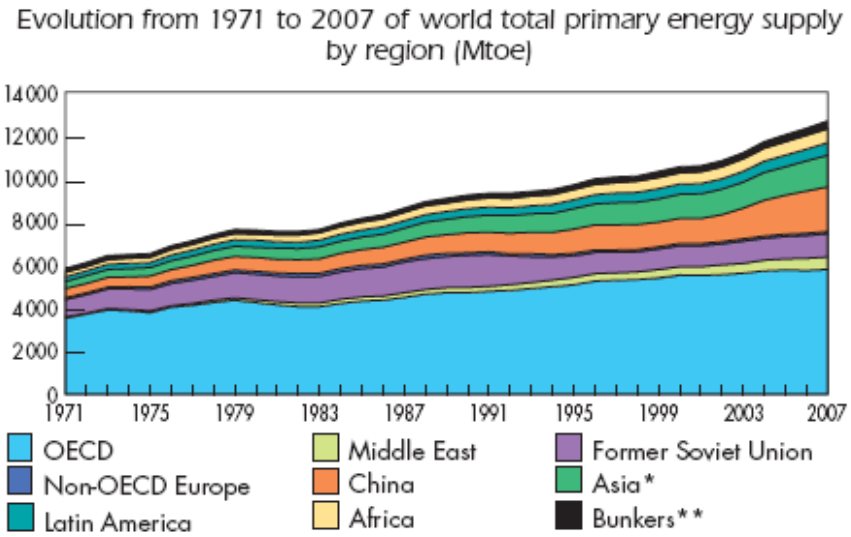

*Asia excludes China.**Includes international aviation and international marine bunkers.

Figure 6: Evolution from 1971 to 2007 of world TPES by region [4].

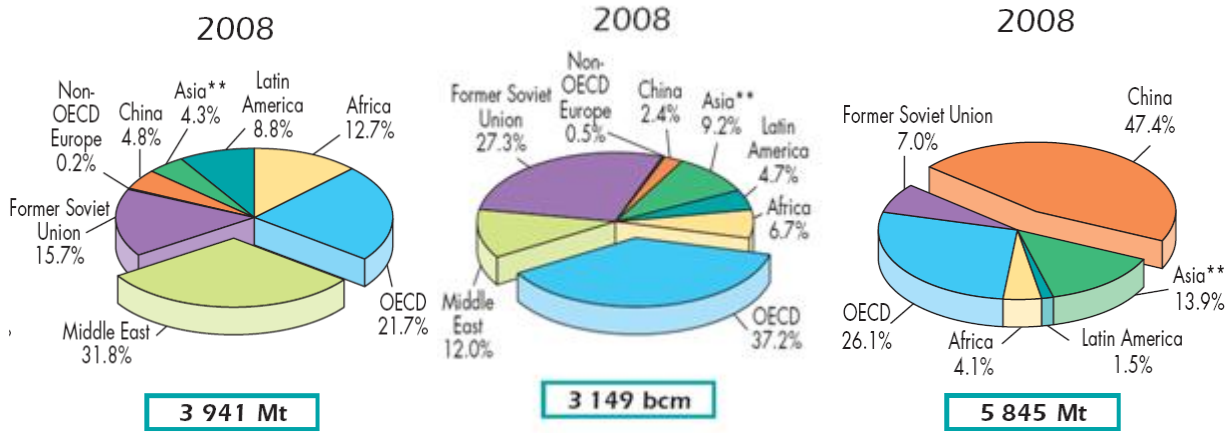

*Includes crude oil, NGL, feedstock, additives and other hydrocarbons. **Asia excludes China. ***Includes recovered coal.

Figure 7: 2008 Regional shares of crude oil, natural gas, coal production [4].

It is then to be expected that fossil fuels will represent the world's main energy source for the years to come. As previously reported one of the main drawbacks in the use of fossil fuel is the increase of gaseous emissions in atmosphere. In particular the rise of CO_2 emissions produced by use of fuel is shown in Figure 8.

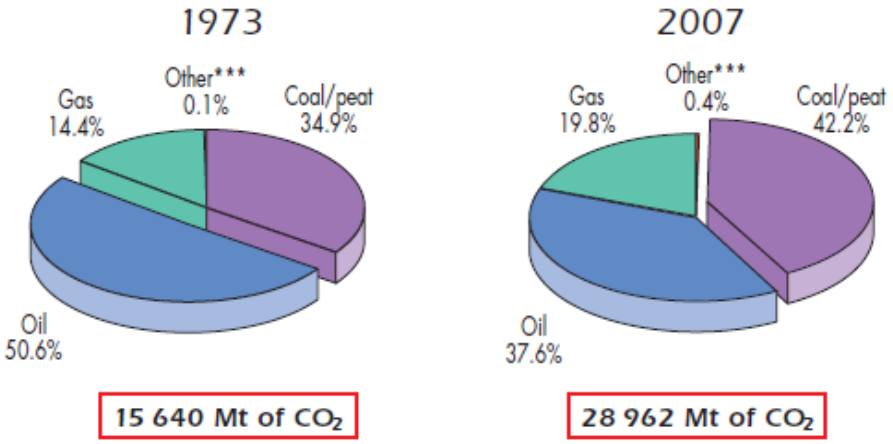

*world includes international aviation and international marine bunkers. ** Calculated using the IEA's energy balances and Revised 1996 IPCC Guidelines. CO_2 emissions are from fuel combustion only.*** Other includes industrial waste and non-renewable municipal waste.

Figure 8: 1973 and 2007 fuel shares of CO_2 emissions [4].

In order to reduce the environmental impact, nations have adopted different measures. For example, Europe has already reduced the incidence of its CO_2 emissions with respect to its energy demand (see Figure 9 and Figure 10).

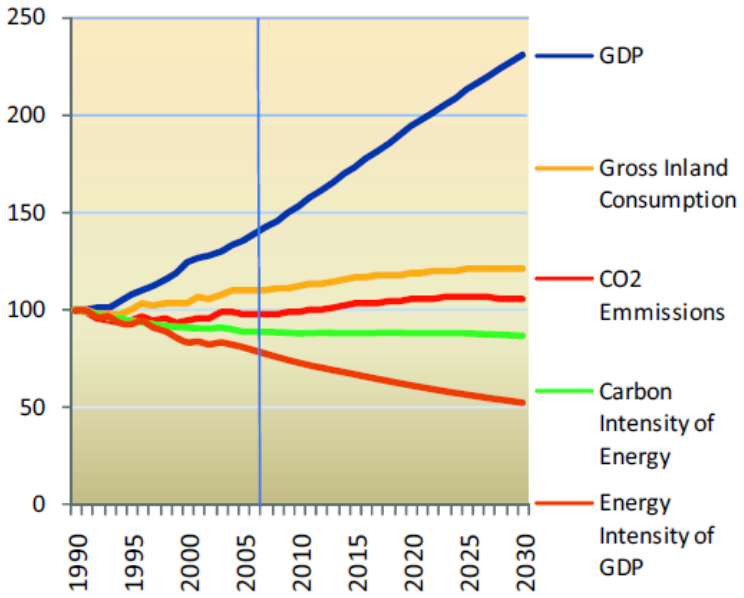

Figure 9: Carbon emission indicators. In Europe the CO_2 emissions in 2000 by 5.6% compared to 1990. (GDP: Gross Domestic Product) [5].

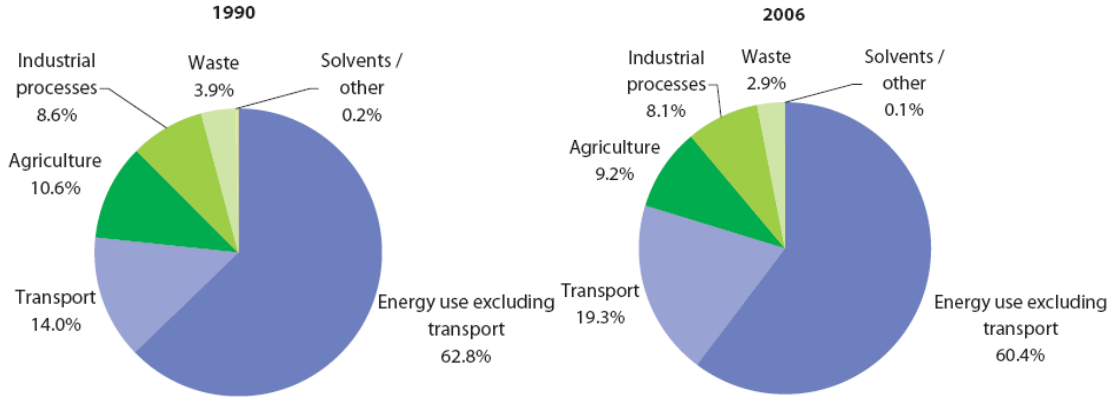

Figure 10: Green-house gas emissions (%) by sector based on data in million tonnes CO_2 equivalent. Data in 2006 refer to EU-27 and sum up to 5.143 million tonnes CO_2 equivalent [6].

Its strategy for the development of sustainable energy systems provokes the transition from the prevalent usage of fossil fuels (and consequently the reduction of their associated emissions) to a wider combination of energy sources, among which renewable energy sources play a key role (see Figure 11) [5].

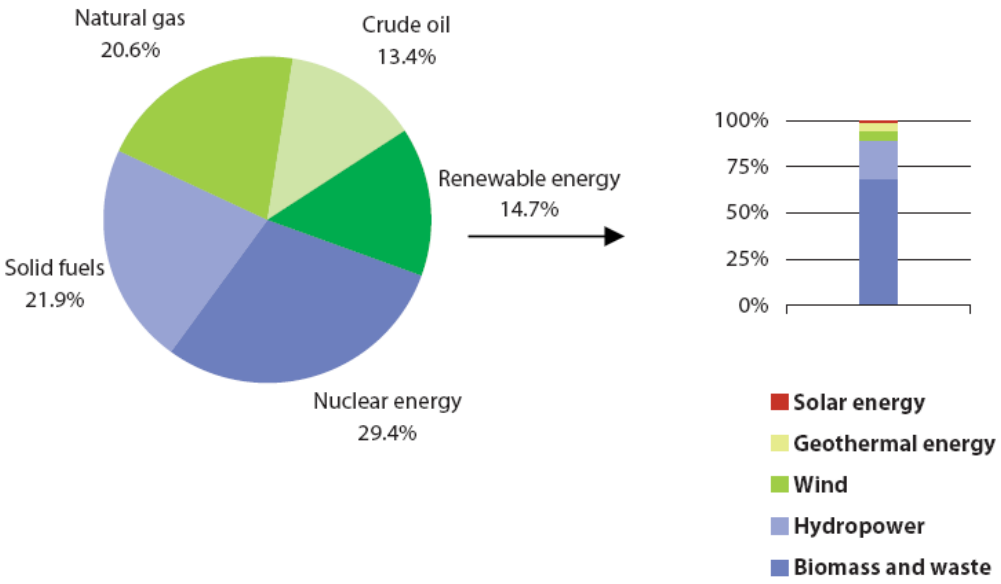

Figure 11: Production of primary energy, EU-27 2006 [6].

Renewable sources, such as water (hydroelectric, wave, tidal), wind, sun (thermal and photovoltaics), biomasses and earth (geothermal), produce energy intermittently and often in remote locations. This calls for an energy storage and transportation likely by means of a suitable energy vector, that is a chemical substance which possesses high energy density and can be easily transportable and stocked.

In this context, hydrogen is progressively considered as one of the most effective long-range and long term environmentally friendly vector [7]. In fact, hydrogen can be obtained by the exploitation of renewable sources and then be stored or transported, before being electrochemically oxidised in a fuel cell to form electric power and water. The only input to this cycle is the clean renewable energy and the only output is electric power [8][9]. This cycle is schematically described in Figure 12 and represents the most sustainable energy cycle.

When hydrogen is combusted electrochemically in a fuel cell no pollution is produced (water is the only product of the reaction): local air emissions, responsible for particulate matter, ozone and acid rains, as well as noise are eliminated by adopting hydrogen fuel cell vehicles. Note that this does not apply to the conventional combustion in an internal combustion engine, for which NO_x emissions have to be accounted for.

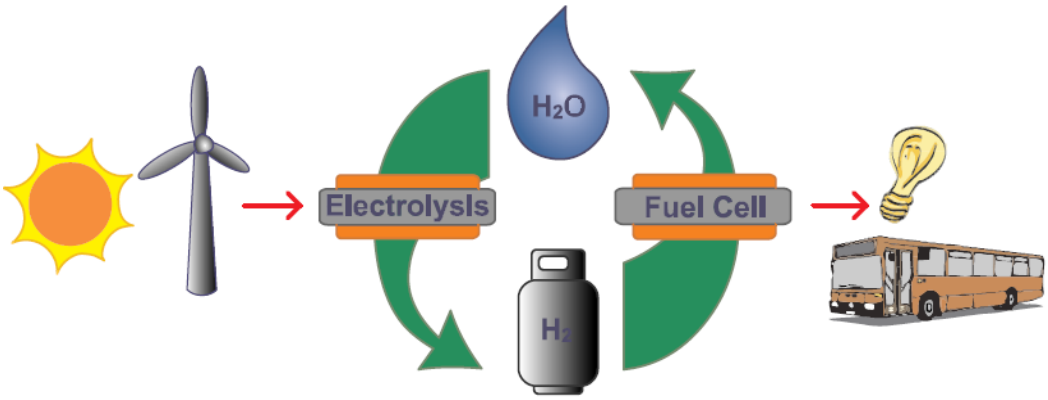

Figure 12: Ideal energy cycle involving hydrogen.

Moreover, hydrogen presents high specific energy. Nonetheless, many aspects must be taken into account while considering hydrogen as an energy vector such as [9]:

- Hydrogen production. Global hydrogen production today is based almost exclusively on fossil fuels. Natural gas reforming, coal gasification and electrolysis are proven technologies for hydrogen production and are applied on an industrial scale all over the world. Steam reforming of natural gas currently is the cheapest production method but CO_2 emissions are present.
- Hydrogen distribution. Different options are available for hydrogen transport and distribution: delivery of compressed gaseous and liquid hydrogen by trucks and of gaseous hydrogen by pipelines. Because of the specific physical and chemical properties of hydrogen, pipelines must be made of non-porous, high-quality materials such as stainless steel. Therefore the investments in a hydrogen pipeline for a given diameter are up to two times higher than those for natural gas pipelines. The costs could be considerably reduced if the natural gas infrastructure could be adapted to hydrogen.
- Hydrogen storage. It is one of the most critical issues, which must be solved before a technically and economically viable hydrogen fuel system can be established. In fact, due to the low-energy density of hydrogen, it is difficult to store hydrogen enough to the use. The physical limits for the storage density of compressed and liquid hydrogen have more or less been reached, while there is still potential in the development of solid materials for hydrogen storage, such as systems involving metal hydrides.

INDUSTRIAL WASTE TREATMENT

In this study a class of highly toxic pollutant such volatile organic compounds are considered.

Volatile organic compounds (VOCs) are an important group of environmental contaminants to monitor and manage in ground water because of their widespread and long-term use [10]. The most usual definition in Europe is the one stated in the Solvent Emissions Directive, which defines a VOC as *'any organic compound having at 293.15°K a vapour pressure of 0.01 kPa or more, or having a corresponding volatility under the particular conditions of use* ' [11].

VOC have a key role in the formation of smog and ozone in the presence of NO_x. High concentrations of ozone at ground level can harm human health, damage crops and affect materials such as rubber. Some VOCs may be directly harmful to human health (*e.g*. as carcinogens), contribute to global warming (*e.g*. methane) or destroy stratospheric ozone needed to shield the earth's surface from harmful ultra violet radiation.

The most common VOC is methane, therefore is sometimes excluded from analysis of other VOCs using the term non-methane VOCs, or NMVOCs.

The production of NMVOCs European from 1990 to 2007 is reported in the next figure:

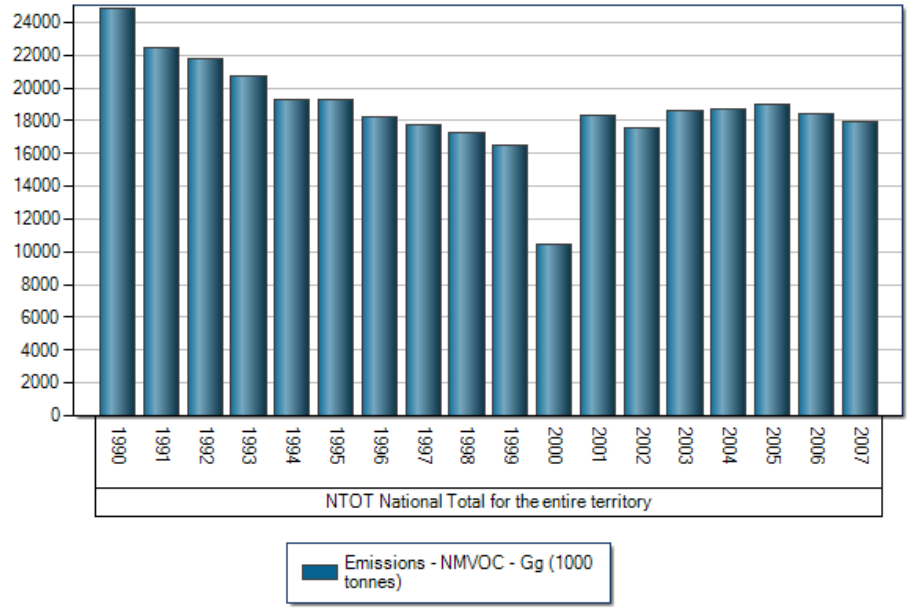

Figure 13: European NMVOC production from 1990 to 2007 [12].

Among VOCs, Halogenated VOCs (VOHs) attract particular consideration because are used in several industrial processes. In fact, chlorinated VOCs include very common solvents such as CH_2Cl_2 (pharmaceuticals, chemical processing, aerosols, etc.), $CHCl_3$, CCl_4, $Cl_2C=CCl_2$ (dry and metal cleaning), and $Cl_2C=CHCl$ (metal cleaning and specialty adhesives).

In order to preserve air quality and prevent health diseases, the European Community (CE) issued the following directives [13][14]:

1. Directive 1999/13/EC and DM 44/2004 (16 gen 04): regulates the emissions of VOC from a wide range of industrial activities. Among these there are printing, surface cleaning, vehicle coating, dry cleaning and manufacture of footwear and pharmaceutical products. It should be noted that the scope of the Directive does not include painting activities. These are regulated separately by the VOC Paints Directive (2004/42/EC).
2. Directive 94/64/EC (20 dec 94): regulates the control of VOC emissions resulting from the storage of petrol and its distribution from terminals to service stations;
3. Directive 2004/42/EC: on the limitation of emissions of volatile organic compounds due to the use of organic solvents in certain paints and varnishes and vehicle refinishing products.

Table 1 reports the maximum tolerable values for some polluting substances in the water and in soil:

Substance	Underground water (µg/L)	Soil (µg/L)	
		A	B
trichloromethane	0.15	0.1	5
vinyl chloride	0.5	0.01	0.1
1,2-dichloroethane	3	0.2	5
1,1-dichloroethylene	0.05	0.1	1
trichloroethylene	1.5	1	10
tetrachloroethylene	1.1	0.5	20
1,1dichloroethane	810	0.5	30
1,2.dichloroethylene	60	0.3	15
1,2-dichloropropane	0.15	0.3	5
1,1,2-trichloroethane	0.2	0.5	15
1,2,3-trichloropropane	0.001	1	10
1,1,2,2-tetrachloroethane	0.05	0.5	10
tribromomethane	0.3	0.5	10
1,2-dibromoethane	0.001	0.01	0.1
dibromochloromethane	0.13	0.5	10
bromodichloromethane	0.17	0.5	10
A: for both green public and green private (*mg of dry part/kg*) B: commercial and industrial sites (*mg of dry part/kg*)			

Table 1: Limit values of some VOH in underground water and soil [15].

Notwithstanding their relatively short atmospheric life-time (Figure 14), their toxicity together with the wide spectrum of waste types (from concentrated organic solutions/emulsions to very dilute

aqueous phases, to airborne streams) constitute serious challenges in developing suitable treatment methodologies.

Dibromomethane	18 min to 48 h
1.1.2-Trichloroethane	21 min
1.2-Dichloroethane	30 min to 4 h
1.2-Dichloroethylene	3 h
Trichloroethylene	Several minutes to several hours
Tetrachloroethylene	27 min to several hours
1.2.4-Trichlorobenzene	4.2 h
1.2-Dichlorobenzene	4.4 h
1.1-Dichloroethane	6.4 h
1.2-Dichloropropane	9 h
Monochlorobenzene	12 h
Hexachloroethane	15 h
Chloroform	36 h
1.1.2.2 Tetrachloroethane	3.5 days
1-Chloro-2-nitrobenzene	33.5 days
2-Chlorophenol	73 days

Figure 14: Evaporation from water (half-life time) [16].

Several biological and physico-chemical methods have been proposed so far but none of them is free from some significant drawback, the most important being:

- formation of undesirable by-products;
- excess of reagent;
- exhaustion of absorbing substrates which require additional treatment steps.

On account on their higher selectivity, milder reaction conditions and simpler process design and operation, electrochemical methods can play a key role in environmental protection and remediation. Although electrooxidative processes are more attractive, because they may lead to the complete mineralization of the substrate, and have been therefore deeply studied [17], their application to VOH degradation may produce undesired chlorinated compounds possibly even more toxic than the original ones. On the other hand, the electroreductive route, leading to hydrodehalogenated derivatives (*e.g.* CH_4, C_2H_6, C_2H_4), represents a convenient way of waste detoxification, provided that the dehalogenation is complete [18][19].

1.2-Syntehsis nanopowders: wet method

In this thesis nanostructured powders were synthesized and characterized. The main advantages in the use of powder materials rely on the possibility of: (i) reducing the particle size and therefore the enhancement of the active surface, (ii) mixing the material with other components that constitute the catalytic layer and (iii) dispersing of precious metal in a diluents matrix.
The materials synthesized are: IrO_2-based materials and silver-based materials. The diluent matrices used are SnO_2 and carbon (Vulcan® XC72R) respectively. The choice of the diluents matrix is made on the basis of cost, stability in the working environment and possible synergistic effects. The method adopted is generically labelled "wet method" and include both the sol-gel method used in the case of IrO_2-based materials and the chemical reduction method used in the Ag-based materials.

Sol-gel technology is a low temperature chemical route which involves the evolution of inorganic networks through the formation of a colloidal suspension (sol) into an organic solvent and, by addition of water, gelation of the sol to form a cross linked network in a continuous liquid phase (gel). This method allows the preparation of highly dispersed materials with physico-chemical properties that can be finely tuned by the appropriate selection of the synthetic parameters, such as:

- hydrolysis temperature;
- reaction pH;
- precursor to solvent molar ratio;
- precursor to water molar ratio;
- solvent removal step which, by itself introduces many variables;
- growing steps (hydrothermal, ultrasound and microwave treatments);
- calcination temperature.

In addition, with respect to other synthetic technologies, sol-gel presents several other advantages like the high purity of the final products [20][21], and their high degree of homogeneity (thanks to the very intimate level of mixing of the reagents). The main drawback, that has limited the industrial application so far, is the use of alcohols as solvents that require apposite standard operating procedures for security.
The main synthetic steps are [22]:

1. Sol formation: a reactive metal precursors, usually an alkoxides or nitrate in an alcohol solution is hydrolyzed by mixing with water. This results in a colloidal suspension.

2. Gel formation: colloidal particles link together to form a three-dimensional network, called gel. The physical characteristics of the gel network depend greatly upon the size of particles and extent of cross-linking prior to gelation. Generally speaking, polycondensation occurs before the hydrolysis process ends; anyhow, the experimental conditions may modulate the relative kinetics. This means that water/solvent and water/alkoxides ratios are relevant parameters that play a key role in terms of surface area, crystallite dimensions and morphology of the final oxide.
3. Drying: the liquid is removed from the interconnected pore network. The drying process can be typically obtained in three modes:
    - by heating under high pressure in supercritical conditions (critical-point drying). The network does not collapse and a low density aerogel is produced. Aerogels can have pore volumes as large as 98% and densities as low as 80 kg/m^3 [22].
    - by simply heating at 1 atm. In this case a so-called xerogel is formed.
    - by lyophilizing the solution (by freezing it under vacuum and then slowly heating it), obtaining a cryogel.
4. Calcination: consists in heating at high temperature the dried gel in order to eliminate water, evaporate or decompose the alcohols used during the process, and increase the crystallinity grade of the material. During this step the polycondensation continues. The choice of the calcinations temperature and its length is not straightforward since increasing the temperature increases the crystallinity level of the material, its structural homogeneity and the sintering between particles.

The method of chemical reduction from aqueous solutions is most preferable for obtaining nano-sized powders and colloidal dispersion of silver. It is common knowledge that the chemical reduction method involves reduction of metal salt in the presence of a suitable protecting agent, which is necessary for controlling the growth of metal colloids [23]. Both the reducing agent and the protecting agent are determinant on the final dimension of silver particles. According to [24], silver powder with particle size 0.1–1.0 μm can be obtained by reduction of silver nitrate with alkylacid phosphate in the presence of gelatin. However, the size of silver particles can be reduced to 100 nm, if the reduction of silver nitrate is realized by hydrazine in the presence of polyvinyl pyrrolidone (PVP) [25]. In this study an investigation of effect on the electrochemical performances of six different protecting agents was carried out.

1.3-Electrocatalysis: fundamentals

Catalysis is the process in which the rate of a chemical reaction is increased by means of a chemical substance known as a catalyst. The catalyst speeds up the reaction but remains unchanged at the end of the reaction. The quantity of catalyst does not change during the reaction because it does not participate at the reaction as a reagent: it provides an alternative mechanism, which, in turn, involves a different transition state and lower overall activation energy (see Figure 15).

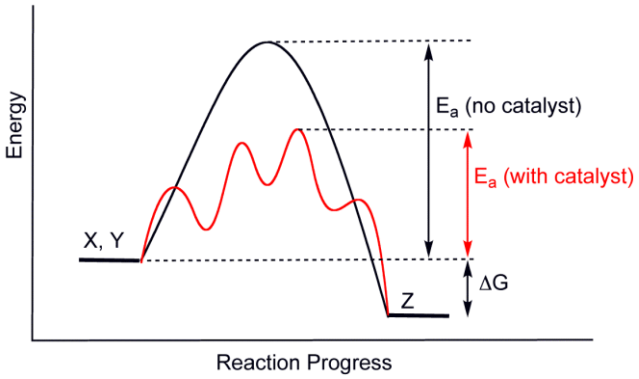

Figure 15: Generic potential energy diagram showing the effect of a catalyst in a hypothetical exothermic chemical reaction X + Y to give Z.

In parallel, in electrochemistry, the electrocatalyst is a substance that increases the reaction rate at the electrode. This implies that electrocatalysis represents the influence of the electrode material on the rate of electrode reaction, *i.e.* the kinetic and mechanistic effects of the bond formed by reactants, products and/or intermediates with the electrode surface [26].

The specific consumption of energy, w (in Wh/kg), related to a generic electrode reaction:

$$R \rightleftharpoons O + ne^- \quad (1)$$

is given by: $$w = \frac{nFE_W}{M_p} \quad (2)$$

where n represents the (mol of e^-)/(mol of product) exchanged in the reaction, F = 26.8 Ah/(mol of e^-) is the Faraday constant, E_W the working electrode potential in Volt (V), and M_p the molar mass of the product in kg mol^{-1}.

The working electrode potential is related to the thermodynamic value, E_{eq} (V), by the sum of different overpotential, η (V), contributions, *i.e.* the sum of the p.d.'s (p.d. = potential difference) bound to dissipative phenomena accompanying the reactions at the electrode:

$$E_W = E_{eq} + \sum \eta = E_{eq} + \sum \eta_{ct} + \sum \eta_{mt} + \sum \eta_\Omega \quad (3)$$

where $\sum\eta_{ct}$ is the sum of the overpotentials due to the electron transfer reaction, $\sum\eta_{mt}$ is the sum of the overpotentials related to the mass transfer of reactants and products to and from the reaction site, and $\sum\eta_{\Omega}$ is the sum of the overpotentials due to the ohmic drops. *i.e.* the transport of charges within the ionic and electronic conductors.

$\sum\eta_{ct}$ is the term which most directly measures electrocatalysis. The relevant relationship between the current density and the overpotential is given by the Butler-Volmer equation:

$$j = j_a + j_c = j_0\{\exp(1-\beta)[F\eta / RT] - \exp[-\beta F\eta / RT]\} \quad (4)$$

where j_a and j_c are the current densities of the forward and backward reaction, respectively, j_0 is the exchange current density, *i.e.* the current density at the thermodynamic equilibrium (when $j = 0$ and $j_{a,0} = j_{c,0} = j_0$), and β is the symmetry factor.

For $\eta \ll RT/F$ or $\eta \gg RT/F$, one of the addendums becomes negligible, thus bringing to the following generalized expression:

$$\eta = b \lg (j/j_0) \quad (5)$$

which is the Tafel equation. The value of *b* is strictly related to the electrocatalytic properties of the material toward the reaction under investigation. The lower the *b* value (and then the line slope), the higher the current density at a given potential. Tafel slopes, together with other parameters like reaction orders, give important clues in the understanding of the reaction mechanism.

Generally speaking, each reaction mechanism is composed by one or more steps. It is assumed all the reaction steps but the slowest are in equilibrium conditions, and hence the overall reaction rate coincides with the slowest one, which is called *the rate determining step* (rds).

However the effectiveness of an electrocatalytic material depends on several factors [26]:

- good electrocatalytic properties;
- high surface area;
- high electrical conductivity;
- long-term mechanical and chemical stability;
- high selectivity;
- availability and low cost;
- health safety;
- environmentally friendly.

1.4-Hydrogen as Energy vector

1.4.1-Hydrogen production

Hydrogen is present in nature in the form of chemical compounds, mostly in water and hydrocarbons. Molecular hydrogen can be obtained by several methods, which implies the use of a high amount of energy.

As already mentioned, natural gas reforming, coal gasification and water electrolysis are proven technologies for hydrogen production and are applied on an industrial scale all over the world. Steam reforming of natural gas is the most used process in the chemical and petrochemical industries; it is currently the cheapest production method and presents relatively low CO_2 emissions. Global hydrogen production today amounts to around 700 billion Nm^3 and is based almost exclusively on fossil fuels [9].

Generally speaking, the steam reforming consists on the reaction between a hydrocarbon and water to give H_2 and CO. In the case of methane, the steam reforming reaction is [27]:

$$CH_4 + H_2O \rightarrow CO + 3H_2 \quad (6)$$

Methane is the best hydrocarbon for steam reforming because of its high H/C ratio.

In the case of production of hydrogen for fuel cells, many purification steps are required. In fact, Pt (the most adopted electrode material on both sides of the cell) is known to be rapidly poisoned by CO, whose content must be lower than 10 ppm.

Less used methods for hydrogen production are [9]:

- Biomass gasification. It is still at an early stage today, but is expected to become the cheapest renewable hydrogen supply option in the coming decades. Biomass gasification is applied in small decentralized plants during the early phase of infrastructure rollout and in centralized plants in later periods.
- Nuclear power plants. Thermo-chemical cycles based on nuclear energy or solar energy are a long term option for hydrogen production with new nuclear technology or in countries with favourable climatic conditions.
- Photo-electrochemical water splitting – photolysis. Still at the level of basic research.
- By-product of chemical industries.
- Water electrolysis. It is the most promising method for highly pure hydrogen production.

The distribution of the primary energy sources for hydrogen production is reported in Figure 16. Water electrolysis accounts for the 4% of global production only.

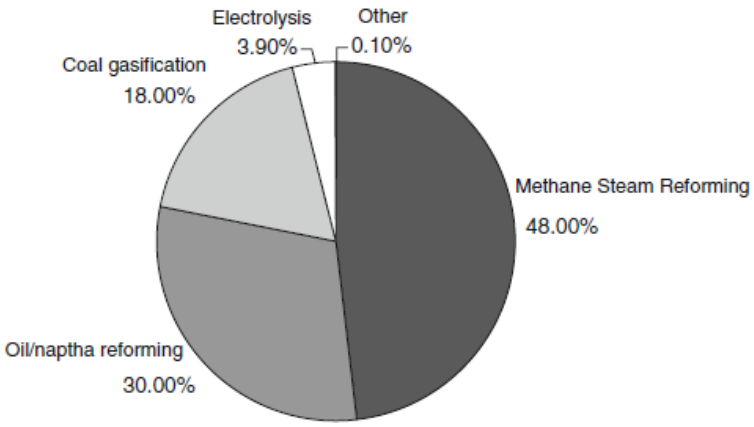

Figure 16: Present distribution of primary energy sources for hydrogen production (data from [28].)

1.4.2-Water electrolysis

Water electrolysis reaction consists on water splitting in H_2 an O_2, as described in the following:

$H_2O\ (l) \rightarrow H_2\ (g) + ½\ O_2\ (g)$ E^0=1.23 V *vs* SHE (7)

$2H^+ + 2e^- \rightarrow H_2$ E^0 = 0 V *vs* SHE (8)

$H_2O \rightarrow ½\ O_2 + 2H^+ + 2e^-$ E^0=1.23 V *vs* SHE (9)

$\Delta G°$ for this reaction at standard conditions is 237.15 kJ/mol corresponding to a minimum request of 1.23V at 25°C.

In particular water electrolysis offers several advantages [28][29]:

- the only by-product is pure oxygen;
- no carbon emissions;
- very pure hydrogen (no CO poisoning of fuel cell catalysts) is obtained;
- no dependence on hydrocarbon sources availability;
- small scale hydrogen supply is possible;
- directly converts electric energy produced from renewable sources into the energy vector.

Traditionally it is carried out in alkaline media and many commercial electrolysers are available on the market. The most used technology adopts 25% KOH aqueous electrolyte and Ni based electrodes. The cell typically operates at 2 kA/m^2 and 80°C and 1.8 - 2.1V [30]-[32]

The most advanced pressurized electrolysers operate at T ≥ 160°C, Ni raney cathodes, Co_3O_4 or spinels anodes, NiO diaphragms, and high concentrated KOH.

The development of solid polymer electrolytes [33][34] shifted the attention toward the acidic water electrolysis (see Figure 17). In this case proton exchange membrane (PEM, *i.e.* Dupont Nafion®) and electrodes stable in acidic conditions are adopted. The "heart" of the system consists on the so called Membrane Electrode Assembly (MEA)

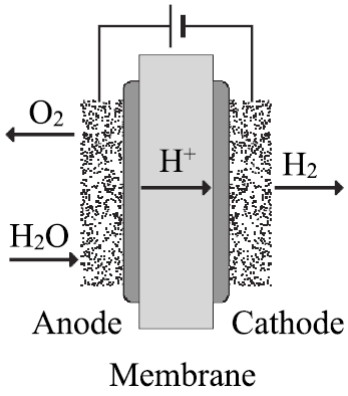

Figure 17: Schematic of PEM based water electrolyser.

The benefits of PEM based electrolysers over alkaline systems are:

- much higher current densities attainable (13 A/cm^2 compared with 0.2 A/cm^2 of alkaline processes [35][36];
- no circulating dangerous electrolyte [37];
- high energy efficiency [38];
- wide range of power loadings [38];
- very rapid power-up/power-down rates [39];
- the possibility of combining fuel cell and electrolyser in the same system (the so-called regenerative fuel cells)[40].

Electrolysers and fuel cells that utilize proton exchange membrane (PEM) technology show high specific energy, therefore have undergone continued development for rigorous aerospace and military applications since the late 1960 [41].

In particular the nature of the electrode materials is still an important research subject especially in the case of the anode, since the oxygen evolution reaction is the main source of energy losses in the whole system. In the membrane-electrode assembly the catalyst is in direct contact with both the gas diffusion layer and the membrane, thus dramatically reducing the contact resistance (Figure 18)[42].

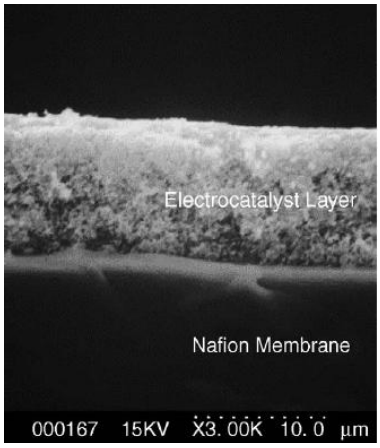

Figure 18: Scanning electron micrograph (SEM) of a cross-section of an electrode assembly [42].

Since the perfluorosulphonated membrane behaves locally as strong acid, the electrocatalytic layers must be stable at the lowest pHs.

1.4.3-Fuel cell

A fuel cell is an electrochemical device which produces electricity when, fed with the reactants into the electrode compartments, is connected to the external load.

In H_2/O_2 fuel cells, molecular hydrogen and oxygen react to produce water and heat. $\Delta H°$ for the reaction is -286 kJ/mol. This means that highest possible energy efficiency of a PEMFC is $\Delta G°/\Delta H° = 83\%$. During the work of the system, the presence of energy dissipations causes the reduction of energy efficiency. Therefore, the development of a system and, in particular, of its electrode materials which is able to reduce this energetic dispersion is required.

In comparison with conventional electricity generators, which involve three conversion steps (chemical energy to thermal energy, thermal energy to mechanical energy and mechanical energy to electricity), the fuel cell directly converts chemical energy into electrical energy [9][42][43]. Theoretically, a fuel cell has the capability of producing electrical energy for as long as the fuel and the oxidant are supplied to the electrodes. This advantage is reinforced by the zero emissions of H_2-fed fuel cells. As for any other real device, degradation (primarily corrosion) of the structural materials and/or malfunction of components limits the durability of fuel cells.

Many kinds of H_2/O_2 fuel cells have been developed in the last decades. They are usually classified on the basis of the ionic conductor and, in turn on the working temperature.

Proton Exchange Membrane Fuel Cells (PEMFCs) operate at low temperatures (80-100°C) thus presenting fast warm-up times and slow degradation of system components. PEMFCs originally thought for automotive applications are now developed for small-to-medium size (1 – 200 kW_{el}) stationary applications: namely, for residential uses and district facilities, and each time high on-off cycles or high load changes are required. Thanks to their fast start-up time, safety (no caustic liquids are present) and high specific power, these type of FC are particularly suitable for non-industrial applications. PEMFCs require noble metal-based catalysts, typically platinum. Beside the high cost of such materials, their extreme sensitivity to CO poisoning implies the use of very pure hydrogen.

Alkaline Fuel Cells (AFCs) are one of the first fuel cell technologies developed and they were the first type used in the United States in the Apollo program to power life-support systems and in Space Shuttle programs both for producing energy, cooling the Shuttle compartments and producing potable water. In Apollo program the AFC which employed an 85% KOH solution at 200-300°C was used, now normally run at operating temperature below 100°C. The AFC has the highest electrical efficiencies of all fuel cells but it only works properly with very pure gasses which considered the major drawback in most applications.

Phosphoric Acid Fuel Cells (PAFCs) are considered the "first generation" of modern fuel cells. This type of fuel cell is typically used for stationary power generation and, more seldom, in large vehicles like city buses. Since PAFCs work at 150-200 °C, the combined use of a heat recovery system can greatly improve the overall fuel efficiency of the cell. As a drawback, PAFCs present very low specific power and power density.

Molten Carbonate Fuel Cells (MCFCs) and Solide Oxide Fuel Cells (SOFCs) operate at high-temperature (650-100 °C) thus eliminating the need of precious-metal catalyst. These systems present a very slow start-up and require an effective thermal insulation. For these reasons MCFCs and SOFCs are suitable for stationary system and are becoming progressively attracting because the produce high temperature steam.

	PEMFC	AFC	PAFC	MCFC	SOFC
Electrolyte	Ion exchange membrane	Potassium hydroxide	Phosphoric acid	Molten carbonate	Ceramic
Temperature range / °C	60-120	<100	160-200	600-800	800-1000
Fuel	Hydrogen	Hydrogen	Hydrogen	Natural gas, coal gas, biogas	Natural gas, coal gas, biogas
Electric efficiency %	40-50	60	40-50	50-55	50-60
Power	100W-500kW	10-100kW	Up to 100MW	100MW	Up to 100MW
Application examples	Vehicles, stationary power systems	Vehicles, military and space applications	Vehicles, stationary power systems	Power plants	Stationary power systems

Table 2: Fuel cells under development. PEMFC: Proton Exchange Membrane FC; PAFC: Phosphoric Acid FC; MCFC: Molten Carbonate FC; SOFC: Solid Oxide FC.

The advantages of fuel cells in comparison with conventional energy production devices are manifold. In particular the benefit over vehicles run by combustion engines consists of higher efficiencies and in the absence of polluting emissions. In the case of stationary energy generation, fuel cell systems present higher efficiencies and reduced emissions compared with the conventional heat and power plants but also represent a fundamental contribution to decentralized electricity production and to the stability of the electric grid. If the hydrogen fed in stationary applications is produced without CO_2 emissions (*i.e.* by water electrolysis), the overall energy cycle does not produce pollutants at all [8].

As already mentioned, PEMFC are best suited for mobile and stationary applications which require frequent load changes and/or heavy on-off cycles. The low operating temperature implies the use of very active electrocatalysts for both the half-reactions.
A general scheme of PEMFCs is shown in the next figure:

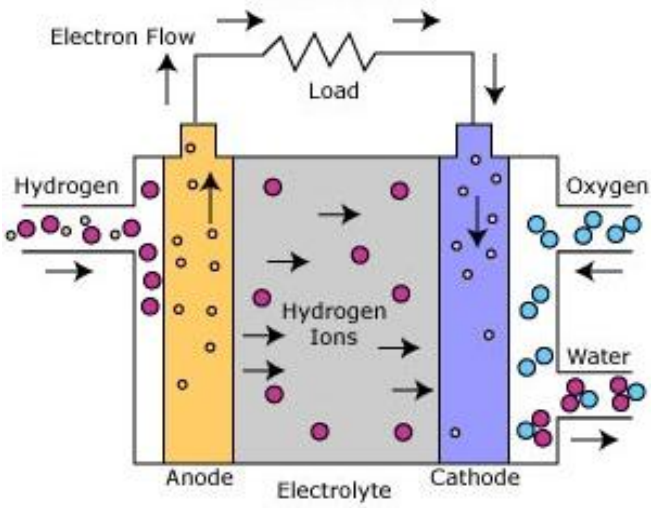

Figure 19: Scheme of a single-cell fuel cell.

The cell reactions are:

$H_2(g) \rightarrow 2H^+(aq, an) + 2e^-$ (negative pole) (10)

$½\ O_2(g) + 2H^+(aq,cat) + 2e^- \rightarrow H_2O(l,cat)$ (positive pole) (11)

$2H^+(aq,an) \rightarrow 2H^+(aq,cat)$ (transport across membrane) (12)

The overall reaction is then:

$½\ O_2(g) + H_2(g) \rightarrow H_2O(l)$ (13)

While H_2 oxidation is known to be fast on Pt-based electrocatalysts, a significant voltage loss occurs at the cathode. Therefore, extensive effort is currently made to develop a high-performance & low-cost catalysts for the O_2 reduction reaction.

1.4.4-Reversible fuel cell (RFC) and Unitised Regenerative Fuel Cell (URFC)

One of the main drawbacks of renewable energy sources is that their availability is often intermittent. This problem can be overcome by connecting a local energy storage system and conventional batteries have been used so far for this purpose, but the storage costs increase significantly with storage capacity. This, in turn, has prompted the research toward a unified cell to be operated on demand either as electrolyser, to generate hydrogen gas, or as fuel cell, by using the stored hydrogen, to generate electricity. This kind of devices is generally known as Reversible Fuel Cell (RFC) or Unitised Regenerative Fuel Cell (URFC).

The complete system, based on RFCs, implies a hydrogen production unit, a storage device and a unit which converts the chemical energy stored to electricity (Figure 20a).

A much smaller and compact system is obtained with the URFC (Figure 20b), where the electrolyser and fuel cell are combined into one unit and only one of the two modes can be operated at one time.

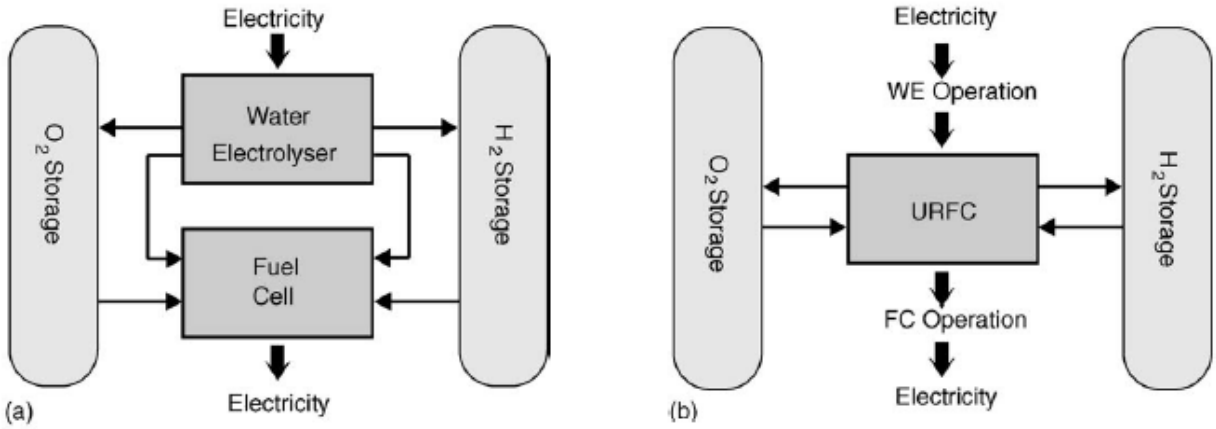

Figure 20: Scheme of (a) Regenerative Fuel Cell (RFC) (b) Unitised Regenerative Fuel Cell (URFC) [42][41].

Since URFC system present high specific energy, they are being designed and developed for a variety of applications that range from high altitude long endurance (HALE) to solar rechargeable aircraft (SRA), zero-emission vehicles (ZEVs), hybrid energy storage/propulsion systems for spacecraft, energy storage for remote (off-grid) power sources, peak shaving for on-grid applications, and portable power systems [42][44][45].

RFC and URFC present many advantages with respect to conventional batteries like zinc/air, zinc/manganese oxide, lead–acid, nickel/metal hydride, etc.

Stored as hydrogen, the energy can be retained for long periods of time and is insensitive to cycle life, temperature, or self-discharge. These advantages can provide both an improvement of energy storage utility for existing applications and can create new opportunities [46].

While lead–acid batteries are now the mature and dominant technology for energy storage, the H_2/O_2 RFC is only one of the several emerging energy storage technologies that are under active development including:

- Lithium polymer batteries;
- Zinc–bromine batteries;
- Nickel–zinc batteries;
- Sodium–sulphur batteries;
- Zinc–air fuel cells;
- Supercapacitors;

- Flywheels;
- Superconducting Magnetic Energy System (SMES).

These technologies span over a wide range of power and energy applications, from the conventional standby role to provision of very high levels of power supplied for a short time. The principal parameters (specific energy and energy density) used to characterize the energy storage system are summarized in Table 3.

Technology	Specific power	Specific energy
Zinc-Air batteries	~100 W kg^{-1}	110-200 Wh/kg
Lithium-bases batteries	100-300 W kg^{-1}	100-150 Wh kg^{-1}
Zin-Bromide batteries	~100 W kg^{-1}	56-70 Wh kg^{-1}
Nickel-Zink batteries	10-600 W kg^{-1}	30-60 Wh kg^{-1}
Sodium sulphur batteries	110-140 W kg^{-1}	90-120 Wh Kg^{-1}
Pb-acid	80-200 W kg^{-1}	1-50 Wh kg^{-1}
Advanced Flywheels	0.5-10 kW kg^{-1}	10-100 Wh kg^{-1}
Conventional Flywheels	0.1-1 kW kg-1	10-30 Wh kg^{-1}
nickel metal hydride batteries	~160 W kg^{-1}	~70 Wh kg^{-1}
Supercapacitors	1-10 kW kg^{-1}	≤5Wh kg^{-1}
H_2/O_2 or H_2-air RFC	0.1 kW kg^{-1}	400-1000 at 200 bar 100-150 at 10-20 bar

Table 3: The H_2/O_2 RFC and other energy storage technologies [46]

As shown here, only RFCs, Zn-Air and Lithium-bases batteries present very high specific energy. However the costs of components system are the principal obstacle of the marketing.

1.4.5-Electrode structures for water electrolysers, FCs, and URFCs

A good electrode is one that correctly balances the transport processes required under working conditions as water electrolyser, fuel cell and URFC.

The transport processes are [47]:

1. protons across the membrane and through the catalyst;
2. electrons from/to the current collector and the catalyst;
3. the reactant and product gases from/to the catalyst layer.

Protons, electrons, and gases individuate the three phases that have to be combined into a catalyst layer. In the optimization of an electrode design a balance between the amount of electrocatalytic material, electronic current collector and proton conductor has to be reached to reduce transport losses.

In this study, an "ink" composed by the electrocatalytic powder, the ionomer additive (Nafion® emulsion) and iso-propylic alcohol was deposited directly onto the perfluorosulphonated membrane. The contact area between the Nafion® membrane and the catalyst is increased by improving the dispersion of the ionomer throughout the catalyst layer.

The thickness of the catalytically active region is usually determined by depth of proton penetration, which in turn is a function of the specific protonic conductivity, the volume fraction and the distribution of the ionomeric electrolyte within the electrode structure. However the increasing the volume fraction of the ionomeric electrolyte also increases the thickness of the electrode and hence the mass transport barrier and the electronic impedance of the electrode same. Thus the volume fraction of ionomer cannot exceed a threshold value, above which the potential drop across the catalytic layer starts to dramatically increase.

The gas diffusion thorough the catalyst layer is hindered by the presence of water and/or ionomer within the pores. However, the permeability of oxygen trough the ionomeric film is acceptable if the diffusion pathways remain below 5 μm [48].

The overall effects suggest that the optimal catalyst layer should be very thin and posses a high volume density of small catalyst particles with the remainder of the volume partially filled with the ionomer. The presence of voids or unfilled pores in the film would favour the gas permeation in the catalytic layer.

1.4.6-Electrocatalyst for Oxygen Evolution Reaction in Acidic Media

The oxygen evolution reaction (OER) is the anode reaction usually coupled with most electrochemical processes in aqueous media. Unfortunately, OER is known to occur with rather high overvoltages. The standard potential for the oxygen electrode is 1.23 V RHE and falls above the standard potentials of almost all the solid elements, so that only a few materials can be considered stable in acidic solution. The OER involves complex pathways of high activation energy and high energetic intermediates. On a bare metal (M), water adsorption and related oxygen species cover the surface before the liberation of O_2 and since the M-O bond strength is always stronger than the O-O dissociation energy, the OER always takes place at an oxide surface [26].
In the following scheme, the reaction mechanisms proposed for OER are summarized:

1) Electrochemical oxide mechanism	***Step (E=Electrochemical, C=Chemical)***
1.1 $S + H_2O \rightleftarrows S\text{-}OH_{ads} + H^+ + e^-$	E
1.2 $S\text{-}OH_{ads} \rightleftarrows S\text{-}O + H^+ + e^-$	E
1.3 $2\ S\text{-}O \rightleftarrows 2\ S + O_{2\,(g)}$	C

2) Chemical oxide mechanism

2.1 $S + H_2O \rightleftarrows S\text{-}OH_{ads} + H^+ + e^-$	E
2.2 $2S\text{-}OH_{ads} \rightleftarrows S\text{-}O + S + H_2O$	C
2.3 $2\ S\text{-}O \rightleftarrows 2\ S + O_{2\,(g)}$	C

3) Krasil' Schikov's mechanism

3.1 $S + H_2O \rightleftarrows S\text{-}OH_{ads} + H^+ + e^-$	E
3.2 $S\text{-}OH_{ads} \rightleftarrows S\text{-}O^- + H^+$	C
3.3 $S\text{-}O^- \rightleftarrows S\text{-}O + e^-$	E
3.4 $2\ S\text{-}O \rightleftarrows 2\ S + O_{2\,(g)}$	C

4) Yeager mechanism (observed in alkali)

4.1 $M^z + OH^- \rightleftharpoons M^z\text{-}OH + e^-$ E

4.2 $M^z\text{-}OH \rightleftharpoons M^{z+1}\text{-}OH + e^-$ E

4.3 $2\ M^{z+1}\text{-}OH + 2\ OH^- \rightleftharpoons O_2 + 2\ H_2O + 2\ M^z$ C

For a given mechanism *b* assumes different values in dependence on the rate determining step, *rds*, and on the surface coverage, θ, of the intermediate compounds. The values in the following scheme refers to the limiting cases $\theta \rightarrow 0$ (low η) e $\theta \rightarrow 1$ (high η).

Mechanism	Step	*b* at low η (mV decade^{-1})	*b* at high η (mV decade^{-1})	Reaction order
1	1.1	120	120	4
	1.2	30	∞	2
	1.3	15	∞	1
2	2.1	120	120	2
	2.2	40	120	2
	2.3	15	∞	1
3	3.1	120	120	2
	3.2	60	60	2
	3.3	40	120	2
	3.4	15	∞	1
4	4.1	120	120	2
	4.2	40	120	2
	4.3	15	∞	1

Table 4: rds values for the four OER mechanisms.

The proposed scheme clearly shows that the role of the adsorbed intermediates is quite important. If the intermediate is weakly adsorbed, it is easily removed and cannot participate to the subsequent step. If otherwise it is too strongly bonded, it will hardly desorbed, thus lowering the rate of the overall reaction. This is the qualitative explanation of the volcano plots, usually encountered both in catalysis and in electrocatalysis. In the case of OER, the volcano plot consists on the correlation between the value of the enthalpy of adsorption of atomic oxygen and the overpotential recorded (at constant current density) on selected materials. Figure 21 reports the volcano plot for OER.

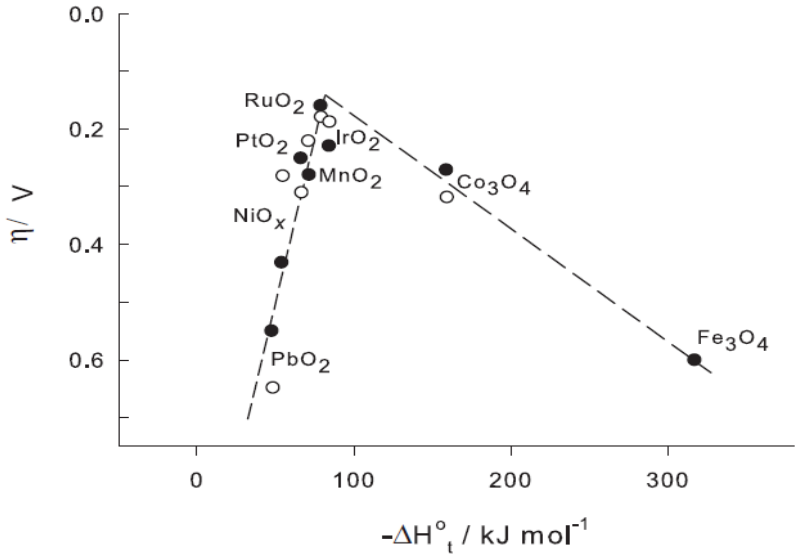

Figure 21: Volcano plot for OER [49].

Note that no metals are considered in Figure 21 since every element is in an oxidized form (at least at the surface) at the potentials at which OER occurs. Obviously, the behaviour of the various oxides is in direct dependence on their electronic configuration. It is well known that in aqueous solutions oxides are covered by OH groups (laying in the so-called oxide layer [50]) having Brønsted acid-base properties:

$$-MOH_2^+ = -MOH + H^+ \quad (14)$$

$$-MOH = -MO^- + H^+ \quad (15)$$

To quantify the acidic properties of the material, the intensive (independent on the surface area) parameter "point of zero charge" (PZC) is defined and represents the condition at which the net charge on the oxide layer is zero. This condition, in turn, may be met by varying the pH of the solution in contact with the oxide material.

Being an intensive parameter, PZC may help in separating the true electrocatalytic, electronic factors from the purely geometric ones (*e.g.* surface area). Thus, PZC completes the information embedded into the slopes *b* of the Tafel lines, whose determination alone is not sufficient to elucidate the whole reaction path. As reported by Ardizzone and Trasatti [51] there is a linear relationship between the PZC and the electronegativity values of a large variety of metallic oxides (see Figure 22). Electronegativity was defined as:

$$\chi_{OX} = \left(M^x O^y\right)^{1/(x+y)} \quad (16)$$

for an oxide of formula M_xO_y where M and O are the Mulliken electronegativities of the metal and oxygen respectively.

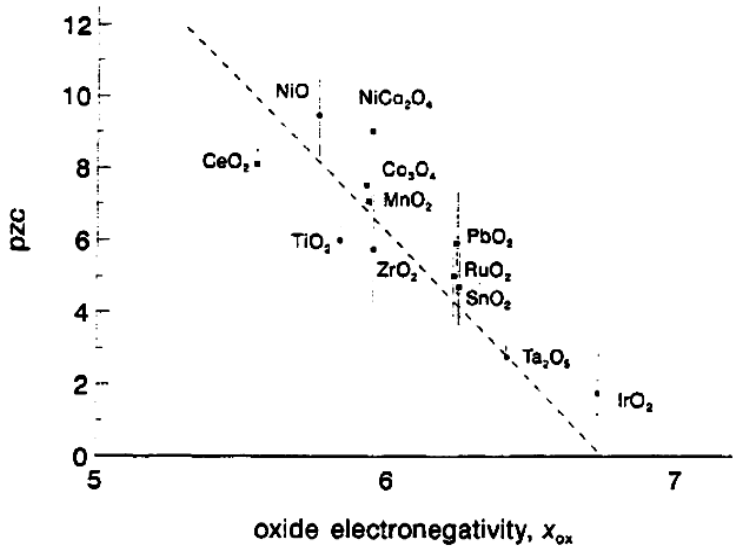

Figure 22: PZC of some oxides as a function of the electronegativity [51].

In particular, at high electronegativity and the low PZC values corresponds the high stability in acidic solutions. Moreover, as observed by [52] the lower the PZC the higher the XPS chemical shift (see Section 2.3.4) and hence the higher the oxygen-metal interactions.

Several oxides have been proposed as electrocatalysts for OER in acid media: IrO_2, RuO_2, PtO_2, MnO_2. In fact, all of them are placed on the top of the volcano curve. Among them, RuO_2 is the most active one, followed by IrO_2 which, in turn, is the most stable in acid media [53]. Consequently, IrO_2 represents the most promising material but, because of its high cost, it must be diluted in a cheap, acid-proof diluent matrix. Several mixed oxide systems have been studied, such as IrO_2+SnO_2[54][57], IrO_2+Ta_2O_5 [58]-[64], IrO_2+Sb_2O_5+SnO_2 [65][66], with the aim of improving both the stability and the electroactivity of the catalyst. In particular, SnO_2 has been used to stabilize iridium-based electrodes with good results [68]. Therefore, in this thesis IrO_2+SnO_2 mixed oxides were prepared in order to analyse the dependence of their electrocatalytical properties on different modulable parameters of the sol-gel synthesis and on the IrO_2 content.

1.4.7-Electrocatalyst for Oxygen Reduction Reaction in Acidic Media

Electroreduction of oxygen is one of the key reactions in electrochemistry because of the central role it plays in fuel cell, corrosion, and industrial processes [67]. Many materials and coatings have been investigated with the aim of developing cheap ad effective electrocatalysts.

The detailed mechanism of ORR is still controversial. In fact, the number and the nature of every reaction step and the overall mechanistic route in the reduction of O_2 to H_2O is still uncertain, especially because it likely depends on the electrode material. Moreover, adsorption of O_2 and many other oxygenated intermediates also occurs, thus further complicating the interpretation of experimental data [69].

However, a generalized mechanism for the ORR in acidic media has been proposed by [70][71] and is presented in the subsequent scheme:

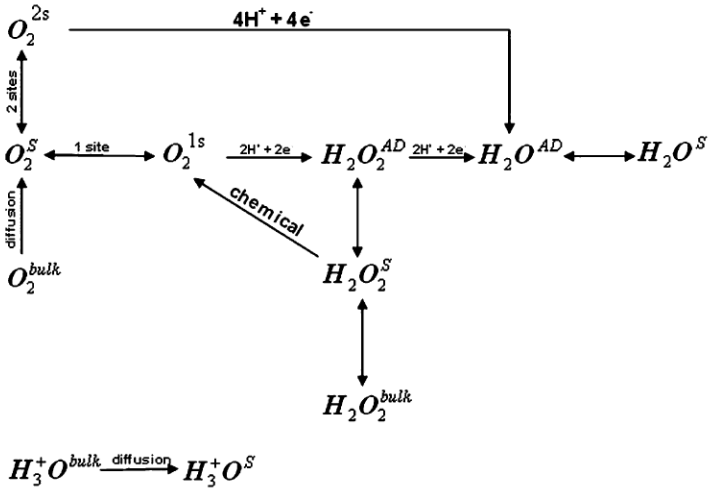

Figure 23: Mechanism for electrochemical reduction of molecular oxygen in acidic media [71].

After molecular oxygen diffuses toward the electrode surface, it is chemically adsorbed in a way that depends on the surface, interacting with either one, O_2^S, or two, O_2^{2S}, catalytic sites. Consequently, two pathways are possible [71][69]:

1. the so called " peroxide pathway", in which oxygen is reduced to water in two step:

$$O_2 + 2H^+ + 2e^- \rightarrow H_2O_2 \qquad E°=0.68 \text{ V } vs \text{ SHE} \qquad (17)$$

$$H_2O_2 + 2H^+ + 2e^- \rightarrow H_2O \qquad E°=1.77 \text{ V } vs \text{ SHE} \qquad (18)$$

$$2H_2O_2 \rightarrow H_2O + O_2 \qquad (19)$$

This mechanism in known to occur on Hg, Au, and C. Moreover, to complete the 4-electron pathway to water, any hydrogen peroxide that is formed would have to undergo rapid 2-electrons reduction to water.

2. the so-called "direct pathway" in which four electrons are exchanged and oxygen is reduced directly to water:

   $O_2 + 4H^+ + 4e^- \rightarrow H_2O$ $\quad E° = 1.23$ V *vs* SHE (20)

   In particular, in the case of a metal M, an initial dissociative chemisorption (equation 21), (*i.e.* the splitting of the O-O bond to form adsorbed oxygen atoms) occurs.

   $2M + O_2 \rightleftharpoons 2M\text{-}O_{ads}$ (21)

   The adsorbed oxygen atoms are then electroreduced to water (equation 22):

   $2\ M\text{-}O_{ads} + 4H^+ + 4e^- \rightleftharpoons 2M + H_2O$ (22)

   Besides, the last step involves several elementary steps.

The second mechanism can be viewed as the direct "oxidation" of the metal atom, M, followed by the electrochemical reduction of the oxide. From a simple analysis of these two reactions, we can suppose that metals for which the M-O bond energy is high, present very negative reduction potentials, generally too negative to be interesting in the operative devices [69].

The Gibbs free energies for reaction 21 versus the standard potential of reaction 22 for several metals and their relevant oxides in the +2 oxidation state are reported in the following figure:

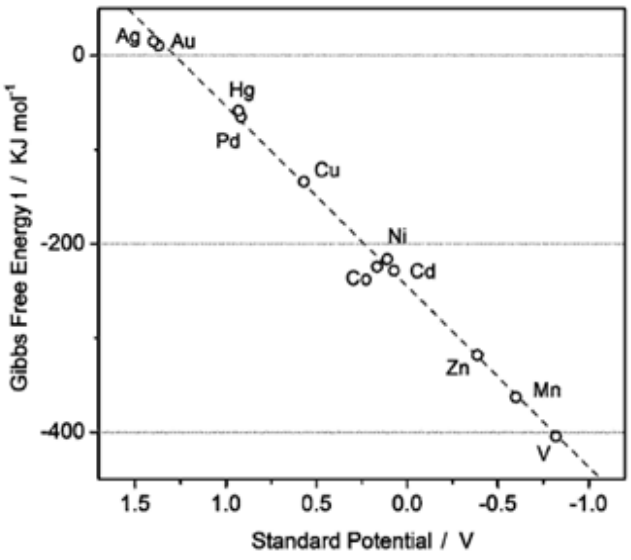

Figure 24: Graph of the Gibbs free energy for reaction 21 versus the standard potential of reaction 22.

The graph clearly demonstrates that metals on the right side of the *x*-axis, *i.e.* those presenting lowest standard potentials, form stabile M-O bond. On the contrary, reaction 21 is

thermodynamically unfavoured on metals who present high standard potentials. These metals form less stable, more easily reducible M-O bonds.

Data reported in Figure 24 can provide initial useful information for selecting the metals which will exhibit a good activity toward the ORR.

Pt and Pt-alloys are still considered the most active catalysts for low-temperature fuel cells. Compared to the standard value of 1.23V *vs* RHE at 298K, the oxygen cathode in a fuel cell has a working potential typically below 0.8V so that, in the best case, overpotentials amount to 400 mV [67][69].

Therefore, research for abundant, inexpensive, and efficient electrocatalytic materials as substitutes for Pt-based oxygen cathodes in polymer electrolyte membrane fuel cells (PEMFC) is currently very intense. In particular, different Pt-free catalysts have been performed such as: Co-based catalysts [71]-[73], Fe-based catalysts [74], various binary and ternary combinations of Pd, Au, Ag, and Co [67][69], Au and Bi-modified Au surface [75].

In particular an improvement of electrocatalytic material was obtained with bimetallic alloys, which combine a good oxygen bond cleaving metal (M) with a second metal (M') on which the adsorbed oxygen (M'-O_{ads}) reduction is more efficient, *i.e.* occurs at a more positive potential [69]. A schematic picture of the process is illustrated in Figure 25.

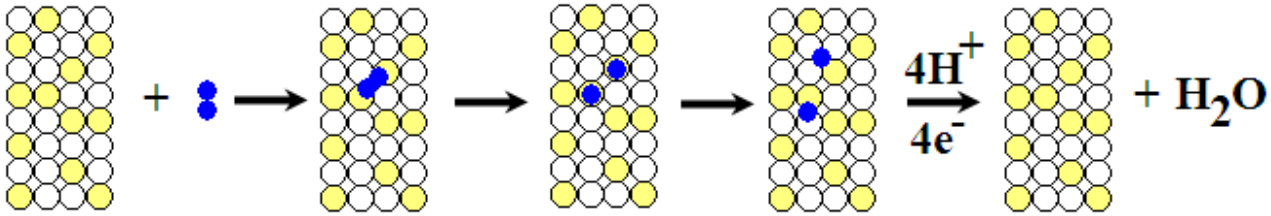

Figure 25: Scheme of mechanism proposed. Yellow circles represent good oxygen bond cleaving metal atom (M) and white circles represent metal atoms that reduce adsorbed oxygen efficiently (M'). Small blue circles represent oxygen atoms [69].

In the proper nanoscale system, migration from the top site of M to a 3-fold site involving M' would be possible since oxygen could be more stable in such a 3-fold site.

In order to develop a reversible fuel cell system an electrodic material able to catalyze both OER and OER is necessary. Since the IrO_2-based electrocatalysts show a good behaviour toward OER, they are also characterized toward ORR.

1.4.8-Electrocatalysts for URFC systems

Since the cell design and the materials used in Solid Polymer Electrolyte water electrolysis present many similarities with those used in PEMFC, the possibility of building the so-called regenerative fuel cells, *i.e.* systems which can be used both as water electrolyser and fuel cell [42], becomes even more attractive. The unitized regenerative fuel cell (URFC) system use single electrochemical cell that can work both as fuel cell and water electrolyser. Most of the energy dissipations in the URFC are caused by the oxygen redox reaction; *i.e.* ORR during the working period as fuel cell (FC) and OER during the working period as water electrolyser (WE). Therefore, the development of an active catalyst for the oxygen redox reaction is quite important for improving the efficiency of the URFC [76]. The bifunctional electrocatalyst must also be chemically stable under operative conditions. Several studies have already highlighted that noble metals and their oxides are promising oxygen electrode catalysts for URFCs, on the basis of their activity and stability. In the previous section, it was affirmed that the best electrocatalyst for ORR is platinum. Recent studies [77]-[79] pointed to iridium oxide (IrO_2) as a good candidate for ORR too. Since it is also well known as the best electrocatalysts for OER, it follows that it is a good candidate as bifuncional electrocatalyst for URFC. Therefore, in this thesis, IrO_2-SnO_2 mixed oxides prepared by sol-gel synthesis were investigated also toward ORR.

So far, many other bifunctional electrocatalysts were proposed for oxygen redox reactions. These include Pt–Ir [80], Pt–Ru–Ir [81][81], Pt–IrO_2 [82][83] and Pt–IrO_2–RuO_2 [84][40].

However, it is quite difficult to compare URFC performances because of the high variety of conditions adopted by the different authors in both the preparation and the characterization of the studied systems.

1.5-Industrial waste treatment

Volatile organic halides (VOH) are a large family of substances that show very high toxicity and are present in a wide spectrum of waste types: from concentrated organic solutions and emulsions to very dilute aqueous phases, to airborne streams. The development of suitable treatment methodologies constitutes a serious challenge. In this context, the high electrocatalytic properties of silver towards organic halide electroreduction have been successfully applied to VOH degradation.

1.5.1-Electrocatalysts for VOH electroreduction: silver electrocatalytic properties

Despite the several biological and physico-chemical methods proposed so far for VOH degradation, none of them is free from significant drawbacks, *e.g.* formation of undesirable by-products, excess of reagents, exhaustion of absorbing substrates, which require additional treatment steps.

Thanks to their higher selectivity, milder reaction conditions and simpler process design and operation, electrochemical methods can play a key role in environmental protection and remediation. The development of electrochemical methods is based on the research of electrocatalytic materials for electroreduction of polluting substances. The metal used as catalyst determines both the reduction efficiency and the products of the reaction. Several metals have been tested: Pt, Pd, Ag, Cu, Ni, Fe, Pb. Between them, silver presents the best electrocatalytic properties, as extensively documented in the past 10–15 years [85]-[90]. This aspect is evident by comparing the voltammetric reduction potential peaks recorded on an inert, non-electroactive electrode like glassy carbon (GC) and on Ag. Silver presents an evident shift (~0.4 ÷1.2 V) toward less negative potentials in the reduction of different substrates (Figure 26):

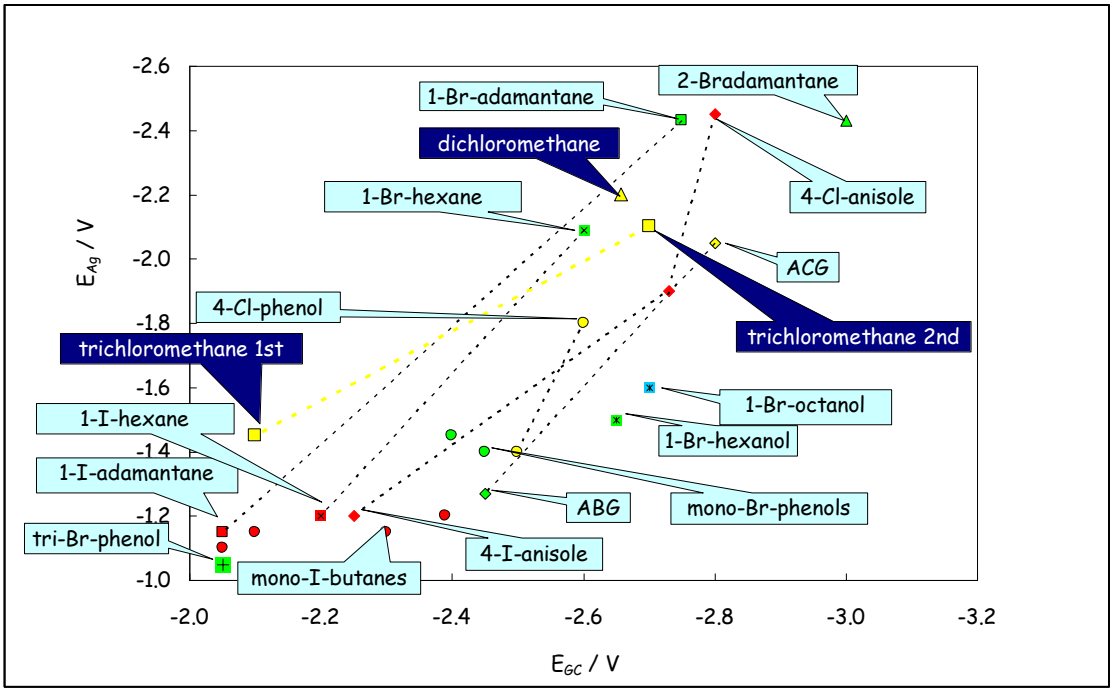

Figure 26: Reduction potentials of different substrates obtained with GC electrode and silver electrode.

This remarkable behaviour of silver allows the decrease of specific energy consumption of processes, thanks to the concomitant reduction of cell voltage and increase in current efficiency and

substrate conversion. This aspect is supposed to be bound to the well-known specific interactions of silver with halide anions [91]-[94]. These interactions are governed by the Ag surface state and its modifications correlated to the reaction medium composition (*i.e.* the halide leaving group, the structure of the organic moiety, the solvent and the supporting electrolyte). In particular, the electrocatalytic activity of silver was reported to increase with increasing surface roughness [95] [96], thus prompting the research toward the development of micro- and nano-sized electrode materials.

Although the electrochemical dehalogenation of VOHs has been widely investigated at various catalytic cathodes and in several media (aqueous and non-aqueous), a complete understanding of the hydrodehalogenation mechanism is still lacking. For the breaking of R-X bond, two paths have been proposed [97][98][99]:

1. Stepwise mechanism: an intermediate radical anion is formed before the C-X bond breaking

   $RX + e^- \leftrightarrows RX^{\bullet -} \rightarrow R^{\bullet} + X^-$ (23)

2. Concerted mechanism: the electron transfer (ET) and the C-X cleavage occurs simultaneously

   $RX + e^- \rightarrow R^{\bullet} + X^-$ (24)

In dependence on the substrate and on the working conditions (solvent, supporting electrolyte, electrode material and potential), a second ET reaction leads to the organic anion:

$R^{\bullet} + e^- \rightarrow R^-$ (25)

Both the anion and the radical can react with the solvent, hydrogen or proton donors, other RX molecules or the organic solvent to give propagation reaction products like dimers and hydrodehalogenated species, as in reactions:

$R^{\bullet} + R^- + HA \rightarrow RH + A^{\bullet}\ (A^-)$ (26)

$R^- + RX \rightarrow R\text{-}R + X^-$ (27)

$R^{\bullet} + R^{\bullet} \rightarrow R\text{-}R$ (28)

Reactions (24) or (25) generally represent the slow steps in the reduction process [17], while reaction (26) is considered very fast and occurs at less negative potential than the first step. Consequently, the CV curves generally exhibit highly irreversible 2-electron peaks for each halide leaving group.

1.5.2-Trichloromethane

In the present study, trichloromethane (also known as chloroform) has been considered as a model substrate. Its physico-chemical properties are shown in the subsequent table:

Chemical or physical property	Value
Molecular formula	$CHCl_3$
Molecular weight (g/mol)	119.38
Physical state at 101.3 kPa	Clear, colourless liquid at 20°C
Melting point (°C) at 101.3 kPa	-63.2
Boiling point (°C) at 101.3kPa	61.3
Density (g/cm^3)	
0°C / 4°C	1.526
25°C / 4°C	1.481
60.9°C / 4°C	1.408
Water solubility (mg/L) at 25°C	7230
Vapour pressure (Pa)	
0°C	8130
10 °C	13400
20°C	21280
30°C	32800
Henry's law constant ($Pa\ m^3$ / mol)	
20°C	303.97
24.8 °C	317.86
Octanol/water partition coefficient (log k_{ow})	1.97
Organic carbon / water partition coefficient (log k_{oc})	1.44-2.79

Table 5: Chemical-physical properties of trichloromethane.

$CHCl_3$ has several industrial uses, including the production of refrigerants for home air conditioners and large commercial freezers, as reagent and solvent in many industrial chemical processes and as a precursor for dyes and pesticides. Moreover, trichloromethane is a by-product of the chlorination of drinking waters and wastewaters, and in the disinfection of domestic and public wells. As a result, it is one of the most frequently detected VOC in ground waters [100].

The main sources of trichloromethane are anthropogenic and are quantified in the next figure:

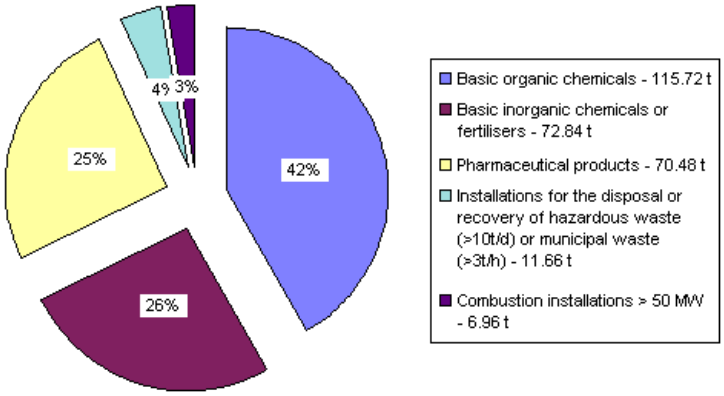

Figure 27: Trichloromethane sources in Europe in the 2004 [12].

The quantity of trichloromethane produced by industries in Europe is reported in the next figure [12]:

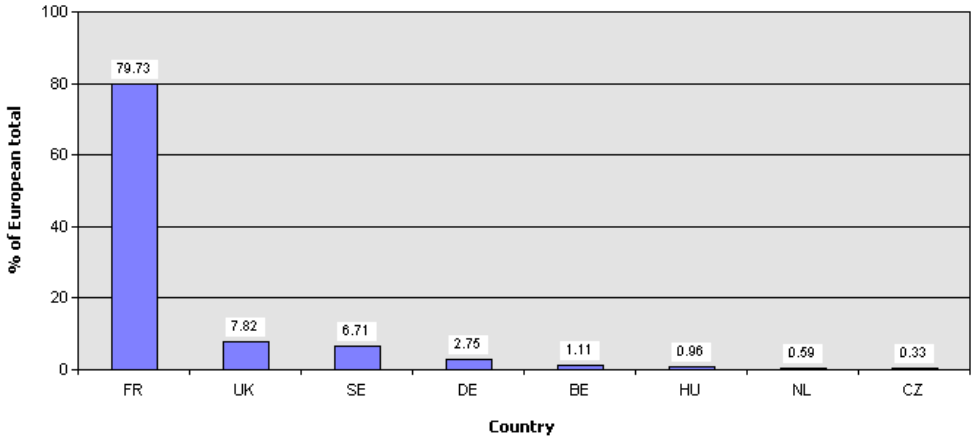

Country	Total emission	% of European total
Czech Republic	0.93 t	0.33
Netherlands	1.64 t	0.59
Hungary	2.66 t	0.96
Belgium	3.08 t	1.11
Germany	7.64 t	2.75
Sweden	18.62 t	6.71
United Kingdom	21.71 t	7.82
France	221.38 t	79.73

Figure 28: Trichloromethane production in the Europe in 2004 [12].

In this study the trichloromethane electroreduction was investigate both in non-aqueous and aqueous method. In particular a first study was carried out in organic solvent, acetonitrile, supported silver prepared using different electrolytic bath: 0.05 M $KAg(CN)_2$ and 0.1 M $AgNO_3$ both in water.

In the second part the characterization of silver nanopowders synthetized using six different surfactants (protecting agent) in aqueous media was carried out.
In order to obtain a comparison among all silver electrodes a commercially available silver micro-sized powder was also tested in both media.

Following the (23)-(28) scheme, the trichloromethane electroreduction on Ag cathodes and in non-aqueous media can be schematised in terms of mono- and bi-electronic paths, as follows:
mono-electronic path

$CH\text{-}Cl_3 + e^- \rightarrow \cdot CH\text{-}Cl_2 + Cl^-$ (29)

$2 \cdot CH\text{-}Cl_2 \rightarrow Cl_2\text{-}HC\text{-}CH\text{-}Cl_2$ (30)

which accounts for the formation of dimers
bi-electronic path

$CH\text{-}Cl_3 + e^- \rightarrow \cdot CH\text{-}Cl_2 + Cl^-$ (31)

$\cdot CH\text{-}Cl_2 + e^- \rightarrow :CH\text{-}Cl + Cl^-$ (32)

$:CH\text{-}Cl + 2\ H\cdot \rightarrow CH_3\text{-}Cl$ (33)

$2\ :CH\text{-}Cl \rightarrow Cl\text{-}HC{=}CH\text{-}Cl$ (34)

$\cdot CH\text{-}Cl_2 + e^- \rightarrow CH\text{-}Cl_2^-$ (35)

$CH\text{-}Cl_2^- + HA \rightarrow CH_2\text{-}Cl_2 + A^-$ (36)

which accounts for the formation of dimers *via* carbanion or bi-radical forms.
Anyhow, previous studies [101] performed in acetonitrile have on one side excluded the formation of the bi-radical intermediate and on the other side highlighted the importance of adding even a small quantity of water as effective proton donor to avoid electrode poisoning.

In aqueous media the reaction stoichiometry is given by:

$CHCl_2Cl\ (g) + 2e^- + H^+\ (aq) \rightarrow CHCl_2H\ (g) + Cl^-(aq)$ (37)

$CH_2ClCl\ (g) + 2e^- + H^+\ (aq) \rightarrow CH_3Cl(g) + Cl^-(aq)$ (38)

$CH_3Cl\ (g) + 2e^- + H^+\ (aq) \rightarrow CH_4\ (g) + Cl^-(aq)$ (39)

which sum up to:

$CHCl_3\ (g) + 6e^- + 3H^+\ (aq) \rightarrow CH_4\ (g) + 3Cl^-(aq)$ (40)

As previously reported in [18][102] the electroreduction of trichloro- and dichloro-methane on silver yields methane as main product.

1.6- Work summary

This work is articulated in two main parts. The first one consists in the synthesis, characterization and reactivity of disperse phase, IrO_2-based electrode materials for URFCs.

The choice of synthesising disperse phase materials offers several advantages not only during the synthetic steps, but also in the preparation of the working electrodes, thanks to easier mixing with others components, dispersion in diluents matrices etc. In addition, the sol-gel methodology offers a wide spectrum of synthetic parameters to achieve the fine tuning of bulk and surface composition and morphology of the target materials.

The powder characterization was performed by both physico-chemical *ex-situ* techniques and electrochemical *in-situ* techniques followed by the investigation of the reactivity toward both Oxygen Evolution Reaction and Oxygen Reduction Reaction of both disperse phase materials and working electrodes.

Materials with different total iridium oxide content were synthesised using different calcination temperatures and methods for adding the iridium salt during the synthetic procedure. In particular $IrCl_3$ is added to either the SnO_2 xerogel or to the tin precursor, so that three main methodologies, with their possible branches, are individuated (see Section 2.1.1).

Physico-chemical characterizations of the powders were carried out by: X-Ray Diffraction (XRD), X-Ray Photoelectron Spectroscopy (XPS), B.E.T. surface area determination by N_2 adsorption/desorption and Scanning Electron Microscopy (SEM) techniques in order to obtain information about the structure, morphology and bulk and surface phase and chemical composition.

For the electrochemical characterization the powders were supported on the Cavity-Micro Electrode (C-ME) and the tests were carried out by cyclic voltammetry in the potential window between OER and ORR in order to avoid the turbulent gas evolution that could affect the electrode response. The principal advantage of the use of C-ME is the possibility of study the powder behaviour without the use of any gluing agent that could interfere with the electrochemical behaviour. This methodology leads to the determination of the key parameter represented by the total number of active sites of the electrocatalytic material.

The reactivity toward OER was evaluated using in-house designed and manufactured electrolytic cells. These cells, denoted in the following as “immersion cell” and as “flux cell”, have a common plate-and-frame structure but differentiate for the modality of the water supply and for the current-collector design and material. In the former, the whole apparatus is fully immersed in a water tank

and the current-collectors are porous Ti sinters. In the latter, the water is pumped through the cell, sealed by fitting, and the graphite end-plates act also as current-collectors.

Both Membrane Electrode Assemblies (MEAs) and Gas Diffusion Electrodes (GDEs) were considered as anode structures. In the former case powders were deposited directly onto a cationic membrane, in the latter a carbon cloth was adopted as support and current collector distribution. In order to obtain a good adhesion of the catalytic layer to the support the final step consists in hot-pressing at 100°C in dependence on the support. MEAs and GDEs were prepared adopting various iridium oxide loading and polymer electrolyte content in the ink.

The electrochemical behaviour was determined by recording the *U vs I* characteristics at room temperature. Note that the *U*/*I* curves sum up the effect of all the preceding steps, from the synthesis, to the electrode preparation to the cell working conditions.

The reactivity toward ORR was evaluated using a Rotating Disk Electrode that allows to work under controlled mass transfer conditions. In this way the contribution of the mere catalytic properties of the powders can be extrapolated.

The second part of this work is devoted to the studies on silver-based materials, their synthesis/preparation procedures and their performances both in aqueous and non-aqueous media, toward the electroreduction of trichloromethane as model substrate.

In non-aqueous media the silver electrodes were:

- silver layers electrodeposited on Pt disks, using different deposition baths and conditions;
- commercial silver microcrystalline powders (2-3.5 μm).

The microcrystalline Ag powder is supported onto the C-ME, thus allowing for the use of the disperse phase metal and also for the possibility of a quick substitution of the analysed powder to avoid poisoning phenomena.

In aqueous media silver nano-particles, synthetized in the presence of suspending agents were investigated. The Ag nano-particles are then dispersed in an active carbon matrix (Vulcan® XC72R) and the metal loading is maintained below 10wt%. In order to obtain a comparison silver microcrystalline powder was also investigated in the same media.

The aim of this characterization is to evaluate both the effect of the suspending substances on the reactivity and the possibility of reducing the silver content in the nanostructured powders. Preparative electrolyses performed with GDEs based on the above nanoparticles have proven the effectiveness of the electrocalytic behaviour of silver even under disperse conditions.

1.7-References

[1] www.iucn.org. Report of the IUCN Renowned Thinkers Meeting: *"The future of sustainability: Re-thinking Environment and Development in the Twenty-first Century"* 29-31 January **2006.**

[2] http://ec.europa.eu/environment/eussd/ Commission of the European Communities: "*Mainstreaming sustainable development into EU policies: 2009 Review of the European Union Strategy for Sustainable Development*" Brussels, 24 July **2009.**

[3] http://crc.nv.gov/index.asp.

[4] http://www.iea.org/statistics/ International Energy Agency "*Key World energy and statistics"* **2009.**

[5] http://www.trb.org/news/blurb_detail.asp?id=8979 European Commission Directorate-General for energy and Transport *"European Energy and Transport trends to 2030 –update 2007"* 8 April **2008**.

[6] http://ec.europa.eu/eurostat Eurostat European Commission: *"Europe in figures Eurostat yearbook 2009"*, European Communities **2009**, ISSN 1681-4789.

[7] http://www.euchems.org/binaries/030882EnergyReport_tcm23-118847.pdf EuCheMS *"Chemistry and Energy: the role of the chemical science in European energy policy"* April **2008**.

[8] H.-J. Neef *Energy* **2009**, 34, 327.

[9] Michael Ball, Martin Wietschel *Int. J. Hydr. Energy* **2009**, 34, 615.

[10] http://www.usgs.gov/ US Department of the Interior US Geological Survey *"Volatile Organic Compounds in the Nation's Ground Water and Drinking-Water Supply Wells-A Summary"* April **2006.**

[11] Official Journal of the European Communities *"Concil Directive 1999/13/EC of 11 March 1999 on limitation of emissions of volatile organic compounds due to the use of organic solvents in certain activities and installations"* (Article 2 sub 17) 23 March **1999**.

[12] http://www.eper.eea.europa.eu

[13] http://www.apat.gov.it/site/it-IT/Temi/Aria/Emissioni/

[14] http://europa.eu.int

[15] APAT Agenzia per la Protezione dell'Ambiente e per i Servizi Tecnici, Dipartimento Difesa del Suolo/Servizio Geologico D'Italia *"Confronto tra concentrazioni limite accettabili ex DM. 471/99 e concentrazioni soglia di contaminazione ex DLgs.152/06"*.

[16] R. Papp *Pure Appl. Chem.* **1996**, 68, 1801.

[17] G. Chen *Sep. Purif. Technol.* **2004**, 38,11.

[18] S. Rondinini, G. Aricci, Z˘. Krpetic´, C. Locatelli, A.Minguzzi, F. Porta, A. Vertova *Fuel Cells*, **2009**, No. 3, 253.

[19] Alberto Vertova, Rachid Barhdadi, Christine Cachet-Vivier, Cristina Locatelli, Alessandro Minguzzi, Jean-Yves Nedelec, Sandra Rondinini *J. Appl. Electrochem.* **2008**, 38, 965.

[20] Kenneth J. Klabunde "*Nanoscale Materials in Chemistry"* John Wiley and Sons Inc, **2001.**

[21] M. Fernndez-Garca, A. Martnez-Arias, J. C. Hanson, and J. A. Rodriguez *Chem. Rev.* **2004** 104, 9, 4063.

[22] Larry L. Hench, and Jon K. West *Chem. Rev.* **1990**, 90, 33.

[23] H.H. Nersisyana, J.H. Leea, H.T. Sona, C.W. Wona, D.Y. Maenga, *Mat. Res. Bul*. **2003**, 38, 949.

[24] G. Tosun, H.D. Glicjsman, US Patent, 4, 978, 98.

[25] Z. Zhang, B. Zhao, L. Hu, *J. Solid State Chem*. **1996**, 121, 105.

[26] S. Trasatti *Electrochim. Acta*, **1984**, V29, N11, 1503.

[27] J. Gellings, H.J.M. Bouwmeester *"The CRC Handbook of Solid State Electrochemistry"* CRC Press, Inc. **1997**.

[28] Ewan, R.W.K. Allen *Int. J. Hyd. Energy* , **2005**, 30, 809.

[29] Aaron Marshall *"Electrocatalysts for the Oxygen Evolution Electrode in Water Electrolysers using Proton Exchange Membranes: Synthesis and Characterisation"* PhD Thesis Norwegian University of Science and Technology, Department of Materials Technology and Electrochemistry, June **2005.**

[30] http://www.electrolysers.com/

[31] http://www.h-tec.com/html/web/industrial/index.asp

[32] http://www.sespi.it/home-page/

[33] Rod Borup, Jeremy Meyers, Bryan Pivovar, Yu Seung Kim, Rangachary Mukundan, Nancy Garland, Deborah Myers, Mahlon Wilson, Fernando Garzon, David Wood, Piotr Zelenay, Karren More, Ken Stroh, Tom Zawodzinski, X James Boncella, James E. McGrath, O Minoru Inaba, Kenji Miyataker, Michio Hori, Kenichiro Ota, Zempachi Ogumi, Seizo Miyata, Atsushi Nishikata, Zyun Siroma, Yoshiharu Uchimoto, Kazuaki Yasuda, Ken-ichi Kimijima, and Norio Iwashita, *Chem. Rev*. **2007,** 107, 3904.

[34] R.C.Agrawal and G. P. Pandey *J. Phys. D: Appl. Phys* **2008**, 41, 22, 223001.

[35] Carl Jochen Wenetr *Int. J. Hyd. Energy*, **1997**, 22, 847.

[36] Dagobert G. Kessel *J. Pet. Sci. Eng*., **2000**, 26, 157.

[37] Y. Zhang, C. Wang, N. Wan, Z. Liu, Z. Mao, *Electrochem. Comm*. **2007**, 9, 667.

[38] E. Rasten, G. Hagen, R. Tunold, *Electrochim. Acta* **2003**, 48, 3945.

[39] P. Millet, F. Andolfatto, and R. Durand. *Int. J. Hyd. Energy*, **1996**, 21, 87.

[40] Y. Zhang, C. Wang, N. Wan, Z. Mao, *Int. J. Hyd. Energy*, **2007**, 32, 400.

[41] L. Carrette, K.A.Friedrich, U. Stimming *Chem. Phys. Chem.* **2000**, 1, 162.

[42] J. Pettersson, B. Ramsey, D. Harrison *J. Power Sources* **2006**, 157, 28.

[43] L.Carrette, K.A.Friedrich, U. Stimming *Fuel Cell* **2001**, 1 N°1, 5.

[44] Fred Mitlitsky, Blake Myers, Andrew H. Weisberg, Trent M. Molter and William F. Smith *Fuel Cell Bulletin* **1999**, Vol 2, Issue 2, 64.

[45] Fred Mitlitsky, Blake Myers, and Andrew H. Weisberg *Energy & Fuels* **1998**, 12, 56.

[46] W. Smith *J. Power Sources* **2000**, 86, 74.

[47] S. Litster, G. McLean *J. Power Sources* **2004**, 130, 61.

[48] M.S.Wilson, S. Gottesfeld *J Applies Electrochem.* **1992**, 22, 1.

[49] "Comprehensive Treatise of Electrochemistry", Edited by Brian E. Comway, John O'M.Bockris, Ernest Yeager, S. U. M. Khan and Ralph E. White, Volume 7.

[50] J. Duval, J. Lyklema, J. M. Kleijn, H. P. van Leeuwen, *Langmuir*, **2001**, 17, 7573.

[51] S. Ardizzone, S. Trasatti, *Adv. Coll. Interf. Sci*. **1996**, 64, 173.

[52] M.G. Cattania, S. Ardizzone, C.L. Bianchi, S. Carella, *Coll. Surf. A,* **1993**, 76, 233.

[53] A. Alves, L. A. da Silva, E. D. Oliveira, J. F. C. Boots, *Mater. Sci. Forum* **1998**,282, 655.

[54] De Pauli, C. P.; Trasatti, S. *J. Electroanal. Chem.* **1995**, 396, 161.

[55] De Pauli, C. P.; Trasatti, S. *J. Electroanal. Chem*. **2002**, 538, 145.

[56] Marshall, A.; Børresen, B.; Hagen, G.; Tsypkin, M.; Tunold, R. *Electrochim. Acta* **2006**, 51, 3161.

[57] S. Aridizzone, C. L. Bianchi, L. Borgese, G. Cappelletti, C. Locatelli, A. Minguzzi, S. Rondinini, A. Vertova, P.C. Ricci, C. Cannas, A. Musinu *J. Appl. Electrochem.* **2009** 39, 2093.

[58] Xu L, K.; Scantlebury, J. D. *J. Electrochem. Soc.* **2003**, 150, B254.

[59] Xu L, K.; Scantlebury, J. D. *J. Electrochem. Soc.* **2003**, 150, B288.

[60] Hu, J. M., Zhang, J. Q., Meng, H. M., Cao C.N. *J. Mater. Sci.* **2003**, 38, 705.

[61] Hu J. M., Meng, H. M., Zhang, J. Q., Cao, C. N. *Corr. Sci.* **2002**, 44, 1655.

[62] Hu, J. M.; Zhang, J. Q.; Cao, C. N. *Int. J. Hydrog. Energy* **2004**, 29, 791.

[63] Morimitsu, M.; Otogawa, R.; Matsunaga, M. *Electrochim. Acta* **2000**, 46, 401.

[64] Da Silva, L. M.; Franco, D. V.; De Faria, L. A.; Boodts, J. F. C. *Electrochim. Acta* **2004**, 49, 3977.

[65] Chen X, Chen G, Yue PL *J. Phys. Chem. B* **2001**, 105, 4623.

[66] Chen X, Chen G, Yue PL *J. Phys. Chem. B* **2002**, 106, 4364.

[67] J. X. Wang, N. M. Markovic, and R. R. Adzic *J. Phys. Chem. B* **2004**, 108, 4127.

[68] B. Correa-Lozano, Ch. Comninellis, A. De Battisti, *J. Appl. Electrochem.* **1997**, 27, 970.

[69] Jose´ L. Fernàndez, Darren A. Walsh, and Allen J. Bard *J. Am. Chem. Soc*. **2005**, 127, 357.

[70] Olivier Antoine, Yann Bultel, Robert Durand *J. Electroanal. Chem*. **2001**, 499, 85.

[71] William E. Mustain , Jai Prakash *J. Power Sources* **2007**, 170, 28.

[72] M. Lefe`vre, J.P. Dodelet, P. Bertrand, *J. Phys. Chem. B.* **2005**, 109, 16718.

[73] N. P. Subramanian, S. P. Kumaraguru, H. Colon-Mercado, H. Kim, B. N. Popov, T. Black, D. A. Chenb, *J. Power Sources*. **2006**, 157, 56.

[74] M. Lefe`vre, J.P. Dodelet, P. Bertrand, *J. Phys. Chem. B.* **2002**, 106, 8705.

[75] Xiao Li and Andrew A. Gewirth *J. Am. Chem. Soc*. **2005**,127, 5252.

[76] Tsutomu Ioroi, Kazuaki Yasuda, Zyun Siroma, Naoko Fujiwara and Yoshinori Miyazaki *J Power Sources* **2002**, 112, 2, 583.

[77] Yoshio Takasu, Norihiro Yoshinaga, Wataru Sugimoto *Electrochem. Comm.* **2008**, 10, 668.

[78] Norihiro Yoshinaga,Wataru Sugimoto, Yoshio Takasu *Electrochim. Acta* **2008**, 54, 566.

[79] Chia-Chin Changa, Ten-ChinWenb, Chien-Hsin Yangc, Yung-Der Juangd *Materials Chemistry and Physics* **2009**, 115, 93.

[80] T. Ioroi, T. Oku, K. Yasuda, N. Kumagai and Y. Miyazaki, *J. Power Sources* **2003**, 124, 385.

[81] G.Y. Chen, D.A. Delafuente, S. Sarangapani and T.E. Mallouk, *Catal. Today* **2001**, 67, 341.

[82] L.L. Swette, N.D. Kackley, A.B. Laconti, *27th Intersoc. Energy Convers. Eng. Conf.* **1992**, 1, 101.

[83] H. Liu, B.L. Yi, M. Hou, J.F. Wu, Z.J. Hou and H.M. Zhang, *Electrochem. Solid-State Lett* **2004**, **7**, 56.

[84] A. Cisar, O. Murphy, E. Clarke, U.S. Patent 0068544, **2003**.

[85] S. Rondinini, A. Vertova, *"Electrochemistry for the Environment"*, (Eds. Ch. Comninellis, G. Chen), Springer, Berlin, **2008**, Ch.10.

[86] S. Rondinini, P.R. Mussini, P. Muttini, G. Sello, *Electrochim. Acta* **2001**, 46, 3245.

[87] L. Falciola, A Gennaro, A. A. Isse, PR Mussini, M. Rossi, *J. Electronal. Chem.* **2006**, 593, 47.

[88] A. A. Isse, S. Gottardello, C. Durante, A. Gennaro, *Phys. Chem. Chem. Phys.* **2008**, 10, 2409.

[89] Sandra B. Rondinini, Patrizia R. Mussini, Federico Crippa, Guido Sello *Electrochem. Comm.* **2000**, 2, 491.

[90] Sandra B. Rondinini, Patrizia R. Mussini, Marco Specchia, and Alberto Vertova *J. Electrochem. Soc.*, **2001**, 148, 7 D102.

[91] G. Valette, A. Hamelin, R. Parsons, Z. *Phys. Chem. Neue Fol*. **1978**, 113, 71.

[92] ML. Foresti, M. Innocenti, F. Forni, R. Guidelli *Langmuir* **1998**, 14,7008.

[93] Mussini PR, Ardizzone S, Cappelletti G, Longhi M, Rondinini S, Doubova LM, *J. Electroanal. Chem.* **2003**, 552, 213.

[94] Migani A, Illas F *J. Phys. Chem. B* **2006**, 110,11894.

[95] Ardizzone S, Cappelletti G, Mussini PR, Rondinini S, Doubova LM *Russ J Electrochem*, (translation of Elektrokhimija) **2003**, 39,170.

[96] Miranda-Hernandez M, Gonzalez I, Batina N, Gennaro A, *Electrochem. Comm.* 2006, 8, 1707.

[97] C. Costentin, M. Robert, J.-M. Savéant, *J. Am. Chem. Soc*. **2003**, 125, 10729.

[98] C. Costentin, M. Robert, J.-M. Savéant, *Chem. Phys*. **2006**, 324, 40.

[99] Abdirisak Ahmed Isse, Giancarlo Sandonà, Christian Durante, Armando Gennaro *Electrochim. Acta* , **2009**, 54:3235.

[100] SGS science for a changing world: "*National water-quality assessment program, national synthesis on volatile organic compounds: Chloroform in the Hydrologic System—Sources, Transport, Fate, Occurrence, and Effects on Human Health and Aquatic Organisms"* **2004** U.S. Department of the Interior; U.S. Geological Survey.

[101] Luca Conti *"Elettroriduzione di policlorometani su electrocatalizzatori di argento"* M.Sc Thesis University of Milan, Department of Physical Chemistry and Electrochemistry, 2003.

[102] Giorgio Fiori, Sandra Rondinini, Guido Sello, Alberto Vertova Magdalena Cirja, and Luca Conti. *J. Appl. Electrochem.* **2005**, 35, 363.

2-Experimental section

The experimental section includes the description of the techniques adopted in this work and the experimental details. The latter may be reported also in the Results and Discussion Chapter for convenience. In every experimental procedure, Milli-Q (Millipore) water has been used.

2.1-Nanoparticles synthesis

2.1.1-IrO_2-based material: the sol-gel technique

The sol-gel technique was adopted for the synthesis of IrO_2-based powders characterized in this thesis.

In particular, SnO_2 xerogel was synthesized starting from $Sn(C_4H_9O)_4$ (Aldrich 99.999%). After dissolving tin terbutoxide in 2-propanol, water was added drop wise, controlling the drop rate at 1 drop s^{-1}. The synthesis was conducted in a stirred (300 rpm) round bottom flask under solvent reflux inside a thermal bath set at 25°C. The molar ratios adopted are:

- water/alcoxide= 81.4
- water/2-propanol= 10.9

After the water addition, the reaction mixture was kept under stirring for two hours. At the end of the synthesis, the gel dispersion was transferred into a large crystallizer and dried in the oven at 80 °C for 22 hours. A xerogel was thus obtained. The dried SnO_2 xerogel was then grinded in an agate mortar and then dehydrated under N_2 (flux 10Nl/h) for 2 hours at 120°C, in order to eliminate water excess.

As alternative route, a cheaper Sn source, namely, $SnCl_4$ (99.995% Aldrich), was considered for the synthesis of the SnO_2 xerogel. The synthetic path was therefore modified. After dissolution of $SnCl_4$ in water, the pH was adjusted by addition of NH_3 up to pH 6 and the precipitation of tin idroxide was verified. By using a centrifuge, the compound was separated and dried in oven at 80°C.

All synthesised powders have been classified on the basis of the method of Ir-precursor addition to the SnO_2 xerogel, as follows:

Impregnation. $IrCl_3$ was dissolved in a small volume (a few cm^3) of diluted aqueous HCl, mixed with 2-propanol (50 ml of solvent/g-of-precursor), and added to the SnO_2 xerogel, in order to impregnate it.

Co-synthesis. The precursors of the two oxides were dispersed in the solvent before water addition. In this case, the synthetic path was slightly modified in dependence on the Sn precursor adopted. When $Sn(C_4H_9O)_4$ was used, the precursors was dispersed in the hydro-alcoholic solution before water addition. The hydro-alcoholic solvent was then removed by evaporation in oven at 80°C. When $SnCl_4$ was used, the precursors were dispersed in water, and pH is adjusted at 9-10 (by addition of NH_3 and HCl, if necessary) and the precipitation of tin hydroxide was verified. Water is subsequently removed by evaporation in an oven at 80°C. In order to remove NH_4Cl, a dialysis procedure was done after the calcination step: the powder was suspended in water and placed within a porous membrane which was then immersed in a vessel containing water. This procedure was repeated several times, until the water contained in the vessel shows a sufficiently low conductivity.

Mechanical mixing. The third method consists in the addition of $IrCl_3$ to the SnO_2 xerogel by mechanical mixing for 10 minutes in an agate mortar.

In the following table, the labels adopted for indicate the method used for preparing the 2-component mixture are listed:

Sn source	method	Label
$Sn(C_4H_9O)_4$	Co-synthesis	CS
$SnCl_4$	Co-synthesis	CS-Cl
$Sn(C_4H_9O)_4$	Impregnation	I
$SnCl_4$	Impregnation	I-Cl
$Sn(C_4H_9O)_4$	Mechanical Mixing	MM

Table 6: List of Sn-precursor used in the powder synthesis.

After the addition of Ir-precursor all the materials were calcined under oxygen flux (50 Nl/h) for 2 hours at the selected temperature (450 or 500°C), reached with a 3-hour ramp.

In Table 7 is reported the list of all the powders synthesized.

n°powder	Composition	IrO_2 wt%	Precursor	method	$T_{calcinations}$ / °C
1	$Ir_{0.15}Sn_{0.85}O_2$	20	$Sn(C_4H_9O)_4$+$IrCl_3$	CS	450
2	$Ir_{0.15}Sn_{0.85}O_2$	20	$Sn(C_4H_9O)_4$+$IrCl_3$	CS	500
3	$Ir_{0.15}Sn_{0.85}O_2$	20	$Sn(C_4H_9O)_4$+$IrCl_3$	MM	450
4	$Ir_{0.15}Sn_{0.85}O_2$	20	$Sn(C_4H_9O)_4$+$IrCl_3$	MM	500
5	$Ir_{0.15}Sn_{0.85}O_2$	20	$Sn(C_4H_9O)_4$+$IrCl_3$	I	450
6	$Ir_{0.31}Sn_{0.69}O_2$	40	$Sn(C_4H_9O)_4$+$IrCl_3$	I	450
7	$Ir_{0.50}Sn_{0.50}O_2$	60	$Sn(C_4H_9O)_4$+$IrCl_3$	I	450
8	$Ir_{0.73}Sn_{0.27}O_2$	80	$Sn(C_4H_9O)_4$+$IrCl_3$	I	450
9	$Ir_{0.15}Sn_{0.85}O_2$	20	$Sn(C_4H_9O)_4$+$IrCl_3$	I	500
10	$Ir_{0.15}Sn_{0.85}O_2$	20	$SnCl_4$+$IrCl_3$	I-Cl	450
11	$Ir_{0.15}Sn_{0.85}O_2$	20	$SnCl_4$+$IrCl_3$	I-Cl	500
12	$Ir_{0.60}Sn_{0.40}O_2$	70	$SnCl_4$+ $IrCl_3$	CS-Cl	500
13	$Ir_{0.70}Sn_{0.30}O_2$	78	$SnCl_4$+ $IrCl_3$	CS-Cl	500
14	$Ir_{0.80}Sn_{0.20}O_2$	85	$SnCl_4$+ $IrCl_3$	CS-Cl	500
15	$Ir_{0.90}Sn_{0.10}O_2$	93	$SnCl_4$+ $IrCl_3$	CS-Cl	500
16	IrO_2	100	$SnCl_4$+ $IrCl_3$	CS-Cl	500

Table 7: List of IrO_2-based synthesized powders.

In the case of CS-Cl method the IrO_2 content is higher than the content in the others powders. This choice was driven by the need of characterizing powders containing high IrO_2 amount toward ORR as a comparison of electrochemical results obtained by scanning electrochemical microscopy [1].

2.1.2-Silver nanoparticles: the chemical reduction method

Silver powders having a nanometre and uniformly distributed sizes are investigated and adopted in many fields including biomedics, photonic band gap material science, chemical catalysis and other industrial applications [2] [3].The intrinsic properties of a metal nanoparticle are mainly determined by its size, shape, composition, crystallinity degree, and structure (solid versus hollow). In principle, it is possible to control any one of these parameters to finely-tune the properties of nanoparticles [4]. Different methods, like chemical reduction [5][6][7], photochemical or radiation–chemical reduction [8][9], metallic wire explosion [10], sonochemical method [11] and polyol method [12] can be applied.

From a practical point of view, the method of chemical reduction from aqueous solutions is most preferable for obtaining nano-sized powders and colloidal dispersion of silver. It is common

knowledge that the chemical reduction method involves reduction of metal salt in the presence of a suitable protecting agent, which is necessary for controlling the growth of metal colloids [13].

In our experimental conditions, novel pale-yellow silver sols composed by Ag nanoparticles have been obtained by reduction of an $AgNO_3$ aqueous solution, under N_2 atmosphere, with $NaBH_4$ in the presence of six different ligands, acting as stabilisers (see Table 8).

Ligand	Chemical formula
L(+)-glutamic acid **M = 147 kg kmol^{-1}**	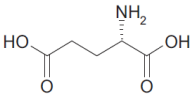
PVA **Poly(vinyl alcohol)** **M = 13,000–23,000 kg kmol^{-1}**	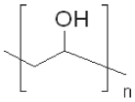
Igepal® CO-720 (branched) **α-(nonylphenyl)-ω-hydroxypolyoxyethylene** **$M \approx$ 749 kg kmol^{-1} n ≈ 12**	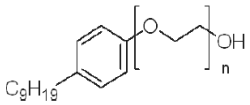
Brij 35® **α -Dodecyl- ω-hydroxypolyoxyethylene** **$M \approx$ 1198 kg kmol^{-1} n ≥ 23**	$CH_3(CH_2)_{10}CH_2(OCH_2CH_2)_nOH$
PEG-BDE **Polyethyleneglycol bisphenol A epichlorohydrin copolymer** **M = 7000–9000 kg kmol^{-1}**	$[C_{15}H_{16}O_2{\cdot}C_3H_5ClO{\cdot}(C_2H_4O)_n{\cdot}H_2O]_x$
PEG **Poliethylene glycol** **$M \approx$ 200 kg kmol^{-1} n ≈ 4**	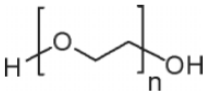

Table 8: List of stabiliser used in the silver nanoparticles synthesis.

In a typical preparation, an aqueous solution of the stabiliser was added to water under vigorous stirring. After that, an aqueous solution of $AgNO_3$ (58 mmol; 1.9×10^{-2} M) was added. An amber glass round bottom flask under N_2 atmosphere was used. After 5 minutes an aqueous solution of $NaBH_4$ was added and a pale yellow sol was immediately formed. The sol was left under stirring for further 30 min. The weight ratios used in the synthesis are reported in the next table.

Ligand	H_2O/Ag w/w ratio	Ag/ligand w/w ratio	Ag/$NaBH_4$ w/w ratio
L(+)-glutamic acid	1:0.1	1:15	1:1
PVA	1:0.1	1:1	1:10
Igepal® CO-720 (branched)	1:0.1	1:1	1:10
Brij 35®	1:0.1	1:1	1:10
PEG-BDE	1:0.1	1:1	1:10
PEG	1:0.1	1:1	1:10

Table 9: w/w ratios used in the silver nanoparticles synthesis.

The sols were immobilised by adding a weighted amount of carbon powder (Vulcan®XC72R, Cabot Corporation) to the colloidal solution. The carbon amount was calculated to obtain a silver loading of 10% w/w. The slurry was stirred for 2h, filtered and the absorption checked by ICP analyses of the filtrate. The pH of the slurry was modified during immobilization to 2 (by adding concentrated H_2SO_4). The supported catalysts were rinsed with large amounts of distilled water and dried under vacuum.

2.2-Electrochemical Techniques

Electrochemical characterization of electrodes was based on potentiostatic and potentiodynamic measurements, and on impedance spectroscopy analysis.

2.2.1-Cyclic voltammetry

Cyclic voltammetry (CV) has become an important and widely used electroanalytical technique in many areas of chemistry. The high versatility of cyclic voltammetry is the result of the possibility of rapidly provide a considerable number of information on the thermodynamics of redox processes, the kinetics of heterogeneous electro-transfer reactions, coupled chemical reactions, adsorption processes etc. This technique consists of scanning the potential of a working electrode, whose actual value is referred to the reference electrode, using a triangular potential waveform (see Figure 29). The measurements are typically carried out in a supporting electrolyte of sufficiently high concentration (in order to unfavour mass transport due to ion migration), with three-electrode experimental set-up: while the potential difference between the working and the reference electrodes is measured, the current flowing between the working and the counter electrodes is measured.

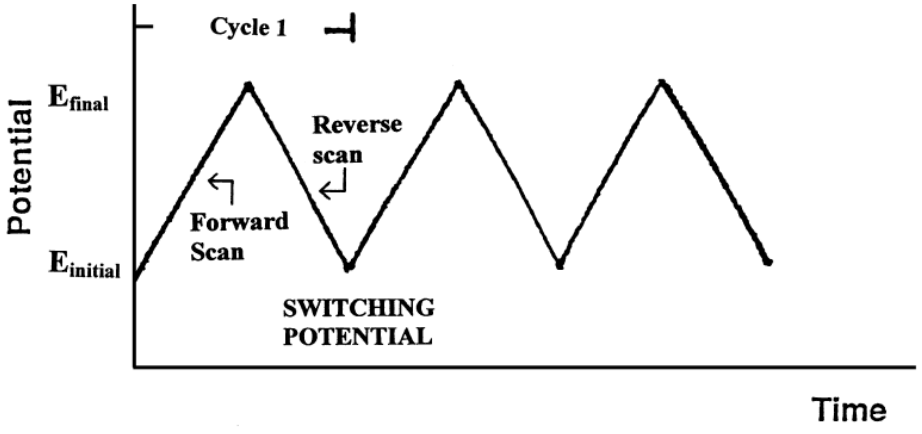

Figure 29: Variation of applied potential with time in cyclic voltammetry, showing the initial potential, $E_{initial}$ the final potential, E_{final}. The scanning rate v (V s^{-1}) is given by dE/dt [14]

The resulting plot of *current* versus *potential* is named a cyclic voltammetry (see Figure 30) and contains several information on the processes occurring at the working electrode.

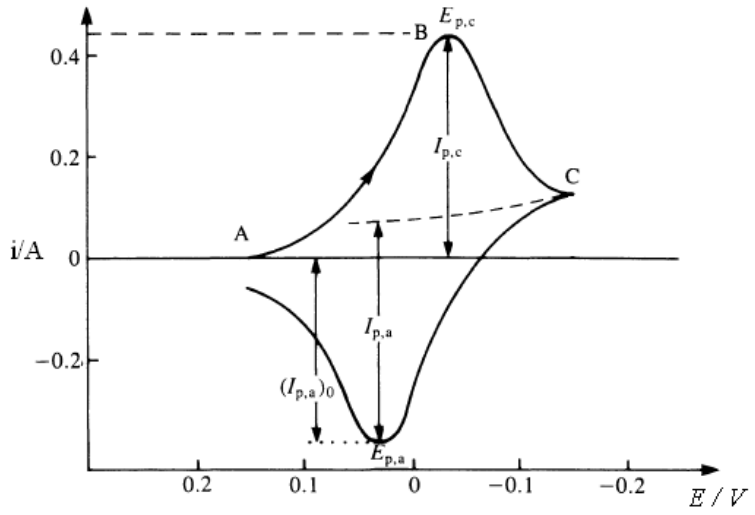

Figure 30: Cyclic voltammogram for a reversible system [15].

The current intensity I (A) recorded is given by:

$$I = I_C + I_F \quad (41)$$

where I_F is the faradaic current due to the electrode reaction, which occurs when the appropriate potential is reached [15]; and I_C is the capacitive current due to the charging of the double layer in proximity of electrode surface and it is proportional to the scan rate, v:

$$I_C = C_{dl}\, v \quad (42)$$

where C_{dl} is the capacitance.

IrO_2-based materials, as well as other similar materials (*e.g.* RuO_2, SnO_2, TiO_2, etc.), present a typical pseudocapacitive behaviour due to solid-state redox transitions which imply the proton insertion/extraction, to balance the electron accumulation/depletion in the metal ion centres. This phenomenon is observed in the potential range between hydrogen and oxygen evolution [16] as showed, in the case of IrO_2 in acidic environment, in Figure 31.

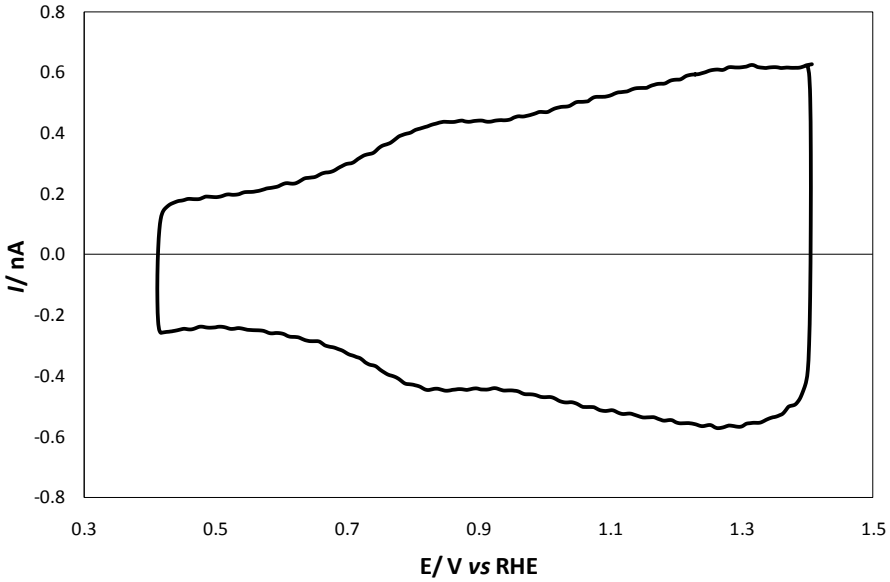

Figure 31: Voltammogram of IrO_2 electrode in 0.1 M $HClO_4$.

During a CV recording the surface is oxidized and reduced reversibly thorough a mechanism involving proton exchange with the solution [16]:

$$MO_x(OH)_y + ze^- \text{ (oxide)} + zH^+ \text{ (solution)} \rightleftharpoons MO_{x-z}(OH)_{y+z} \quad (43)$$

This process can be described as pseudo-capacitance, as the adsorbed species effectively store charge on the electrode surface. Since it involves a charge transfer between electrolyte-electrode interface, in parallel with a faradaic process, it still substantially differences from a double layer capacitance, which is based on pure physical phenomena [16]. The modifications take place only in a given potential window and the quantity of voltammetric charge (Q, C) is proportional to the number of active sites, the "electrochemical" surface area.

Obviously,

$$Q = \int_{t_1}^{t_2} I \, dt \quad (44)$$

and considering that $v = dE/dt$

$$Q = \int_{E_1}^{E_2} \frac{I}{v} dE \quad (45)$$

where E_1 and E_2 are the initial and final potentials of the scan, respectively.

The sweep-rate dependence of Q is related to the existence of less accessible surface regions (loose grain boundaries, pores, cracks etc) which become progressively excluded as the rate of reaction is enhanced. This implies that a fraction of available surface sites exchange proton with more difficult

during the voltammetric determination of *Q*. This becomes a rate determining step in particularly hidden surface regions. It is then possible to write:

$Q_{tot} = Q_{in} + Q_{out}$ (46)

where Q_{tot} is the total voltammetric charge, Q_{in}, is the charge related to the "inner" surface (less accessible) and Q_{out} is the charge related to the "outer" surface, proportional to the number of the more accessible sites. By considering the total current is the sum of the capacitive and pseudo-capacitive (*i.e.* faradaic, under H^+ diffusion control) contributions:

$I = I_C + I_F = C_{dl}\,v + kv^{1\backslash 2}$ (47)

Equation 45 becomes:

$$Q = \int_{E_1}^{E_2} \frac{C_{dl}v + k\,v^{1/2}}{v} dE = C_{dl}\,(E_2 - E_1) + \int_{E_1}^{E_2} \frac{k}{v^{1/2}} dE = C_{dl}\left(E_2 - E_1\right) + \frac{k}{v^{1/2}}\left(E_2 - E_1\right) \quad (48)$$

and Q_{tot}, Q_{in}, Q_{out} are then evaluated as follows:

- $Q_{tot} = \dfrac{1}{\lim_{v^{1/2}\to\infty}\left(\dfrac{1}{Q}\right)}$ by extrapolation of the *1/Q vs* $v^{1/2}$*;*
- $Q_{out} = \lim_{1/v^{1/2}\to 0}(Q)$ by extrapolation of the *Q vs 1/* $v^{1/2}$*;*
- $Q_{in} = Q_{tot} - Q_{out}$

Examples of the extrapolations are shown in Figure 32.

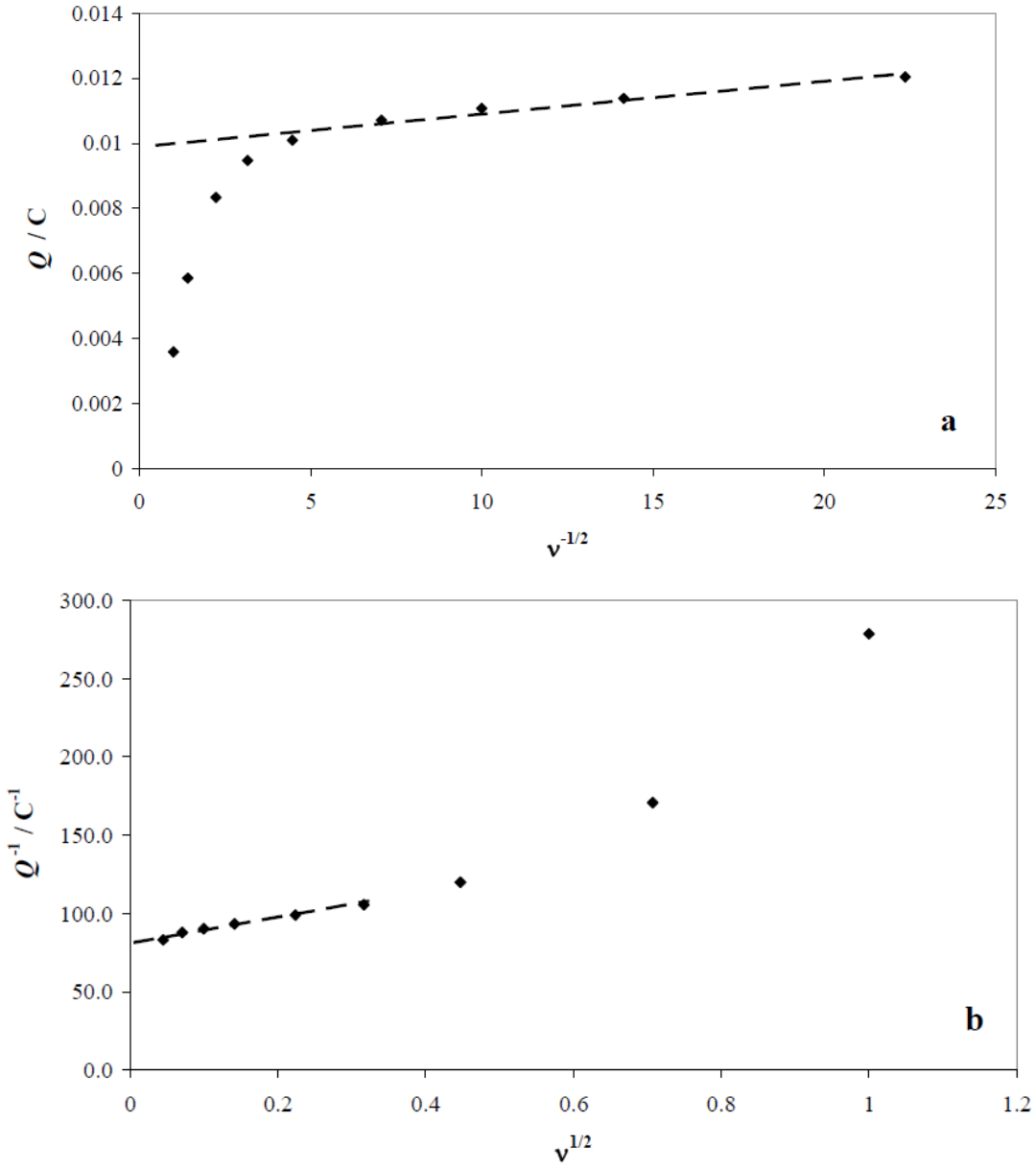

Figure 32: Extrapolations of voltammetric charge for the calculation of (a) Q_{out} and (b) Q_{tot} .

For the present application, the evaluation of Q_{tot}, Q_{out} and Q_{in} was restricted to the potential window from 0.4 to 1.4 V *vs* RHE, in order to avoid any contribution from OER and the hydrogen evolution reaction (HER).

In this work, Q was evaluated by using the Origin 6.0 professional (Microcal Software Inc.) software.

The CV measurements were carried out in a conventional three-electrode glass cell (volume 50 cm^3) except for Ti-supported electrodes in which a 4-compartments cell is adopted.

The working conditions are summarised in the next table.

Working electrode	Reference electrode	Counter electrode	Instrument
C-ME	SCE*	Pt foil	IrO_2-based material: Solartron Analytical Potentiostat (model 1287) driven by the Corrware Scribner Associated Inc software. Silver powders: PAR 273A potentiostat/galvanostat driven by a PC controlled by POWER SUITE® software.
Ti-plates	SCE*	Two Pt-foils	Solartron Analytical Potentiostat (model 1287) driven by the Corrware Scribner Associated Inc software
RDE	SCE*	Carbon felt**	Solartron Analytical Potentiostat (model 1287) driven by the Corrware Scribner Associated Inc software
Silver electrodeposited	SCE*	Pt foil	AMEL 5000 potentiostat/galvanostat driven by Corrware Scribner Associates Inc.
*calomel saturated electrode equipped with a double bridge, in order to avoid Cl^- leakage toward in the solution. **the use a carbon felt is necessary in order to avoid the release and the following deposition of metal ions on the working electrode if a metal counter electrode would be adopted.			

Table 10: Resume of the experimental condition adopted in cyclic voltammetric studies.

2.2.2-Reference Electrode: the Calibration of Saturated Calomel Electrode (SCE)

Part of this thesis topic is centred on processes which involve both electron and H^+ ions at the interface described in Section 2.2.1 equation 43. In particular, the thermodynamic potential of O_2/H_2O redox couple is:

$¼\ O_2 + e^- + H^+ = ½\ H_2O$ (49)

and the relevant Nernstian expression is:

$$E_{O_2/H_2O/H^+} = E^0_{O_2/H_2O/H^+} + \frac{RT}{4F}\ln(p_{O_2}) + \frac{RT}{4F}\ln\left(\frac{a_{H^+}}{a^{1/2}_{H_2O}}\right) = E^0_{O_2/H_2O/H^+} + \frac{k}{4}\lg(p_{O_2}) - kpH - \frac{k}{2}\ln(a_{H_2O}) \quad (50)$$

Therefore, the O_2/H_2O redox potential under reversible thermodynamic reversible conditions has the same pH dependence as the H^+/H_2 couple:

$2H^+ + 2e^- = H_2$ (51)

$$E_{H^+/H_2} = \frac{RT}{2F}\ln(p_{H_2}) + \frac{RT}{F}\ln(a_{H^+}) = \frac{k}{2k}\lg(p_{H_2}) - kpH \quad (52)$$

where R is the gas constant, T the absolute temperature F = 96485.309 C/eq, p_{O_2} e p_{H_2} are the oxygen and hydrogen partial pressures respectively.

It is then convenient to use the Reversible Hydrogen Electrode (RHE) as the reference electrode, since it permits to quantify the working electrode potentials independently from pH when studying oxygen evolution and reduction reactions. However, a RHE reference electrode requires experimental equipments which make the whole system difficult to handle. On the other hand, Saturated Calomel Electrode (SCE) is very easy to handle but its potential is independent on pH:

$$E_{SCE} = E^0 - k\lg(a_{Cl^-,sat}) \qquad (53)$$

SCE was therefore used as operational reference electrode, while the working electrode potentials are referred to RHE, by periodically calibrating SCE against RHE. Figure 33 reports the experimental setup used for calibration procedure.

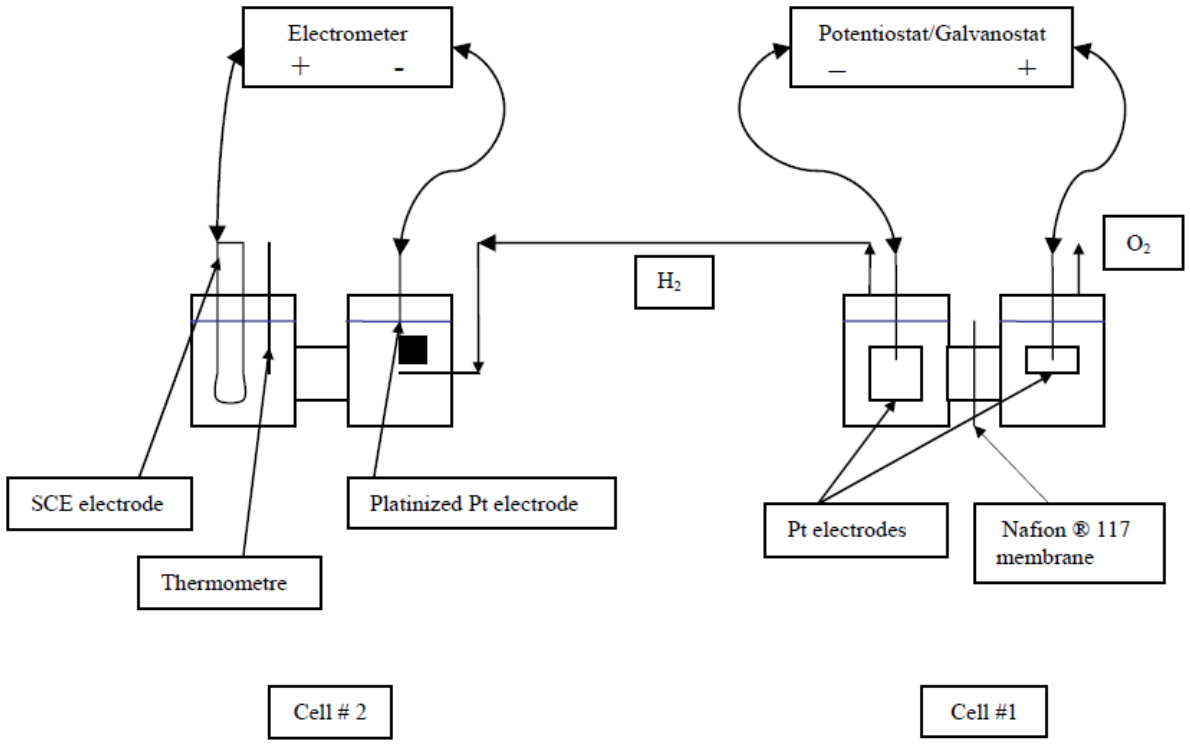

Figure 33: Experimental setup for the calibration procedure of SCE *vs* RHE at different pHs.

Hydrogen is produced in Cell #1 (a two compartment cell divided by a cationic membrane) by water electrolysis using aqueous $HClO_4$ 0.1M as supporting electrolyte, and is fed to Cell #2. Cell #2 is composed by an SCE on one side and a half immersed platinized Pt foil. In this way the following galvanic chain is obtained:

-Pt,H_2|aqueous electrolyte solution||KCl sat|Hg_2Cl_2|Hg|Pt+

The cell potential is measured by an electrometer. The procedure is repeated varying the electrolyte solution used the Cell #2. The following solutions, of different pH values, are used:

- $HClO_4$ 0.1M
- $NaClO_4$ 0.1M
- $NaClO_4$ 0.1M adjusted to pH 9-10 by NaOH 0.1M additions.

The pH value is measured by using a glass electrode (with internal reference electrode: Ag/AgCl in KCl 3M) and a pH-meter. The glass electrode and the pH-meter are calibrated by using pH 7 and pH 4 buffer solutions.

OPERATIVE PROCEDURE

Hydrogen produced in Cell #1 was bubbled in the RHE compartment in Cell #2. Measurements were conducted at ambient temperature (T ~ 22±2 °C). Potential differences between SCE and RHE were recorded until a stable value is obtained (E_∞ at $\Delta E/\Delta t < 3$ mVs^{-1}). The values obtained must be reported to the standard conditions (p_{H_2} = 101325 Pa). This requires the determination of the actual p_{H_2} value within the cell, by applying the following equation:

$$p_{H_2} = P_{atm} + p_h - p_{vap} \quad (54)$$

where P_{atm} is the atmospheric pressure, p_h is the pressure due to the hydrostatic heads in the cell and p_{vap} is the vapour pressure of the solution.

Atmospheric pressure was measured by using an Hg barometer. p_h is null since the RHE chamber is in direct contact with the atmosphere, vapour pressure is obtained from the literature [17].

The correct value of the *d.d.p.* between SCE and RHE is then:

$$E_{corr} = E_\infty + \frac{RT}{2F}\ln\frac{1}{p_{H_2}} \quad (55)$$

The values $E_{corr} = E_{SCE} - E_{RHE}$ are linearly dependent on pH:

$$E_{corr} = E_{SCE} - E_{RHE} = m\,pH + q \quad (56)$$

2.2.3-Potentiostatic technique

A potentiostatic technique consists in the application of a fixed controlled potential between the working electrode and the reference electrode. Nonetheless, the potential may be varied, with the condition that every potential value is applied until a steady state condition is reached in the system. In this optics, the measurements are performed as a stair-step voltammetry. The wave form of the potential in the time is reported in the next figure:

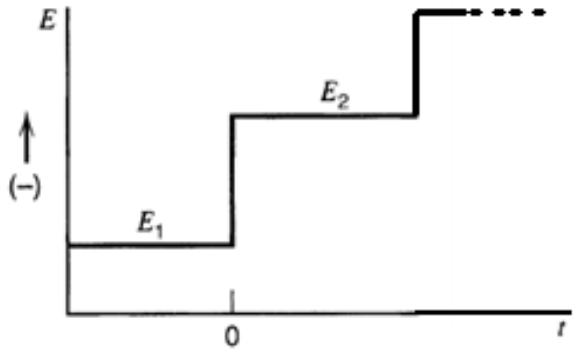

Figure 34: waveform of the potential in the polarization analysis [18].

The application of a potential step represents an instantaneous alteration of the electrochemical system. The analysis of the evolution of the system after this perturbation permits to obtain information about the electrode reactions [15]. After each potential pulse the resulting current-time response is reported in the next figure:

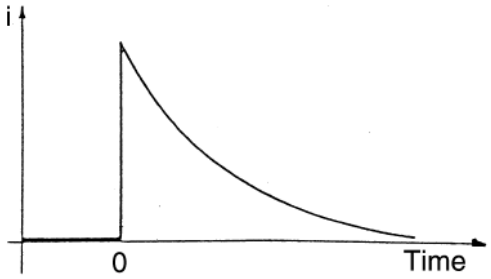

Figure 35: Current-time waveform after each potential pulse [15].

Current intensity is read immediately before the end of each step, in order to obtain information corresponding to the system under steady-state conditions. Therefore, a Tafel line can be easily obtained by plotting the results as an *E vs* lg *j* graph. In this way, as discussed above, it is possible to obtained information about the reaction mechanism and on the electrocatalytic activity of the material under investigation (see Section 1.3).

The polarization measurements on RDE were carried out in a conventional three-electrode cell glass. The reference electrode used was a calomel saturated electrode (SCE) equipped with a double bridge, in order to avoid Cl^- leakage toward in the solution. The counter electrode was a carbon felt. The last was used in the case of the characterization of IrO_2-based material toward ORR by Rotating Disk Electrode /RDE) in order to avoid the release and the following deposition of metal ions on the working electrode if a metal counter electrode would be adopted. The instrument used

was a Solartron Analytical Potentiostat (model 1287) driven by the Corrware Scribner Associated Inc software.

2.2.4-Electrochemical Impedance Spectroscopy (EIS)

Electrochemical impedance spectroscopy (EIS) studies the system response under application of a small periodic electrical perturbation (current or potential) of selected frequency. The frequency of this sinusoidal perturbation can be varied over a range of values (typically in the kHz to mHz range) and the response of the electrode is recorded. The wide range of frequencies employed gives an impedance spectrum which enables the investigation on several electrode processes, a feature not easily accessible with dc measurements. The method becomes more effective when superimposing the alternate potential, a.c., signal to a fixed potential value applied to the working electrode.

The fundamental parameters involved in EIS are:

$$E(t) = E_0 sen(\omega t) = E_0 e^{i\omega t} \qquad (57)$$

where E(t) is the a.c. applied potential, E_0 is the potential amplitude, $\omega = 2\pi f$ is the angular frequency, f (s^{-1}) the frequency and t (s) the time.

It is possible to represent this potential as a vector rotating (that is a *phasor*) like the one pictured in Figure 36.

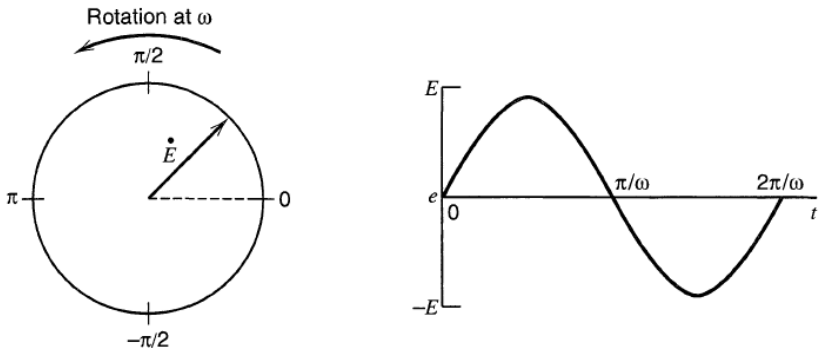

Figure 36: Phasor diagram for an alternating voltage.

The system responds with a sinusoidal current signal:

$$I(t) = I_0 sen(\omega t + \varphi) = I_0 e^{i(\omega t + \varphi)} \qquad (58)$$

where I(t) is the a.c. current, I_0 is current amplitude.

Potential and current oscillate with the same frequency but their phases can be shifted by an angle φ. It is convenient to represent vectors **I** and **E** as rotating vectors (or *phasors*) in the complex plane.

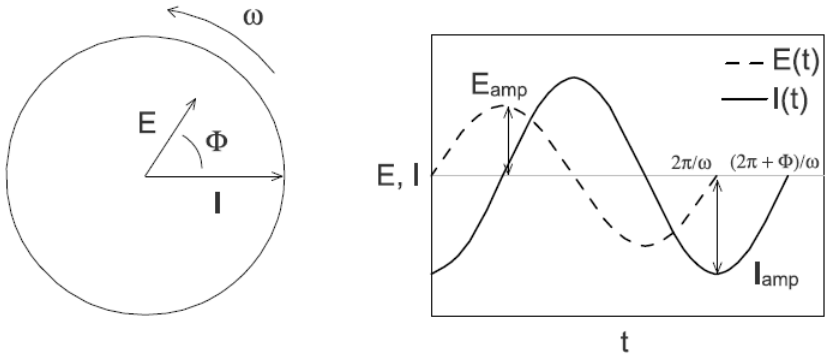

Figure 37: Phasor diagram showing the relationship between alternating current and voltage.

The impedance of the electrode response is then given by the relationship:

$$|Z(\omega)| = \frac{E(\omega)}{I(\omega)} \qquad (59)$$

Therefore:

$$Z = \frac{E_0}{I_0}\frac{sen(\omega t)}{sen(\omega t + \varphi)} = \frac{E_0}{I_0}\frac{e^{i\omega t}}{e^{i(\omega t+\varphi))}} = Z_0 e^{-i\varphi} = Z_0(sen(-\varphi) + i\cos(\varphi)) \qquad (60)$$

Impedance data are usually represented in the Nyquist plot (imaginary part of *Z*, *Z*'', *vs* its real part, *Z*') and the Bode plot (*Z module* and *φ vs f*), but several other representation plots can be used (*e.g.* *Z*' and *Z*'' *vs f*).

The interpretation of impedance spectra often is done mainly in two ways:

- by interpreting the experimental in terms of an *equivalent circuit*, *i.e.* by a suitable combination in series/parallel of electrical elements, which has the same response as the investigated real system and whose combination follows the rules of electrotechnics;
- by the optimization of the parameters in equations which analytically describes the physical properties of the system.

As a first approach to EIS, it is useful to analyze the simpler circuits and their response to the application of an a.c. signal:

Resistors

The electrical current flowing through a pure resistance R when a sinusoidal voltage signal is applied is given by:

$\boldsymbol{I}(t) = \boldsymbol{E}(t)/\mathrm{R}$ (61)

therefore:

$$I(t) = \frac{E_0}{\mathrm{R}} sen(\omega t) = \frac{E_0}{\mathrm{R}} e^{i\omega t} \quad (62)$$

Considering the variables on the complex plane, the impedance vector is given by:

$$Z = \frac{E}{I} = \frac{E_0 e^{i\omega t}}{\frac{E_0}{\mathrm{R}} e^{i\omega t}} = \mathrm{R} \quad (63)$$

In a pure resistive circuit, no phase shift between potential and current exists and impedance modules $|Z|$ is equal to R. This means that only the real part of Z exists and it does not depend on frequency. In the Nyquist plot, this circuit is represented by a point on the abscissa axis, which corresponds to the R value.

Capacitor

In the case of a pure capacitance, C, the following equation is valid:

$$I = C\frac{dE}{dt} \quad (64)$$

thus:

$$I = \omega C E_0 \cos(\omega t) = \omega C E_0 sen(\omega t + \frac{\pi}{2}) = \omega C E_0 e^{i(\omega t + \pi/2)} \quad (65)$$

The impedance vector is given by:

$$Z = \frac{E}{I} = \frac{E_0 e^{iwt}}{E_0 \omega C e^{i(\omega t + \pi/2)}} = \frac{1}{\omega C} e^{-i\pi/2} = \frac{1}{\omega C}\left[\cos\left(-\pi/2\right) + i sen\left(\pi/2\right)\right] = 0 - i\frac{1}{\omega C} \quad (66)$$

For a pure capacitive circuit, Z is composed only by its imaginary part. In this case, the Nyquist plot is a line lying onto the ordinate axis.

Constant phase element (CPE)

In practice, the connection of simple R-C-L elements is not always adequate for describing correctly an electrochemical system. Deviations from the ideal capacitive behaviour are often observed then the connection of simple R-C-L elements is not adequate for completely describe the system. For that reason, the classical simple elements are often substituted by empirically derived elements which better describe the results. Capacitive phenomena are those more often deviated with respect to an ideal capacitive behaviour, likely because of microscopic roughness caused by scratches, pits, etc., always present on solid surfaces. Microscopic roughness would then cause a dependence of capacitance on the frequency. In such cases the double-layer capacitance may be expressed in terms of a *constant phase element* (CPE). Its impedance, Z_{CPE}, is described by:

$$Z_{CPE} = \frac{1}{T(i\omega)^{S^P}} \quad (67)$$

where T is a constant in Ω^{-1}, s^p which corresponds to real capacitance term for p=1 and to resistance term for p=0. Notwithstanding the usefulness of an adjustable *p* parameter in the fitting procedure, it has to be outlined that the meaning of CPE, as well as of other *ad-hoc* designed elements, is still not fully explained [18].

Parallel resistance and capacitance

In the case of a parallel RC circuit:

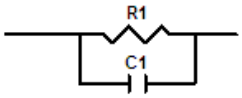

$$Z = \frac{1}{1/R + i\omega C} = \frac{R}{1 + i\omega RC} \quad (68)$$

which leads to:

$$Z' = -\sqrt{Z''(R - Z'')} \quad (69)$$

which resembles the equation of a circumference. In fact, the resulting Nyquist plot for is:

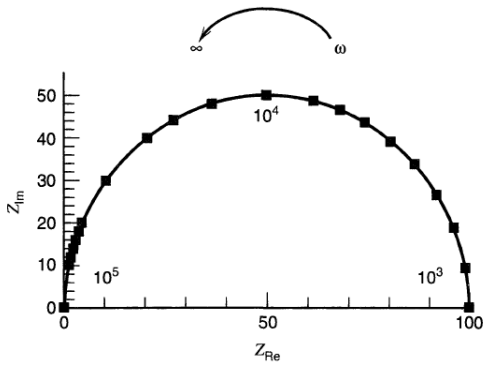

Figure 38:Nyquist plot for a parallel circuit with R =100 Ω and C=1μF.

As mentioned before, in more complicated cases, is not possible to build an equivalent circuit which fully describes the system and therefore EIS data can be interpreted by using a physical model instead of equivalent circuits. Particularly important in the study of porous material are the so-called *distributed elements*. In this case, each pore is seen as a transmission line, *i.e.* a series of infinitesimal circuits connecting the current collector and the electrolyte solution.

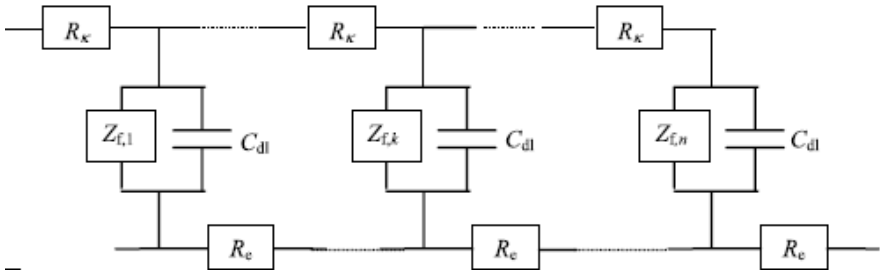

Figure 39: Scheme of a distributed element circuit. (R_k: ionic resistance, Z_{fk}: faradaic impedance and R_e: electronic resistance, C_{dl}: double layer capacitance).

Impedance spectra for water electrolyser were obtained for different cell potential values adopting a two-electrode, four-terminal configuration. EIS measurements were performed using Solartron Analytical Instrumentations (model 1287 potentiostat and model 1260 Frequency Response Analyzer (FRA)). EIS were recorded in the frequency range of 0.01Hz e 1MHz and the signal amplitude was 10mV.

2.2.5-Working Electrodes and operative conditions

In this study different working electrodes were used. On base the type of electrode different preparation procedure were adopted. In this section both the electrode descriptions and the experimental condition applied were reported.

(I) Cavity MicroElectrode (C-ME)

The term *microelectrode* denotes electrodes for which at least one dimension is below 25µm. Different geometries are possible: spherical, hemispherical, cylindrical, and planar (disk). Cavity micro-electrode is a recessed microdisk. It consists of a glass tube (glass diameter: 5 to 6 mm) containing a Pt wire (diameter Pt: 25 to 50 µm, length 3 cm) that ends near the bottom of the glass tube, thus providing a cylindrical cavity (Figure 40) [19].

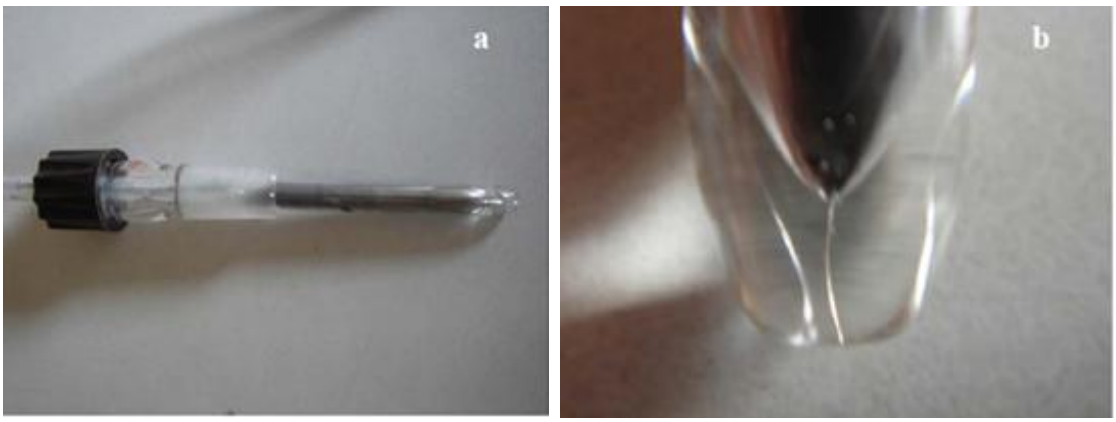

Figure 40: Picture of a C-ME (a) the whole electrode (b) the micro Pt wire.

The use of C-MEs presents the following advantages:

- very low amount of powder is needed, then it is possible to consider this technique as non-destructive;
- enables to study the powder materials without any sticking agent;
- enables quick and reliable renovation of the electrode surface by emptying and reloading the cavity;
- low currents are recorded thus making the *IR* correction not necessary;
- better peak resolution due to low capacitive currents.

C-ME PREPARATION

A platinum wire (0.05mm diameter, GoodFellow Cambridge) was sealed into a glass tube (length ca 10 cm, diameter 6-10 mm). The absence of air bubbles in the glass was verified by optic microscope. This aspect is very important because the presence of air bubbles leads to an uncorrected determination of the volume. The electric contact between Pt wire and Cu wire was guaranteed by a conductive carbon powder (Vulcan® XC72 R) inserted in the glass tube.

An experimental evaluation of the platinum radius was carried out measuring the steady state reduction current in 1 mM $Ru(NH_3)Cl_3$ in 0.1 M KNO_3 at 1mV s^{-1} aqueous solution. A sigmoidal signal was obtained (see Figure 41).

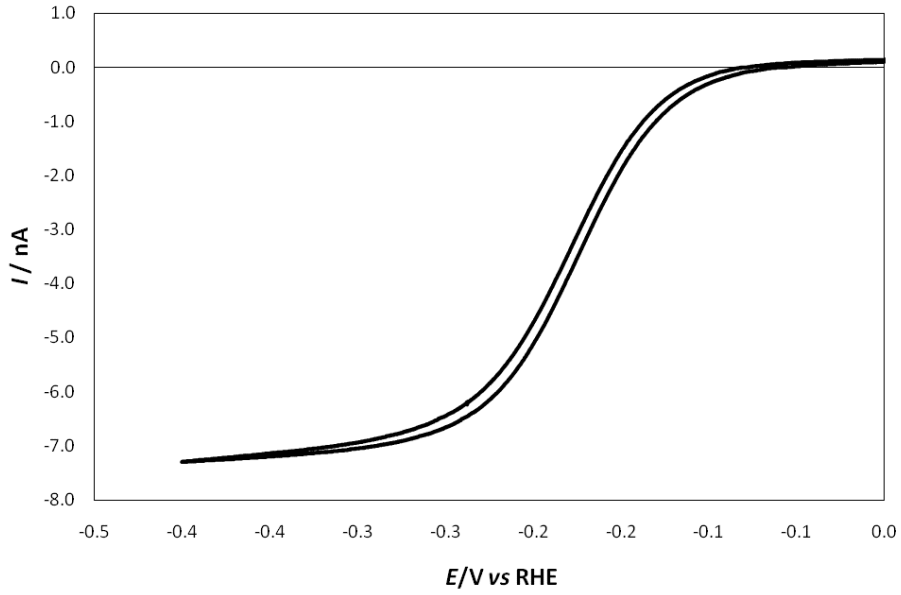

Figure 41: CV characteristics in 1 mM $Ru(NH_3)Cl_3$ and 0.1 M KCl aqueous solution of a Pt microdisk.

The disk radius can be finally determined by inserting the steady state current in the following equation:

$$i_{ss} = 4nFD_0C_0^*r_0 \qquad (70)$$

where *n* is the number of moles of electrons *per* mole of reactant, *F* is the Faraday constant, and D_0 and C^*_0 are the Ru(III) complex concentration and diffusion coefficient, respectively and r_0 is the disk radius.

The recess was then obtained by a controlled dissolution of platinum in boiling aqua regia (37 wt% HCl, 60 wt% HNO_3 3:1 volume ratio) for 3' and left in the hot solution for 12' during its cooling. This procedure was repeated until the desired depth was reached. The determination of the recess depth was done by measuring the steady state reduction current in an 1mM $Ru(NH_3)_6Cl_3$ aqueous solution and solving for *L* the following equation [21]:

$$L = \frac{4\pi FC_0^*D_0r^2}{4L + \pi r} \qquad (71)$$

where *L* and *r* are the depth and radius of the recess respectively, C_0^* and D_0 are the Ru(III) complex concentration and diffusion coefficient respectively and *F* is the Faraday constant.
The geometric characteristics of the adopted C-MEs are:

C-ME	Radius /µm	Depth /µm	Volume / µm^3
1	25.8	26.4	55300
2	25.2	21.5	42893
3	28.5	24.9	63290
4	28.8	42.5	110849
5	27.9	29.9	73192

Table 11: Geometric characteristic of C-MEs realised.

All C-ME present similar equivalent radii (since the same wire is adopted) but different depth values. The Pt wire used in C-ME has a radius of 25µm but its experimental determination always gives higher values. This can be due to many factors, which are not necessarily included in the tolerance declared by the supplier (±10%) but also from the not perfect perpendicularity of the disk with respect to the wire axis, as well as disk surface roughness.

USAGE OF THE C-MEs

The cavity was filled with the desired powder material using the electrode as a pestle. The filling of cavity was controlled by optical microscopy in order to verify that no particles remain stuck onto the glass surface outside the cavity.

At the end of the characterization the C-ME was emptied by immersing it in an ultra sound bath in concentrated HNO_3 aqueous solution (10') and then in acetonitrile (2') in the case of Ag-based powders and in H_2O (4') and in acetone (2') in the case of IrO_2 –based powders.

ELECTRODE CHARACTERIZATION

IrO_2-based powders

The electrochemical characterization was conducted by cyclic voltammetry (CVs were recorded between 0.4 and 1.4 V *vs* RHE at 20, 10, 5 and 2 mV s^{-1}) in 0.1 M aqueous $HClO_4$.

By the analysis of the quantity of charge in dependence on the scan rate it was possible to evaluate Q_{tot}, Q_{out} and Q_{in} values as described in 2.2.1.

After the recording of CVs at different scan rates, 0.725mL of $Fe(ClO_4)_3$ were added to electrolyte solution in order to reach a 0.01M Fe^{3+} concentration in solution and CVs between 0.4 and 1.4 V *vs* RHE at 5 and 2 mV s^{-1} were recorded (see Figure 42).

The characterization in the presence of a redox couple in solution is another method for the evaluation of the active area. In aqueous solution, two of the most popular couples are Fe^{3+}/Fe^{2+} aquo-cations and $Fe(CN)_6^{3-}/Fe(CN)_6^{4-}$, both studied at different electrode materials and in different

conditions of reactant concentrations, supporting electrolyte and temperature [22]-[27]. Particular care is required in choosing the experimental conditions in order to avoid the presence of ions (especially anions) that can alter the results. For the specific case of the Fe^{3+}/Fe^{2+} redox system, that is more used for the characterization of electrocatalytic materials, working in perchloric acid medium is the optimal choice [28].

The activation energy for the reaction

$$Fe^{3+} + e^- = Fe^{2+} \quad (72)$$

consists essentially in the reorganization energy of solvent molecules around the ion that change its charge. The electrode surface may have a secondary effect on the reaction rate trough the structure of electric double layer at the metal/solution interface. In fact at the same overpotential, the potential in the outer Helmoltz plane (OHP) where the reacting species are supposed to be located, is usually different at different metals [29]. As reported in [22][29][30] the effect of different surfaces is also observed in the case of metal oxide electrodes. In particular a correlation between PZC and Fe^{3+}/Fe^{2+} is observed: low PZC values correspond to high j_0 and k_0 values.

Since the PZC of IrO_2 is significant lower than PZC of SnO_2 (see Figure 22), in the case of a IrO_2-SnO_2 mixture the high sensitivity of Fe^{3+}/Fe^{2+} toward Ir species can be used for the determination of the Ir surface active sites.

In this study the IrO_2-based powders were supported on C-ME. Assuming that the materials present high electric conductivity it is possible to approximate the behaviour of the filled C-ME with that of a microdisk electrode, and characterize the electrode by the analyzing the steady state current obtained from CV recorded at 2 mV s^{-1} in the presence of 0.01 M $Fe(ClO_4)_3$. Figure 42 shows an example of the relevant data obtained in the presence of the powder (i) in $HClO_4$ only (the so-called back-ground signal – dashed line); and (ii) after the addition of 0.01M $Fe(ClO_4)_3$ (thick black line). The thin black line represents the subtraction between steps (ii) and (i). From the steady state current, i_{SS}, the "equivalent" radius r_0 of the hypothetical disk can be obtained via:

$$r_0 = \frac{i_{ss}}{4nFD_0C_0^*} \quad (73)$$

where F is a Faraday constant, D_0 is the coefficient diffusion of reactant, C^*_0 is the concentration of reactant.

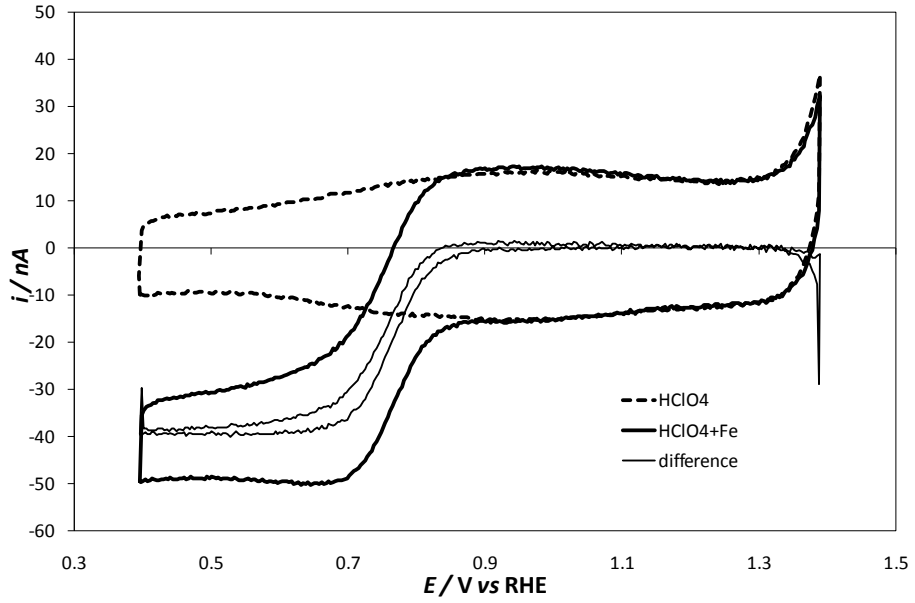

Figure 42: Characteristic CVs obtained in presence of Fe^{3+}/Fe^{2+} couple in $HClO_4$ 0.1M. A solution of $Fe(ClO_4)_3$ 0.01M is present in the cell. Scan rate: $2mVs^{-1}$.

The equivalent radius is representative of the active area that is correlated to the presence of Ir species on the surface and therefore to the active area of the material characterized.

Considering the height and shape of the wave it is possible to extrapolate kinetic information.

The wave shape is an useful indicator of the kinetic regime. Table 12 reports a summary of the expected values of experimental parameters for sampled-current voltammetry based on transients [18].

Kinetic regime	$\lvert E_{3/4}-E_{1/4}\rvert$* (mV)	β**
Reversible (n ≥1)	56.4/n	---
Quasi-reversible (n=1)	Between 56.4 and 45.0/α	0.3÷0.7
Irreversible (n=1)	45.0/β	0.3÷0.7
* $E_{3/4}$ and $E_{1/4}$ correspond to the potential values which the current is equal to ¾ and ¼ of steady-state current ** transfer coefficient values, β,is valid for the one-step, one-electron mechanism.		

Table 12: Wave shape characteristics at 25°C in sampled-current voltammetry.

Therefore considering the $|E_{3/4}-E_{1/4}|$ value it is possible to determine β, and by applying the following equation to extrapolate the standard heterogeneous rate constant k_0 values:

$$E_{1/2} = E^{\circ'}_{Fe^{2+}/Fe^{3+}} + \frac{RT}{\beta F}\ln\frac{r_0 k_0}{D_0} \qquad (74)$$

where $E_{1/2}$ is the potential value at which the current is equal to 1/2 of steady-state current, $E^{\circ'}_{Fe^{2+}/Fe^{3+}}$ is the formal potential of redox couple in 0.1M $HClO_4$ at 25°C (the value considered is 0.735V vs NHE [31]), R is the gas constant, T is the temperature, F is the Faraday constant, r_0 is the "equivalent" radius of the electrode and D_0 is the reactant diffusion coefficient in the reaction media.

It has to be noted, however, that these kinetic parameters are obtained under the assumption of a hemi-spherical electrode surface, which is a rather drastic approximation for our microelectrode.

Ag-based powder in non-aqueous solution

The electrochemical characterization was conducted in a glass cell (volume of 50 cm^3) using tetraethylammonium tetrafluoborate (TEATFB, Aldrich ≥99.8%) 0.1 M in acetonitrile (CH_3CN, Merck C 99.8%) as background electrolyte.

The desired trichloromethane concentrations were obtained by adding appropriate amounts of 0.5 M $CHCl_3$ (Merck C 99.8%) in CH_3CN. In this case it is crucial to eliminate the presence of oxygen in the cell because it originates different peaks in the same window in which the reduction of trichloromethane takes place.

Therefore, in order to avoid the presence of oxygen in the cell, the following procedure was adopted:

1. deaeration with N_2 for 30';
2. positioning the syringe, filled with the needed amount of $CHCl_3$, through a rubber septum;
3. intake of N_2 in the syringe needle in order to avoid any leakage of $CHCl_3$ into the solution;
4. recording the CV in the sole presence of the background electrolyte;
5. polarization at -2V (SCE) for 2 minutes;
6. recording the CV in the sole presence of the background electrolyte after the polarization period;
7. injecting the $CHCl_3$ and recording the CVs.

Cyclic voltammograms were recorded between -0.5 V and -2.3 V (SCE) at different scan rates: 2000, 1000, 500, 200, 100, 50 and 20 mV s^{-1}.

Ag-based powders in aqueous solution

In this case the adopted electrolyte was aqueous 0.1M $KClO_4$. All voltammetries were recorded adopting a trichloromethane concentration of 0.01 M. This is due to the solubility of

trichloromethane in water. Due to the high volatility of $CHCl_3$, a fresh aqueous solution was prepared just before each run. Before each recording the solutions were deaerated by N_2 bubbling. To avoid any change in the $CHCl_3$ concentration, nitrogen was pre-saturated with the same solution under investigation. CVs were always preliminary recorded on the background electrolyte only, between -0.5V and -1.2 V *vs* SCE, at scan rates between 100 and 5000 mV s^{-1}.

(II) Powders supported on Ti plate

In order to test the performance of electrocatalyst under operative conditions, membrane electrode assemblies (MEAs) were prepared and tested in a two-electrode water electrolysis cell, as will be described subsequently. However, the adoption of a classical 3-electrode configuration enables to measure the working electrode potential independently on the counter one. This is highly convenient in order to deeply investigate the electrochemical properties of the inks prepared for being sprayed on to a membrane for MEAs preparation. In particular the contribution of the ionomer loading on the electrode properties was analysed.

ELECTRODE PREPARATION

In order to simulate the behaviour of the mixture deposited onto the membrane, square Ti lamina (geometric surface area about 2 cm^2) was used (see Figure 43). Before the powder deposition, Ti plates were sandblasted in order to both remove the oxide layer and to enhance the surface roughness thus increasing the adhesion of the powder to the support. A final treatment in 10wt% oxalic acid aqueous solution for 1 hour completes the oxide layer removal.

Figure 43: Ti plate support used for powders characterization.

The deposition was carried out depositing an ink which, like in the case of MEAs, was made by the electrocatalytic powder, a Nafion® emulsion and 2-propanol. The deposition was performed by using a glass capillary. In order to obtain a homogenous deposit, the ink was mixed using ultra sounds. Drops of ink were homogenously distributed onto the surface in order to simulate the spraying technique used in the MEA preparation (see next Section). Finally, the electrodes were dried by putting them onto a warm (about 50 °C) surface.

The compositions of the electrodes tested are reported in the following table:

n° electrode	n° powder	Nafion® loading (mg cm^{-2})	IrO_2 loading (mg cm^{-2})
Ti-1	5	0.00	2
Ti-2	5	0.07	2
Ti-3	5	0.17	2
Ti-4	5	0.20	2
Ti-5	5	0.29	2
Ti-6	5	0.64	2

Table 13: Compositions of Ti-thin plates supported electrodes tested.

ELECTRODE CHARACTERIZATION

The cell used for the characterization of Ti-deposited inks is reported in the following picture.

Figure 44: Cell used for electrochemical characterizations on Ti and GC supported powders.

It includes two counter electrode chambers, in order to permit the best cell symmetry with respect to the working electrode planar geometry.

The Ti-deposited inks were characterized by cyclic voltammetry in aqueous 0.5 M H_2SO_4 between 0.4 and 1.4V *vs* RHE at 2, 5, 10 and 20 mV s^{-1}.

(III) Membrane Electrode Assemblies (MEA)

The core of the reversible proton exchange membrane fuel cells technology is the Membrane Electrode Assembly (MEA). It consists of a cation-exchange membrane, which is the physical separator of the anode and cathode cell compartments and the support of electrocatalytic powders.

Nafion® (Dupont de Nemours, Delaware, U.S.A.) is the most used proton-conducting ionomer. It consists in a perfluorinated polymer that contains small proportions of sulfonic functional groups. Its general chemical structure shown in Figure 45, where X is a sulphonic group and M can be either a metal cation neutralized form or an H^+ ion.

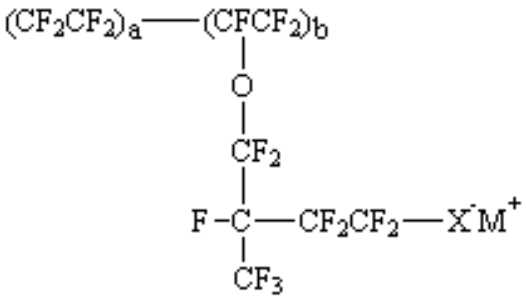

Figure 45: Nafion® perfluorinated ionomer.

MEAs are usually prepared by depositing both catalyst layers directly on the two sides of the membrane. Finally, in order to obtain a stronger adhesion, the assembly is hot-pressed. The interface between the membrane and the electrode is critical. The two electrodes and the membrane are intimately in contact in order to obtain a "zero-gap" cell, thus optimizing the three-phase contact (see Section 1.4.5). Together with the choice of the appropriate electrocatalytic material, the main factor affecting the behaviour of the whole system consists in the right preparation of the "ink" which will be deposited onto the membrane, that consists in the correct mixture of the different actors, each responsible of a particular task.

In our case the inks, which were water based, were applied by a spraying technique which was preferred due to its simplicity and because of it permits an easy control of the catalyst loading.

ELECTRODE PREPARATION

The MEAs were prepared in the following way.

Step 1: Pre-treatment of Nafion® membrane.

The adopted membrane was the Nafion® 115. The membrane needed different treatment steps before the ink was deposited: first, it was boiled in pure water for 2 hours then in aqueous 0.5M H_2SO_4 for 1 hour and again in water for 3 hours.

Because the ink deposition was carried out while the membrane was placed on a heating plate at 80°C, a further treatment with triethanolamine was necessary. This consisted in the immersion of the membrane in triethanolamine (20%wt aqueous solution) for 24 h and drying in a filter paper. Since triethanolamine boiling point is 208 °C (at 20 hPa), it remains in the membrane during the deposition of the ink, thus avoiding the complete drying and shrivelling of the membrane.

Step 2: Deposition of catalyst ink

The cathodic and anodic layers were deposited directly on the membrane by a manual spryer. The membrane was placed on the heating plate at 80°C. An ink containing the appropriate amount of all components suspended in 2-propanol was treated with ultrasound for different times (between 2 and 20 minutes) and sprayed directly onto the membrane in order to create a homogeneous film on it. The depositions of the two catalyst layers were carried out separately, firstly the cathode layer (Pt-based catalyst, platinum E-TEK 28.6% wt) and then the anode one (IrO_2-based catalysts).

To limit the cathodic overvoltage, a high Pt loading was used: 1 mg cm^{-2}. The anodic layer compositions adopted are reported in Table 14.

Sample	Electrocatalyst powder	IrO_2 loading (mg cm^{-2})	Nafion® loading (mg cm^{-2})	Others components
MEA 1	5	0.6	0.6	Vulcan (6mg cm^{-2})
MEA 2	5	2.9	5	------
MEA 3	5	1.2	0.6	------
MEA 4	5	1.2	0.6	------
MEA 5	6	1.2	0.6	-----
MEA 6	7	1.2	0.6	------
MEA 7	8	1.2	0.6	------

Table 14: Anodic layer compositions of MEAs tested.

STEP 3: pressing

All MEAs were hot-pressed at 100°C , 176 kg cm^{-2} for 5 minutes.

STEP 4: Hydration and washing of MEA.

The electrode was hydrated for 2 hours by immersion into water and then washed under water flux for 1h. The latter treatment is very important in order to completely remove the triethanolamine present in the membrane pores. The MEA was then immersed in aqueous $HClO_4$ 0.1M for 24 h and in H_2O for 48 h, changing frequently both the acid and the water.

The triethanolamine removal effectiveness is verified by impedance measurements. A reduction of the cell resistance values (read at 500Hz) from 1.6 Ω to 0.2 Ω is observed.

ELECTRODE CHARACTERIZATION

The MEAs have been tested in electrochemical cells specifically designed for reproducing industrial operative conditions. Different cell designs have been adopted, in dependence on the water supply method.

PASSIVE (IMMERSION) CELL

This cell was used fully immersed in still MilliQ water. Due to the high resistivity of the water, no short circuit between the electrodes is possible.

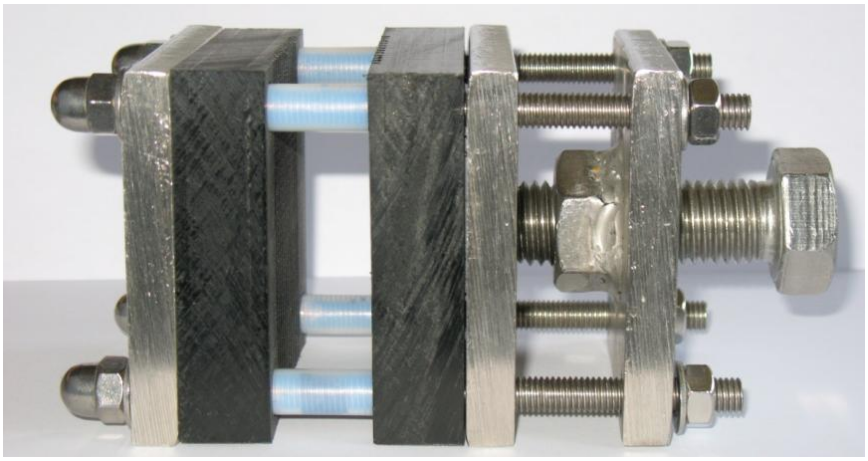

Figure 46: Immersion cell.

The electrodes and the current-collectors (see Figure 47) were inserted between two polyethylene plates which were previously grooved (each vertical groove is 4mm depth and 2 mm width) in order to facilitate the gas removal from the electrode. The whole was blocked between two steel plates that allow the application of a homogeneous pressure.

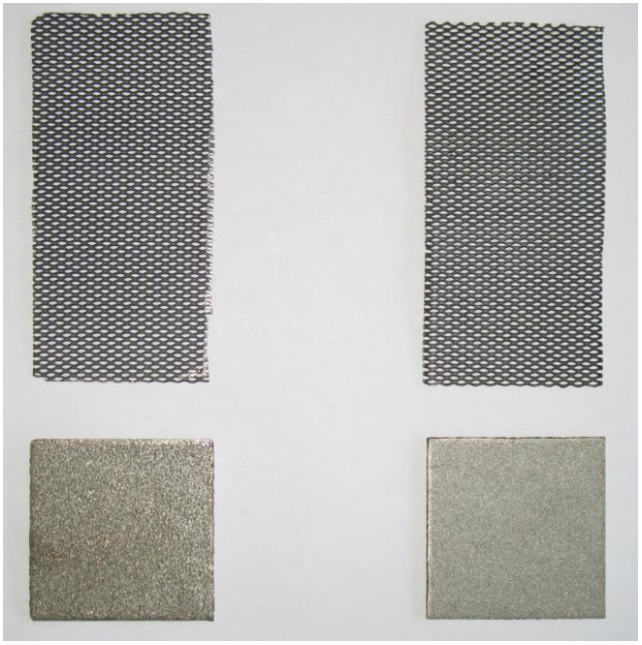

Figure 47: Current collectors used in the immersion cell.

Each current collector consisted in a Ti-sinter (4x4 cm^2, 2 mm thick). The electrical connection between each Ti-sinter and the external circuit was obtained by interposing a Ti-activated net, *i.e.* a Ti net covered by a layer of IrO_2-based oxide, between the Ti-sinter and the polyethylene plate. Both the Ti-sinters and the electrode surfaces areas are 16 cm^2. Ti sinters, purchased by GKN Sinter Metals, porosity ~65%, are elastic elements that favour the water supply to the electrode and the escaping of gas from the electrode surface. Before their usage, all Ti-sinters were treated in an aqueous solution of oxalic acid (10wt%) in order to remove the native TiO_2 oxide on Ti. The whole cell was then assembled and tightened at 45 kg cm^{-2}.

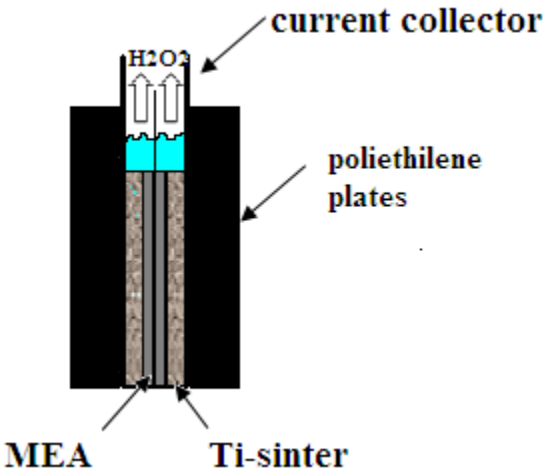

Figure 48: Scheme of the immersion cell in the operative condition.

The MEAs were tested under electrolytic conditions at room temperature and the cell voltage was measured at different current density values, usually between 0.1 and 1 kA m^{-2}, each value applied until a steady state condition was reached. The intensiostatic steps were applied using an ELIND DC Regulated power supply (0-60V). The potential was recorded by a Keithley 199 system DMM Scanner.

ACTIVE (FLUX) CELL

MEAs were tested also under forced circulation of water, by adopting the cell shown in Figure 49:

Figure 49: Flux cell.

In this case, graphite plates were used as both current collectors and end plates of the cell. As shown in Figure 50, in each plate the water inlet and outlet are also drilled.

Figure 50: Graphite current collector used in the flux cell.

The electrode surface was in this case reduced to 4.6 cm^2. The portion of graphite collectors in direct contact with MEA present 2 mm depth and 2 mm in width grooves. In order to obtain a better current distribution a carbon cloth was placed between the electrode surfaces and the current collectors. After the assemblage of the whole cell, it was tightened with a pressure of 68 kg cm^2.

Water electrolyses were performed at room temperature and the cell voltage was measured at current density steps, usually between 0.1 and 10 kA m^{-2}. In this case, current was measured by an ammeter connected in series. The current values were applied using an ELIND DC Regulated power supply (0-60V).

(IV) Rotating Disk Electrode (RDE)

A RDE consists of a rod of electrode material embedded in an insulating cylinder, so that only a disk surface is exposed (Figure 51). The electrode is attached to a motor directly by a chuck or by a flexible rotating shaft or pulley arrangement and is rotated at a certain frequency, f (s^{-1}). The more useful descriptor of rotation rate is the angular velocity, ω (s^{-1}), where $\omega = 2\pi f$. Electrical connection is made to the electrode by means of a brush contact [18].

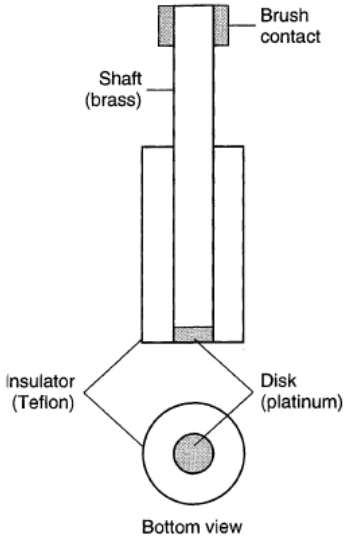

Figure 51: Rotating disk electrode [18].

Rotating the electrode at known rate enables the control of the thickness of the reagent/product diffusion layer at the electrode surface.

Therefore, when the electrode potential is scanned and reaches the potential at which the electron transfer for the considered redox couple can take place, the current starts to flow and progressively increases at increasing applied potential, until the limiting conditions are reached (the current

assumes a constant value, independent on the applied potential) when the process is controlled by mass transport.

The advantages of RDE are [20]:

1. the rate of mass transport of reactants to the electrode surface is controlled precisely by fixing the angular velocity (ω). The solution flows toward the electrode surface as shown in Figure 52.

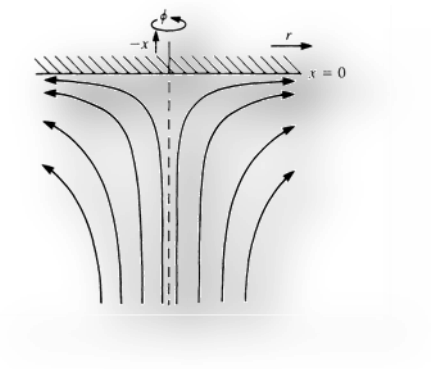

Figure 52: Streamlines near the rotating ring-disk electrode [18].

1. the electrode current (I) quickly achieves steady-state values ($dI/dt=0$) upon application of the electrode potential (E_{app}).
2. the current response at the RDE is insensitive to incidental vibrations of the apparatus, therefore it is possible bubbling gas in solution while recording the signal.

From the analysis of the relationship between the recorded current and the rotation speed, many information can be extracted. In particular, considering the dependence of the current intensity on the square root of the angular velocity, $\omega^{1/2}$ (see Figure 53) three zones can be distinguished [18].

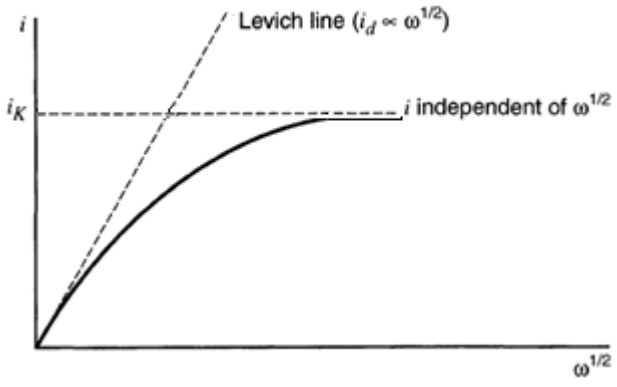

Figure 53: Variation of *i* with $\omega^{1/2}$ at an RDE (at constant *E*) for an electrode reaction[18].

Under fast electron transfer conditions, *i.e.* at low $\omega^{1/2}$ values, the limiting current is proportional $\omega^{1/2}$ [20], in accordance with the Levich equation:

$$i_L = 0.62nFAD_0^{2/3}\nu^{-1/6}c_0\omega^{1/2} \quad (75)$$

where n is the mol of electrons per mol of reactant; F is the Faraday constant (C mol^{-1}); A is the electrode area (cm^2); D_0 is the reagent coefficient diffusion (cm^2 s^{-1}); ν is the fluid kinematic viscosity (cm^2 s^{-1}); c_0 is the reagent concentration in the electrolyte solution (mol cm^{-3}); ω is the angular velocity (s^{-1}).

If the diffusion process of reagent is the rate determining step, an increase of the rotation speed leads to an increase in current, since the thickness of the diffusion layer is reduced and the transport process is faster.

At higher $\omega^{1/2}$ values, the current reaches a constant value and becomes independent on the rotation speed. This means that the charge-transfer is the rate determining step of the whole process, and the acceleration of mass transport (increase of ω) does not lead to an increase of the current intensity.

In this case the current intensity is defined by:

$$i_k = nFAk_hC_s \quad (76)$$

with

$$k_h = k_0 \exp\left[-\frac{\beta F\eta}{RT}\right] \quad (77)$$

where C_s is the reagent concentration at the surface, k_h and k_0 are the heterogeneous rate constant and standard heterogeneous rate constant for electron transfer respectively, β is the transfer coefficient, η is the overpotential, R is the gas constant and T is the temperature.

At intermediate $\omega^{1/2}$ values, the mass transport and electron transfer rates are comparable. This condition is described as *mixed transport-kinetic control*. The correlation between I and $\omega^{1/2}$ is given by the Koutecký-Levich equation.

$$\frac{1}{i} = \frac{1}{i_k} + \frac{1}{i_L} = \frac{1}{i_k} + \frac{1}{0.62nFAD_0^{2/3}\omega^{1/2}\upsilon^{1/6}c_0} \quad (78)$$

where i_K represents the current that would flow under the kinetic limitation and i_L that would flow under diffusion limitation.

By plotting *1/i vs* $1/\omega^{1/2}$, a linear correlation is obtained:

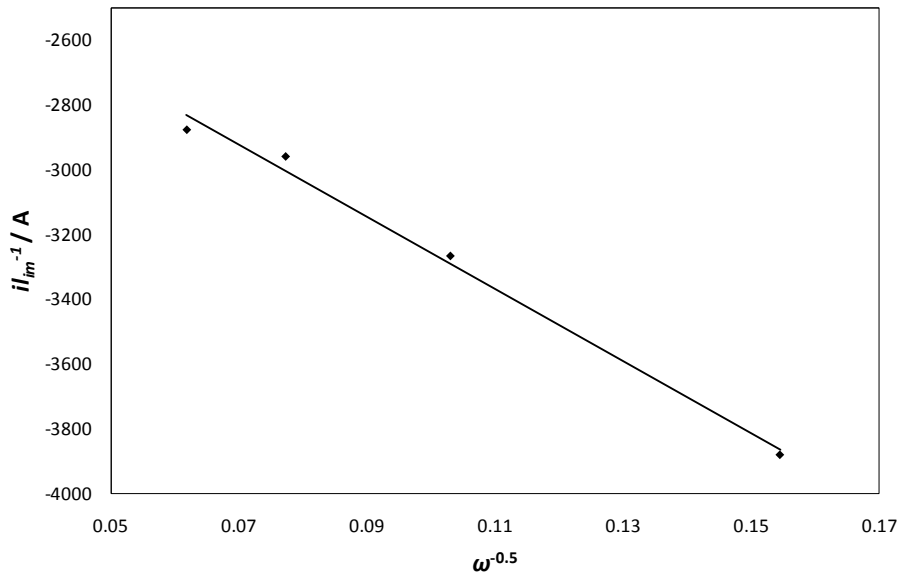

Figure 54: Koutecký-Levich graph for a general electrocatalyst.

The slope gives information on the active surface of the electrode while the intercept ($1/i_K$) provides information on the kinetics of the electron transfer process.

Beside the kinetic current a very important parameter is given by the potential values which the ORR begins, usually indicated as E_{ORR}, which is typicality measured adopting two different methods [32]: as the potential at which the additional cathodic current due to the ORR process begins to be distinguishable or as the potential at which current reaches 20 μA/cm^2 (geometric area). Between the two, the latter is less affected by the operator evaluation but is not applicable in our case because the electrodes have the same geometric areas and the specific surface area is the determinant parameter. Therefore the evaluation of E_{ORR} is conducted considering the *dE/dI vs E* (RHE) characteristics. Figure 55 show an example of determination of E_{ORR}.

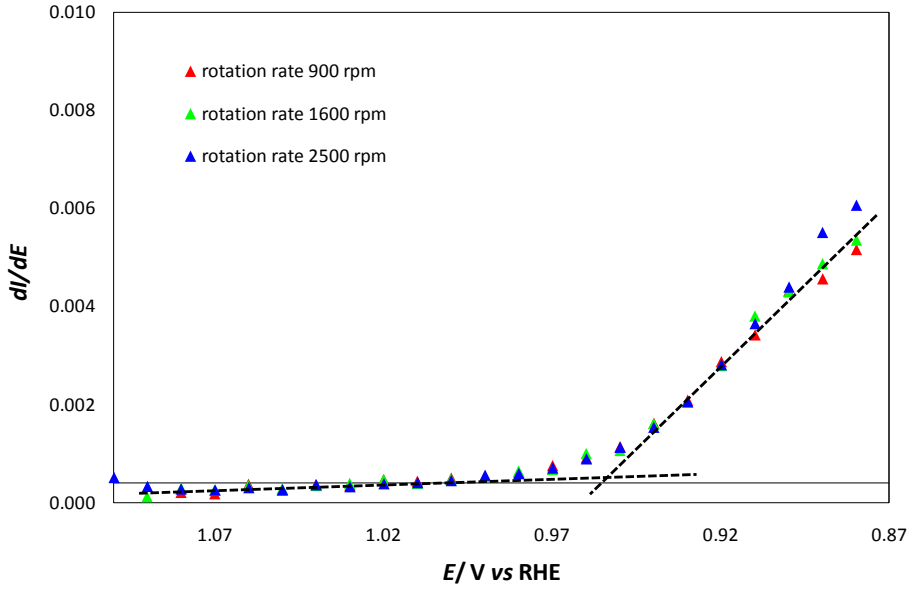

Figure 55: Example of elaboration for the E_{ORR} determination.

The intersection point between the two straight lines gives the E_{ORR} value. This method facilitates the determination of E_{ORR} because the variation slope is easily visible thus reducing the subjective error of the operator.

ELECTRODE PREPARATION

The RDE technique was applied for the characterization of IrO_2-based and Pt/C powders toward oxygen reduction reaction. Before use, the RDE electrode (area: 0.196 cm^2) was polished using Emery papers of 1000, 2400 and 4000 meshes and Al_2O_3 abrasive powder (0.05 μm). Finally the electrode was treated in an ultrasound bath both in water and acetone for 2' each. The effectiveness of the cleaning procedure was verified recording a CV curve between 1.4 V and -0.2 V *vs* RHE at 100 mV s^{-1} in background electrolyte. An example of CV corresponding to a clean glassy carbon surface is shown in the next figure:

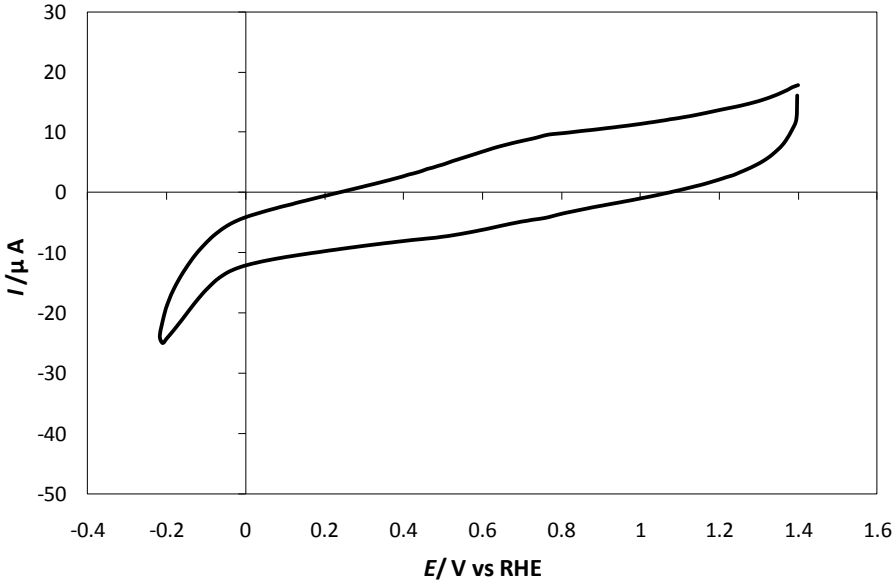

Figure 56: CV corresponding to glassy carbon cleaned.

The surface of the electrode was then modified as shown in Figure 57:

Figure 57: Schematic procedure for the modification of the rotating disk electrode.

The powder materials, dispersed in water by treatment in ultrasound, were deposited by a micropipette on the RDE surface. A 20 µL drop remains confined within the graphite disk because the Teflon matrix is highly hydrophobic. After deposition the drop was dried by a hot air flow. Different Ir loadings were obtained by varying the number of drops. In order to obtain the adhesion of the catalyst layer on the graphite support, a drop of Nafion® emulsion was also deposited.

A constant ratio of 0.03 (mg/mg) between the weight of powder and the one of the Nafion® dry polymer was adopted.

The thickness of the Nafion® film was always <0.2 μm [33][34] thus the whole process was not significantly affected by the O_2 diffusion through the Nafion® layer.

All the deposits characterized are reported in the next table:

n°electrode	n° powder	Metal loading (mg cm^{-2})	Nafion® thickness (nm)	Vulcan loading (mg cm^{-2})	Electrolyte
RDE-1	Pt/C (E-TEK)	0.1	12	----	H_2SO_4 0.5M
RDE-2		0.3	12	----	H_2SO_4 0.5M
RDE-3		0.5	12	----	H_2SO_4 0.5M
RDE-4		0.7	40	----	H_2SO_4 0.5M
RDE-5		0.5	3	----	$HClO_4$ 0.1M
RDE-6		0.5	6	----	$HClO_4$ 0.1M
RDE-7		0.5	12	----	$HClO_4$ 0.1M
RDE-8		0.5	24	-----	$HClO_4$ 0.1M
RDE-9	SnO_2	0.5	6	-----	$HClO_4$ 0.1M
RDE-10	Vulcan XC72R	----	20	0.03	$HClO_4$ 0.1M
RDE-11	Glassy carbon	0	0	----	$HClO_4$ 0.1M
RDE-12	Powder 5	0.3	12	----	$HClO_4$ 0.1M
RDE-13		0.5	20	----	$HClO_4$ 0.1M
RDE-14		0.7	30	----	$HClO_4$ 0.1M
RDE-15		1	40	----	$HClO_4$ 0.1M
RDE-16		1.3	40	----	$HClO_4$ 0.1M
RDE-17		1.5	50	-----	$HClO_4$ 0.1M
RDE-18	Powder 6	0.1	5	0.01	$HClO_4$ 0.1M
RDE-19		0.25	10	----	$HClO_4$ 0.1M
RDE-20		0.5	20	----	$HClO_4$ 0.1M
RDE-21		0.5	20	0.05	$HClO_4$ 0.1M
RDE-22		0.7	20	----	$HClO_4$ 0.1M
RDE-23		1	30	----	$HClO_4$ 0.1M
RDE-24		0.3	12	0.03	$HClO_4$ 0.1M
RDE-25		0.3	12	0.09	$HClO_4$ 0.1M
RDE-26		0.3	12	0.15	$HClO_4$ 0.1M
RDE-27	Powder 7	0.25	6	----	$HClO_4$ 0.1M
RDE-28		0.5	10	----	$HClO_4$ 0.1M
RDE-29		0.7	15	-----	$HClO_4$ 0.1M
RDE-30		1	20	----	$HClO_4$ 0.1M
RDE-31	Powder 8	0.3	10	----	$HClO_4$ 0.1M
RDE-32		0.5	6	----	$HClO_4$ 0.1M
RDE-33		0.7	10	----	$HClO_4$ 0.1M
RDE-34		1	10	----	$HClO_4$ 0.1M
RDE-35	Powder 12	0.5	6	----	$HClO_4$ 0.1M
RDE-36	Powder 13	0.5	6	----	$HClO_4$ 0.1M
RDE-37	Powder 14	0.5	6	----	$HClO_4$ 0.1M
RDE-38	Powder 15	0.5	6	----	$HClO_4$ 0.1M
RDE-39	Powder 16	0.5	6	----	$HClO_4$ 0.1M

Table 15: List of RDEs characterized.

In order to compare the Pt/C (E-TEK), the amount of IrO_2-based powders deposited is indicated in terms of Ir loading (1 mg cm^{-2} of Ir = 1.17 mg cm^{-2} of IrO_2).

ELECTRODE CHARACTERIZATION

The electrolyte solutions adopted were: 0.1 M $HClO_4$ or 0.5 M H_2SO_4. The characterization was carried out by potentiodynamic (CV) and potentionstatic experiments. In particular, in the case of IrO_2-based materials, the following procedure was adopted:

1. recording of CV curves between 1.4 V and 0.4 V *vs* RHE at 20 mV s^{-1} at 0, 400, 900, 1600, 2500 rpm;

2. recording of polarization curves between 1.1 V and 0V *vs* RHE at 400, 900, 1600, 2500 rpm. Each voltage step has 10 mV of amplitude and 10 second length.

3. recording of a CV curve at 20 mV s^{-1} at 0 rpm.

The whole procedure was performed in N_2 saturated solution first and subsequently in O_2 saturated solution. All the measurements were conducted at 25°C.

In the case of Pt/C powder the procedure is:

1. recording of CV curves between 1.4 V and 0 V *vs* RHE at 20 mV s^{-1} at 0, 400, 900, 1600, 2500 rpm;

2. recording of polarization curves between 1.1 V and 0V *vs* RHE at 400, 900, 1600, 2500 rpm. The step has 10 mV of amplitude and 10 second length.

3. recording of a CV curve at 20 mV s^{-1} at 0 rpm.

Also in this case the whole procedure is performed in N_2 saturated solution first and subsequently in O_2 saturated solution. All the measurements were conducted at 25°C.

(V) Electrodeposited Silver electrodes

As reported in the *Introduction* chapter (see section 1.5.1), silver presents good electrocatalytic properties toward volatile organic halides electroreduction.

In this study, electrodeposited silver electrodes were prepared with the aim of comparing their electrochemical response with those obtained with silver powders. The experimental conditions, and specifically the electrodeposition bath composition, the applied current densities, the time of electrodeposition, are determinant on the deposit morphology. In particular, two electrodeposition

baths, aqueous 0.05M $KAg(CN)_2$ and 0.1M $AgNO_3$ were considered and the effect of the deposition bath nature on the morphology was preliminary investigated.

ELECTRODE PREPARATION

The silver electrodeposition was carried out in a 50 cm^3 glass cell protected from light. The substrate was either a Pt disk (3 mm diameter) embedded in a PTFE matrix or a Pt wire (0.5mm diameter, 1 cm length).

The counter electrode was a silver wire, previously treated in aqueous 65% HNO_3 and aqueous 30% NH_4OH.

Before the silver deposition, the Pt disk was polished using Emery paper (2400 and 4000 mesh) and Al_2O_3 water slurry (medium particle diameter: 0.05 and 0.03 μm). The deposit homogeneity was checked using a Wild Photomakroskop M400 optical microscope.

The conditions adopted are reported in the next table:

Electrode name	Support	Bath	j_{app} (mA cm^{-2})	Electrodeposition time	Deposited thin (μm)
$AgNO_3$-high	Pt disk	$AgNO_3$ 0.1M	5	18 min	0.6
AgCN-high	Pt disk	$KAg(CN)_2$ 0.05M	5	18 min	0.6
AgCN-low	Pt wire	$KAg(CN)_2$ 0.05M	0.5	18 hours	20

Table 16: List of electrodeposition conditions of silver and respectively supports.

ELECTRODE CHARACTERIZATION

Silver electrodeposits were characterized by CV in HPLC grade acetonitrile (CH_3CN, Merck C99.8%) containing tetraethylammonium tetrafluoborate (TEATFB, Aldrich ≥99.8%) 0.1 M. The desired trichloromethane concentrations were obtained by adding appropriate amounts of 0.5 M $CHCl_3$ (Merck C99.8%) in CH_3CN. The procedure consisted in:

1. deaeration by N_2 bubbling in the solution for 10 minutes;
2. recording of CVs in the presence of the background electrolyte between -0.5 and -2.8 V *vs* SCE at 10, 20, 50, 100, 200, 500, 1000, 2000, 5000mV/s;
3. Addition $CHCl_3$ (Merck C99.8%);
4. recording of CVs between -0.5 and -2.8 V *vs* SCE at 10, 20, 50, 100, 200, 500, 1000, 2000, 5000mV/s.

At the end of the characterization, the silver deposit was removed by alternate immersion in aqueous 65% HNO_3 and aqueous 30% NH_4OH. The effectiveness of the cleaning procedure was verified by CV recording between -0.25 and 1.2 V *vs* SCE at 100 mV s^{-1} in aqueous H_2SO_4 0.5 M. The CV shape corresponding to a cleaned electrode is reported in the next figure:

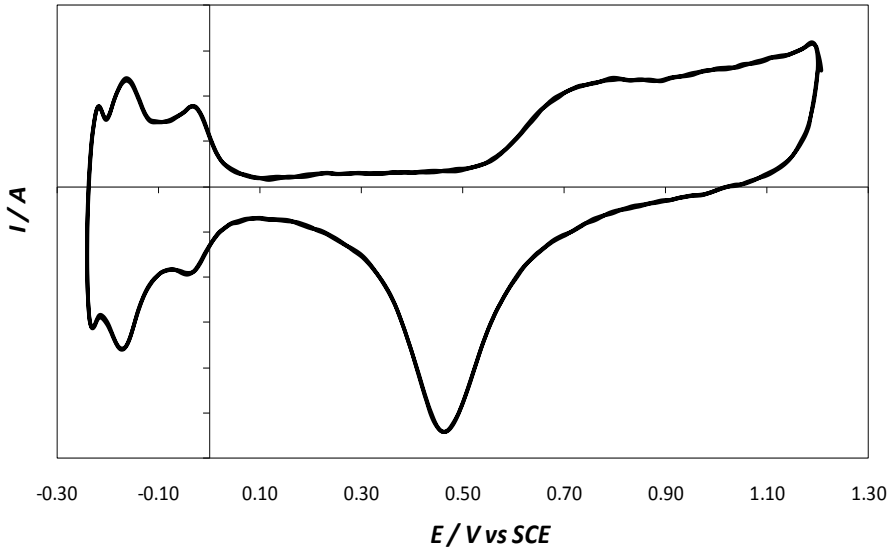

Figure 58: CV corresponding to the Pt electrode cleaned.

As further treatment, the Pt disk can be cleaned electrochemically, by polarization at:

1. 1.5V (SCE) for 30 s;
2. 0.9V (SCE) for 30 s;
3. -0.25V (SCE) for 30 s;
4. 0.9V (SCE) for 30 s;
5. 1.5V (SCE) for 30 s;

The procedure was repeated 5 times.

2.3-Physico-chemical techniques

2.3.1-Specific Surface Area Determination

Specific surface area measurements (expressed as area per weight unit) are common in a high number of applications, principally when the surface extension is a key factor in the material performance as in catalysis. As discussed above, electrode properties are strictly connected to the material geometric effects. In particular, the materials show better performances at increasing surface area. Moreover considering the same material, by reducing the particle size *i.e.* by increasing the surface area, the number of surfaces defects is likely to increase. Defective sites usually play an important role in the material properties. The most widely used method for the determination of the specific surface area is the so-called BET method (Brunauer, Emmett and Teller, 1938 [35]). This method consists in the physical adsorption/desorption of a probe molecule onto the solid surface. The sample material is placed in a vacuum chamber at a constant and very low temperature, usually at the temperature of liquid nitrogen (-195.6 °C), where the pressure is widely varied in order to generate adsorption and desorption of the gas. Typical probe molecules are inert gases, the most used nitrogen, since they are not specifically adsorbed on almost every type of surface. The adsorption on the surface does not involve specific interaction but only Van der Waals interactions (physisorption). This is particularly important in order to collect experimental data which depend only on the solid properties. Also, nitrogen molecules are very small, being able to penetrate in very narrow pores. Knowing the area occupied by one adsorbate molecule, σ (for example, σ = 16.2 Å for nitrogen), and using an adsorption model, the total surface area of the material can be determined. The instrument response consists in the volume, *V*, of adsorbed gas *vs* P/P_0 (where P and P_0 are the equilibrium and the saturation pressure of the adsorbate at the temperature of adsorption, respectively), and provides important information not only on the surface extension but also about the quantity, shape and diameter distribution of pores. The elaboration of isotherms is based on theories developed for gas/solid interfaces.

The method is based on the Langmuir theory, which describes monolayer molecular adsorption, extended to multilayer adsorption. According to both theories, each adsorbed layer has equal adsorption and desorption rates and the adsorption heat is independent on the surface coverage (absence of interaction between the adsorbed molecules). In the case of multilayer formation, the following further assumptions are made:

1. gas molecules physically adsorb on a solid surface as a semi-infinite stack of layers;
2. the Langmuir theory can be applied to each layer;

3. there are lateral interactions between molecules;
4. adsorption rate is considered to be proportional to the uncovered fraction of the underneath layer and the desorption rate is proportional to the coverage of the desorbing layer.

The resulting BET equation is expressed by:

$$\frac{P}{V(P_0 - P)} = \frac{1}{V_m C} + \frac{(C-1)P}{V_m C P_0} \quad (79)$$

where V is the adsorbed gas volume at the pressure P, V_m is the monolayer volume, and C is a constant related to the adsorption heat for the first monolayer and to the gas liquefaction heat.

By plotting $P/[V(P_0-P)]$ *vs* (P/P_0), V_m and C can be obtained. In particular, the specific area S, can then be derived:

$$S = N_A V_m \sigma \quad (80)$$

where N_A is Avogadro's number and σ is area occupied by one adsorbate molecule.

The specific surface area that can be determined by gas sorption ranges from 0.01 to over 2000 m^2/g. Determination of the pore size and the pore size distribution of porous materials can be made from the adsorption/desorption isotherm using a model based on the Kelvin equation:

$$\ln\left(\frac{P}{P_0}\right) = -\left(\frac{2\gamma v \cos\Theta}{RTr_p}\right) \quad (81)$$

where P is the equilibrium vapour pressure of the liquid contained in a pore of radius r_p and P_0 is the equilibrium pressure of the same liquid exhibited on a planar surface, γ and v are the liquid surface tension and the molar volume respectively, Θ is the contact angle at which the liquid is in contact with the pore wall.

The range of pore sizes that can be measured using gas sorption is from a few ångstroms up to about half a micrometer.

The isotherms can have very different shapes depending on the type of adsorbent, the type of adsorbate, and intermolecular interactions between the gas and the surface. The first systematic attempts to interpret the adsorption isotherm for gas-solid equilibrium was introduced by Brunauer, Deming, Deming and Teller (BDDT) in 1940 [36]. These authors classified isotherms into five types.

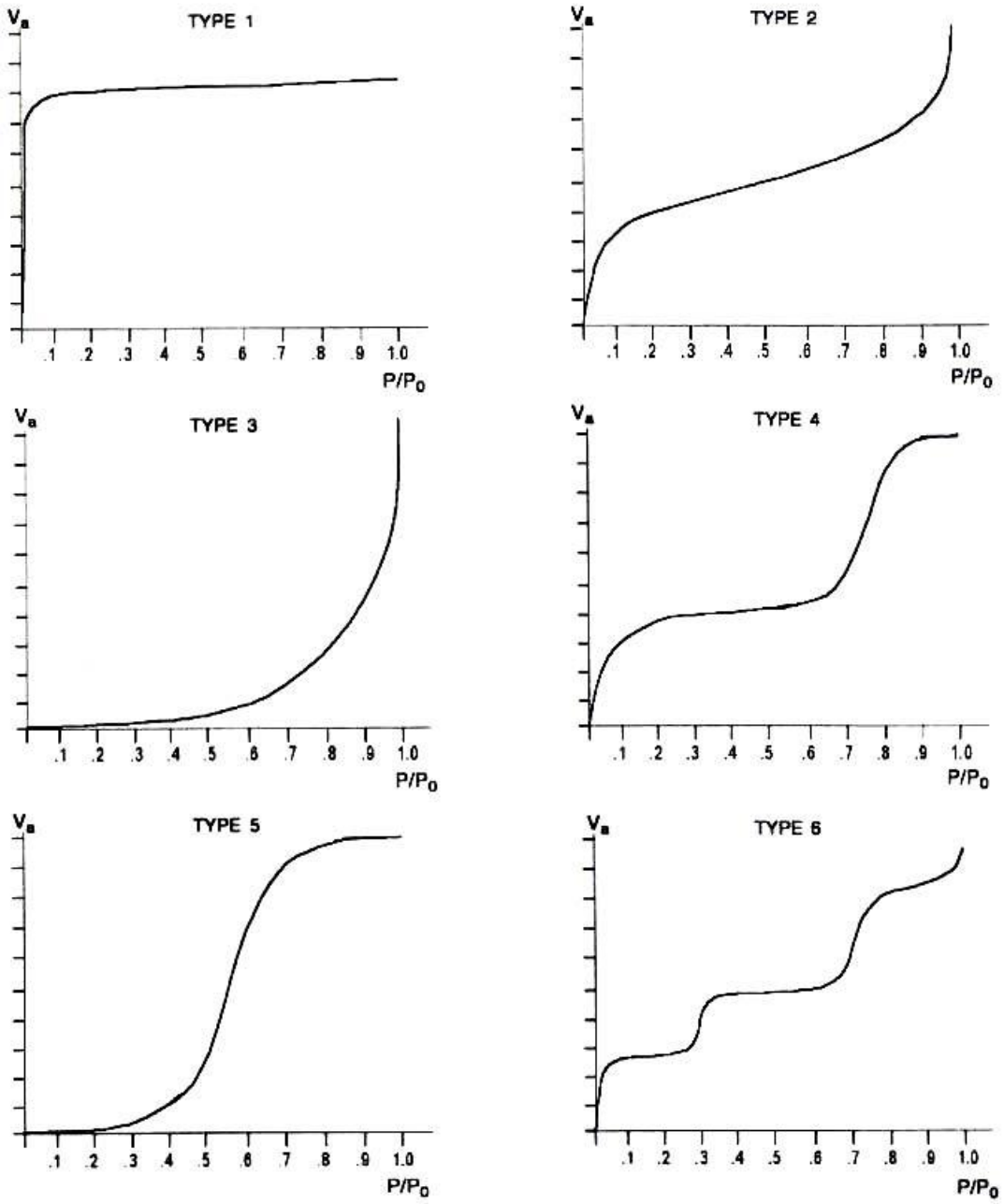

Figure 59: Qualitative representation of the six adsorption isotherm.

The first one is often indicated as Langmuir's isotherm. The adsorbed volume reaches an asymptotic value that corresponds to a surface which is completely occupied. This situation is rarely observed in porous materials.

Type II has a sigmoidal shape. A plateau is observed when a monolayer is formed, then the adsorption continues up to infinite adsorbed gas volume. This trend is obtained with material without porosity or with porous larger than few micrometer. Type III it is rarely observed. This

isotherm is recorded when the gas does not wet the surface. In this way, after adsorption starts, further adsorption is facilitated and volume rapidly goes to infinite values.

Type IV is the most frequently found in porous materials. At low coverage grade the shape is similar to type II. The second plateau is observed when the micropores are completely filled.

Type V rarely occurs. This case is similar to type III but is occurs on porous materials.

Type VI is indicative of a nonporous solid with a step like monolayer.

In the case of type IV, V and VI isotherms hysteresis phenomena are usually observed. This is due to capillary condensation that occurs in the narrow pores (up to 50 nm diameter).

It is widely accepted that there is a correlation between the shape of the hysteresis loop and the pore shapes. An empirical classification of hysteresis is given by the IUPAC which is based on earlier classification by de Boer.

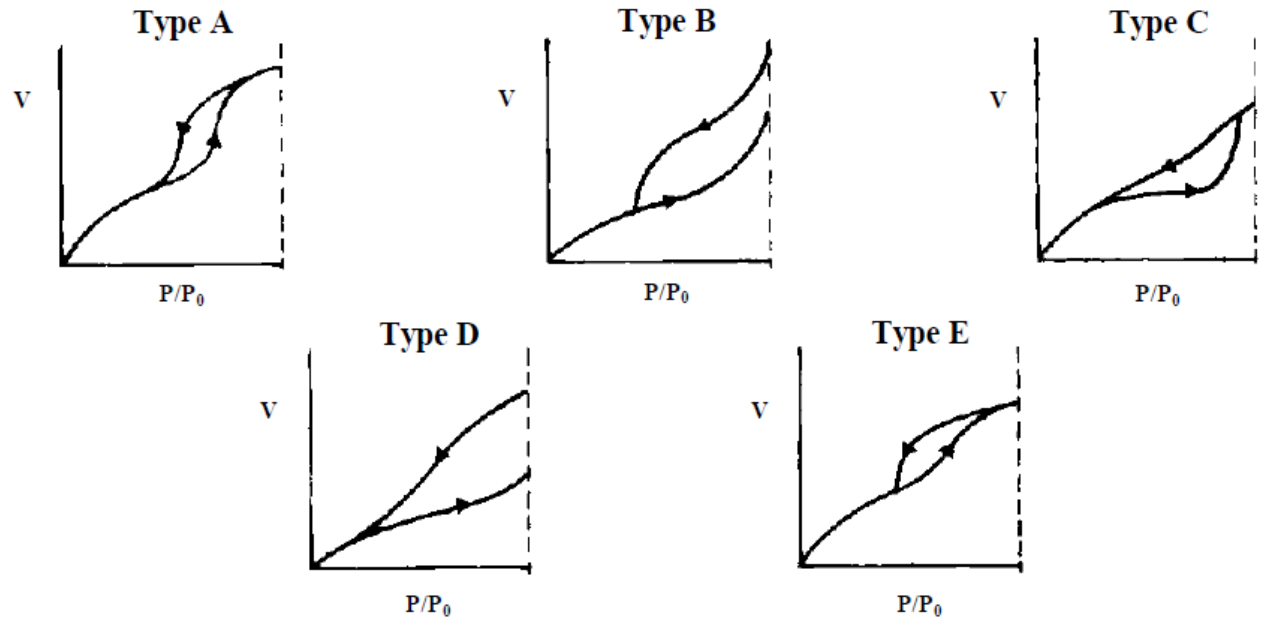

Figure 60: Qualitative representation of the five De Boer hysteresis loop shapes.

Type A hysteresis is due principally to cylindrical pores open at both the ends.

Type B hysteresis curve is associated with slit-shaped pores or the space between parallel plates.

Type C and D hysteresis are produced by a mixture of tapered or wedge-shaped pores open ends in the first case or having narrow necks at one or both open ends in the second case.

Type E is related to the presence of "bottle-neck" pores.

In this work, specific surface area values was obtained by N_2 adsorption/desorption under isothermal conditions at -196 °C using a *Coulter SA 3100* instrument. Pores dimension distributions were calculated by adopting the Barrett, Joyner e Halende (BJH) method.

2.3.2-UV-VIS Spectroscopy

The ultraviolet region of the spectrum is generally considered to range from 200 to 400 nm and the visible region from 400 to 800 nm. Absorption of electromagnetic radiation in the visible and ultraviolet regions of the electromagnetic spectrum results in the promotion of an electron from an occupied orbital to an unoccupied or partially occupied orbital.

As energies of these orbitals are quantized, it follow that each transition is associated with a specific amount of energy. The energy of the electronic transition from the highest occupied molecular obital (HOMO) to the lower unoccupied molecular orbital (LUMO) often corresponds to ultraviolet (UV) or visible (VIS) region of electromagnetic spectrum.

At low temperature, most of the molecules are in the lowest vibrational state of the lowest electronic energy level, the ground state. Adsorption of UV or visible light leads to promotion of an electron from ground state to excited electronic level (Figure 61).

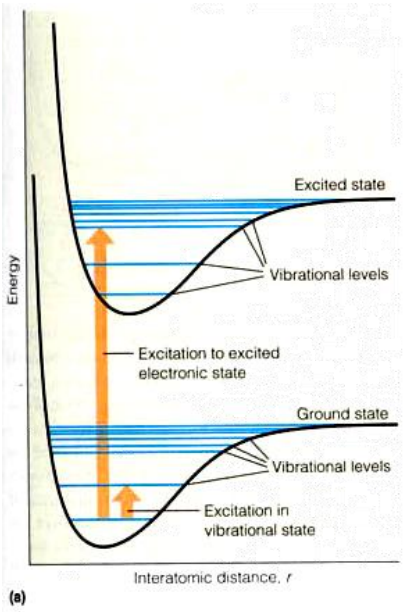

Figure 61: Schematic diagram showing possible molecular electronic transitions and vibrational and rotational energy levels.

The adsorption of a photon is fast and is more rapid than molecular vibration or rotations. Accordingly, the electronic transitions are a "snapshot" of the molecule in a particular vibrational and rotational state at a particular moment in time; this is the so called Frank Condon Principle. Since the vibrational and rotational energy levels are much more closely spaced than the electronic levels, a broad band is observed in the electronic spectrum. Although many electronic transitions are possible they will not necessary occur. There are complex selection rules based on the symmetry of the ground and excited states of the molecule under examination. Basically, electronic transitions

are allowed if the orientation of the electron spin does not change during the transition and if the symmetry of the initial and final functions is different; these are called the spin and symmetry selection rules, respectively. However the so-called "forbidden" transitions can still occur but give rise to weak absorption.

The amount of light absorbed by a given sample is governed by Lambert Beer law. This law states that the absorbance *A* of a solution is directly proportional to the path length and the concentration of absorbing molecules:

$$A=\varepsilon c l \quad (82)$$

where ε is the molar extinction coefficient of the absorbing molecule, l (cm) is the length of the cell containing the solution, and c ($molcm^{-3}$) is the substance concentration. The molar absorptivity ε, characteristic of the molecule, is a measure of the intensity of the absorption and usually ranges from 0 to 10^8 cm^2 mol^{-1}. The grater the probability of a particular absorption and its associated electronic transition, the higher the ε. For most molecules, absorption associated with the $\pi \rightarrow \pi^*$ transition have higher ε values than the $n \rightarrow \pi^*$ transitions. In general, forbidden transition give rise to low-intensity (low ε) absorption bands (ε < 10000 cm^2 mol^{-1}) but two important forbidden absorption are encountered quite commonly: the $n \rightarrow \pi^*$ transition of ketones at approximately 300 nm (ε usually 10-100 cm^2mol^{-1}) and the weak $\pi \rightarrow \pi^*$ absorption of benzene rings at about 260 nm (ε about 100-1000 cm^2mol^{-1}).

UV-Vis spectroscopy is effective for the characterization of metallic nanoparticles, especially those containing gold, silver, and/or copper. These three elements have a specific plasmon absorption *i.e.* a collective oscillations of conduction electrons at the metal surface (typical of nanosized metal particles), in a visible region which varies with size and environment. The colour change is a very useful and convenient method to identify the chemical change from metal ions in solution to dispersed metal nanoparticles. The colloidal dispersion of Au, Ag, and Cu have a colour which varies from red to yellow, and the position of the corresponding plasmon absorption peak varies depending on the particle size and the extent of coagulation [37].

In this work UV-Vis spectroscopy was used for the characterization of silver nanoparticles. This characterization was carried out by a JASCO V-530 UV–Vis spectrophotometer. For the UV–Vis analysis, the Ag sols were diluted 1:4 and the absorption spectra were recorded in the 250–700 nm range.

2.3.3-X-Ray Powder Diffraction (XRPD)

X-ray diffraction is a versatile analytical technique for the examination of crystalline solids, which include ceramics, metals, electronic materials, geological materials, organic solids and polymers. It is useful for both qualitative and quantitative analysis of solids as well as for structural and morphological investigations. It can be performed on both single crystals and powder materials.

It is based on the diffraction of X-rays by the crystal lattice. Atoms and molecules that compose substances are commonly arranged at a distance ranging from 0.1 to 0.5 nm. When the material is irradiated with a beam of monochromatic X-rays having a wavelength λ close to the inter-atomic or intermolecular distance *d*, the diffraction of the X rays at various angles with respect to the primary beam is observed.

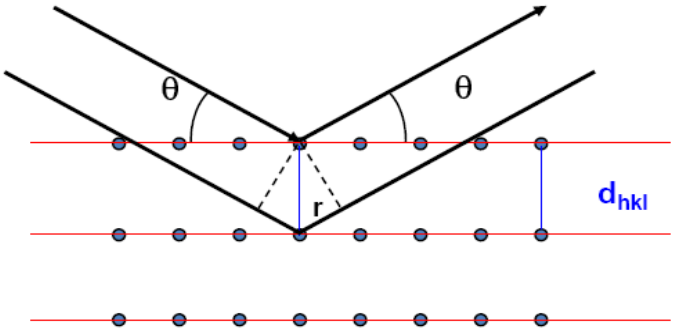

Figure 62: Illustration of Bragg's law.

The diffraction phenomena are due to constructive or destructive interference between the x-ray scattered by atoms. The conditions for constructive interference are described by the Bragg law:

$$n\lambda = 2d \sin\theta \qquad (83)$$

where *n* is an integer number, λ is the wavelength of the radiation, *d* is the spacing between the planes of atoms, and θ is the incident angle [38].

In general the d-spacing is a function of the lattice parameters (a,b,c) and angles (α,β,γ) which define the unit cell and the Miller indices (h,k,l). It is the geometry of the crystal lattice that determines the position of the peaks in an X-ray diffraction pattern [39]. In the powder method, the sample is a large collection of very small crystals, randomly oriented. This means that the diffracted rays are arranged as a series of concentric cones. By sampling along a longitudinal circle the intensities of the cones, provided that there are no preferred orientation effects, a series of peaks is obtained, by which a large number of information are obtainable.

In this work, room temperature patterns were collected between 10 and 80° (2θ range Δ2θ = 0.02°, time per step = 10s, scan speed = 0.002°/s) with a Siemens D500 diffractometer, using Cu Kα

radiation. Rietveld refinement has been performed using the GSAS software suite 2 and its graphical interface EXPGUI 3. The broadening due to the instrumental contributions was taken into account by means of a calibration performed with a standard Si powder. Components of peak broadening due to strain were not varied in the fitting procedure. The convergence was in any case satisfactory. The backgrounds have been subtracted using a shifted Chebyshev polynomial. The diffraction peak's profile has been fitted with a pseudo-Voigt profile function. Site occupancies and the overall isotropic thermal factors have been varied.

2.3.4- X-Ray Photoelectron Spectroscopy (XPS)

X-ray photoelectron spectroscopy (XPS) is based on the photoelectric effect. When a sample is irradiated with monochromatic X-rays, core-level electrons from the inner shells of atoms in the sample are ejected from the sample to the surrounding vacuum.

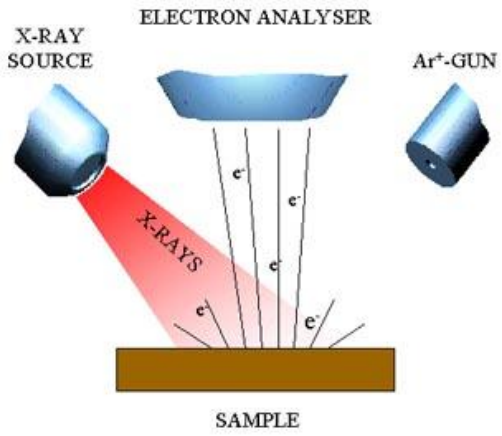

Figure 63: Scheme of XPS analysis.

The kinetic energy, E_k, of the emitted photoelectron is given by:

$$E_b = hv - E_k - \Phi \quad (84)$$

where E_b is the binding energy of the electron, hv is the energy of the exciting radiation, and Φ is the spectrometer work function, a constant for a given analyzer.

Since hv and Φ are constants, the binding energy is dependent only on the kinetic energies of the emitted photo-electron and is characteristic of the emitter atom.

XPS instruments include an electron energy analyzer that separates electrons having different kinetic energy and a detector that counts the number of electrons. By plotting the number of electrons (*i.e.* number of electrons) versus the binding energy, qualitative and quantitative information on the surface (around 10 nm thicknes) are obtained. Other effects are visible in XPS

spectra, such as spin-coupling effect and the influence of the chemical status of the emitting atoms (*chemical shift*).

In particular, in term of atomic configurations, the elimination of an electron after the photoelectric effect leaves an unpaired electron in the valence shell. In the case of orbitals having nonzero orbital angular momentum, a coupling between the spin of the unpaired electron and the angular momentum happens. In this case, the ionization gives rise to two states, thus generating a doubled of peaks in the XPS spectra (this is observed, for example in the Ir 4f peak).

There are many applications of XPS, particularly in the area of surface analysis. The penetration of X-rays into solids is 5nm, so XPS gives information only about surface state.

From an analytical standpoint, the utility of XPS is that it provides information about the surface region without seriously damaging that region. Any solid material can be studied and all elements (except hydrogen) can be detected by this technique, its detection limit being 0.1 % atomic.

In this work, XPS spectra were recorded by an *M-Probe (Surface Science Instruments)* instrument and a monochromatic X-Ray beam of 1486.6eV (radiation Al Kα). Irradiated spot was 200 x 750 μm^2 wide. The binding energies (E_b) are corrected for specimen charging by referencing the C 1s peak to 284.6 eV, and the background was subtracted using Shirley's method [40]. The deconvolutions were performed using only Gaussian line shapes. The peaks were fitted without E_b or FWHM (Full Width at Half Maximum) constraints. The accuracy of the reported E_b can be estimated to be ± 0.1 eV. With a monochromatic source, an electron flood gun is required to compensate the build up of positive charge on the samples during the analyses, when insulating samples were analysed: a value of 5 eV has been selected.

2.3.5-Scanning and Transmission Electron Microscopies (SEM, TEM)

Electrons microscopes are useful techniques for the analysis of the morphology of solids. In particular, in order to study the shape, the size and the structure of nanoparticles, electron microscopies are the most suitable techniques. In SEM and TEM techniques, electrons are emitted from a metal cathode, and are focused onto the sample surface. The electron beam is then scanned over a desired portion of the sample.

These techniques are characterized by very low resolution limits: usually about 2nm for SEM and ca 0.5 Å for TEM.

The high resolution is the result of the small effective electron wavelengths λ of electrons, which is given by the de Broglie relationship:

$$\lambda = \frac{h}{\sqrt{2m_e q_e V_e}} \qquad (85)$$

where m and q are the mass and the charge of electron respectively, h is Plank's constant and V_e is the potential difference through which the electrons are accelerated.

In particular, in the case of *scanning electron microscopy* (SEM), secondary electrons, produced after the interaction of the primary beam with the matter, are collected by an analyzer placed on the top of the sample at a given angle with respect to the incident beam, as shown in Figure 64.

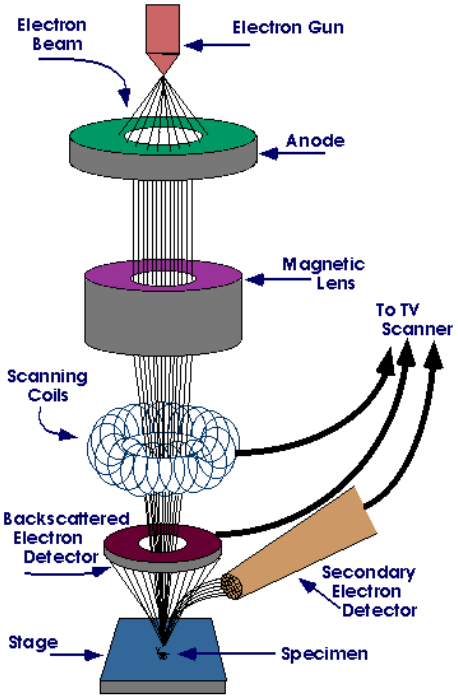

Figure 64: Scheme of SEM instrument.

The electron beam comes from a filament, which can be made of various types of materials (tungsten, lanthanum hexaboride) and focused on the sample by the objective magnetic lens. The primary electron beam is scanned across the surface of a sample and various phenomena can occur as shown below.

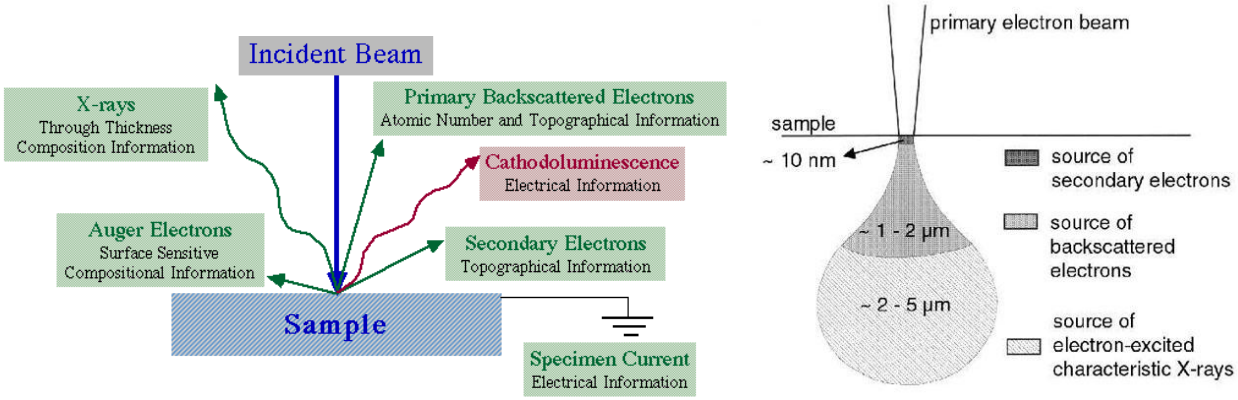

Figure 65: Scheme of the possible electron-matter interactions and the relative sample regions involved.

In particular:

- *Backscattered Electrons (BSE)*: consist of high-energy electrons that are reflected or back-scattered out of the specimen interaction volume by elastic scattering interactions with specimen atoms. Since heavy elements (high atomic number) backscatter electrons more strongly than light elements (low atomic number), and thus appear brighter in the image, BSE are used to detect contrast between areas with different chemical compositions.

- *Secondary Electron:* are electrons ejected from the K-orbitals of the specimen atoms by inelastic scattering interactions with the electron beam. Due to their low energy (50eV), these electrons originate within a few nanometers from the sample surface. The recording of morphology images is related to the collection these electrons.

- *Auger Electron:* originated by the energy loss of the atom occurring after a secondary electron emission. Since a core energetic electron is emitted from the atom (usually from K-shell) during the secondary electron emission, an electron vacancy is generated. An outer energy electron from the same atom can then "fall" to fill the vacancy. This creates an energy excess that can be transferred to another electron that, in turn, is ejected from the atom. The ejected electron is called Auger Electron. Auger electrons can be correlated to the nature of the emitter atom.

- *X-rays:* originated by the energy loss of the atom after the emission of a secondary electron. Since a core (usually K-shell) electron was emitted from the atom during the secondary electron emission, an electron vacancy is present. An electron from an outer shell then fills the hole, and the difference in energy between the outer shell and the inner shell may be

released in the form of an X-ray. X-rays emitted from the atom have a characteristic energy which is unique to the element from which is emitted.

In the SEM the secondary electrons emitted from the sample are collected. An electron detector is used to convert the amount of secondary electrons collected during the scan into a topographic image. Since only the sample surface is the source of secondary electrons, and since the emission coefficient depends on the angle between the incident beam and the surface, this technique gives an image of the sample surface.

Otherwise, transmission electron microscopy (TEM) is a useful tool for the analysis of the structures of very thin specimens through which electrons are transmitted. Figure 66 shows a scheme of a TEM instrument.

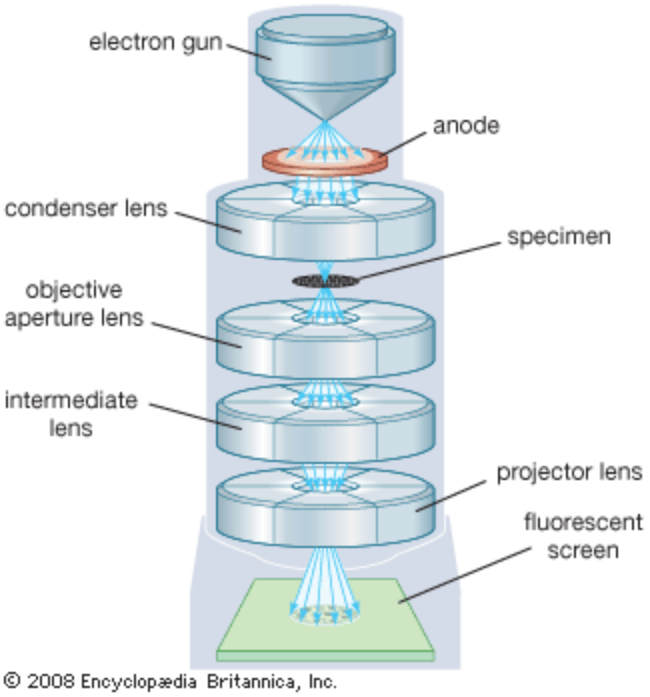

Figure 66: Scheme of TEM instrument.

In the TEM technique electrons are accelerated to 100keV or higher (up to 1MeV) and then focused onto a thin specimen (less than 200 nm) by means of a condenser lens system. Accelerated electrons can then penetrate the sample. The greatest advantages that TEM offers are the high magnification factor ranging from 50 to 10^6 and its ability to provide morphology images, diffraction patterns, and elemental analysis during the same working session. By selecting between direct electrons (brightfield, BF) or scattered one (dark field, DF), different information can be obtained.

Elastic scattering does not provoke energy losses and gives rise to diffraction patterns. Inelastic interactions between incident beam and sample electrons occur in the presence of heterogeneities

such as grain boundaries, dislocations, second-phase particles or defects, thus leading to a spatial variation in the intensity of transmitted electrons.

High voltage TEM instrument have the additional advantage of a deeper electron penetration because high-energy electrons interact less strongly with the matter than lower-energy ones. One limitation of the TEM is its limited depth resolution.

The higher the operating voltage of the TEM instrument, the greater its lateral spatial resolution.

It is also very useful, in terms of morphological and structural investigations, to tilt the sample in a particular angle, in order to produce many diffraction beams. In this case, a structural image is produced, showing dark column corresponding to atoms that form fringes. In this case the technique is called high resolution TEM (HRTEM).

In addition, electrons are diffracted by the sample and the diffraction pattern can be recorded in order to obtain a complementary information about the sample structure. This technique is called selected-area electron diffraction (SAED). It offers unique capability to determine the crystal structure of individual nanomaterials such as nanocrystals and nanorods, and the crystal structures of different part of the sample.

In the case of characterization of silver nanoparticles TEM micrographs of the colloidal dispersions were obtained using an EF TEM LEO 912AB instrument operated at an accelerating voltage of 120 kV. Specimens for imaging by TEM were prepared by evaporating a droplet of silver colloids onto carbon-formvar[1] copper grids.

2.3.6-Optical Microscopy

To record optical images of experimental set-ups, a conventional digital photocamera was used. For electrode pictures, a *Wild Photomakroskop M400* optical microscope equipped with a *JVC TK-C1380* camera was used.

[1] Formvar is poly[vinyl formal]: 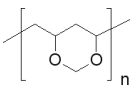

2.4-References

[1] A. Minguzzi, M. A. Alpuche-Aviles, J. R. López, S. Rondinini, and A. J. Bard *Anal. Chem.* **2008,** 80, 4055.

[2] P.C. Andersen, K.L. Rowlen, *Appl. Spectrosc*. **2002**, 56,124A.

[3] A.D. McFarland, R.P. Van Duyne, *Nano Letters* **2003**, 3,1057.

[4] Yugang Sun and Younan Xia, *Science* 2002, 298, 2176.

[5] Kan-Sen Chou_, Chiang-Yuh Ren *Mat. Chem. Phys.* **2000**, 64, 241.

[6] H. H. Nersisyan, J. H. Lee, H. T. Son, C. W. Won, D. Y. Maeng, *Mater. Res. Bull*. **2003**, *38*, 949.

[7] U. Nickel, A. Castell, K. Poppl, S. Schneider, *Langmuir* **2000**, 16, 9087.

[8]Y. Zhu, Y. Qian, M. Zhang, Z. Chen, *Mater. Lett*. **1993**, 17, 314.

[9] H.S. Zhou, T. Wada, H. Sasabe, H. Komiyama, *Appl. Phys. Lett*. **1996**, 68 ,1288.

[10] Y.A. Kotov, O.M. Samatov, *Nanostructured Mat*. **1999**, 12 ,119.

[11] K. Okitsu, H. Bandow, Y. Maeda, *Chem. Mater.* **1996** 8, 315.

[12] P.Y. Silvert, R. Herrera-Urbina, N. Duvauchelle, V. Vijayakrishnan, *J. Mater. Chem*. **1996**, 6, 573.

[13] H.H. Nersisyana, J.H. Leea, H.T. Sona, C.W. Wona, D.Y. Maenga, *Mat. Res. Bul*. **2003**, 38, 949.

[14] Joseph Wang *"Analytical electrochemistry"* Second edition, Wiley-VCH, **2000.**

[15] Cristopher M. A. Brett and Ana Maria Oliveira Brett *"Electrochemistry: principles, methods and applications"* Oxford University Press, **1993**.

[16] S. Ardizzone, G. Fregonara and S. Trasatti, *Electrochim. Acta* **1990**, Vol 35, n°1, 263.

[17] Perry's Chemical Engineers' sixth edition (Robert H.Perry, Don Green, McGraw-Hill International editions, Chemical Engineering Series).

[18] Allen J. Bard Larry R. Faulkner "*Electrochemical methods: Fundamentals and Applications*" John Wiley & Sons. Inc 2000.

[19] C. Cachet-Vivier , V. Vivier, C.S. Cha, J.-Y. Nedelec, L.T. Yu *Electrochim. Acta* 2001, 47, 181.

[20] Stephen Treimer, Andrew Tanga, and Dennis C. Johnson, *Electroanalys*. 2002, 14, n°3, 165.

[21] Alan M. Bond, Darryl Luscombe, Keith B. Oldham and Cynthia G. Zoski *J. Electroanal. Chem* **1988**, 249, 1.

[22] Ferro, S.; De Battisti, A. *Electrochim. Acta* **2002**, *47*, 1641.

[23] Erika Herrera Calderon, Rolf Wüthrich, Philippe Mandin, György Fóti, Christos Comninellis *J. Appl. Electrochem.* **2009**, 39, 1379.

[24] Magdalena Hromadova´ and W. Ronald Fawcett, *J. Phys. Chem. A* **2001**, *105*, 104.

[25] W. R Fawcett,. *Electrochim. Acta* **1997**, *42*, 833.

[26] Qingyun Chen and Greg M. Swain. *Langmuir* **1998**, *14*, 7017.

[27] Granger, M. C.; Witek, M.; Xu, J.; Wang, J.; Hupert, M.; Hanks,A.; Koppang, M. D.; Butler, J. E.; Lucazeau, G.; Mermoux, M.; Strojek, J. W.; Swain, G. M. *Anal. Chem.* **2000**, *72*, 3793.

[28] J. Weber, Z. Samec, V. Mareček *J. Electroanal. Chem.* **1978**, 89. 271.

[29] Dario Gallizzioli, Sergio Trasatti *Electroanal. Chem. and Interf. Electrochem.* **1973**, 44, 367.

[30] Sergio Ferro, Christina Urgeghe and Achille De Battisti *J. Phys. Chem. B* **2004**, 108, 6398.

[31] www.unive.it/media/allegato/ecotossicologia/CapI_Chimicadibase.pdf

[32] Yoshio Takasu, Norihiro Yoshinaga, Wataru Sugimoto *Electrochem. Comm.* **2008**, 10, 668.

[33] H. Takenaka, E. Torikai, Y. Kawami, and N. Wakabayashi. *Int. J. Hydrogen Energy*, **1982**, 7, 397.

[34] T. J. Schmidt, H.A.Gasteiger *"Handbook of fuel cell-Fundamentals technology and applications"* Wolf Vielstich **2003** chapter 22.

[35] S.Brunauer, P.H. Emmet, E. Teller *J. Am Chem Soc*, **1938**, 60, 309.

[36] S. Brunauer, L. Deming, W. Deming, E. Teller *J. Am. Chem. Soc.* **1940**, 62, 1723.

[37] Montinari Adachi, David J. Lockwood *"Self-organized Nanoscale Materials"* Springer, **2006.**

[38] McGraw Hill *"Dean's Analytical chemistry handbook"* Second Edition Pradyot Patnaik.

[39] F. A. Settle *"Handbook of instrumental techniques for analytical chemistry"* Prentice Hall PTR **1997.**

[40] D. Shirley, *Phys. Rev.* B **1997,** 5, 4709.

3. Results and Discussion

PART-1: DEVELOPMENT OF ELECTROCATALYSTS FOR URFC SYSTEM

3.1-Characterization of IrO_2-SnO_2 nanopowders

3.1.1-Introduction

The electrochemical applications of IrO_2-based materials range from sensors [1][2] to electrochromic devices [3][4] to electrocatalytic coatings of dimensionally stable anodes (DSAs) in chlor-alkali technology [5][6]. More recently acid water electrolysis, finalized to the production of high purity hydrogen, has become a key process in the conversion and storage of energy from renewable sources.

Moreover, thanks to the development of the technology of solid polymer electrolyte cells, reversible proton exchange membranes electrolysers/fuel cells (RFC) devices are becoming increasingly attractive for environmentally respectful distributed systems. The choice of electrode coating is mainly restricted to IrO_2 or RuO_2-based materials, which conjugate high electrocatalytic activity for oxygen evolution reaction (OER) with high stability in acidic environment. Although RuO_2 has a higher electrocatalytic activity than IrO_2 and lower costs, its service life is about 20 times shorter [7] thus shifting the interest toward IrO_2-based mixed oxides in which the precious metal is diluted by a cheap hosting matrix. In particular binary SnO_2–IrO_2 mixtures [9]-[17] result especially stable under extensive O_2 evolution; consequently electrodes containing more than 10% of precious metal oxide are known to proceed in acidic solutions with kinetic parameters close to those of pure IrO_2 [10]- [12]. Moreover, IrO_2-based oxides have been recently investigated as energy storage materials [18] and as electrocatalysts for oxygen reduction reaction (ORR) [19]-[21], hydrogen evolution reaction (HER) [22][23] and electroxidation of organic pollutants [24]-[26].

The adopted synthetic route contributes significantly to the tailoring of the material and consequently to its final performance, the more so in the case of multicomponent nanocristalline systems. Recently the effectiveness of the low-temperature sol-gel synthetic process to produce tailored nanostructured materials also in the case of the base matrix of SnO_2 was documented [27][28].

In the present thesis particular attention was dedicated to the analysis of both the structural features and the electrochemical behaviour of the SnO_2–IrO_2 mixed oxides.

In particular powder materials prepared by adopting different synthetic parameters (*e.g.* the choice of the precursors, the method of iridium salt addition and the selection of the calcination temperatures as describe in Section 2.1.1), were considered.

A first physico-chemical characterization by XRPD, BET, XPS, SEM techniques were carried out. The powders materials considered in this case are reported in the subsequent table.

n° powder	Composition	IrO_2 wt%	Precursor	Method	$T_{calcinations}$ / °C
3	$Ir_{0.15}Sn_{0.85}O_2$	20	$Sn(C_4H_9O_4)+IrCl_3$	MM	450
4	$Ir_{0.15}Sn_{0.85}O_2$	20	$Sn(C_4H_9O_4)+IrCl_3$	MM	500
5	$Ir_{0.15}Sn_{0.85}O_2$	20	$Sn(C_4H_9O_4)+IrCl_3$	I	450
6	$Ir_{0.31}Sn_{0.69}O_2$	40	$Sn(C_4H_9O_4)+IrCl_3$	I	450
7	$Ir_{0.50}Sn_{0.50}O_2$	60	$Sn(C_4H_9O_4)+IrCl_3$	I	450
8	$Ir_{0.73}Sn_{0.27}O_2$	80	$Sn(C_4H_9O_4)+IrCl_3$	I	450

Table 17: List of powders characterized by physic-chemical techniques.

Here, CS, MM, I and I-Cl denote the different ways adopted for the iridium addition, has been explained in Section 2.1.1.

The aim is the determination of the correlation between structural, morphological and surface properties on one side and the electrochemical performances on the other side.

The electrochemical characterization by cyclic voltammetry was performed. Usually CVs between 0.4 – 1.4 V *vs* RHE in 0.1 M $HClO_4$ aqueous solution (if not differently indicated) at 20, 10, 5 and 2 mV s^{-1} were recorded. All potentials value reported were referred to the reversible hydrogen electrode (RHE). The chosen methodology provides both the total number of active sites by the determination of the voltammetric charge, Q (C), from the integration of the I/E curves recorded and the active sites accessibility from the dependence of Q from the scanning rate (see Section 2.2.1). Three different supports were considered: cavity micro-electrode (C-ME), rotating disk electrode (RDE) and Ti plate. More details regard to design, electrode preparation procedures and operative conditions were reported in the sections 2.2.5-I, 2.2.5-IV and 2.2.5-II respectively. In particular using of C-ME a further characterization in presence of a redox couple (Fe^{3+}/Fe^{2+}) a probe was also conducted. The aim is determining the equivalent radius of surface that is correlated to the active area of the powder analysed (see Section 2.2.5-I '*Electrode characterization*').

C-ME allows the study of the material without the influence of additional components such as, *e.g.* any gluing agent. The powders characterized by C-ME are reported in Table 18.

n°powder	Composition	IrO_2 wt%	Precursor	Method	$T_{calcinations}$ / °C
1	$Ir_{0.15}Sn_{0.85}O_2$	20	$Sn(C_4H_9O)_4$+$IrCl_3$	CS	450
2	$Ir_{0.15}Sn_{0.85}O_2$	20	$Sn(C_4H_9O)_4$+$IrCl_3$	CS	500
3	$Ir_{0.15}Sn_{0.85}O_2$	20	$Sn(C_4H_9O)_4$+$IrCl_3$	MM	450
4	$Ir_{0.15}Sn_{0.85}O_2$	20	$Sn(C_4H_9O)_4$+$IrCl_3$	MM	500
5	$Ir_{0.15}Sn_{0.85}O_2$	20	$Sn(C_4H_9O)_4$+$IrCl_3$	I	450
6	$Ir_{0.31}Sn_{0.69}O_2$	40	$Sn(C_4H_9O)_4$+$IrCl_3$	I	450
7	$Ir_{0.50}Sn_{0.50}O_2$	60	$Sn(C_4H_9O)_4$+$IrCl_3$	I	450
8	$Ir_{0.73}Sn_{0.27}O_2$	80	$Sn(C_4H_9O)_4$+$IrCl_3$	I	450
9	$Ir_{0.15}Sn_{0.85}O_2$	20	$Sn(C_4H_9O)_4$+$IrCl_3$	I	500
10	$Ir_{0.15}Sn_{0.85}O_2$	20	$SnCl_4$+$IrCl_3$	I-Cl	450
11	$Ir_{0.15}Sn_{0.85}O_2$	20	$SnCl_4$+$IrCl_3$	I-Cl	500

Table 18: List of material powders characterized by C-ME.

An evaluation on the synthesis method, calcination temperature and IrO_2 content can be carried out.

RDE allows working in controlled mass transfer condition and therefore to extrapolate information about the kinetic behaviour of the material characterized. This support was used for investigate the reactivity of IrO_2-based materials toward oxygen reduction reaction. Therefore the CVs were recorded both under nitrogen and oxygen atmospheres. The IrO_2-based powders characterized by RDE reported are reported in the next table.

n°powder	Composition	Ir wt%	Precursor	Method	$T_{calcinations}$ / °C
5	$Ir_{0.15}Sn_{0.85}O_2$	20	$Sn(C_4H_9O)_4$+$IrCl_3$	I	450
6	$Ir_{0.31}Sn_{0.69}O_2$	40	$Sn(C_4H_9O)_4$+$IrCl_3$	I	450
7	$Ir_{0.50}Sn_{0.50}O_2$	60	$Sn(C_4H_9O)_4$+$IrCl_3$	I	450
8	$Ir_{0.73}Sn_{0.27}O_2$	80	$Sn(C_4H_9O)_4$+$IrCl_3$	I	450
12	$Ir_{0.60}Sn_{0.40}O_2$	70	$SnCl_4$+ $IrCl_3$	CS-Cl	500
13	$Ir_{0.70}Sn_{0.30}O_2$	78	$SnCl_4$+ $IrCl_3$	CS-Cl	500
14	$Ir_{0.80}Sn_{0.20}O_2$	85	$SnCl_4$+ $IrCl_3$	CS-Cl	500
15	$Ir_{0.90}Sn_{0.10}O_2$	93	$SnCl_4$+ $IrCl_3$	CS-Cl	500
16	IrO_2	100	$SnCl_4$+ $IrCl_3$	CS-Cl	500

Table 19: List of material powders characterized by RDE.

The preparation procedure of RDEs consists in dropping a suspension of electrocatalytic powder in water, as described in Section 2.2.5-IV "*Electrode preparation"*. One of the principal advantages on the use of this support is the possibility of studying the effect of additional components in the catalytic layer. In particular the effect of Vulcan XC72R® loading was evaluated.

In order to exclude the contribution on ORR reaction both the glassy carbon support and diluents matrices (SnO_2 and Vulcan XC72R®) were characterized in the same conditions. Moreover since the Pt based materials are the most materials used electrocatalysts for ORR, a commercial powder (Pt/C 28.6wt% E-TEK) were also characterised in order to obtain a comparison. In this case different Pt and Nafion® loadings were investigated.

The composition of deposited investigated are reported in the next table:

n°electrode	n° powder	Metal loading (mg cm^{-2})	Nafion® thickness (µm)	Vulcan® loading (mg cm^{-2})	Electrolyte
RDE-1	Pt/C (E-TEK)	0.1	12	----	H_2SO_4 0.5M
RDE-2		0.3	12	----	H_2SO_4 0.5M
RDE-3		0.5	12	----	H_2SO_4 0.5M
RDE-4		0.7	40	----	H_2SO_4 0.5M
RDE-5		0.5	3	----	$HClO_4$ 0.1M
RDE-6		0.5	6	----	$HClO_4$ 0.1M
RDE-7		0.5	12	----	$HClO_4$ 0.1M
RDE-8		0.5	24	-----	$HClO_4$ 0.1M
RDE-9	SnO2	0.5	6	-----	$HClO_4$ 0.1M
RDE-10	Vulcan XC72R®	----	20	0.03	$HClO_4$ 0.1M
RDE-11	Glassy carbon	0	0	----	$HClO_4$ 0.1M
RDE-12	Powder 5	0.3	12	----	$HClO_4$ 0.1M
RDE-13		0.5	20	----	$HClO_4$ 0.1M
RDE-14		0.7	30	----	$HClO_4$ 0.1M
RDE-15		1	40	----	$HClO_4$ 0.1M
RDE-16		1.3	40	----	$HClO_4$ 0.1M
RDE-17		1.5	50	----	$HClO_4$ 0.1M
RDE-18	Powder 6	0.1	5	0.01	$HClO_4$ 0.1M
RDE-19		0.25	10	----	$HClO_4$ 0.1M
RDE-20		0.5	20	----	$HClO_4$ 0.1M
RDE-21		0.5	20	0.05	$HClO_4$ 0.1M
RDE-22		0.7	20	----	$HClO_4$ 0.1M
RDE-23		1	30	----	$HClO_4$ 0.1M
RDE-24		0.3	12	0.03	$HClO_4$ 0.1M
RDE-25		0.3	12	0.09	$HClO_4$ 0.1M
RDE-26		0.3	12	0.15	$HClO_4$ 0.1M
RDE-27	Powder 7	0.25	6	----	$HClO_4$ 0.1M
RDE-28		0.5	10	----	$HClO_4$ 0.1M
RDE-29		0.7	15	-----	$HClO_4$ 0.1M
RDE-30		1	20	----	$HClO_4$ 0.1M
RDE-31	Powder 8	0.3	10	----	$HClO_4$ 0.1M
RDE-32		0.5	6	----	$HClO_4$ 0.1M
RDE-33		0.7	10	----	$HClO_4$ 0.1M
RDE-34		1	10	----	$HClO_4$ 0.1M
RDE-35	Powder 12	0.5	6	----	$HClO_4$ 0.1M
RDE-36	Powder 13	0.5	6	----	$HClO_4$ 0.1M
RDE-37	Powder 14	0.5	6	----	$HClO_4$ 0.1M
RDE-38	Powder 15	0.5	6	----	$HClO_4$ 0.1M
RDE-39	Powder 16	0.5	6	----	$HClO_4$ 0.1M

Table 20: List of RDEs characterized.

In order to compare the Pt/C (E-TEK), the amount of IrO_2-based powders deposited is indicated in terms of Ir loading (1 mg cm^{-2} of Ir = 1.17 mg cm^{-2} of IrO_2). In the case of CS-Cl method the IrO_2 content is higher than the content in the others powders. This choice was driven by the need of

characterizing powders containing high IrO_2 amount toward ORR as a comparison of electrochemical results obtained by scanning electrochemical microscopy [29].

The Ti plate supports allow to investigate the electrochemical behaviour of deposits similar to one deposited on the Nafion® membrane in the case of MEAs. In fact the electrode preparation consists in the deposition of an ink constituted by electrocatalytic powder, Nafion® emulsion in iso-propylic alcohol. More details on the procedure adopted are reported in Section 2.2.5-III *"Electrode Preparation"*. Using this support only the powder n°5 (composition: $Ir_{0.15}Sn_{0.85}O_2$, impregnation method, calcination temperature 450°C) was characterized. The aim is determining the contribution of Nafion® in the electrocatalytic layers on the electrode response. The compositions of deposits characterized are reported in the Table 21.

n° electrode	n° powder	Nafion® loading (mg cm^{-2})	IrO_2 loading (mg cm^{-2})
Ti-1	5	0.00	2
Ti-2	5	0.07	2
Ti-3	5	0.17	2
Ti-4	5	0.20	2
Ti-5	5	0.29	2
Ti-6	5	0.64	2

Table 21: Compositions of Ti-thin plates supported electrodes tested.

3.1.2-Structural, morphological and surface properties

In this section the effect of the IrO_2 content in the SnO_2 matrix in relationship with the structural and morphological properties is discussed. Figure 67 reports the X-ray diffraction lines of the samples synthesized by I method at increasing IrO_2 amount (red curves), calcined at 450°C. Reference spectra (pure IrO_2 and SnO_2, black lines, at the top and the bottom of the figure respectively) are reported for comparison.

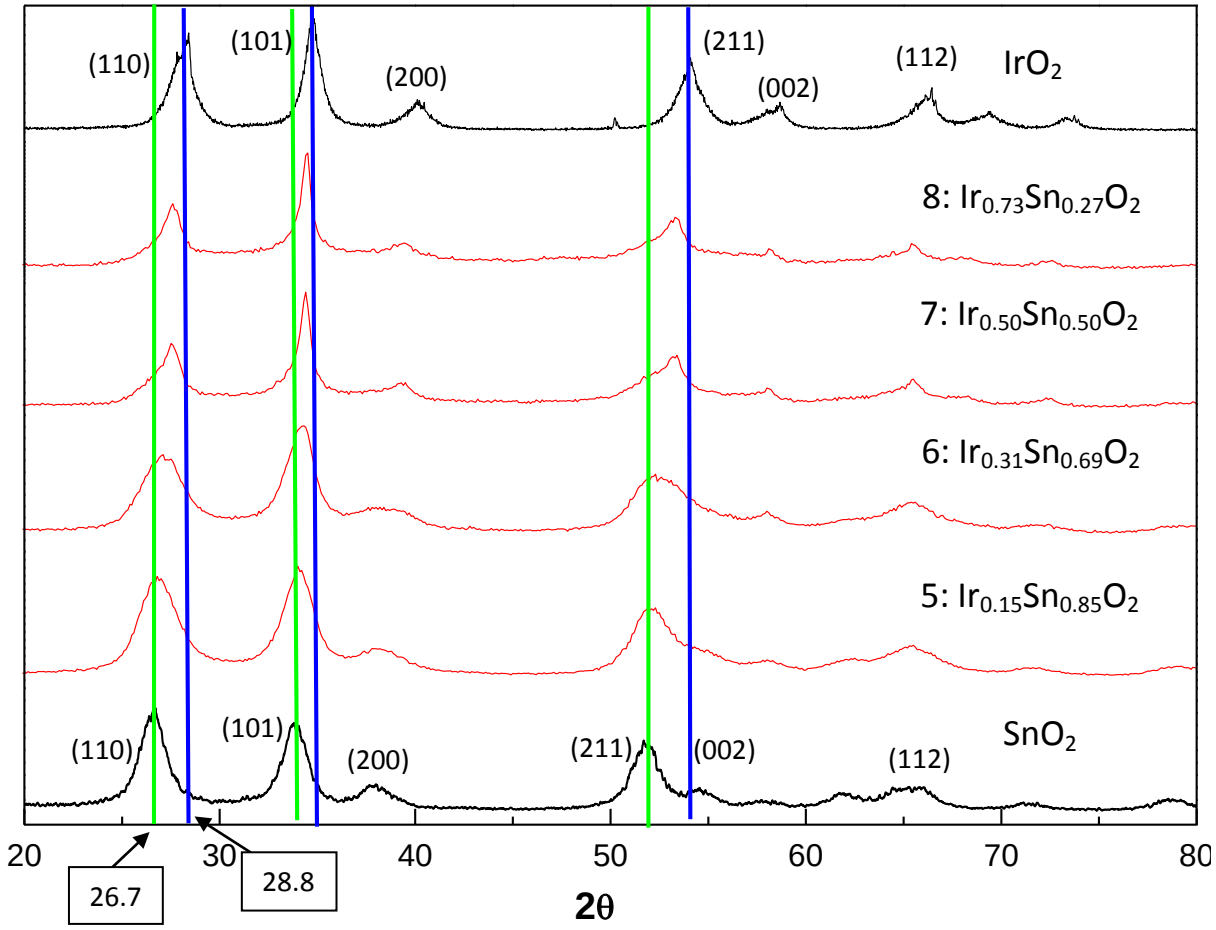

Figure 67: Effect of IrO_2 content on XRD diffractograms. The vertical line indicates the peak position of references: blue line for IrO_2 and green line for SnO_2.

Pure tin and iridium oxides are structurally isomorphs: the respective diffraction lines show characteristic peaks, due to the same *hkl* planes, but the peak position is slightly shifted. The 2θ values of the most intense peak of both SnO_2 and IrO_2 are located at 26.7 and 28.8, respectively.

At increase of IrO_2 content the characteristic peaks (in particular the most intense one located at ca 27) are composed by two different components (both IrO_2 and SnO_2 polymorphs); this produces a progressive broadening of the peaks. Therefore the 2θ shift of the position of the main peak (110 plane) from 26.7 to 28.8 is due to the prevalence of IrO_2 phase. In the case of powders 7 and 8 (higher Ir/Sn molar ratios) a clear preponderance of IrO_2 phase is appreciable, since the characteristic peaks are close to the pure IrO_2. Nevertheless a broad shoulder peaked at 52.9° suggests the presence of small amount of SnO_2 domains.

Figure 68 shows the BET results. A linear correlation (R^2 = 0.955) between specific surface area, S_{BET} (m^2g^{-1}), and the nominal Ir content is observed. The progressive decrease of S_{BET} with increasing IrO_2 amount can be ascribed to the formation of larger crystalline IrO_2 aggregates.

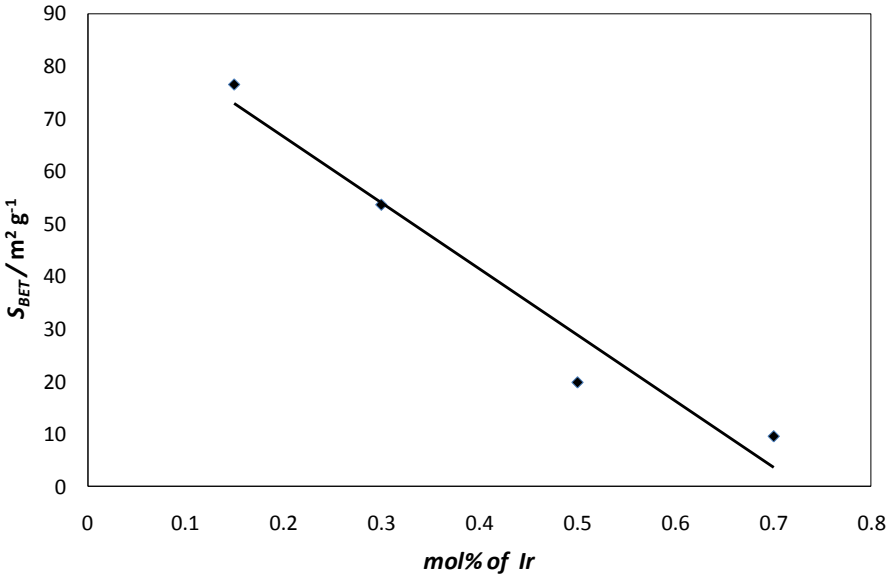

Figure 68: Ir content on BET results.

XPS results (see Table 22, 6th column) show, for the samples with the higher nominal Ir/Sn molar ratio (5th column), a sharp increase of Ir surface concentration (more than one order of magnitude).

n° powder	Composition	$T_{calcinations}$ / °C	Method	nominal Ir/Sn	Ir/Sn surface
3	$Ir_{0.15}Sn_{0.85}O_2$	450	MM	0.18	0.17
4	$Ir_{0.15}Sn_{0.85}O_2$	500	MM	0.18	0.12
5	$Ir_{0.15}Sn_{0.85}O_2$	450	I	0.18	1.45
6	$Ir_{0.31}Sn_{0.69}O_2$	450	I	0.45	46.6
7	$Ir_{0.50}Sn_{0.50}O_2$	450	I	1.00	58
8	$Ir_{0.73}Sn_{0.27}O_2$	450	I	2.70	∞

Table 22: XPS results.

In addition, the comparison between powders calcined at the same temperature and with the same nominal Ir/Sn ratio, *e.g.* powder 3 (prepared by the MM method) and powder 5 (prepared by the I method) highlights how the impregnation method leads to a ten-fold enrichment of Ir at the surface. This enrichment is greatly enhanced with the Ir content, so that in powder 8 only Ir species are localized at the surface.

The morphological features of the calcined samples are investigated by SEM technique. As an example the SEM image corresponding to powder 7 is shown in Figure 69. All the prepared composites show similar morphologies, characterized by round shape aggregates of 20-40 nm.

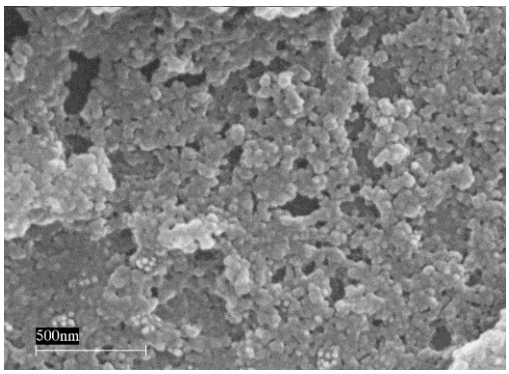

Figure 69: SEM photographyes (5000X).

3.1.3- Electrochemical behaviour

In this section are reported the electrochemical results subdivided on base of the support used for the characterization.

(I) Cavity-Microelectrode (C-ME)

C-MEs having different volumes (see Section 2.2.5-I *"C-ME preparation"*) were used. The powder n° 5 was investigated with all C-MEs and the Figure 70 reports the Q_{tot} *vs* the volume of the cavity.

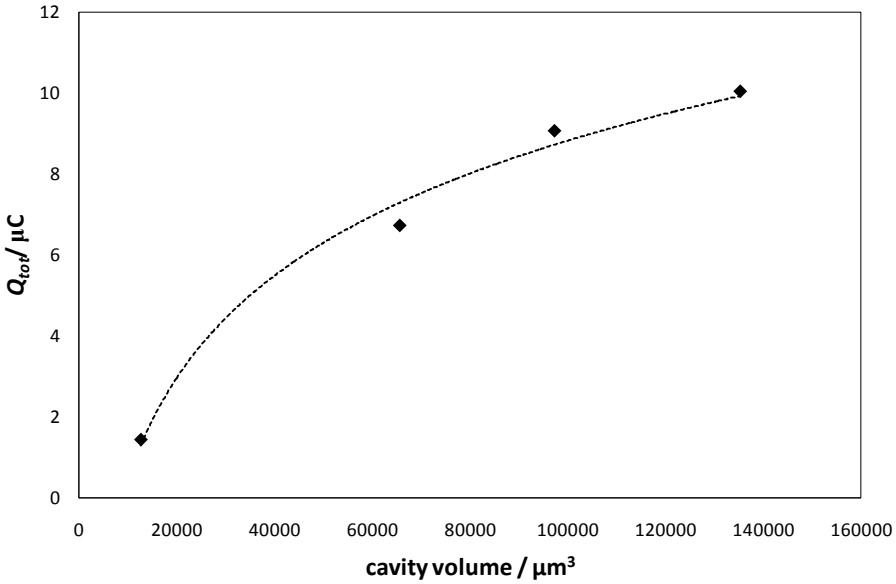

Figure 70: Q_{tot} *vs* C-ME volumes used in the characterization of powder n° 5 in 0.5 M H_2SO_4. The dashed line was added to facilitate the reading and without any interpolation purpose.

At increasing cavity volumes the parallel increase of Q_{tot} is observed, even if a sort of saturation effect seems to be evident at higher volume values. At present, although the increase of the cavity depth seems to be at the base of the observed trend, this effect was still not fully clarified, therefore

for comparing the electrochemical behaviour of different powders supported C-MEs having the same volume were to be used.

On this basis, the Q_{tot}, Q_{out}, and Q_{in} values were used for comparing ranking the powders according their synthetic method. Figure 71 and Figure 72 show how the method of addition of the Ir-precursor and the temperature of calcination influence the Q values.

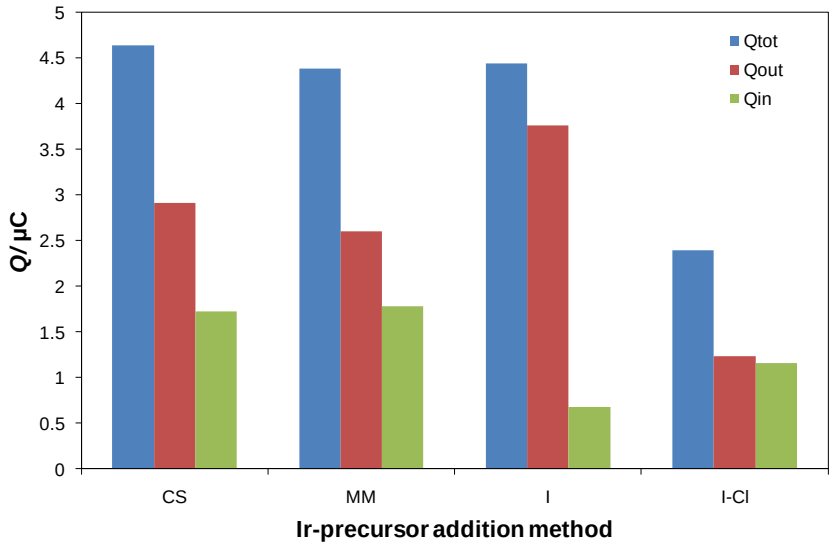

Figure 71: Effect of the method of addition of Ir-precursor on *Q* values. The characterization was carried out using the C-ME1.

CS, MM and I methods leads to the higher Q_{tot} while a significant reduction is observed in the case of I-Cl method. By comparing the Q_{out}/Q_{tot} ratio, which is an index of the accessibility of the active sites, the I method shows the best performance.

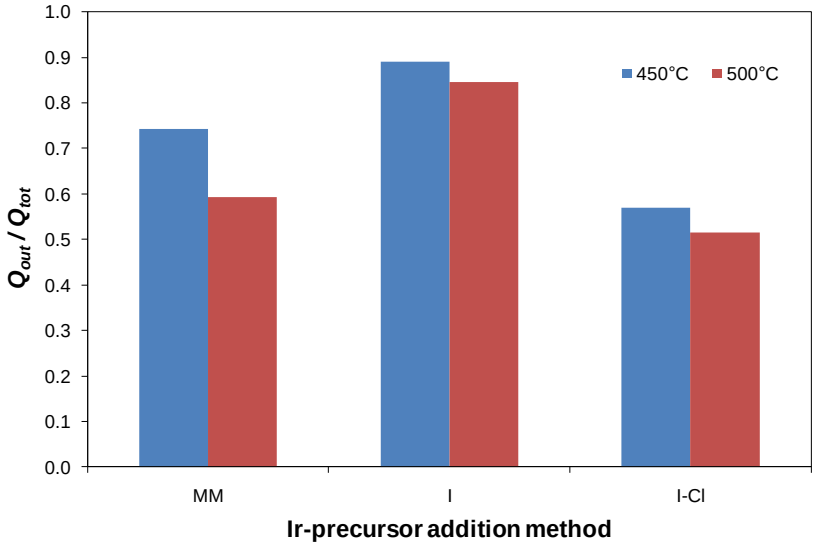

Figure 72: Effect of the calcination temperature on Q_{out}/Q_{tot}. The characterization was carried out using the C-ME1

A significant decrease of active sites accessibility is observed when the temperature is increased from 450°C to 500°C. This could be correlated to a sintering effect at higher calcination temperature that leads to large IrO_2 crystallites that reduce the active area.

The active area was independently characterized in presence of a redox couple, as described in the Section 2.2.5 -I "*Electrode characterization"*. The Fe^{3+}/ Fe^{2+} couple was chosen since its kinetic is enhanced on IrO_2. As already discussed the response can be represented by the equivalent radius, r_0 (μm) of the hypothetical microdisk electrode. In Figure 73 *Q vs* r_0 are reported.

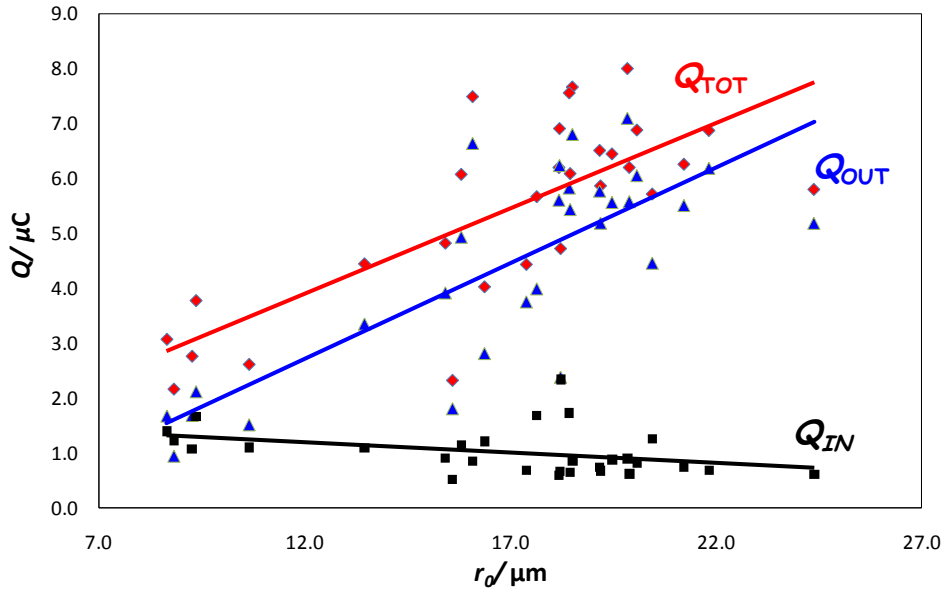

Figure 73: Correlation between Q_{tot} and r_0 (all powders). Background electrolyte: 0.1 M $HClO_4$ using C-ME1.

Good linear correlations between *Q*'s and r_0 are observed; in particular two groups of powders can be recognized: in the first one there are powders having higher values of Q_{tot}, Q_{out} and r_0 and in the second one there are powders having low Q_{tot}, Q_{out} and r_0 values.

Powders with high Q_{tot} (*i.e.* high number of active sites) have also comparable Q_{tot} and Q_{out} values (*i.e.* active sites easy accessible) and constitute to ones with the best performances. The easy accessibility of the active sites can be demonstrated considering CVs normalized by the scan rate (see Figure 74)

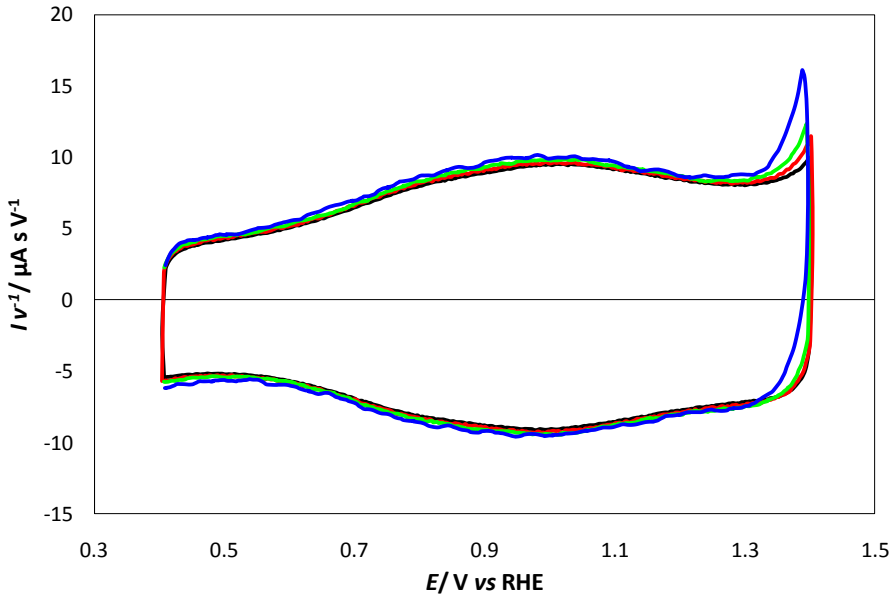

Figure 74: CVs of powder n°5 normalized by scan rate. Background electrolyte: 0.1M $HClO_4$.

In the absence of a diffusion controlled process the capacitive behaviour is prevalent and the quantity of charge varies linearly with scan rate.

On the opposite, the increase of the Q_{in} values is an index of a strong diffusion limited contribution that leads to the reduction of the electrochemical. In this case the no superimposition of the CVs normalized by the scan rate is observed (see Figure 75).

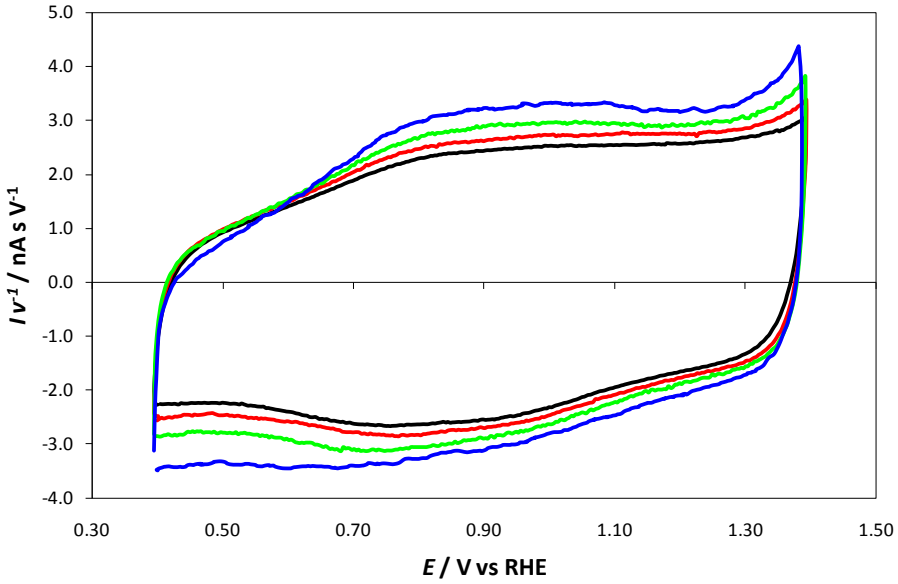

Figure 75: Characteristic CVs of powder n°10 normalized for scan rate. Background electrolyte: 0.1M $HClO_4$.

In Figure 75 a resistive contribution on the CV shape can also be observed. This is probably due to the influence of the SnO_2 matrix on the electrochemical response. It is important to observe that powders belonging to this group show r_0 values significantly lower (*ca.* 7-12 µm) than the platinum wire (*ca.* 25µm). As described in Section 2.2.5-II, Fe^{3+}/Fe^{2+} kinetic is selectively faster on IrO_2 sites than on SnO_2 ones.

Despite most of the powders have the same Ir/Sn nominal ratio, the synthetic route leads to different Ir/Sn surface ratios (see XPS results previously reported). The effect of the synthesis method on r_0 and Q_{tot} values is reported in Figure 76.

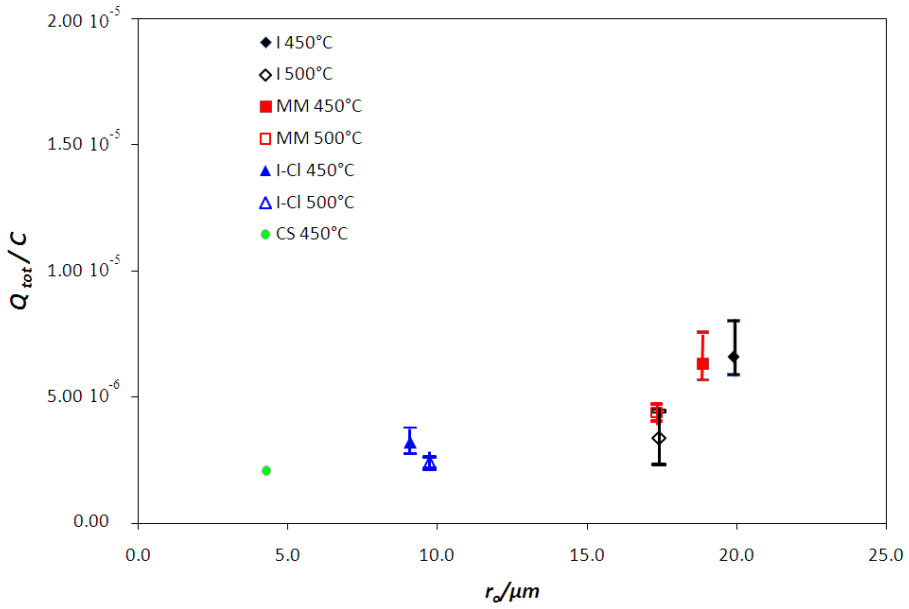

Figure 76: Effect of the synthesis method on Q_{tot} and r_0 values.

The powders prepared by MM method (calcined at 450°C), which does not produce any enrichment of IrO_2 at the surface, are less active and present lower equivalent radiuses than powders prepared by I method. A negative effect of the calcination temperature can be observed. Considering powders with the same synthesis method (except for I-Cl) the increase of the calcination temperature leads to a decrease both the Q_{tot} and r_0 values. This comparison is not possible in the case of CS method at 500°C because the steady-state current is very critical (see Figure 77).

Figure 77 shows the CVs at 2 mV s^{-1} after the subtraction of the corresponding background current. At low scan rate a sigmoid is obtained.

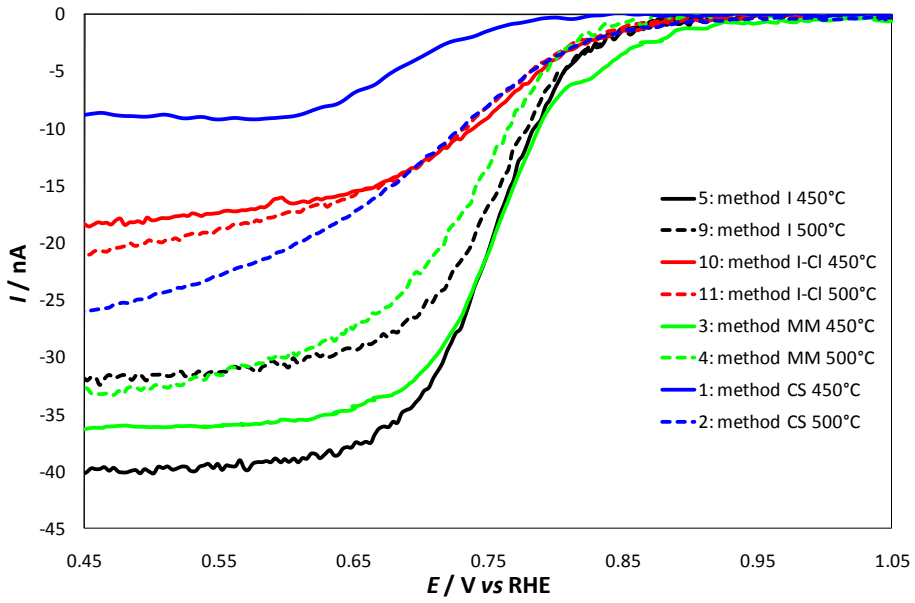

Figure 77: CVs difference representative of the powders investigated. CVs at 2 mV s^{-1} which the correspondent CV of only background electrolyte was subtracted. Background electrolyte: 0.1M $HClO_4$, support used C-ME1.

Two principal characteristics can be distinguished: (i) the values of the steady-state current (i_{ss}) and (ii) the slope at the flexus, that is dependent on the reaction kinetics. In particular for low reaction rates (low values of rate constant of reaction, k_0) a distortion of the sigmoid is verified and the stationary state is reached at less positive potential.

Now, considering powders synthesised by the same method but calcined at different temperatures, it is possible to note that the increase of the calcination temperature leads to a worsening on the reaction kinetics, $Fe^{3+} + e^- = Fe^{2+}$, since the stationary state is reached at less positive potential.

The effect of the temperature on the steady-state currents is very evident in the case of I and MM methods, while is minimal on the I-Cl powders. In the case of CS the powder calcined at higher temperature presents higher i_{ss} value but the reaction rate is slower.

These aspects are confirmed considering the kinetic parameter reported in Table 23. As already mentioned in Section 2.2.5-I *"Electrode Characterization"*, these kinetic parameters are obtained under the assumption of a hemi-spherical electrode surface, which is a rather drastic approximation for our microelectrode. Consequently, the β and k_0 values are given in italics to denote their semi-quantitative meaning.

Method	$T_{calcination}$ (°C)	$\lvert E_{3/4}-E_{1/4}\rvert$ (mV)	β	k_0 (cm s^{-1})
I	450	70	*0.64*	*4.44 10^{-04}*
I	500	70	*0.64*	*5.67 10^{-04}*
MM	450	70	*0.64*	*5.53 10^{-04}*
MM	500	90	*0.50*	*3.51 10^{-04}*
I-Cl	450	110	*0.41*	*7.03 10^{-04}*
I-Cl	500	140	*0.32*	*5.86 10^{-04}*
CS	450	80	*0.56*	*4.57 10^{-05}*
CS	500	150	*0.30*	*2.94 10^{-04}*

Table 23: Kinetic parameters correlated to the reduction reaction of Fe^{3+} obtained by application of Tomeš criterion .

The reduction reaction is quasi or totally irreversible on IrO_2-based materials since that the $|E_{3/4}-E_{1/4}|$ and β values vary between 65 ÷150 mV and 0.3÷0.7 respectively (see Section 2.2.5-I).
In particular, in the case of I method (powders calcined both at 450°C and 500°C) and the MM method (powders calcined at 450°C) the lower irreversibility degree is observed.
The CS and I-Cl calcined at 500°C leads to powders with the less satisfying kinetic performances.
Also in this case it is possible to observe the negative effect of the higher calcination temperature. In fact, considering powder synthesised by the same method, lower k_0 values are observed, the only exception being the I method for which the kinetic performances are comparable.

On the basis of the Q_{tot}, Q_{tot}/Q_{out}, i_{ss} , values and the kinetic parameters, the powder synthesised at 450°C by I method show the best performance. This is probably due to the enormous enrichment of IrO_2 on the surface as showed in the XPS results (nominal Ir/Sn ratio « surface Ir/Sn ratio; see Table 22). Therefore I method was chosen for preparing powders with different IrO_2 content.
The CVs characteristics are reported in Figure 78.

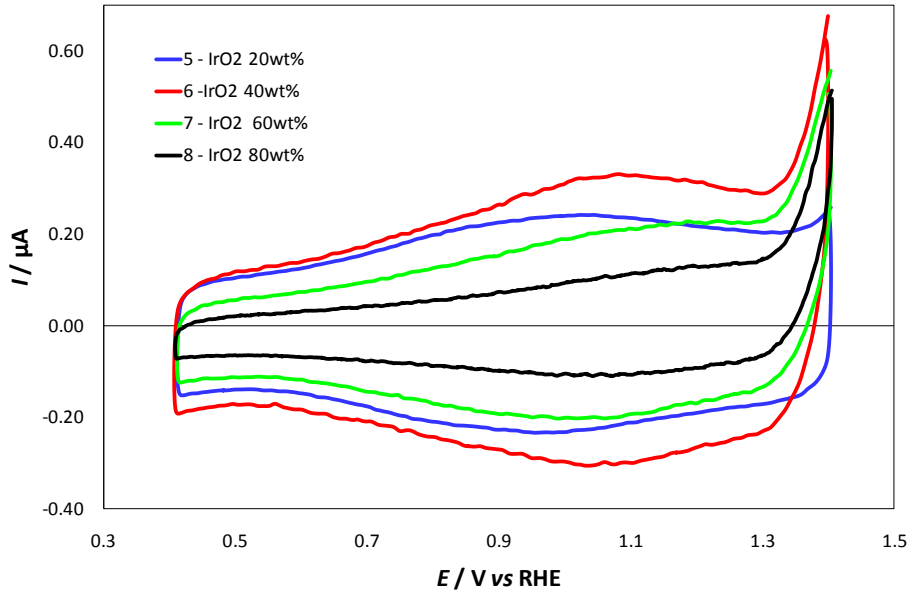

Figure 78: Effect of IrO_2 content on the CV characteristics. Powders supported on C-ME4. Background electrolyte: 0.1M $HClO_4$ scan rate: 20mV s^{-1}.

For all the composites the typical pseudo-capacitive behaviour is observed. At the positive end of the potential window, the evident current increase, which follows the parallel nominal increase of the Ir/Sn ratio, is likely correlated to either the transition of IrO_2 toward the higher oxidation states or the beginning of oxygen evolution reaction. Considering the CV shape at increasing IrO_2 content a broadening of CV curves at more positive potential region is observed. This effect is correlated to the progressive influence of the IrO_2 phase on the electrochemical response. The CVs indeed becomes similar to the pure IrO_2 (see Figure 79).

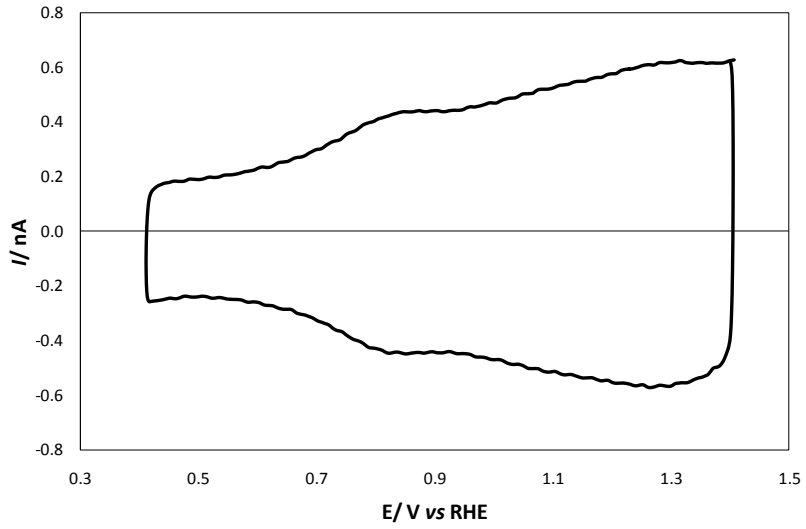

Figure 79: Characteristic CV of IrO_2 pure. Background electrolyte: 0.1M $HClO_4$ scan rate: 20mV s^{-1}. Powder supported in C-ME 3.

Once again the voltammetric charges highlight an interesting behaviour, shown in Figure 80.

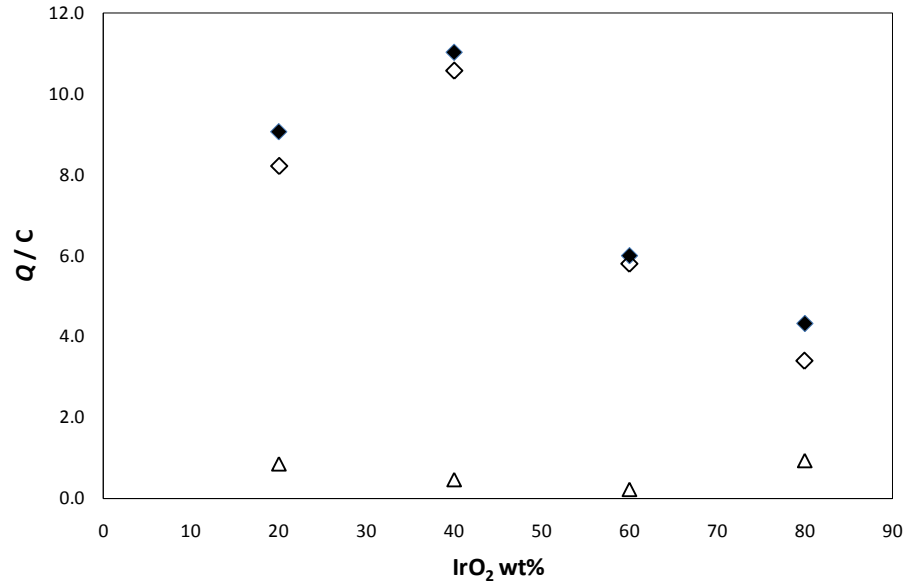

Figure 80: Correlation between *Q* values and nominal IrO_2 content. Q_{tot}: full diamonds; Q_{out} empty diamonds; Q_{in} empty triangles. Powders were synthesized by I method and calcined at 450°C. Background electrolyte: 0.1M $HClO_4$. Powdders supported using C-ME4.

In all the composites Q_{out} values are very similar to Q_{tot}. This demonstrates that the I method leads to powders with active sites easy accessible also in the case of different Ir/Sn nominal ratios. A maximum is observed for Q_{tot} at 40wt% (~30mol%) of IrO_2. This result is in line with the ones reported in the literature [12]. Note that, on that the basis of XPS data, at increasing IrO_2 content the surface becomes progressively saturated by Ir species, therefore a further IrO_2 enrichment does not lead to a significant improvement on the electrochemical response.

(II) Rotating Disk Electrode (RDE)

IrO_2-based Materials

As described in the Section 2.2.5-IV "*Electrode Preparation*", the preparation procedure of the working RDE samples is crucial and requires to be carefully checked. Therefore the validity of the preparation procedure was verified by both comparing the reproducibility of the response of electrodes having the same kind of catalytic layer but prepared at different times, and verifying the linearity between the voltammetric charge and the Ir loading on the electrode.

The results are reported in Figure 81 and Figure 82.

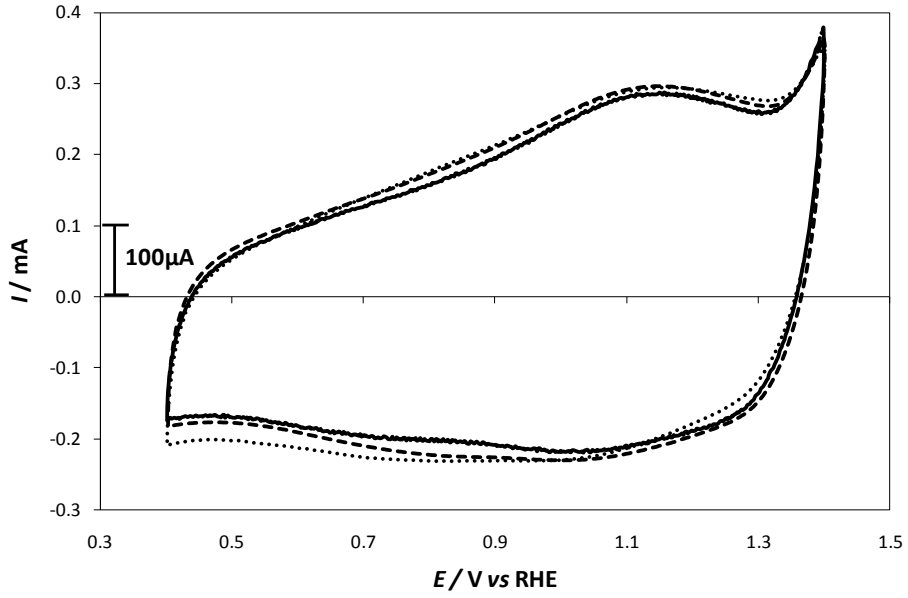

Figure 81: Reproducibility of RDE preparation. Powder n°6 (Ir loading=0.5 mg cm^{-2}) at 25°C under N_2 atmosphere. Background electrolyte: 0.1M $HClO_4$; scan rate: 20mV s^{-1}; scan rate: 20 mVs^{-1}; rotation rate 1600 rpm.

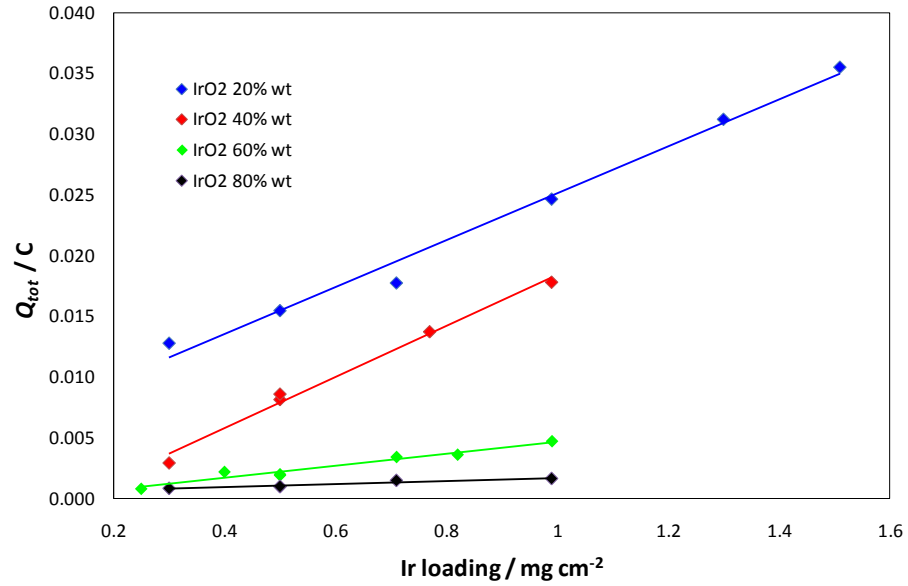

Figure 82: Correlation between Q_{tot} and Ir loading on the electrode.

Both the good superimposition of the responses obtained testing electrodes prepared in the space of several days (see Figure 81), and the good linearity (R^2 = 0.98, see Figure 82) of the total voltammetric charge with Ir loading demonstrate the validity of electrode preparation. Figure 81 reported the responses obtained with powder n°6 as example but the reproducibility was also verified with electrodes prepared using the other powders.

As previously mentioned (see Table 19) RDE was used to characterize powders prepared by two different routes and with different IrO_2 content.

In Figure 83 and Figure 84 are reported the CV recorded under N_2 atmosphere of the powders 5-8 (previously described using the C-ME as support) and 12-16 respectively. In particular the comparison is carried out considering electrodes having the same Ir loading.

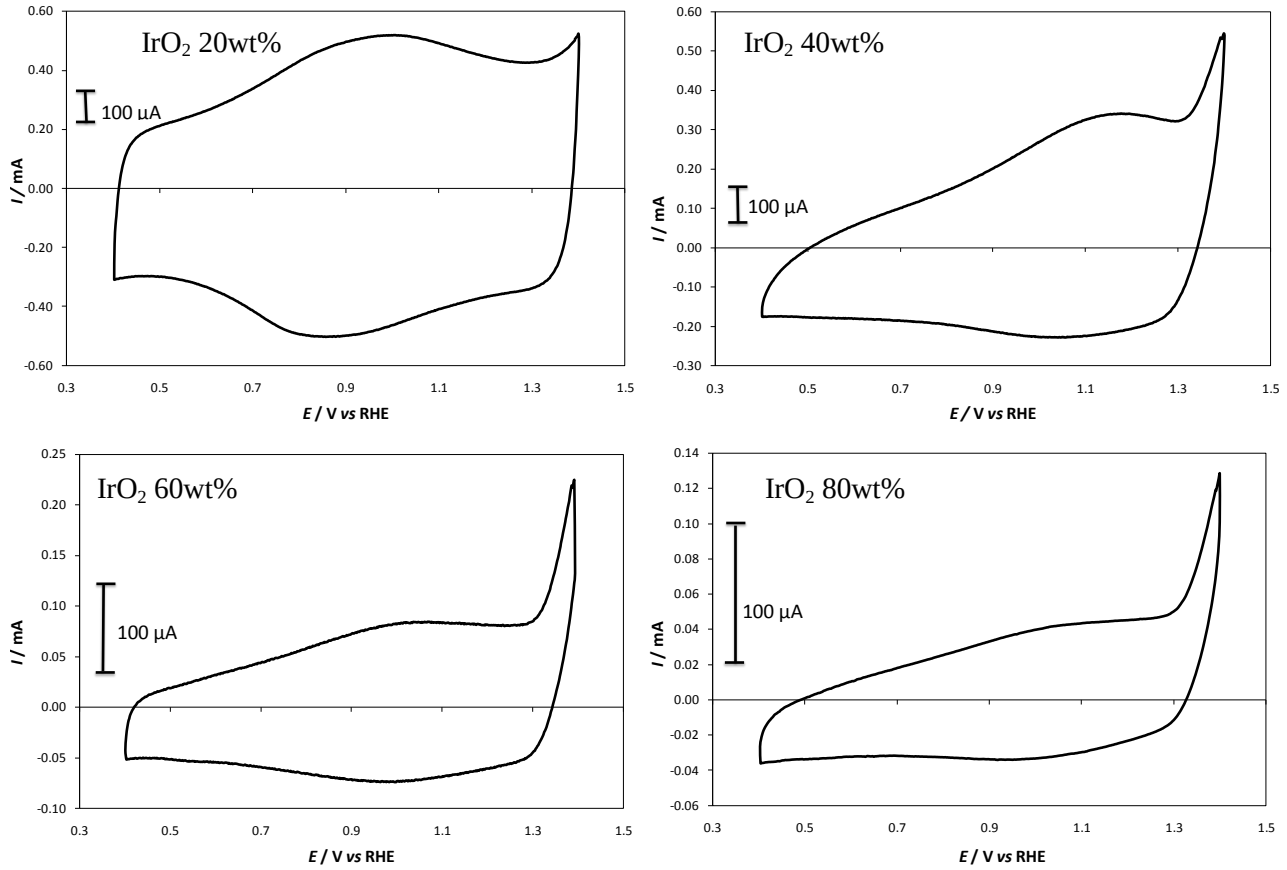

Figure 83: Characteristic CVs of powders synthesised by I method (Ir loading = 0.5 mg cm^{-2}). Background electrolyte: 0.1M $HClO_4$, scan rate 20 mV s^{-1}, rotation rate 1600 rpm, N_2 atmosphere.

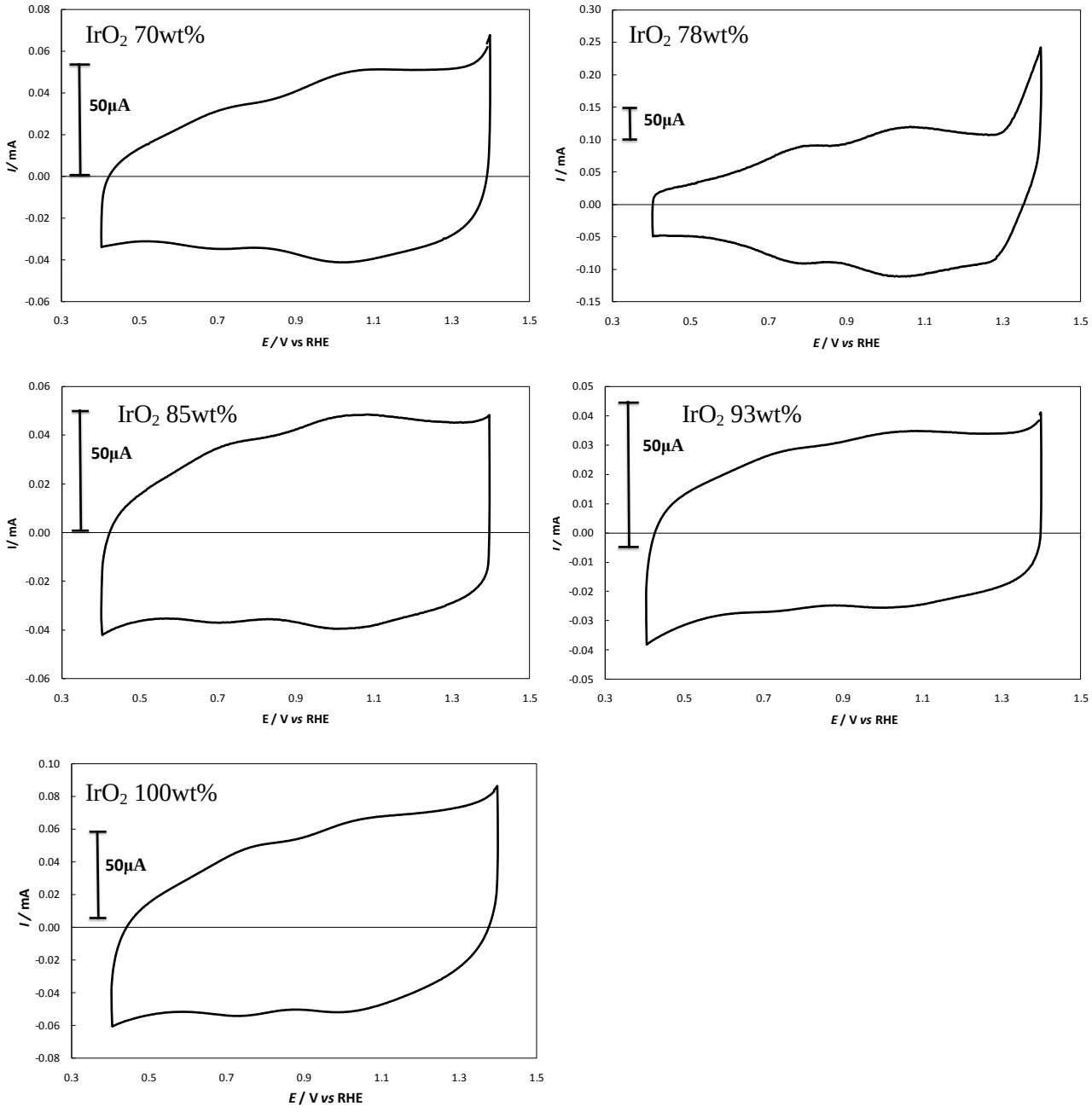

Figure 84: Characteristic CVs of powders synthesised by CS-Cl method (Ir loading = 0.5 mg cm^{-2}). Background electrolyte: 0.1M $HClO_4$, scan rate 20 mV s^{-1}, rotation rate 1600 rpm, N_2 atmosphere.

In all the CS-Cl composites the transition of Ir oxide toward the highest oxidation states are well visible. Considering only this group of powders, powder n°13 (78wt% of IrO_2) presents higher capacitive currents and a higher current at the positive potential end point.

The behaviour of the powders 5-8 is similar to the one obtained using C-ME as support (see Figure 78). The effect of the broadening of the CV curves at increasing IrO_2 content is observed also in this

case. *Vice versa*, substantial differences are observed in the Q_{tot} *vs* IrO_2 content trend, since the *Q*'s monotonically decrease with IrO_2 wt % (full diamonds in Figure 85).

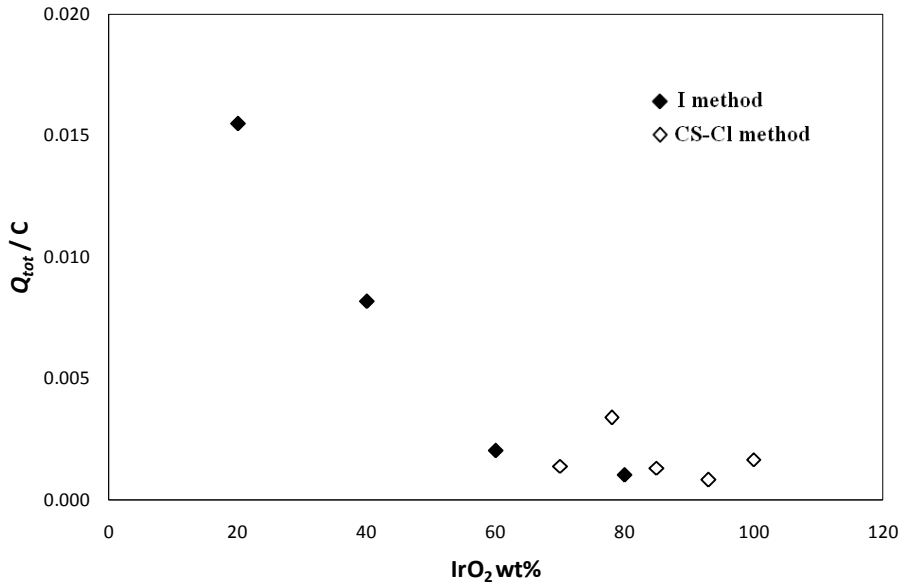

Figure 85: Effect of the IrO_2 content on the voltammetric area.

As can be recalled, using C-ME as support a maximum at IrO_2 40wt% was observed, while on RDE the highest Q_{tot} value corresponds to the IrO_2 20wt% powder. Although this last result is in line with the S_{BET} values previously reported (see Section 3.1.2) – where a progressive decrease of the active surface with the increase of IrO_2 content was observed – the difference of responses obtained using the two supports can be very likely correlated to the presence of Nafion® in the catalytic layer in the case of RDE. In fact, the presence of the ionomer improves the proton conduction in the layer. This improvement is more visible in the case of powder n°5 because of the smaller size of the nanoparticles, which favours a more homogeneous dispersion of Nafion® in the layer.
If only the CS-Cl powder group is considered, the powder with 78wt% of IrO_2 presents the highest Q_{tot} value.

Since the RDE support was used to evaluate the reactivity of IrO_2-based powders toward ORR, the CVs were also recorded by bubbling oxygen in the solution. The effect of the presence of oxygen in the case of powders synthesized by I method is shown in Figure 86.

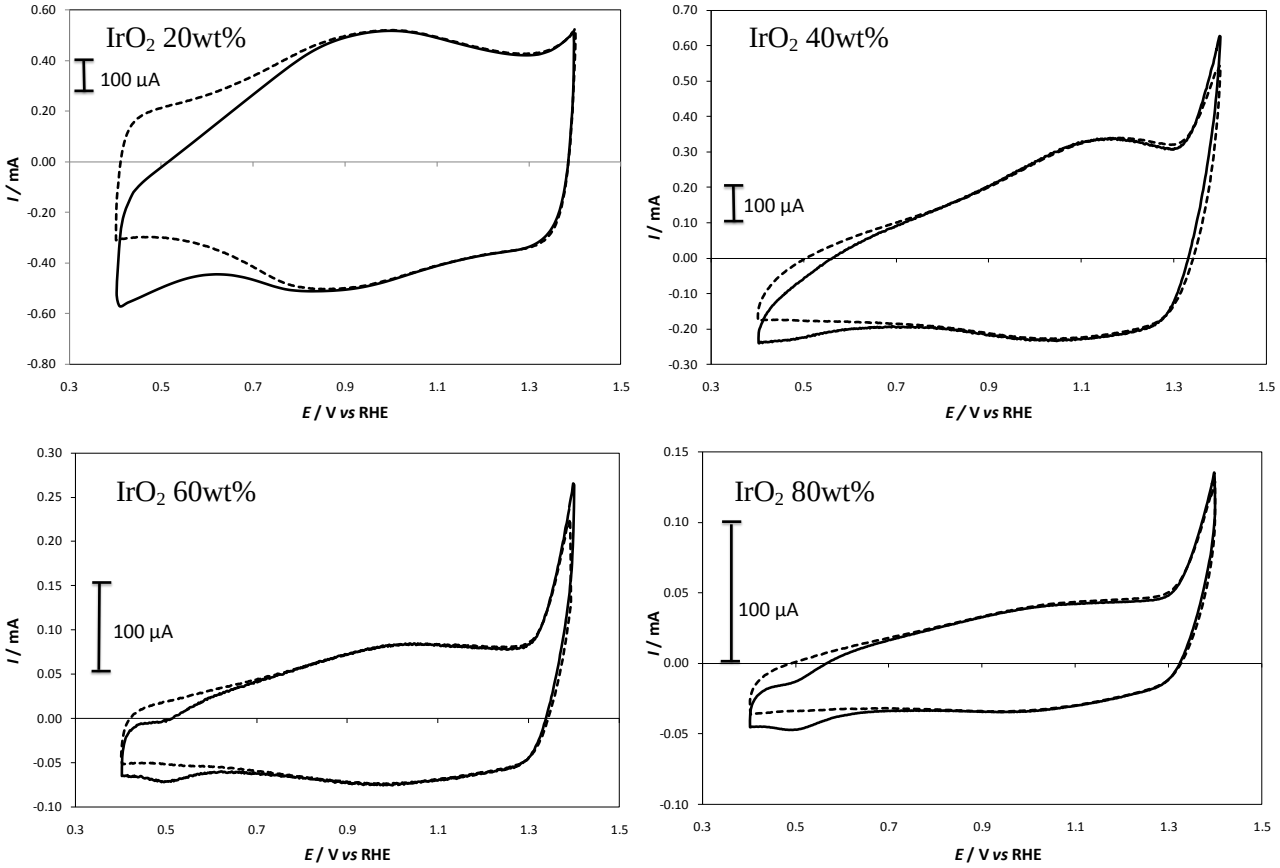

Figure 86: Characteristic CVs of powders synthesized by I method (Ir loading = 0.5 mg cm^{-2}). Background electrolyte: 0.1M $HClO_4$; scan rate: 20mV s^{-1}; rotation rate 2500 rpm. Dashed line: background under N_2 atmosphere, black line under O_2 atmosphere.

In the presence of oxygen a cathodic current at less positive potentials is observed. In particular in the case of powder with the lowest IrO_2 content highest current intensities is recorded. At increasing IrO_2 content the current decreases and a peak is visible.

A comparison of the electrochemical behaviour in the presence of oxygen between I and CS-Cl methods is reported in Figure 87. In particular powders having the same IrO_2 content (~80wt%) are considered.

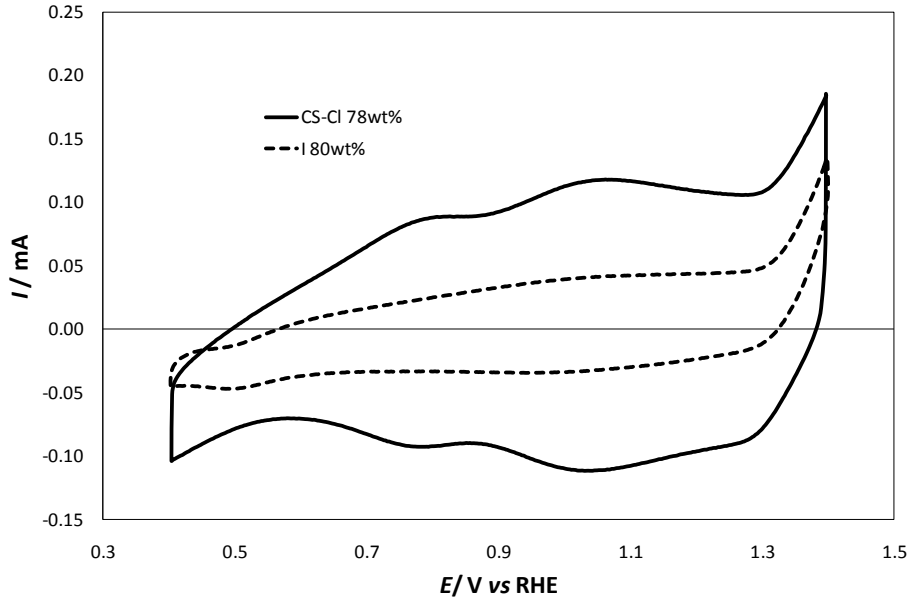

Figure 87: Comparison between powder n°8 (dashed line) and 12 (black line) under O_2 atmosphere. Background electrolyte: 0.1M $HClO_4$ scan rate: 20mV s^{-1}; rotation rate: 2500 rpm.

Powder n°13, synthesized by CS-Cl method, shows the best performance. Together with the highest capacitive currents, the cathodic current due to the oxygen reduction is more visible, in spite of the highest calcination temperature adopted in the synthesis (500°C respect to 450°C used in the case I method). As reported previously (section 3.1.3-I) high calcination temperature leads to a decrease of the electrochemical performance. This is an index that the CS-Cl method is more suitable for the synthesis of powder with high IrO_2 content.

Effect of Vulcan® in the catalytic layer

The addition of conductive matrices as Vulcan XC72R® in the catalytic layer could improve the electrochemical behaviour reducing the electric resistance of the catalytic layer.

Therefore, electrodes based on powder n°6 and with different carbon loading were prepared and characterized. The Ir loading was maintained constant at 0.3 mg cm^{-2}. The reported weight % of Vulcan® is referred to the amount of Ir loading. The effect on the CVs is reported in Figure 88.

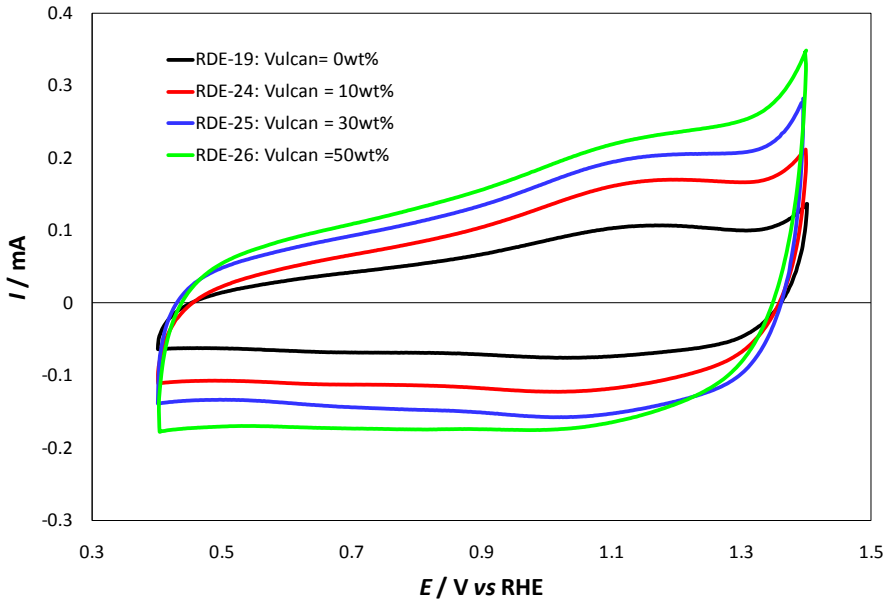

Figure 88: CVs of powder n°6 deposits with different Vulcan® loading. Ir loading = 0.3 mg cm^{-2}; background electrolyte: 0.1M $HClO_4$; scan rate: 20 mV s^{-1}; rotation rate: 1600 rpm .

An increase of the voltammetric charge at increasing Vulcan® loading is observed. In particular the voltammetric area varies linearly (R^2=0.99) with the Vulcan® content (see Figure 89).

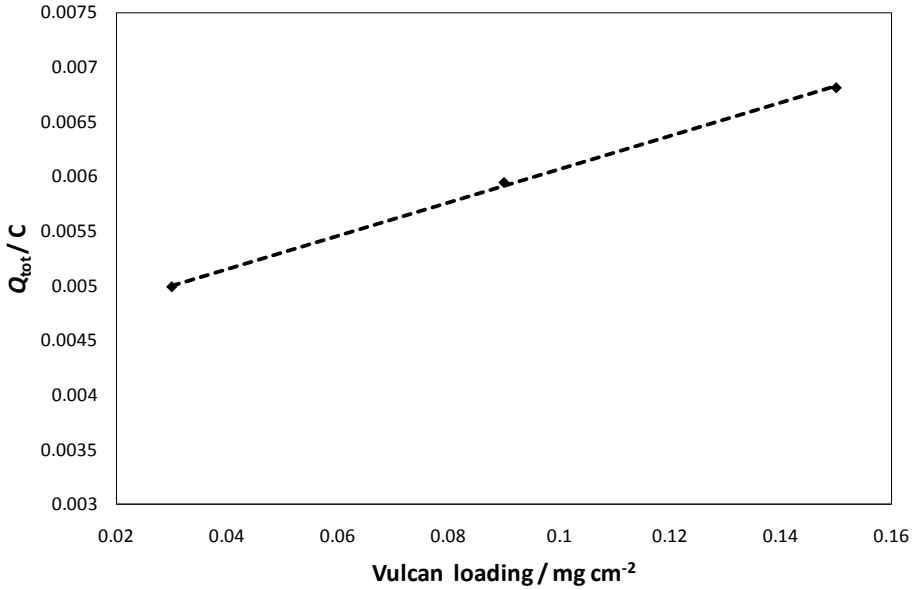

Figure 89: Linear correlation between Q_{tot} and Vulcan® loading in the catalytic layer.

In presence of oxygen (see Figure 90) a distortion on the CVs at the less positive potential due to the ORR is observed.

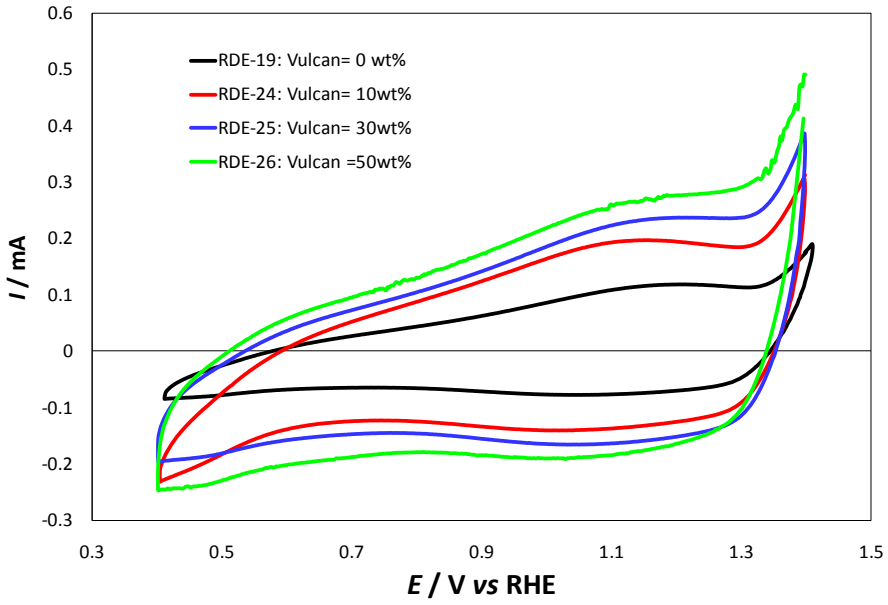

Figure 90: Effect of oxygen on the CVs. Electrode prepared with different Vulcan® content. Ir loading: 0.3 mg cm^{-2}; background electrolyte: 0.1 M $HClO_4$; scan rate: 20mv s^{-1} rotation rate 1600 rpm.

The cathodic current increases at increasing Vulcan® loading in the catalytic layer. In particular the best improvement is obtained in the case of RDE-24 (Vulcan® = 10wt%). The cathodic current is significantly higher than the current in capacitive zone. In the case of the RDE-26 (Vulcan® = 50wt%) the currents at the less positive end potential are comparable with those recorded on RDE-24, which is at variance with the behaviour observed under steady-state polarization. However, under potentiodynamic conditions RDE-26 has a far larger capacitive contribution to the overall current than RDE-24 (see Figure 89), for which the current increase can instead safely attributed to the faradaic process of oxygen reduction.

To study the effect of Ir loading the Vulcan® loading was fixed at the 10% of the Ir loading (by weight).

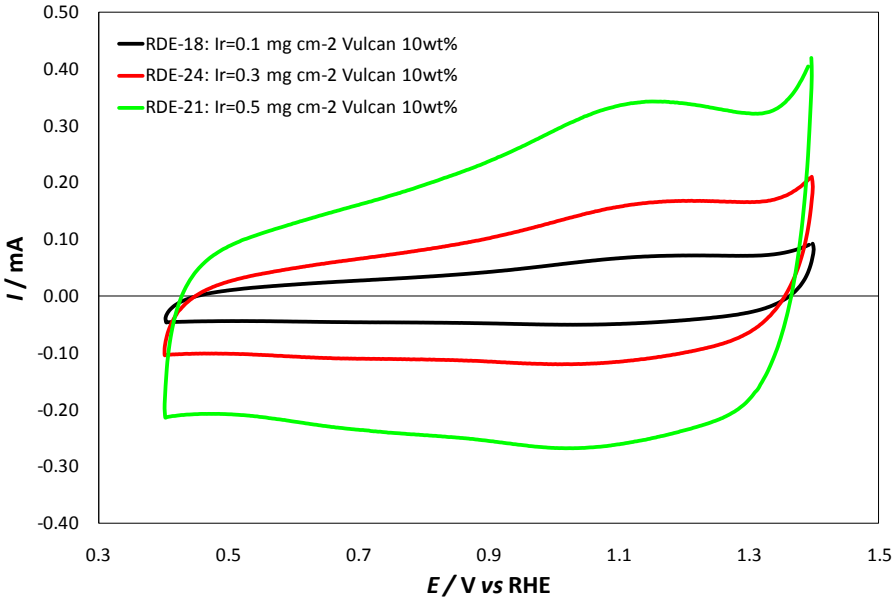

Figure 91: CVs of electrodes having the same Vulcan®/Ir loading ratio and increasing Ir loading. Background electrolyte: 0.1M $HClO_4$, scan rate: 20mV s^{-1}; rotation rate 1600 rpm under N_2 atmosphere.

The voltammetric charge increases at the increasing of Ir loading on the electrode. In particular a linear dependence (R^2=0.99) is observed (see Figure 92).

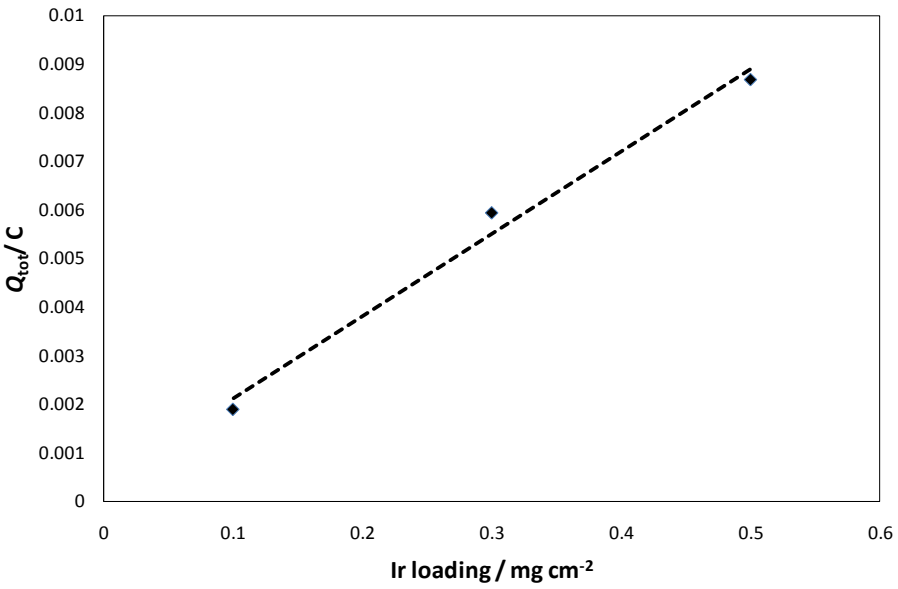

Figure 92: Experimental (diamond) and interpolated (dashed line) Q_{tot} *vs* Ir loading. Electrodes with Vulcan® loading equal to 10% (by weight) of the Ir loading in the catalytic layer.

In presence of oxygen the parallel electrochemical responses are reported below.

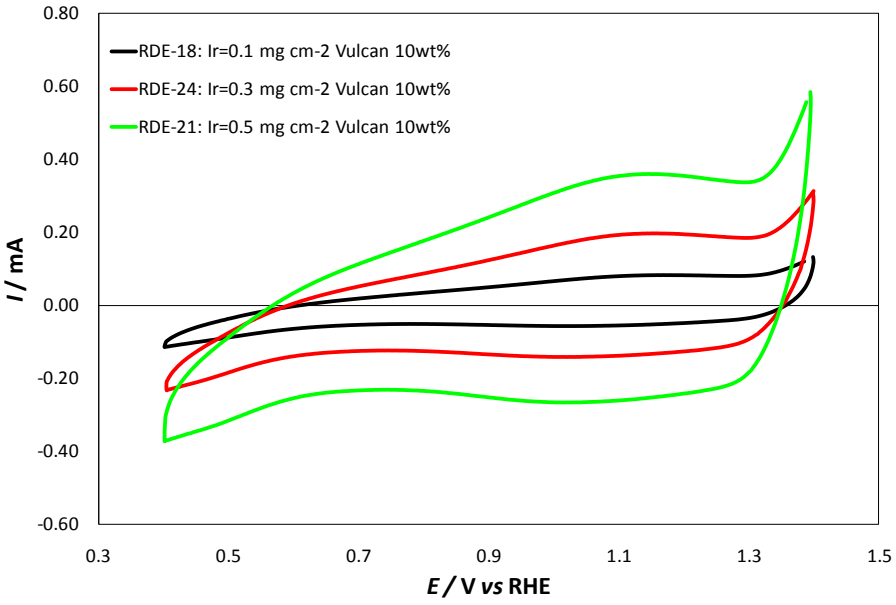

Figure 93: CVs of electrodes having the same Vulcan®/Ir loading ratio and increasing Ir loading. Background electrolyte: 0.1M $HClO_4$; scan rate: 20mVs^{-1}; rotation rate 1600 rpm under O_2 atmosphere.

An increasing Ir loading the cathodic current correlated to ORR becomes progressively more visible. This is an obvious result since the IrO_2 is the electrocatalytic component. The effective enhancement of activity can be verified by recording polarization curves.

Diluent matrices and support

Both the glassy carbon support and the diluents matrices (Vulcan XC72R®, SnO_2) were also characterized in order to exclude their influence on the ORR. The CV behaviours are shown in Figure 94.

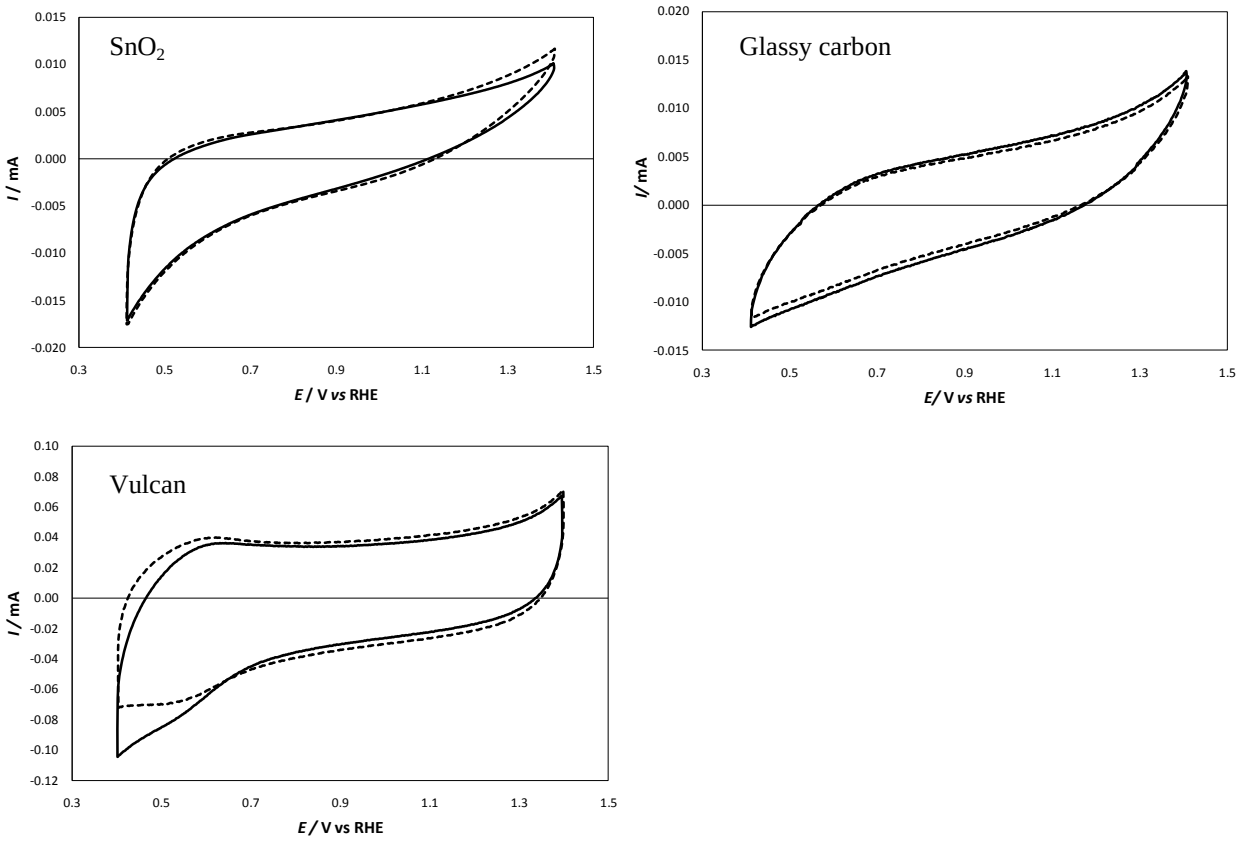

Figure 94: CV characteristics of support and diluents matrices under N_2 atmosphere (dashed line) and under O_2 atmosphere (black line). Background electrolyte: 0.1M $HClO_4$; scan rate: 20mV s^{-1}; rotation rate 1600 rpm.

The good superimposition of the cycles recorded under N_2 and O_2 atmosphere obtained for SnO_2 powder and glassy carbon support indicate the absence of any oxygen contribution. Vulcan® powder presents capacitive currents higher than ones obtained with the bare glassy carbon support. This is very likely due to the large increase of the surface area in the presence of Vulcan®, for which a current increase at the less positive potentials is observed. In order to exclude the activity of Vulcan® toward ORR a further investigation by recording polarization curves will be carried out.

Pt/C (28.6wt%) E-TEK

Since Pt-based materials are the most used electrocatalysts for ORR a commercial Pt/C (E-TEK) powder was characterized. In this case the active area was obtained considering the monoatomic hydrogen adsorption/desorption region (between 0 and 0.4 V *vs* RHE) as schematised in Figure 95.

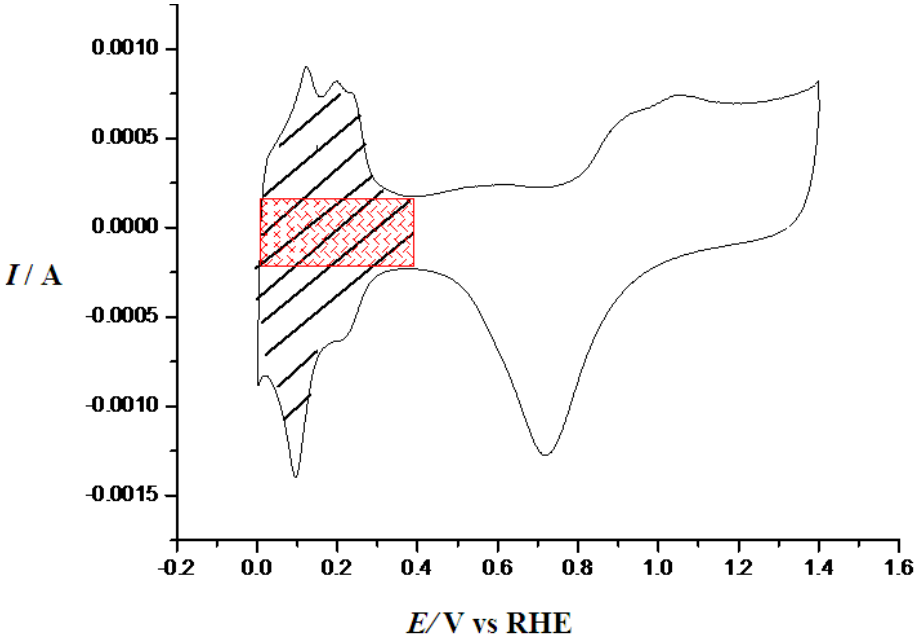

Figure 95: Example of the CV areas considered in the evaluation of Q_{H+} values.

In particular:

$$Q_{H+}=0.5\ (Q_{tot}-Q_{DL}) \qquad (86)$$

where Q_{H+} is the quantity of charge correlated to the H adsorption on the surface, Q_{tot} is the total quantity of charge obtained by integration of CV between 0 and 0.4 V *vs* RHE (black line dashed area) and Q_{DL} is the double layer charge corresponding to the red line dashed area.

Figure 96 shows the correlation of Q_{H+} and the Pt loading.

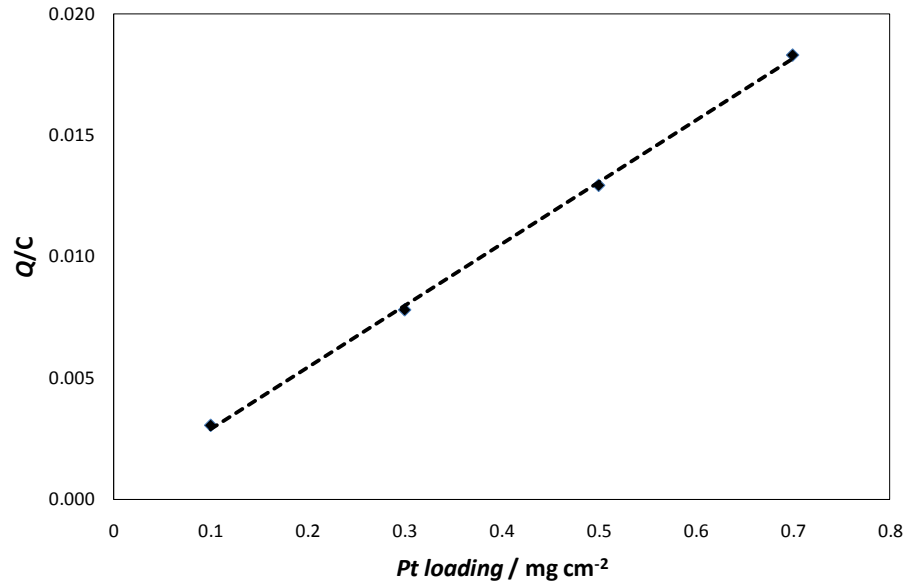

Figure 96: Experimental (diamonds) and interpolated (dashed line) values of Q_{H+} *vs* Pt loading on the RDE. Background electrolyte: 0.5M H_2SO_4, scan rate: 20 mVs^{-1}, rotation rate 2500 rpm under N_2 atmosphere.

As expected, the linear correlation between these parameters is very good (R^2= 0.998).

This result further substantiates the validity of the preparation procedure of the RDE electrodes.

In Figure 97 the effect of the presence of oxygen bubbled in the solution during the CVs recording is shown.

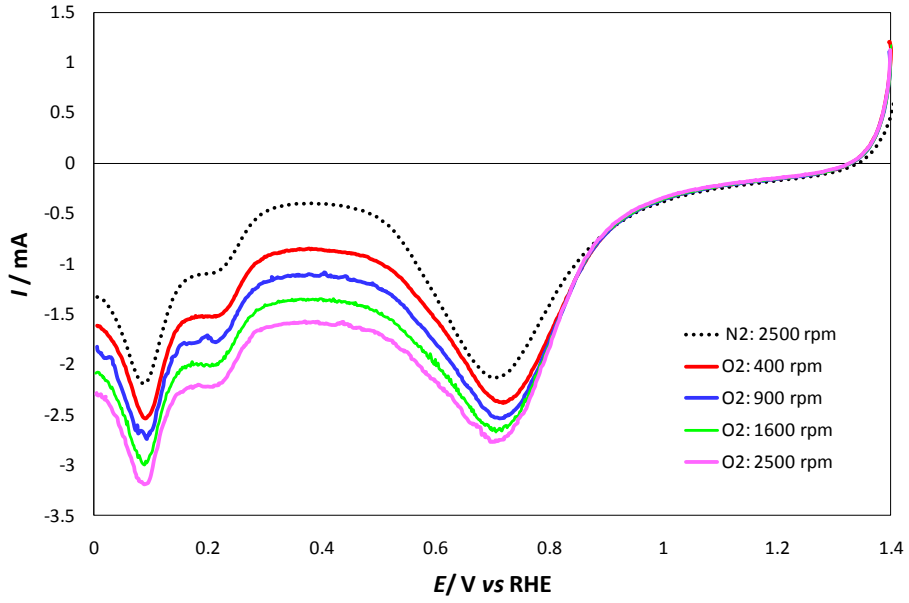

Figure 97: Characteristic CVs of Pt/C (RDE-3) at different rotation rates. Background electrolyte: 0.5 M H_2SO_4 under O_2 atmosphere. Dashed line correspond the CV (scan rate: 20mVs^{-1}) obtained under N_2 atmosphere at 2500 rpm as rotation rate. For Figure readability only the first half-cycles are reported.

The electrocatalytic activity of Pt/C powder is well evident; at potential values lower than ~0.9 V *vs* RHE the presence of an additional current is visible, which increases at increasing rotation rates, as expected in the presence of reactant mass transfer controlled by diffusion.

The effect of Nafion loading in the catalytic layer was evaluated considering electrodes having the same Pt content (0.5 mg cm^{-2}) but different Nafion® thickness. The results are shown in Figure 98.

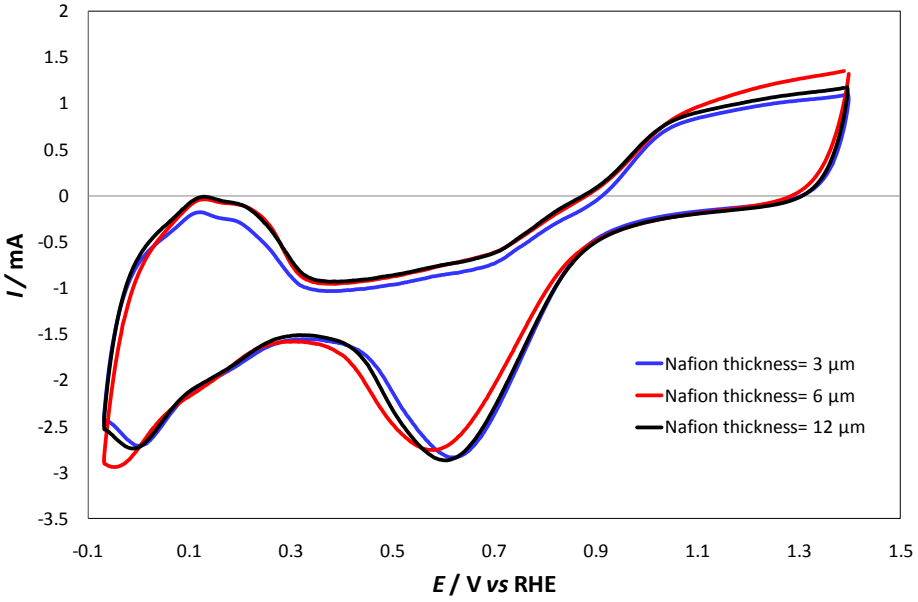

Figure 98: CV characteristics of Pt/C (E-TEK) with different Nafion® thickness. Pt loading: 0.5 mg cm^{-2}; background electrolyte: 0.1M $HClO_4$; scan rate 20 mV s^{-1}; rotation rate: 1600 rpm.

As can be observed the differences between CVs obtained at different Nafion® are negligible.

(III) Ti-plate

Ti-plate support allows the characterization of the electrochemical behaviour of an ink similar to the one adopted for MEAs preparation. This is a way to investigate the electrochemical response of the catalytic layer in the absence of OER, using a typical cell composed by three electrodes. The test were carried on to investigate the effect of the Nafion® emulsion in the catalytic layer For this characterization powder n°5 was used, at 2 mg cm^{-2} of Ir loading. This high Ir loading was used in order to minimize the effect of the support on the response. The CVs obtained with electrodes with different Nafion® loading are reported in Figure 99.

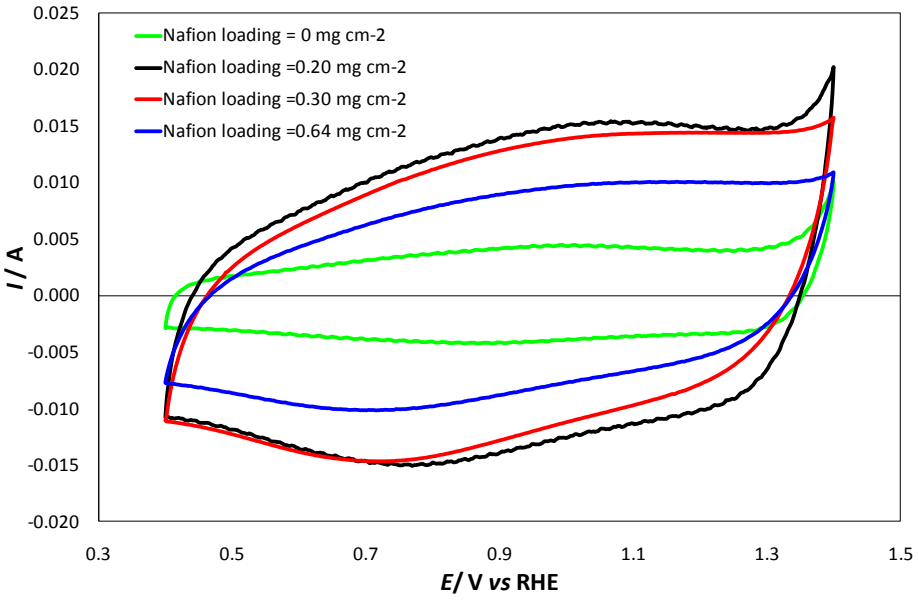

Figure 99: CVs of Ti-supported electrodes. Effect of the Nafion® loading in the catalysts layer. Ir loading= 2 mgcm^{-2}; background electrolyte: 0.5M H_2SO_4; scan rate 20 mV s^{-1}.

It can be noted that for Nafion® loading up to 0.2÷0.3 mg cm^{-2} the capacitive area increases. A further Nafion® increase not only leads to a reduction of the voltammetric charge but also introduces a slight distortion of the CVs due the onset of a resistive contribution. Figure 100 collects the *Q* values as a function of Nafion® loading.

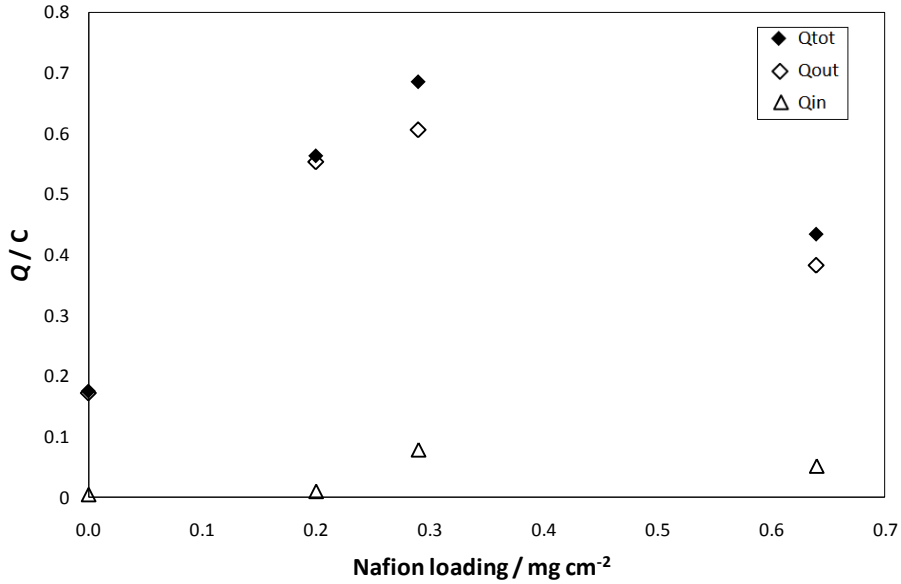

Figure 100: Effect of Nafion® loading in the Ti supported electrodes on *Q* values. Q_{tot}: full diamonds; Q_{out}: empty diamonds; Q_{in}: empty triangles.

The presence of Nafion® in the layer certainly favours the proton conductivity. Considering a Nafion® loading up to 0.2 mg cm^{-2}, a higher number of easily accessible active sites is obtained. A further increase of loading (0.3 mg cm^{-2}) leads to a limit condition. The Q_{tot} value increase but parallely slightly increase the no accessible active sites (represented by Q_{in}). When the Nafion® content is excessive a resistive contribution is introduced and the presence of diffusion phenomena due to the increase of layer thickness leads to a decrease of total number of active sites.

3.1.4- Supports comparison

The total quantity of charge accumulated (Q_{tot}) preserves its role of cumulative electrochemical active surface parameter, as evidenced in Figure 101.

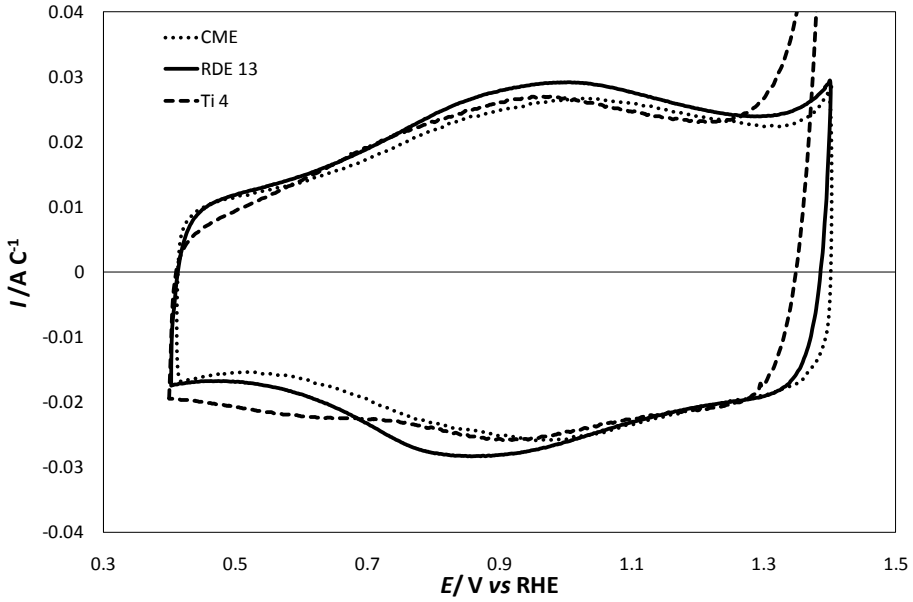

Figure 101: CV of powder n°5 recorded on Rotating Disk Electrode (RDE, black line), C-ME electrodes (dotted line) and Ti-thin plate electrode (dashed line). Currents are normalized by Q_{tot}. Curves were recorded at 20 mVs^{-1} in the 0.4 – 1.4 V potential range in 0.1 M $HClO_4$ in the case of RDE and 0.5M H_2SO_4 in the case of C-ME and Ti-thin plate.

Figure 101 refers to the behaviour of powder n°5 supported on C-ME (in 0.5M H_2SO_4), RDE (electrode number: RDE-13; in 0.1M $HClO_4$) and Ti thin plate (electrode number: Ti-4; in 0.5M H_2SO_4). The normalized I/Q_{tot} (AC^{-1}) currents are reported on the *y*-axis. In this way, curves, which on the *I* scale would be separated by more than 5 orders of magnitude, result fully comparable on the *I*/*Q* scale, thus confirming the total equivalence between the three supports used.

3.1.5-Conclusions

Nanostructured Ir-Sn based materials were obtained by sol-gel technique. The aim of this first part of work is to study the effect of both different synthetic parameters (method of addition Ir-precursor, calcination temperature, IrO_2 content in the powder) and the composition of the catalytic layer (Vulcan® and Nafion®). The investigation was carried out by both physico-chemical ex-situ techniques and electrochemical techniques.

PHISICO-CHEMICAL CHARACTERIZATION

The structural, morphological and surface properties are investigated by XRPD, BET, XPS and SEM techniques. This characterization was carried out considering essentially powders prepared by I method and having different IrO_2 content.

In XRPD analysis the presence of both oxides, IrO_2 and SnO_2, leds to the formation of broad peaks located at intermediate position between pure IrO_2 and pure SnO_2. For increasing IrO_2 content peaks appears shifting toward the peaks position of pure IrO_2. Moreover the increase of IrO_2 content leads to a decrease of the active area (S_{BET}) − due to the formation of larger crystalline IrO_2 aggregates − and to an enrichment of surface with Ir species (XPS results). The surface composition is strictly correlated to the synthetic route adopted. In fact in the case of MM method the Ir/Sn ratio at the surface is the same of nominal Ir/Sn ratio.

ELECTROCHEMICAL CHARACTERIZATION

C-ME. The electrochemical characterization was carried out and discussed on the basis of the Q_{tot}, Q_{out} and Q_{in} values and of the r_0 values obtained in the presence of Fe^{3+}/Fe^{2+} as testing probe. In the last case information about both the active surface and qualitative information about the kinetic parameters of Fe^{3+} reduction reaction obtained applied the Tomeš criterion can be extrapolated. Both the methods lead to concordant conclusions:

- the enhancement of the calcination temperature reduces the electrochemical performance; lower Q_{tot}, Q_{out}/Q_{tot}, r_0 values were obtained. This is correlated to the reduction of the active surface probably correlated to sintering effects.
- the impregnation method leads to materials with the highest electrochemical performances, and among them the best behaviour was observed for the powder having the 40wt% of IrO_2.
- the inferior response obtained with materials prepared along the other synthetic paths is probably correlated to the influence of SnO_2 on the behaviour. This is visible considering

both the CV shapes and the distorted sigmoid signals obtained in the presence of the redox couple.

RDE. I and CS-Cl powders having different IrO_2 content were investigated. Since the RDE was used for studying the reactivity of these materials toward ORR, the CVs were recorded under both N_2 and O_2 atmosphere.

Comparing the synthetic methods, also in this case the I method shown the best performance. Very interestingly, the higher ORR currents were obtained in the case the lowest IrO_2 content (20wt%).

The CS-Cl method is the more suitable method for the synthesis of powders with high IrO_2 content.

The presence of Vulcan® as diluent leads to a reduction of the electronic resistance in the layer and to a significant improvement of the electrochemical performance. In particular the adoption of a fixed Vulcan/Ir loading of 10% (by weight) is the optimal condition. Rather obviously increasing the Ir loading produces a further improvement.

Both the diluent matrix and the glassy carbon support do not significantly influence the electrochemical response in presence of oxygen. Otherwise the Pt/C powders showed a good electrocatalytic activity. The reactivity of these materials will be also investigated by recording polarization curves (see Section 3.3.3)

Ti-plate support allowed the investigation of the electrochemical properties of the catalytic layers having very similar properties of the ones deposited directly on MEAs. In particular the effect of the Nafion® loading in the layer was investigated and an optimal value of 0.3 mg cm^{-2} was found.

A comparison of the behaviour of the same powder using the different support was also reported and discussed. CVs normalised for the total voltammetric charge present a good superimposition in spite of the significant differences in the necessary amount of powder. This indicates the negligible influence of the support on the electrochemical response.

3.1.6-References

[1] Izutsu K, Yamamoto H *Anal. Sci.* **1996**, 12,905.

[2] Yao S, Wang M, Madou M *J. Electrochem. Soc.* **2001**, 148, H29.

[3] Patil PS, Kawar RK, Sadale SB *Appl. Surf. Sci*. **2005**, 249, 367.

[4] Gottesfeld S, MnIntyre JDE, Beni G, Shay JL *Appl. Phys. Lett*. **1978**, 33, 208.

[5] Savinell RF, Zeller RLIII, Adams JA *J. Eletcrochem. Soc*. **1990**, 137, 489.

[6] Ribeiro J, Alves PDP, De Andrade AR *J. Mat. Sci.* **2007**, 42, 9293.

[7] Cardarelli F, Taxil P, Savall A, Comninellis Ch, Manoli G, Leclerc O *J. Appl. Electrochem.* **1998**, 28, 245.

[8] Marshall A, Borresen B, Hagen G, Tsypkin M, Tunold R, *Mater. Chem. Phys*. **2005**, 94, 226.

[9] Marshall A, Tsypkin M, Borresen B, Hagen G, Tunold R, *J. New. Mater. Electrochem. Syst*. **2004**, 7, 197.

[10] Ortiz PI, De Pauli CP, Trasatti S, *J. New. Mater. Electrochem. Syst.* **2004**, 7, 153.

[11] De Pauli CP, Trasatti S, *J. Electroanal. Chem.* **2002**, 538, 145.

[12] De Pauli CP, Trasatti S, *J. Electroanal. Chem*.**1995**, 396, 161.

[13] Marshall A, Borresen B, Hagen G, Sunde S, Tsypkin M, Tunold R, *Russ. J. Electrochem*. **2006**, 42, 1134.

[14] Rasten E, *"Electroctalysis in water electrolysis with solid polymer electrolyte"* PhD Thesis, NTNU, Trondheim, Norway, **2001**.

[15] Silvia Ardizzone, Claudia L. Bianchi, Laura Borgese, Giuseppe Cappelletti, Cristina Locatelli, Alessandro Minguzzi, Sandra Rondinini, Alberto Vertova, Pier Carlo Ricci, Carla Cannas and Anna Musinu, *J. Appl. Electrochem.* **2009**, 39, 2093.

[16] Alessandro Minguzzi, Mario A. Apulche-Aviles, Joaquin Rodriguez Lopez, Sandra Rondinini and Allen J. Bard, *Anal. Chem*. **2008**, 80 (11), 4055.

[17] A. Vertova, L. Borgese, G. Cappelletti, C. Locatelli, A. Minguzzi, C. Pezzoni, S. Rondinini, *J. Appl. Electrochem.*, **2008**, 38(7), 973.

[18] Grupioni A.A.F., Arashiro E., Lassali T.A.F., *Electrochim. Acta* **2002,** 48, 407.

[19] Yoshinaga N., Sugimoto W., Takasu Y. , *Electrochim Acta* **2008**, 54, 566.

[20] Takasu Y, Yoshinaga N, Sugimoto W *Electrochem. Comm*. **2008**, 10, 668.

[21] D'Urso C, Morales LS, Di Blasi A, Baglio E, Ornelas R, Orozco G, Arriaga LG, Antonucci V, Arico` A *ECS Trans*. **2007**, 11, 191.

[22] Trasatti S *Port. Electrochim. Acta* **2001**, 19, 197.

[23] Burke LD, Naser NS, Ahern BM *J. Solid. State Electrochem*. **2007**, 11, 655.

[24] Tian M, Bakovic L, Chen A , *Electrochim. Acta* **2007**, 52, 6517.

[25] Va´zquez-Go´mez L, Horva´th E, Kristo´f J, Re´dey A ´ , De Battisti A *Appl. Surf. Sci*. **2006**, 253, 1178.

[26] Robert Mattehew Asmussen, Min Tian and Aicheng Chen *Environ. Sci. Technol.* **2009,** *43,* 5100.

[27] Ardizzone S, Cappelletti G, Ionita M, Minguzzi A, Rondinini S, Vertova A *Electrochim. Acta* **2005**, 50, 4419.

[28] Ionita M, Cappelletti G, Minguzzi A, Ardizzone S, Bianchi CL, Rondinini S, Vertova A *J. Nanopart. Res*. **2006**, 8, 653.

[29] A. Minguzzi, M. A. Alpuche-Aviles, J. R. López, S. Rondinini, and A. J. Bard Anal. Chem. 2008, 80, 4055.

3.2- Reactivity of IrO_2-SnO_2 nanopowders toward OER

3.2.1-Introduction

Fossil fuel consumption and global climate changes [1] in connection with environmental hazard have prompted research for alternative and clean energy sources [2]-[5]. The challenging subject known as "hydrogen economy" [6]-[10] has experienced a wide interest due to the possibility of direct conversion between chemical and electrical energy through an electrochemical reaction, a truly "green process". Since H_2 is an energy carrier and is not directly available in nature, the energy conversion is a "green process" only if hydrogen is produced using non-fossil primary energy sources, *e.g.* by electrolysis driven by renewable sources [11]. The electrolytic processes are of particular interest due to their intrinsic harmless operational conditions and low running costs, provided that renewables like solar or wind energies [12]-[14], can be used to supply electricity to the electrolyser.

Until now, industrial water electrolysis has been carried out in aqueous media containing an alkaline electrolyte at high concentrations (typically KOH 25%), a mature and robust technology that nonetheless presents some disadvantages, the main one related to the presence of a caustic liquid and its possible leakage. Other disadvantages are the low specific production rates and the necessity of a subsequent hydrogen purification from unavoidable alkaline "fogs". Recently, water electrolysis in acidic media, which uses highly purified water and adopts a polymer electrolyte membranes (PEM) in an arrangement similar to that of PEM fuel cell systems, has gained interest for several reasons: greater safety and reliability, high operating current density and efficiency and construction simplicity[15][16].

In this context, the development of new electrocatalytic materials for the OER is necessary both for improving the anode chemical stability in acidic medium and for reducing power consumption [15]. Since the 1970s, with the introduction of Dimensionally Stable Anodes, DSA, in the chlor-alkali process, studies on noble metal oxide electrodes have led to the development of new electrocatalytic materials both for the OER [15][17] and for the Hydrogen Evolution Reaction (HER) in acidic media [18]. It was demonstrated that among noble metal oxides IrO_2 has good corrosion resistance in strong acidic solutions [19][20], even though its activity is slightly lower than RuO_2 and its cost is prohibitive for industrial applications.

However, new composite materials, based on IrO_2 dispersed in a less expensive but highly stable metal oxide, can lead to the development of new electrodes with good chemical resistance to the acidic environment and good electronic conductivity [17][21]. A large number of oxide systems

have been considered, thanks to the possibility of varying the nature of the active component and of the dispersing agent, the synthetic procedure and the mass ratio between components [17][21]-[29].
In this part of the thesis, the characterization of electrodes based on SnO_2–IrO_2 nanoparticles is discussed. The sol–gel synthetic methodology (Impregnation method) was chosen for all materials, since this technique produces powders with very promising electrochemical behaviour (see Section 3.1). The compositions of the investigated powders are reported in the following table:

n°powder	Composition	Precursor	Method	$T_{calcinations}$ / °C
4	$Sn_{0.85}Ir_{0.15}O_2$	$Sn(C_4H_9O_4)+IrCl_3$	MM	500
5	$Sn_{0.85}Ir_{0.15}O_2$	$Sn(C_4H_9O_4)+IrCl_3$	I	450
6	$Sn_{0.69}Ir_{0.31}O_2$	$Sn(C_4H_9O_4)+IrCl_3$	I	450
7	$Sn_{0.50}Ir_{0.50}O_2$	$Sn(C_4H_9O_4)+IrCl_3$	I	450
8	$Sn_{0.27}Ir_{0.73}O_2$	$Sn(C_4H_9O_4)+IrCl_3$	I	450

Table 24: List of powders characterized by MEA electrolysis.

Two kinds of electrodes were prepared: Gas Diffusion Electrodes (GDEs) and Membrane Electrode Assemblies (MEAs). Although they structurally differentiate for the nature of their support: a carbon cloth in the first case and a cationic membrane in the second one, their operation conditions are deeply different. GDEs are simply in contact with the proton conducting polymer electrolyte, while MEAs have the electrocatalytic layer directly deposited onto the proton conducting membrane.
In the case of GDE the anodic layer was made of a mixture composed by the electrocatalyst powder (powder n°4, Ir loading = 0.6 mg cm^{-2}), Nafion® emulsion, active carbon (Vulcan® XC72R) and polytetrafluoroethylene (PTFE) in the weight ratio 1:0.1:0.5:0.5. The mixture was suspended in 2-propanol and deposited onto a graphite cloth which was then hot-pressed.
In the case of MEAs, the cathode and the anode (which composition is reported in the following table) were deposited directly onto the membrane, in a way similar to the one adopted for the preparation of GDEs and hot pressed.

Sample	Electrocatalyst powder	IrO_2 loading (mg cm^{-2})	Nafion® loading (mg cm^{-2})	Others components
MEA 1	5	0.6	0.6	Vulcan (6mg cm^{-2})
MEA 2	5	2.9	5	------
MEA 3	5	1.2	0.6	------
MEA 4	6	1.2	0.6	-----
MEA 5	7	1.2	0.6	------
MEA 6	8	1.2	0.6	------

Table 25: Anodic layer compositions of MEAs tested.

Two different electrolytic cells were used (Section 2.2.5-III "*Electrode Characterization*") and MEA-3 tests were replicated in both of them.

In all cases the cathodic layer consisted in 28.6wt% Pt on Vulcan® XC72R (E-TEK) directly deposited onto the opposite side of the membrane. The Pt loading is 1mg/cm^2 in order to avoid any appreciable HER overvoltage on the cell voltage. The detailed descriptions of the operational procedures for the preparation of MEAs and GDEs are reported in the section 2.2.5-III *"Electrode Preparation".*

The electrochemical behaviour of GDEs and MEAs was determined adopting the two cell designs described in section 2.2.5-III, by recording the *U vs I* characteristics between 100 and 10,000 Am^{-2} and by impedance measurements (10 mV amplitude over the frequency range of 100 kHz–0.1 Hz). All measurements were carried out at room temperature.

The two cell designs present a common plate-and-frame structure but differentiate for the modality of the water supply and for the current-collector design and material. When the immersion cell was adopted, the whole apparatus was immersed in a water tank and the current-collectors are porous Ti sinters. When the flux cell was used, the water was pumped through the cell and a homogeneous current distribution was reached by adopting two graphite end-plates (more detailed information about the cell structures was reported in Section 2.2.5.-III *"Electrode Characterization").*

This part of work is centred on the optimization of both cell designs and operation conditions (tightening pressure of the cell, efficiency of the water supply and of the gas removal) and the catalytic layer composition, in order to optimize the IrO_2 and the Nafion® loadings.

3.2.2-Immersion cell

The first considered parameter was the pressure used to tighten the cell, and its effects on the cell voltage. The contact resistance between the two current collectors and the two electrodes is one critical point that can affect the performance of the cell. Figure 102 shows the *U vs I* characteristics of the same GDE obtained applying different pressures on the cell.

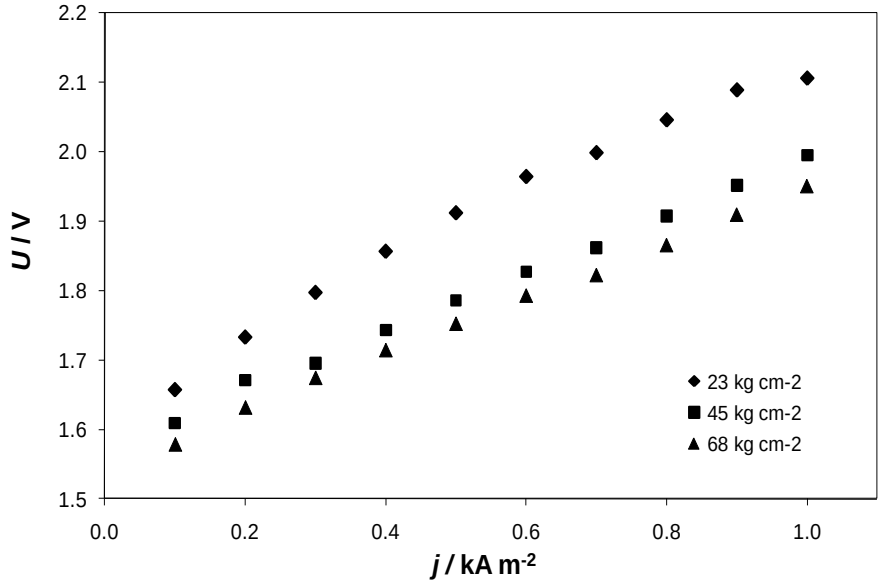

Figure 102: Effect of the pressure applied for tightening the immersion cell on its performances adopting a GDE electrode. Water electrolysis were carried out at room temperature.

The increase of the tightening pressure from 23 kg cm^{-2} to 68 kg cm^{-2} lowers the cell voltage of about 150 mV at 1.0 kA m^{-2}. This is likely due to both an improvement of the current distribution over the electrode surface and the reduction of the contact resistance. Moreover, pressures greater than 45 kg cm^{-2} do not lead to a further significant decrease of the voltage drop (45mV at 1.0 kAm^{-2}). Therefore, this value was adopted for all the following measurements.

In the case of MEAs, the intimate adhesion of the catalyst powder with the membrane leads to a significant increase of the electrochemical performances with respect to those determined when GDEs were tested. A GDE and a MEA having the same IrO_2 loading were compared. The superior performance showed by the MEA is clearly visible.

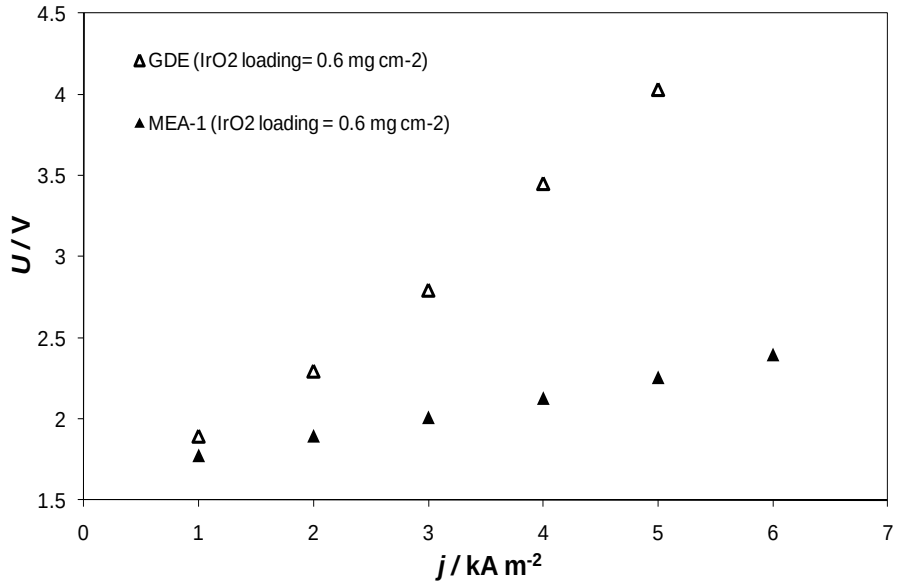

Figure 103: Comparison between MEA1 and GDE performances. Water electrolysis were conducted at room temperature.

The effect of increasing the IrO_2 loading is reported in the following Figure.

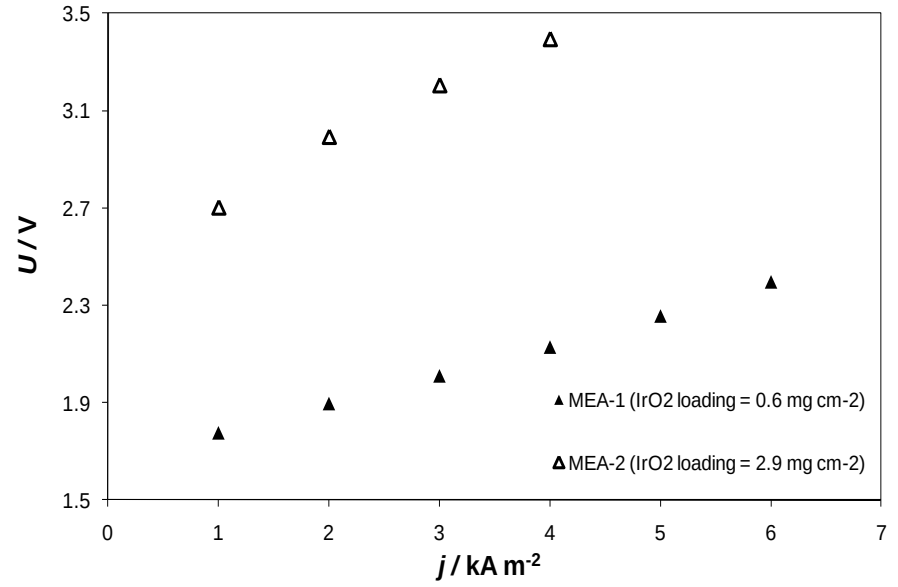

Figure 104: Comparison between MEA-1 and MEA-2 characteristics. Water electrolysis were conducted at room temperature.

The increase of the IrO_2 content leads to a worsening of the electrochemical behaviour. This surprising result is probably due to the high amount of Nafion® loaded in the catalytic layer of MEA-2 (5 mg cm^{-2} versus 0.6 mg cm^{-2} in MEA-1); as showed in Table 25, MEA-2 presents higher Nafion®/IrO_2 weight ratio than MEA-1.

One possible explanation is bound to the critical balance between the electronic and protonic conduction within the layer. For increasing the Nafion® content, the electronic conduction is lowered, while the proton conduction is enhanced so that the electron transfer process shifts toward the inert Ti sinter, used as current collector.

This hypothesis was confirmed by parallel measurements carried out at various Nafion® content by supporting the powders on Ti-plates, as discussed in section 3.1.3-III. A loading of 0.3 mg cm^{-2} was found as optimal condition. However, a loading of 0.6 mg cm^{-2} was adopted in the case of MEAs because at lower loadings a faster powder detachment was observed.

Further evidence is provided by the *U vs I* characteristics recorded adopting two kinds of current collectors: (i) Ti nets activated with IrO_2-based materials, which are active toward OER, and (ii) porous metallic titanium sheets (Ti-sinters), which are completely inert toward OER. The results are shown in Figure 105.

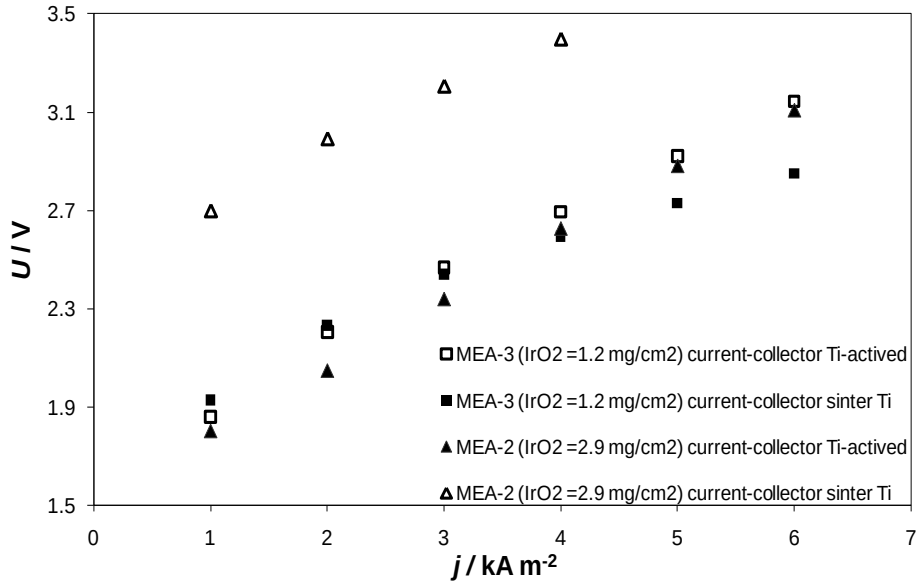

Figure 105: Effect of the Nafion® emulsion loaded in the catalyst layer. Water electrolysis were conducted at room temperature.

In the case of MEA-2, which contains a high Nafion® loading, the use of an inert current collector provokes a dramatic decrease of the electrochemical performance. A difference of 0.77V at 4 kAm^{-2} is observed. In the case of MEA-3 (low Nafion® loading) the responses obtained with the two current collectors are very similar. In particular, up to 3 mA m^{-2}, *U vs I* curves are almost superimposable and, at higher current densities, MEA-3 shows a significant decrease of the cell voltage when the Ti-sinter is used. These results confirm that at high Nafion® content the enhancement of the proton conduction within the catalytic layer, together with the parallel increase

of its electric resistance, "short-circuits" the layer and the electron transfer occurs at the current collector. The results also demonstrate that the current collector does not influence the electrochemical response provided that a Nafion® loading ≤0.6 mg cm^{-2} is adopted.

Notwithstanding the optimization of the ionomer loading, the electrochemical performance of the MEAs is still apparently inversely dependent on the IrO_2 content. This is well shown in Figure 106:

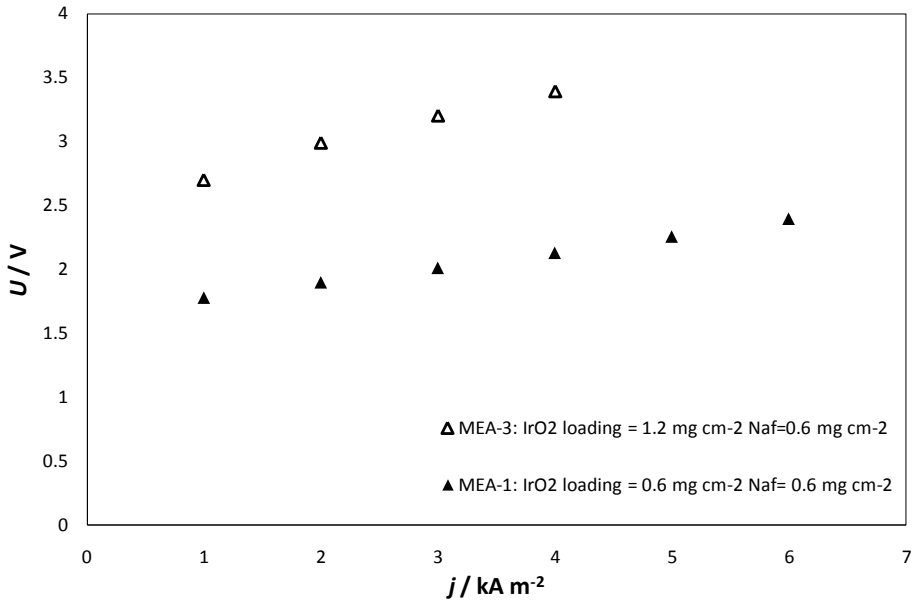

Figure 106: Effect of Ir loading in the catalytic layer of MEA. Water electrolysis were conducted at room temperature.

MEA-3 which contains the highest IrO_2 content, shows the highest *U* values, with an increase of the cell potential up to 65% with respect to MEA-1, which contains 0.6 mgcm^{-2} of IrO_2.

In order to investigate the reasons of this unexpected behaviour, EIS measurements were carried out adopting the set-up described in section 2.2.4.

EIS spectra have been interpreted with the usual equivalent circuit proposed for PEMFC electrodes. Impedance spectra for FC electrodes typically include two arcs, the one at higher frequency is generated by the charge transfer resistance in parallel with the double-layer capacitance within the catalyst layer while the one at lower frequencies is due to mass-transport limitations[30]. The high frequency intercept with the real axis can be correlated with the electric resistance of the whole apparatus. The equivalent circuit is represented by distributed elements connecting the current collector and the electrolyte solution (see Figure 107).

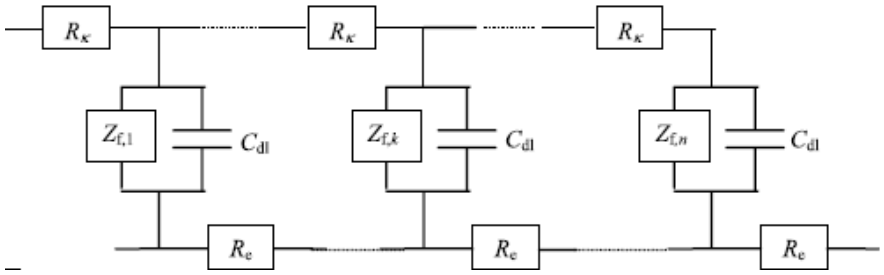

Figure 107: Scheme of a distributed element circuit. (R_k: ionic resistance, Z_{fk}: faradaic impedance and R_e: electronic resistance, C_{dl}: double layer capacitance).

Figure 108 shows the results obtained on MEA-3.

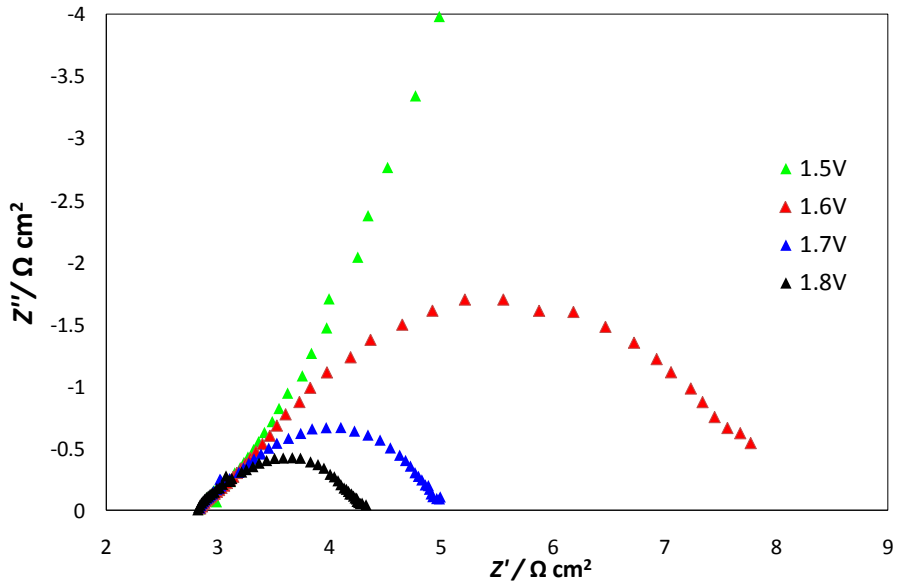

Figure 108: Impedance spectra of MEA3 recorded at different cell potentials.

The high frequency intercept on the real axis amounts to 2.8 Ω cm^2 at all the applied potential values. At the same time, the diameter of the low frequency arc increases at decreasing of potential applied. This is likely related to the increase of the electron transfer resistance. The reason of the high electron transfer resistance has been evidenced by recording consecutive EIS measurements at constant cell voltage.

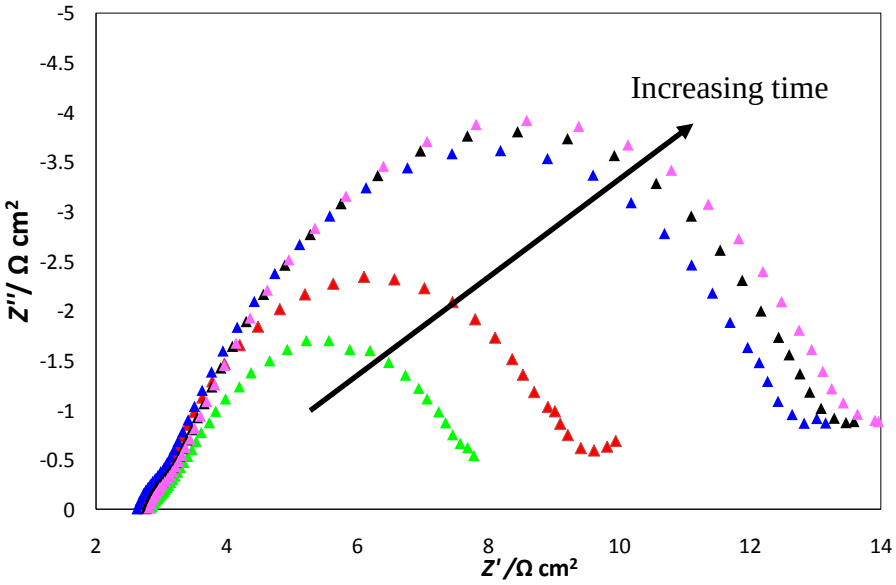

Figure 109: Impedance of MEA3 as a function of time. *U* applied is 1.6 V .

EIS spectra recorded consecutively show a progressive increase of the diameter of the low frequency arc. This phenomenon indicates an enhancement of the polarization resistance probably due to the progressive increasing hindrance of the water supply within the active layer.

Therefore, the worst performance of MEA-3 with respect to MEA-1 is a sort of boomerang effect: the higher electroactivity of the higher IrO_2 loaded layer leads to a faster water consumption which is immediately reflected by the drying of the layer and of the membrane, thus pointing to a poor water supplying with this cell design.

3.2.3-Flux cell

In this cell design, current distributors were graved directly onto one side of the graphite blocks adopted to apply a homogeneous pressure on the MEA. Graphite blocks also include passages for water, which can be forced through the catalyst layer by pumping.

The first result, recorded on MEA-3, was not encouraging since a progressive enhancement of the cell voltage was observed:

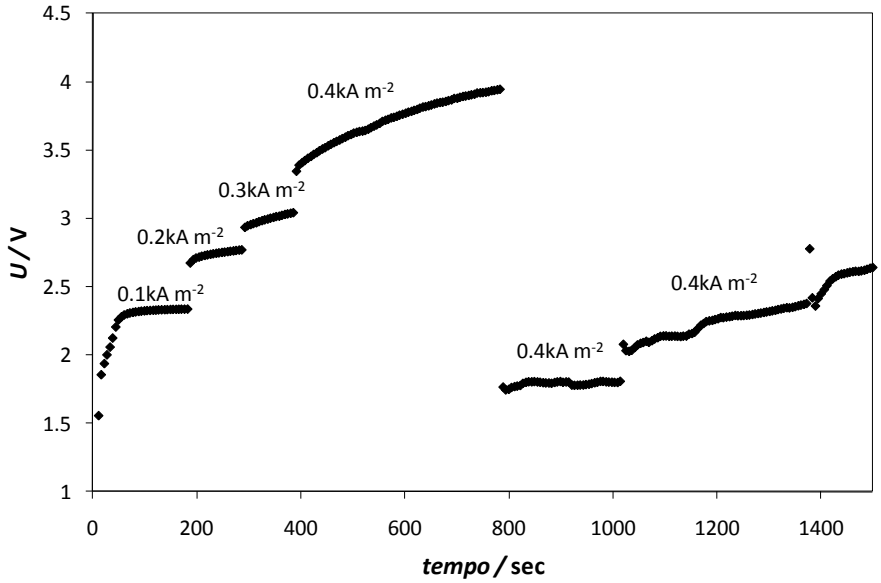

Figure 110: *U vs time* behaviour of MEA-3 tested with the flux cell.

This is probably due to the formation of a gas film, which would hinder water supply, onto the electrode surface under working conditions. This hypothesis is confirmed by the observation of sharp potential drops during the recording, likely caused by the detachment of large gas bubble from the surface. In order to favour the gas removal, water inlets were enlarged as shown in Figure 111.

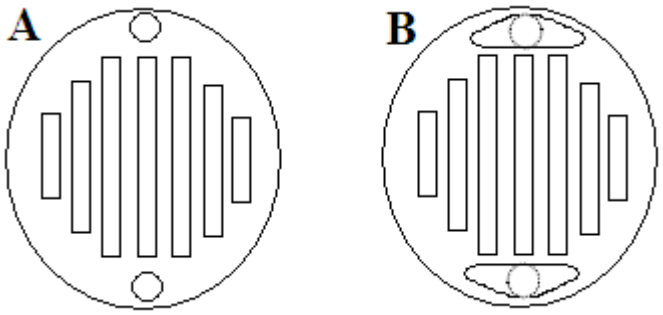

Figure 111: Scheme of the two kinds of graphite plates. A: plates with narrow water inlet/outlet; B: plates with broad water inlet/outlet.

The goal was promptly reached, as shown in the next figure, which reports the *U* vs *time* characteristics of MEA-3 recorded using the new cell design.

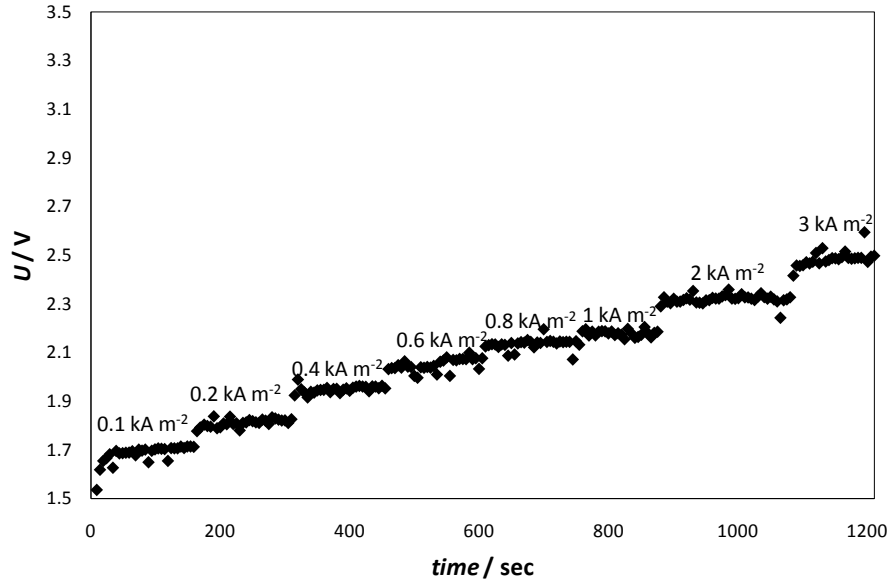

Figure 112: *U vs time* characteristics of MEA-3 tested with the flux cell with broaden water outlets.

It is possible to observe that *U* is stable also at the highest current densities. This means that the gas removal is more efficient. In order to evaluate the cell resistance, EIS measurements were carried out at different *U* values.

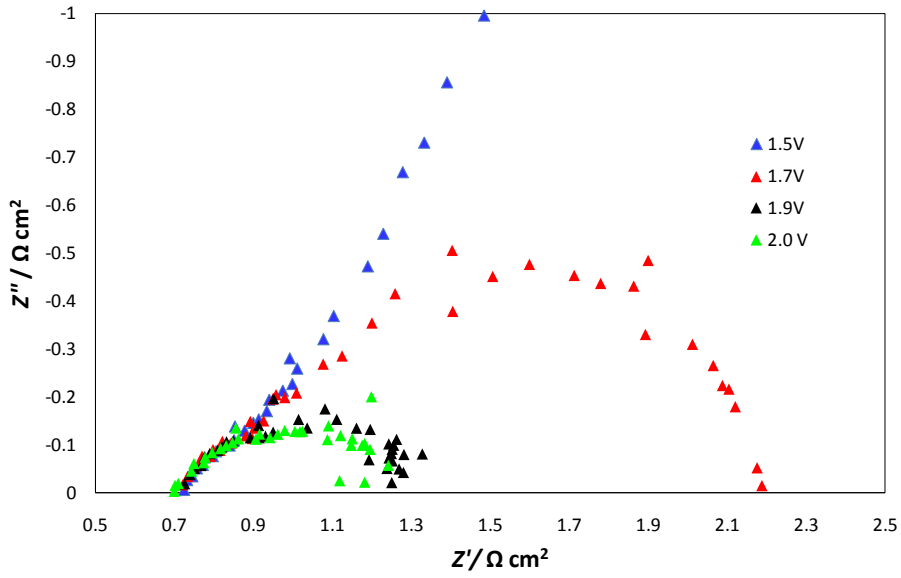

Figure 113: Impedance of MEA-3 as a function of cell voltage.

The signal noise is likely correlated with the water flux inside the cell during the measurements. The use of the graphite plates as current collectors leads to a best contact and, in turn, to an evident decrease of the high frequency intercept with the real axis (0.7 Ωcm^2 for the present flux cell *vs*

2.8 Ω cm^2 in the case of the immersion). This performance improvement is also visible comparing the same MEA in the two different cells (see Figure 114).

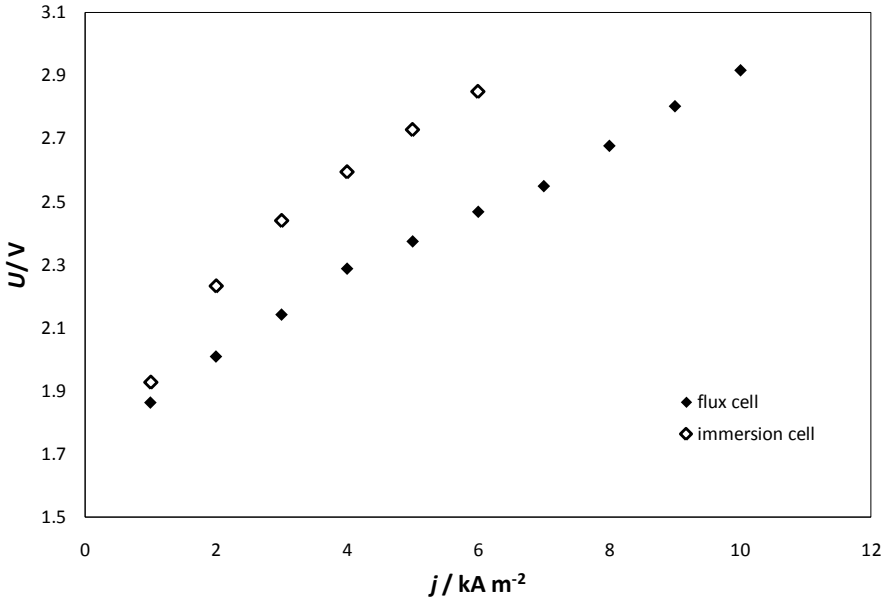

Figure 114: Comparison of MEA-3 behaviour using the immersion cell (empty points) or the flux cell (full points).

A decrease of the cell voltage of 0.39V at 0.6 kA m^{-2} is observed. In the case of the flux cell, both the easier gas removal and the more efficient water supply allow the application of higher current densities.

Using the flux cell, MEAs containing powders having different IrO_2 contents were characterized both by EIS and potentiostatic measurements. The catalytic layer deposited on the Nafion®-115 has the same IrO_2 and Nafion® loadings.

The results are reported in Figure 115 and Figure 116.

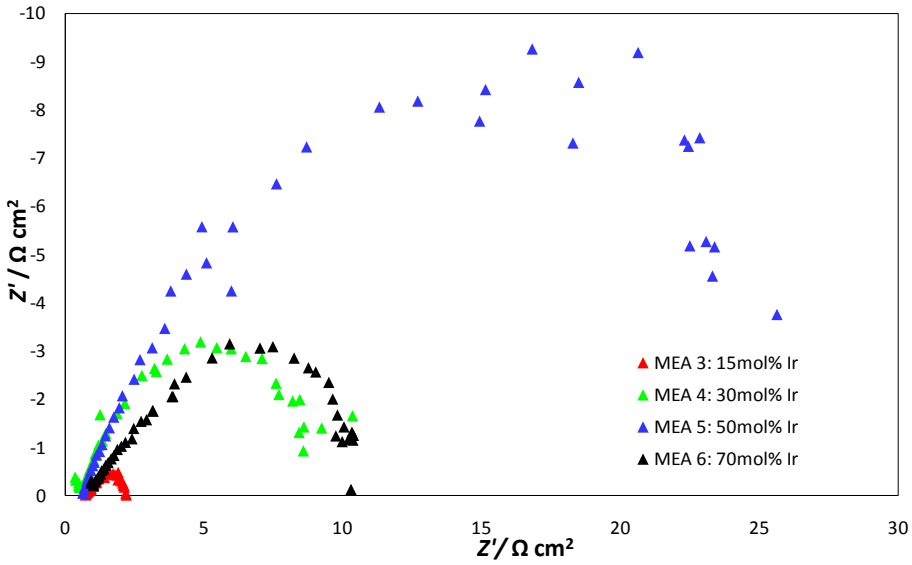

Figure 115: EIS spectra recorded on MEAs containing different IrO_2 percentages. IrO_2 loading on the MEA= 1.2 mg cm^{-2}. The applied cell voltage is 1.7V. Water electrolysis were conducted at 28°C.

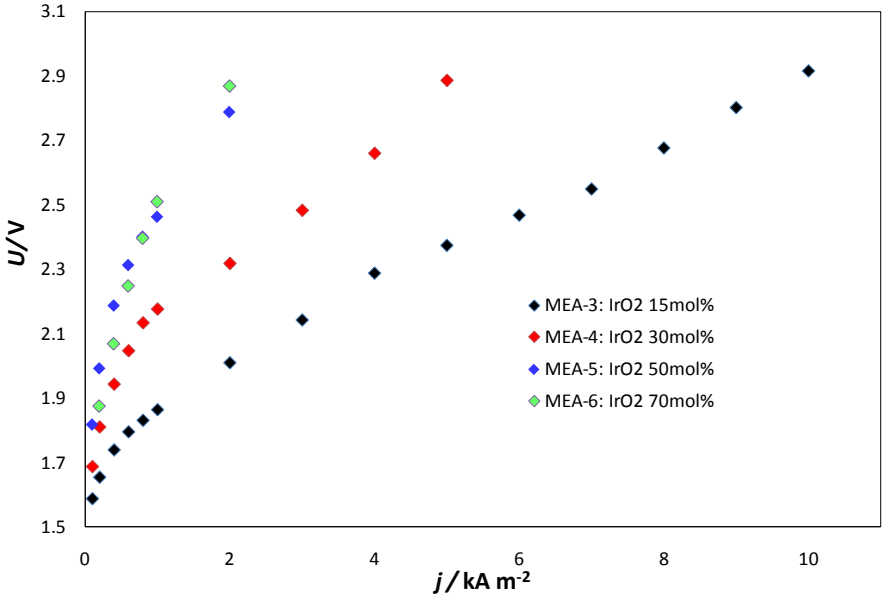

Figure 116: Potentiostatic measurements recorded on MEAs containing different IrO_2 percentages. IrO_2 loading on the MEA= 1.2 mg cm^{-2}. Water electrolysis were conducted at 28°C.

In EIS spectra, the intercept with the real axis at high frequencies, equal to 0.6 Ω cm^2 is not modified by the increase of the IrO_2 content. Otherwise, MEA-3, which contains the electrocatalytic powder with the lowest IrO_2 content, shows the lowest electron transfer resistance. Then, a

progressive increase of the lower frequency resistance is observed with a maximum at IrO_2 50 mol%.

These results are confirmed by polarizations curves. The best performances are recorded in the case of the MEA-3. By increasing the IrO_2 content in the powder, a progressive increase of the cell voltage values are observed. In particular, the polarization curves for MEA-4, MEA-5, MEA-6 were interrupted at low values of current densities. This could be due to either the influence of the mass transfer control and/or the persistent difficulty of the gas removal that determine the progressive increase of *U* with.

Now, having removed most of the spurious experimental effect, one has to recognize that the worsening of the response at increasing IrO_2 content, but constant Ir loading, is in line with the specific surface areas reported in section 3.1.2. The higher the IrO_2 content, the greater the formation of segregate phases and the lower the amount of easily accessible active sites. In order to eliminate the others resistance contributions, a further cell optimization is needed. Nevertheless, an evaluation of effect of powders composition on their activity toward OER was possible

3.2-3-Conclusions

Powders synthetized by sol-gel technique and adopting the Impregnation method were characterized in terms of their activity toward the OER using two different cell designs: an immersion cell and a flux cell. Both EIS and potentiostatic analysis were performed in order to highlight the most important parameter influencing electrochemical performance:

- current collectors-electrodes-membrane electric contacts. The intimate adhesion of the catalytic particles with the membrane in the case of MEA led to a significant reduction of the cell voltage at constant current density. In particular, the use of the flux cell that implies the use of graphite plates led to a significant reduction of the resistance.
- The ionomer loading in the electrode layer. High ionomer loadings led to the formation of a high number of proton pathways from the membrane to the current collector. This shifts toward the current collector the triple contact (electrons, protons and water) requested for the reaction to occur. Moreover, the ionomer is an electronic insulator so that is can hindrance the contact between particles. On the other hand, if the ionomer loading is too low, homogeneous protonic conduction is not guaranteed. Experimental results showed that the loading of 0.6 mg cm^{-2} is the optimal one.
- The efficiency of the water supply. This aspect was significant improved using the flux cell, where water continuously flows during the measurements. In particular, the application of

high current densities (higher than 6 kA m^{-2}) could be possible only in the absence of mass transfer control conditions.

- The efficiency of gas removal. The formation of a gas film stops the water access toward the electrode surface. This phenomenon was avoided by optimizing the water flux inside the cell.
- The IrO_2 content in the composite powder. The best performance was obtained adopting the powder having the lowest IrO_2 content. A progressive worsening of the electrochemical response was observed, in line with the lowering of the specific surface areas with increasing IrO_2 content.

3.2.4-References

[1] Wuebbles DJ, Atul KJ *Fuel Process. Technol*. **2001**, 71, 99.

[2] Chalk SG, Miller JF *J. Power Sources* **2006**, 159, 73.

[3] Ecsedy CJ, Murphy CG *Water Environ. Res.* **1992**, 64, 647.

[4] Alejaldre C, De Marco F, Finzi U et al *Nucl. Fusion* **2005**, 45, A1.

[5] Schultz MG, Diehl T, Brasseur GP, Zittel W *Science* **2003**, 302, 624.

[6] Dunn S Int. *J. Hydrogen Energy* **2002**, 27, 235.

[7] Turner JA *Science* **2004**, 305, 972.

[8] Stavy M *J. Sol. Energy Eng*. **2005**, 127, 161.

[9] Hetland J, Mulder G *Int. J. Hydrogen Energy* **2007**, 32, 736.

[10] Granovskii M, Dincer I, Rosen MA *Int. J. Hydrogen Energy* **2007**, 32, 927.

[11] Schug CA *Int. J. Hydrogen Energy* **1998**, 23, 1113.

[12] Bilgen E Sol. Energy **2004**, 77, 47.

[13] Ogden JM, Williams RH Int. J. Hydrogen Energy **1990**, 15, 155.

[14] Trasatti S *Port. Electrochim. Acta* **2001**, 19, 197.

[15] Rasten E, Hagen G, Tunold R *Electrochim. Acta* **2003**, 48, 3945.

[16] Slavcheva E, Radev I, Bliznakov S et al *Electrochim. Acta* **2007**, 52, 3889.

[17] De Pauli CP, Trasatti S *J. Electroanal. Chem*. **2002**, 538, 145.

[18] Krstajic N, Trasatti S *J. Appl. Electrochem*. **1998**, 28, 1291.

[19] Cardarelli F, Taxil P, Savall A et al *J. Appl. Electrochem*. **1998**, 28, 245.

[20] Horvath E, Kristof J, Frost RL et al *J. Thermal Anal. Calorim*. **2004**, 78, 687.

[21] Chen X, Chen G, Yue PL *J. Phys. Chem. B* **2001**, 105, 4623.

[22] Comninellis Ch, Vercesi GP *J. Appl. Electrochem*. **1991**, 21, 335.

[23] De Pauli CP, Trasatti S *J. Electroanal. Chem*. **1995**, 396. 161.

[24] Lassali TAF, Boots JFC, Bulhoes LOS *Electrochim. Acta* **1999**, 44, 4203.

[25] Da Silva LA, Alves VA, de Castro SC, Boots JFC *Colloid. Surface A* **2000**, 170, 119.

[26] Chen X, Chen G, Yue PL *J. Phys. Chem. B* **2002**, 106, 4364.

[27] Ortiz PI, De Pauli CP, Trasatti S *J. New Mat. Electrochem. Syst*. **2004**, 7, 153.

[28] Chen X, Chen G *J. Electrochem. Soc*. **2005**, 152, J59.

[29] Marshall A, Børresen B, Hagen G et al *Energy* **2007**, 32, 431.

[30] E. Springer, A. Zawodzinski, M. S. Wilson, and S. Golfesfeld *J. Electrochem. Soc*. **1996**, V. 143, No.2.

3.3- Reactivity of IrO_2-SnO_2 nanopowders toward ORR

3.3.1-Introduction

A regenerative fuel cell (RFC) is a promising energy storage and conversion system that uses hydrogen as energy medium. The RFC system produces hydrogen and oxygen from water electrolysis, using electrical power, but the same system can also produce electrical power, when energy is needed, operating as fuel cell and burning the previously produced and stored hydrogen This RFC system has a distinctive advantage over secondary batteries as it is capable of long-term energy storage without permanent losses by self discharge and has high-specific energy (above 400 Wh/kg) [1][2]. In the usage of the RFC system, the limiting factors for wide application are cost and electric efficiency. In order to reduce the cost, unitized regenerative fuel cell (URFC) system, using a single electrochemical cell that can work both as fuel cell and water electrolyser, was developed. On the other hand, in order to improve the URFC system efficiency, the implementation of electroactive materials for both oxygen reduction and water oxidation is a commitment for the scientific community. The bifunctional electrocatalyst also should be resistant to anodic corrosion during water electrolysis. Several previous studies have reported some noble metals and metal oxides as promising oxygen electrode catalyst for URFC system on the basis of catalyst activity and stability [3]-[8].

Since iridium oxide based materials presents a high resistance to corrosion in acidic solutions and is one of the outstanding electrocatalysts for oxygen evolution reaction, in this thesis they were characterized toward oxygen reduction reaction (ORR).

This evaluation was carried out using rotating disk electrode (RDE) which allows to work under controlled mass-transfer conditions, thus enabling the accurate evaluation of the electron transfer (ET) kinetic contribution.

The electrochemical investigation was carried out recording polarization curves at selected potential levels, between 1.1V and 0V *vs* RHE, by applying steps of 10 mV by 10, both under nitrogen and oxygen atmosphere. All the electrochemical experiments were performed at 25°C.

All the polarization curves reported here were obtained by subtracting the polarization curve recorded under N_2 atmosphere to the polarization curve recorded in presence of O_2, at the same rotation rate.

More detailed information about both the electrode preparation and characterization are reported in Section 2.2.5-IV "*Electrode preparation*".

The IrO_2-based powders investigated are reported in Table 26.

N° sample	Composition	Precursor	Method	$T_{calcinations}$ / °C
5	$Ir_{0.15}Sn_{0.85}O_2$	$Sn(C_4H_9O_4)+IrCl_3$	I	450
6	$Ir_{0.31}Sn_{0.69}O_2$	$Sn(C_4H_9O_4)+IrCl_3$	I	450
7	$Ir_{0.50}Sn_{0.50}O_2$	$Sn(C_4H_9O_4)+IrCl_3$	I	450
8	$Ir_{0.73}Sn_{0.27}O_2$	$Sn(C_4H_9O_4)+IrCl_3$	I	450
12	$Ir_{0.60}Sn_{0.40}O_2$	$SnCl_4+ IrCl_3$	CS-Cl	500
13	$Ir_{0.70}Sn_{0.30}O_2$	$SnCl_4+ IrCl_3$	CS-Cl	500
14	$Ir_{0.80}Sn_{0.20}O_2$	$SnCl_4+ IrCl_3$	CS-Cl	500
15	$Ir_{0.90}Sn_{0.10}O_2$	$SnCl_4+ IrCl_3$	CS-Cl	500
16	IrO_2	$SnCl_4+ IrCl_3$	CS-Cl	500

Table 26: Electrocatalytic powder characterized toward ORR.

In particular two different synthesis methods were considered (I and CS-Cl method) and the effect of both the IrO_2 content of the powder and the composition of the catalytic layer (Ir loading, Vulcan® loading) were investigated. In the case of CS-Cl method, powders with high IrO_2 content were synthesized on account of their similarities with the $IrSnO_2$ spots investigated by Scanning Electrochemical Microscopy experiments [9]

Since the Pt based electrocatalyst is the most used material to prepare electrodes for ORR, the commercial Pt/C 28.6wt% (E-TEK) electrocatalyst was also investigated and used as reference for comparison with $IrSnO_2$-based matrices. Different Pt loading (0.1÷0.7 mg cm^{-2}) and Nafion® thicknesses (3÷24 nm) were considered. The Nafion® thickness was always lower than 0.2 µm therefore the diffusion effect into Nafion® layer was negligible [10][11].

In order to rule out possible effects of the glassy carbon support and the diluent matrices (SnO_2 and Vulcan®), the characterization of these materials were also carried out in the same conditions.

The compositions of RDEs tested are reported in the Table 27.

n°electrode	n° powder	Metal loading (mg cm^{-2})	Nafion® thickness (nm)	Vulcan loading (mg cm^{-2})	Electrolyte (M)
RDE-1	Pt/C (E-TEK)	0.1	12	----	H_2SO_4 0.5M
RDE-2		0.3	12	----	H_2SO_4 0.5M
RDE-3		0.5	12	----	H_2SO_4 0.5M
RDE-4		0.7	40	----	H_2SO_4 0.5M
RDE-5		0.5	3	----	$HClO_4$ 0.1M
RDE-6		0.5	6	----	$HClO_4$ 0.1M
RDE-7		0.5	12	----	$HClO_4$ 0.1M
RDE-8		0.5	24	-----	$HClO_4$ 0.1M
RDE-9	SnO_2	0.5	6	-----	$HClO_4$ 0.1M
RDE-10	Vulcan® XC72R	----	20	0.03	$HClO_4$ 0.1M
RDE-11	Glassy carbon	0	0	----	$HClO_4$ 0.1M
RDE-12	Powder 5	0.3	12	----	$HClO_4$ 0.1M
RDE-13		0.5	20	----	$HClO_4$ 0.1M
RDE-14		0.7	30	----	$HClO_4$ 0.1M
RDE-15		1	40	----	$HClO_4$ 0.1M
RDE-16		1.3	40	----	$HClO_4$ 0.1M
RDE-17		1.5	50	----	$HClO_4$ 0.1M
RDE-18	Powder 6	0.1	5	0.01	$HClO_4$ 0.1M
RDE-19		0.25	10	----	$HClO_4$ 0.1M
RDE-20		0.5	20	----	$HClO_4$ 0.1M
RDE-21		0.5	20	0.05	$HClO_4$ 0.1M
RDE-22		0.7	20	----	$HClO_4$ 0.1M
RDE-23		1	30	----	$HClO_4$ 0.1M
RDE-24		0.3	12	0.03	$HClO_4$ 0.1M
RDE-25		0.3	12	0.09	$HClO_4$ 0.1M
RDE-26		0.3	12	0.15	$HClO_4$ 0.1M
RDE-27	Powder 7	0.25	6	----	$HClO_4$ 0.1M
RDE-28		0.5	10	----	$HClO_4$ 0.1M
RDE-29		0.7	15	-----	$HClO_4$ 0.1M
RDE-30		1	20	----	$HClO_4$ 0.1M
RDE-31	Powder 8	0.3	10	----	$HClO_4$ 0.1M
RDE-32		0.5	6	----	$HClO_4$ 0.1M
RDE-33		0.7	10	----	$HClO_4$ 0.1M
RDE-34		1	10	----	$HClO_4$ 0.1M
RDE-35	Powder 12	0.5	6	----	$HClO_4$ 0.1M
RDE-36	Powder 13	0.5	6	----	$HClO_4$ 0.1M
RDE-37	Powder 14	0.5	6	----	$HClO_4$ 0.1M
RDE-38	Powder 15	0.5	6	----	$HClO_4$ 0.1M
RDE-39	Powder 16	0.5	6	----	$HClO_4$ 0.1M

Table 27: Composition of RDEs characterized toward ORR.

In order to compare the Pt/C (E-TEK), the amount of IrO_2-based powders deposited is indicated as metallic Ir loading (1 $mgcm^{-2}$ of Ir = 1.17 $mgcm^{-2}$ of IrO_2).

3.3.2-Support and diluents matrices characterizations

The glassy carbon support, SnO_2 and Vulcan® XC72R powders were characterized with the same experimental parameters used for the characterization of IrO_2-SnO_2 powders and composites in order to rule out their influence on the ORR.

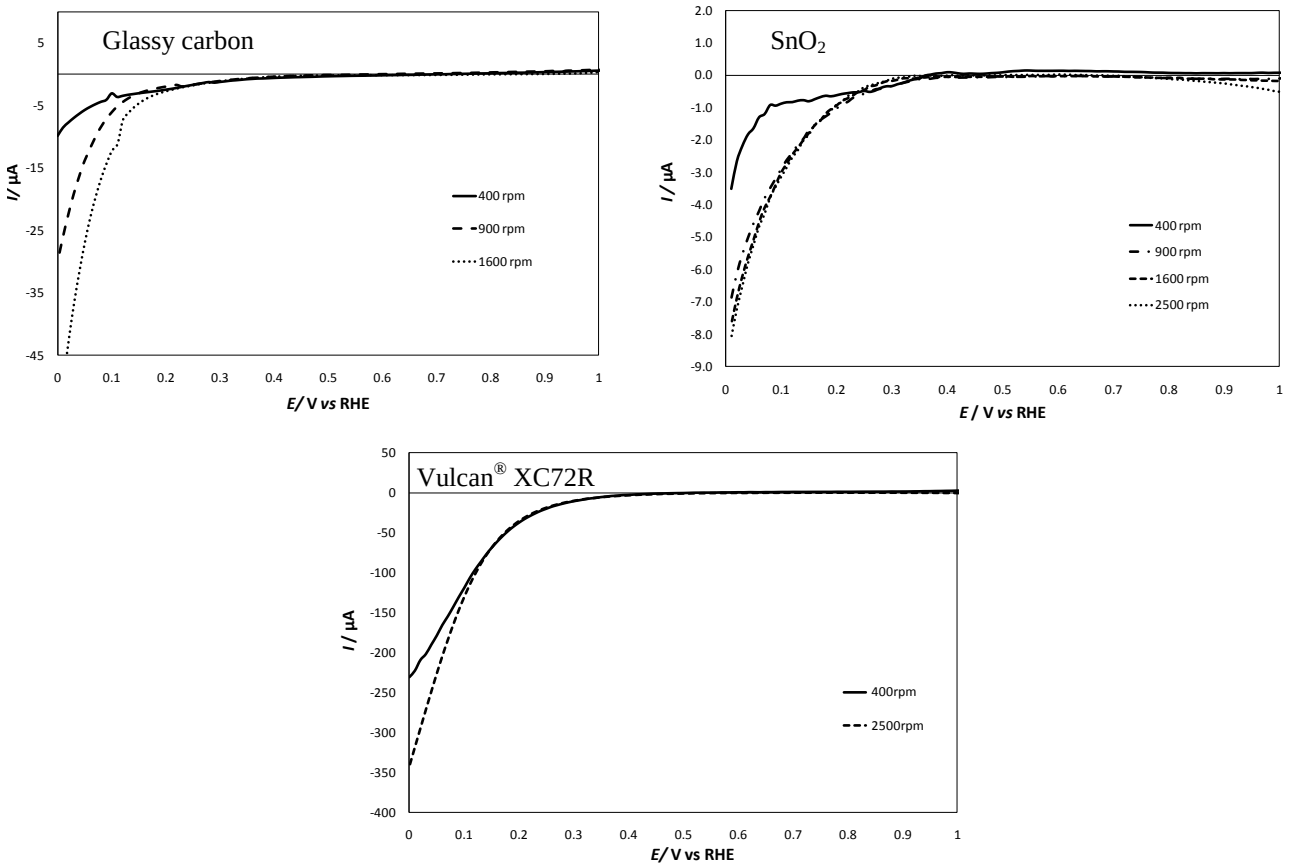

Figure 117: Polarization curves of support and diluent matrices. Background electrolyte: 0.1M $HClO_4$; scan rate 10 mV s^{-1}; rotating rate is evidenced in each graph.

At the less positive potentials the current increase is due to the ORR. On the tree materials, as is visible from the graph, the ORR potential (E_{ORR}) at which the oxygen reduction starts is less positive than the ones obtained in the presence of an electrocatalytic powder (≥0.5V vs RHE), thus indicating that SnO_2, glassy carbon and Vulcan® are inert toward the reaction under investigation. E_{ORR} values obtained from the polarization curves are reported in Table 28. The three materials considered present E_{ORR} significantly lower than the value obtained with Pt-based electrodes (~ 0.9V vs RHE).

Material	E_{ORR}/ V *vs* RHE
SnO_2	0.30
Glassy carbon	0.37
Vulcan XC72R	0.37

Table 28: E_{ORR} values for different material tested.

3.3.3-Pt/C (E-TEK)

The activity of Pt/C powders, already discussed in Section 3.1.3-II is also confirmed by considering the polarization curves (see Figure 118).

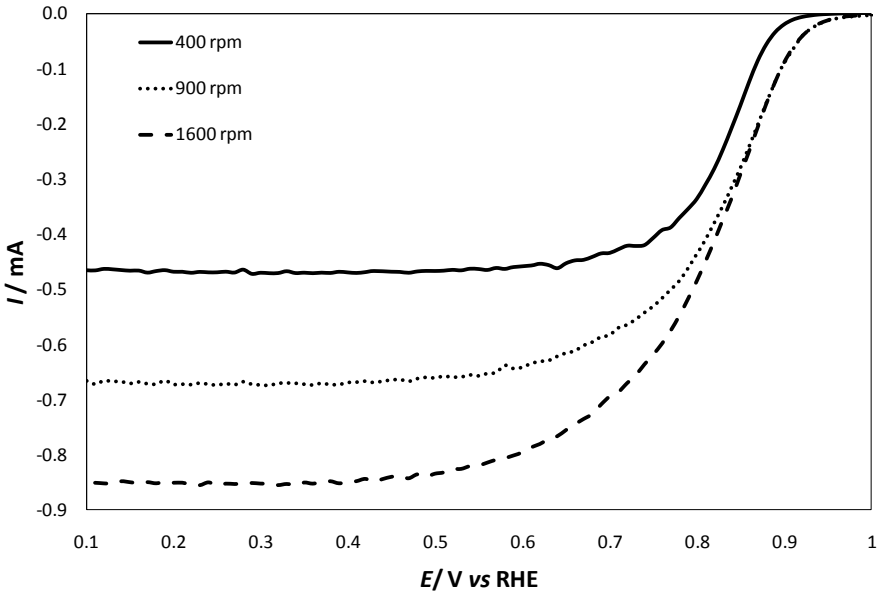

Figure 118: Polarization curves of RDE-3. Background electrolyte: 0.1M $HClO_4$; scan rate 10 mV s^{-1}; rotating rate is evidenced on the graph.

The presence of a plateau is observed and the plateau current increases at increasing rotation rate. As described in Section 2.2.5-IV the average value of this current is used in the Koutecký-Levich equation for extrapolating the kinetic current, whose values are reported below.

As the electrode preparation can be done with different amount of the suspension containing the same powder, a normalization procedure has been used to compare the different electrodes based on the same powder. To this end, the i_k/Q ratio is useful to evaluate the kinetic properties of the material under investigation, since it is independent on the amount of the material loaded on the support. Electrodes with different Pt loading were characterised and the effect on E_{ORR} and i_k/Q values is reported in the next figures.

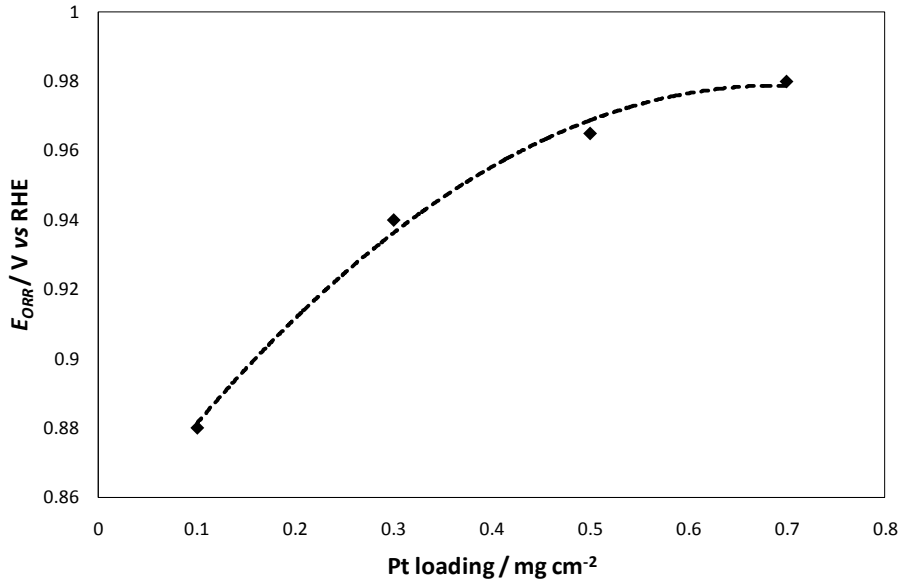

Figure 119: Effect of Pt loading on the E_{ORR}.

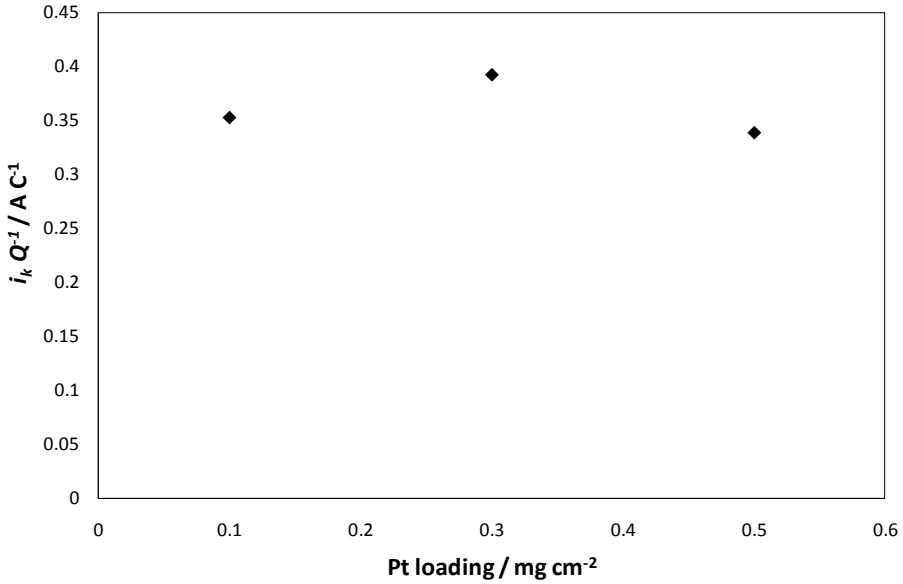

Figure 120: Effect of Pt loading on the normalized i_k values.

Increasing the Pt loading from 0.1 to 0.7 mg cm^{-1} shifts the E_{ORR} by 100mV toward more positive (that is favourable) values. The i_k/Q values (see Figure 120) are independent from the Pt loading until 0.5 mg cm^{-2}. For the highest metal loading (not shown in Figure 120) i_k/Q becomes negative, which has no physical meaning, and this could be correlated to the high Nafion® thickness necessary to avoid the powder detaching, when an higher Pt loading is used (40nm respect to 12nm).

The effect of Nafion® thickness at constant loading (0.5 mg cm^{-2}) was also evaluated. The results are reported in Figure 121.

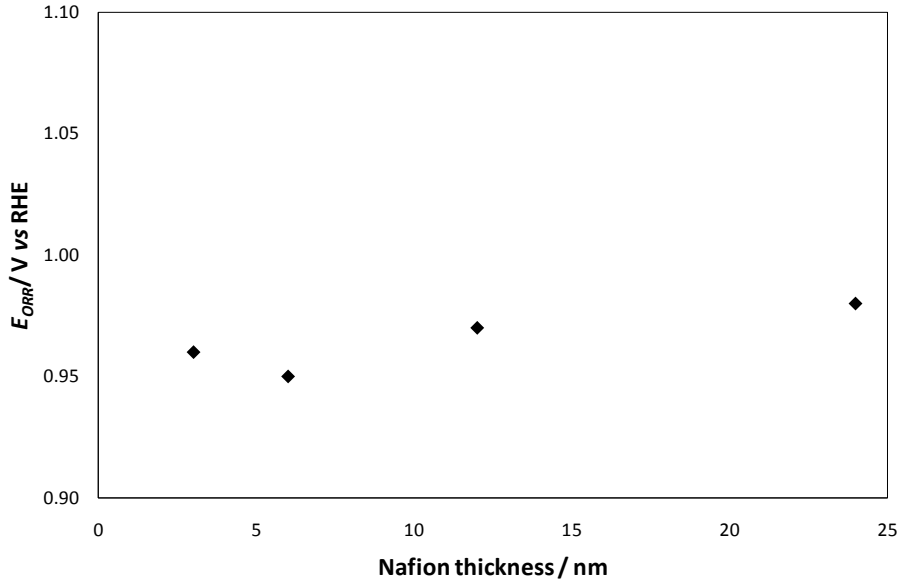

Figure 121: Effect of the Nafion® thickness on the E_{ORR} values.

E_{ORR} values are independent on the Nafion® thickness on the electrode and the average of the potential values is 0.97±0.01V *vs* RHE. On the basis of the kinetic currents the best composite performance was obtained in the case of a Nafion® thickness of ~12nm, which corresponds to a powder/Nafion® ratio = 0.03 mg/mg. It has to be reminded that Nafion® not only facilitates the powder adhesion on the support, but also promotes the proton conducting in the catalyst layer; nevertheless when its amount is high an increase of resistance contribution, due to the increase of electron transfer resistance, was verified.

3.3.4-IrO_2-based materials

In this paragraph the polarization curves obtained with powders synthesized by I and CS-Cl methods are presented and discussed. An evaluation of the role of synthesis method and of Ir loading on electrochemical behaviour can be drawn.

The results obtained with powder synthesized by I method are shown in Figure 122.

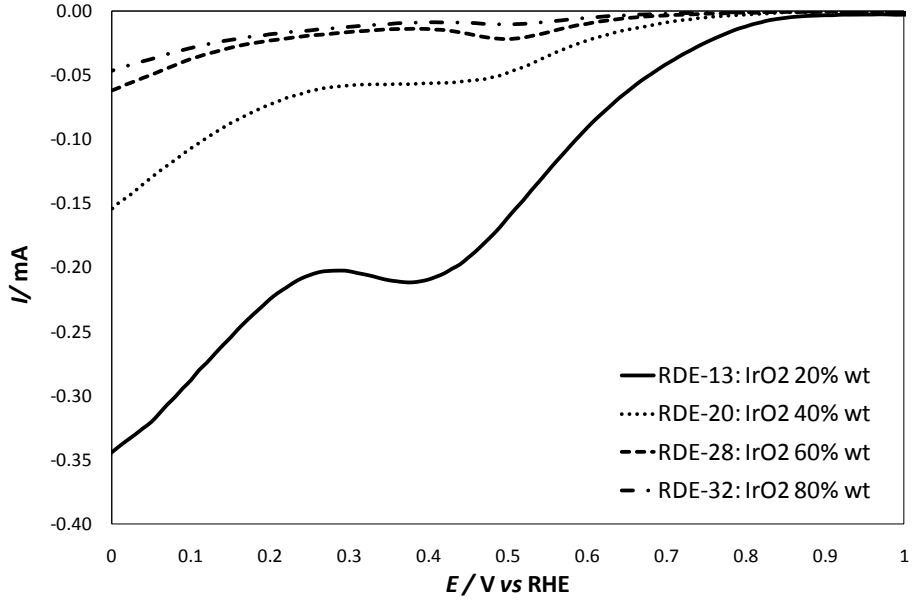

Figure 122: Polarization curves obtained with different IrO_2 content in the powder prepared by I method (0.5mg cm^{-2} Ir loading on the electrode). Background electrolyte: 0.1M $HClO_4$; scan rate 10 mV s^{-1}; rotating rate 2500 rpm.

Moving toward less positive potentials a progressive increase in current intensity, due to the ORR, is observed. Unlike the Pt/C powder, a plateau is not reached. This is probably due to a superimposition of different process due to the presence of SnO_2, which constitutes the diluent matrix in the sample. The semiconducting properties of the SnO_2 electrodes can give rise to the emptying/filling effect of the electronic traps within the band gap, with the subsequent current increase at the less positive potential, and this may lead to the lack of the plateau [12]. It has to be highlighted that, in terms of current intensity, the highest values was obtained using composite electrodes with the lowest IrO_2 content.

The effect of IrO_2 content in the powder on E_{ORR} is showed in the next figure.

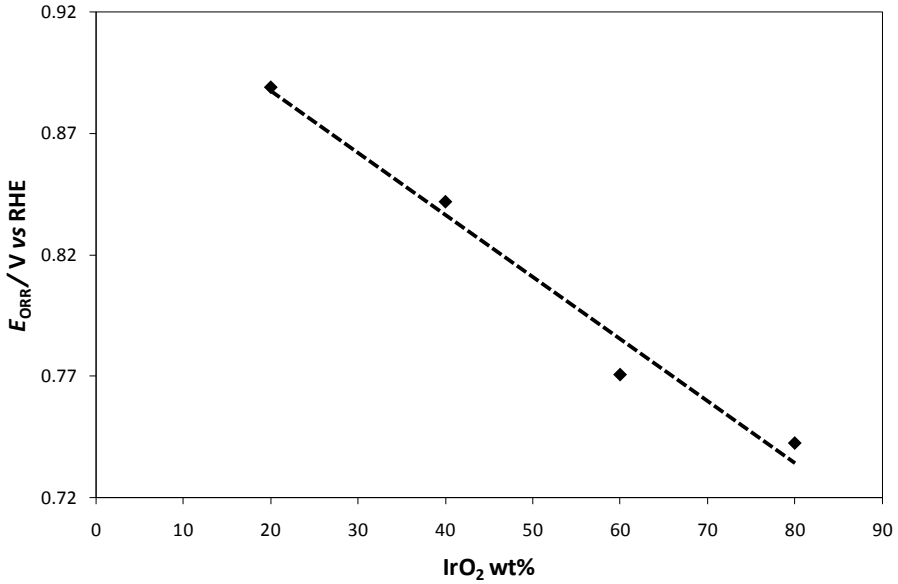

Figure 123: Variation of E_{ORR} with the IrO_2 content in the I powders.

A good linear correlation is observed (R^2=0.97). Increasing IrO_2 content the potential values shift toward less favourable conditions. This phenomenon is probably due to a synergistic effect of the diluents matrix (SnO_2) on the oxygen reduction mechanism.

For the determination of i_k values, in the absence of a plateau, the steady-state current in correspondence of the peak, in particular at the point of maximum current value, was used.

Figure 124 reports, as example, the variation of i_k/Q values obtained with electrodes having the same powder (powder n° 5) but with different Ir loading on the composite electrode.

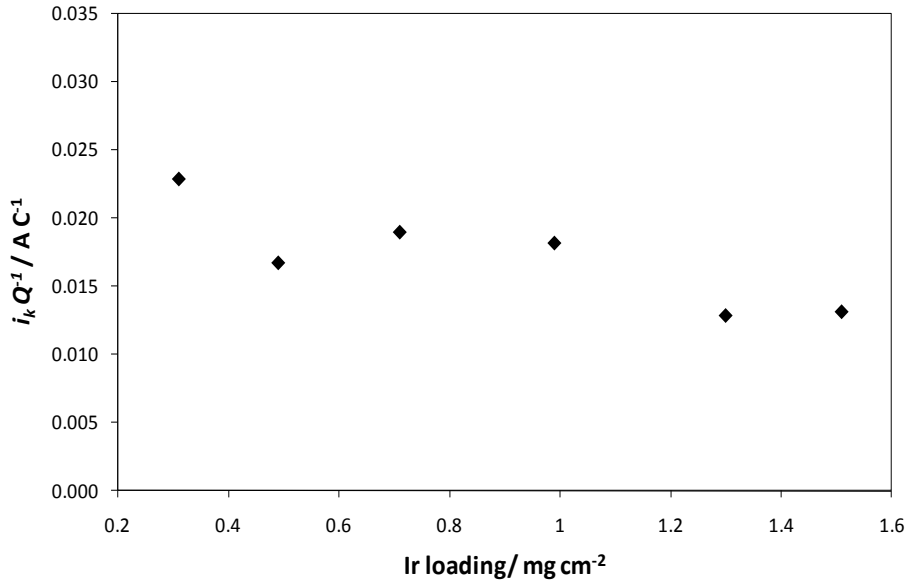

Figure 124: i_k/Q values obtained by characterization of powder n° 5 with different Ir loading on the electrode.

As can be seen, the kinetic current is substantially independent on the Ir loading (i_k/Q = 0.017±0.004 AC^{-1}), if the powder has the same composition.

The effect of the different IrO_2 content in the powder, and so the electrocatalytic effect of the metal amount on the reaction, is reported in Figure 125, in which four different powders, with different composition, are compared.

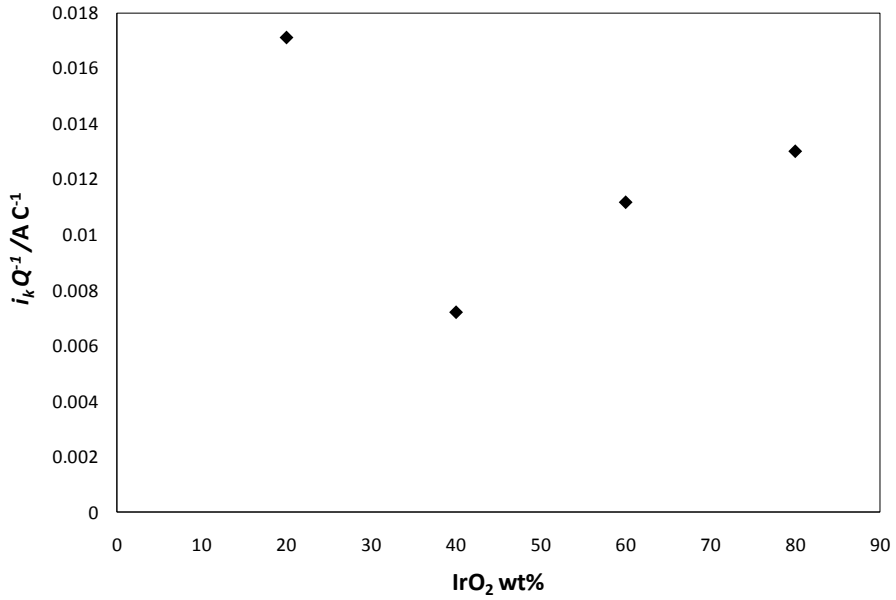

Figure 125: Dependence of i_k/Q values obtained varying the IrO_2 content in electrocatalytic materials synthesized by I method.

Powder having the lowest IrO_2 content (20wt%) presents the best behaviour. The increase of the IrO_2 content to 40wt% leads to a significant decrease of electrochemical performance, but a further IrO_2 enrichment leads to a progressive improvement of the electrocatalytic behaviour, probably due to a gradually increase of the IrO_2 influence on the electrocatalyst.

Figure 126 shows the polarization curves obtained with powders prepared by CS-Cl method.

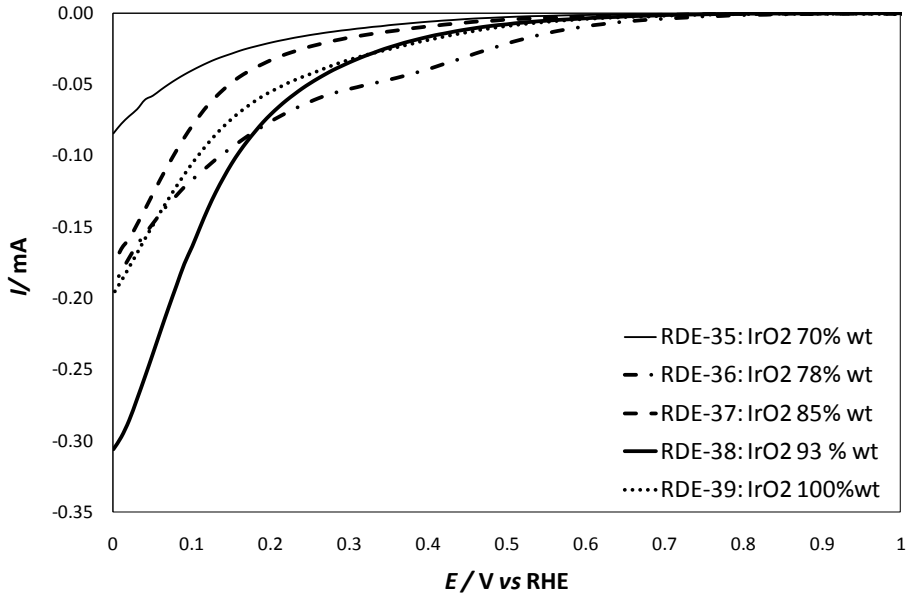

Figure 126: Polarization curves obtained with different IrO_2 content in the powder prepared by CS-Cl method (0.5mg cm^{-2} Ir loading on the electrode). Background electrolyte: 0.1M $HClO_4$; scan rate 10 mV s^{-1}; rotating rate 2500 rpm.

In the potential window above 0.2V the best performance is obtained with the powders having 78wt% IrO_2 content (RDE-36), since the highest current values are observed. For less positive potentials, below 0.2V, the highest polarization currents are obtained for the powder containing 93wt% of IrO_2 (RDE-38). The effect on E_{ORR} is reported Figure 127.

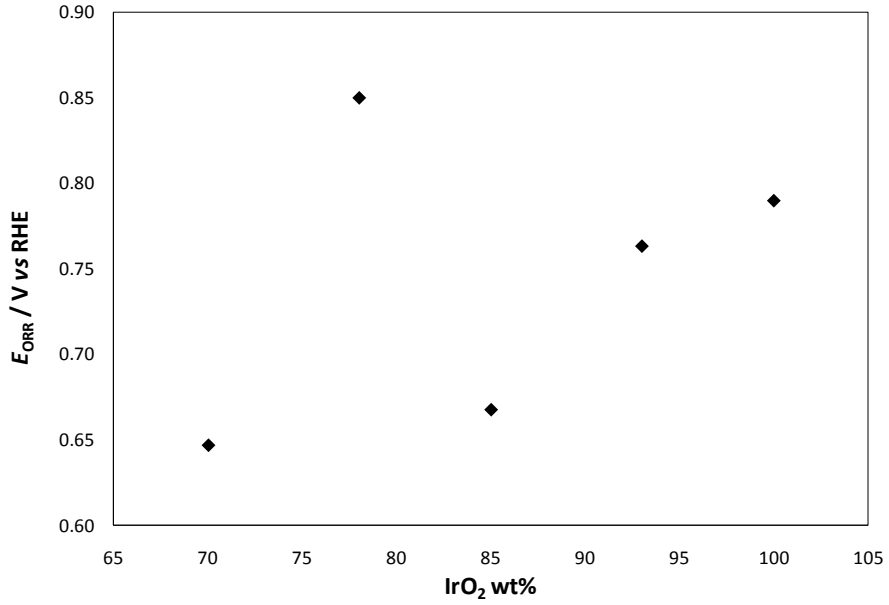

Figure 127: Variation of E_{ORR} values in function of IrO_2 content in the CS-Cl powders.

In term of ORR potential on-set the most favourable value is obtained for composite with IrO_2 content of 78wt%. Also in this case a gradual increase of the electrochemical performance at increasing IrO_2 content is observed.

Figure 128 shows the effect of the two synthesis method considered on the polarization curves.

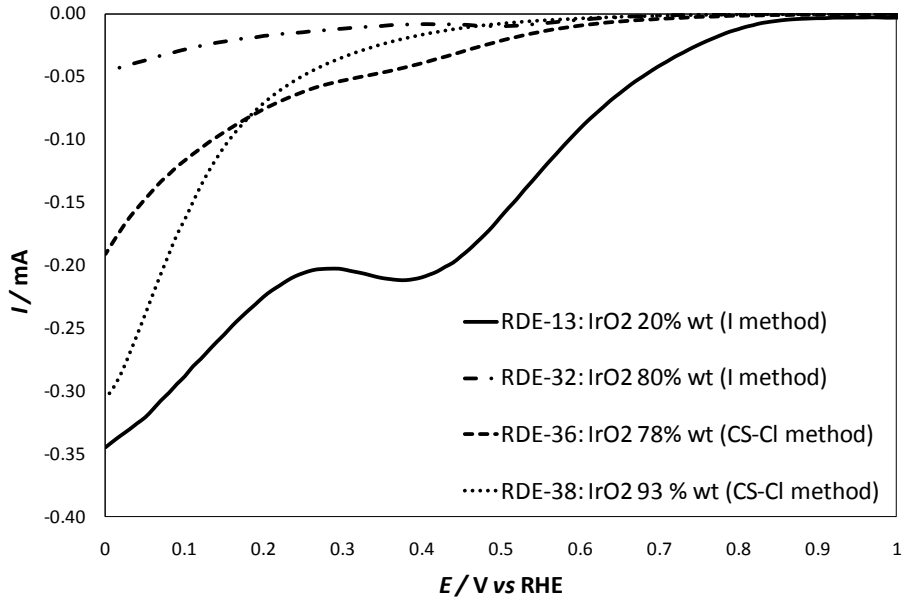

Figure 128: Polarization curves of powders synthesized by method I and CS-Cl method. Ir loading on the electrode: 0.5 mg cm^{-2}; background electrolyte: 0.1M $HClO_4$; scan rate: 10 mV s^{-1}; rotating rate: 2500 rpm.

The best performances were obtained with the powder synthesized by I method with the lowest IrO_2 content (20wt%). Considering powders having the same high IrO_2 content (~80wt%) but prepared following different synthesis routes, the powder prepared *via* CS-Cl method shown the best performances in spite of the highest calcination temperature (500°C respect to 450°C of I method). This confirms the CV results discussed in section 3.1.3-II. This is probably due to the larger surface area that the CS-Cl powder still presents after the calcination at 500°C in comparison with the I powders.

3.3.5-Effect of active carbon in the catalytic layer

The aim of this part of the work is to evaluate if active carbon (Vulcan® XC 72TR) added to the catalytic layer improves the electronic contact among the catalyst particles, thus improving the electrode performance. These studies were carried out considering electrodes prepared with the same Ir loading (powder n°6) but different Vulcan® content expressed as Ir/Vulcan® weight ratio Figure 129 shows the effect of the presence of Vulcan® in the composite electrode on the polarization curves.

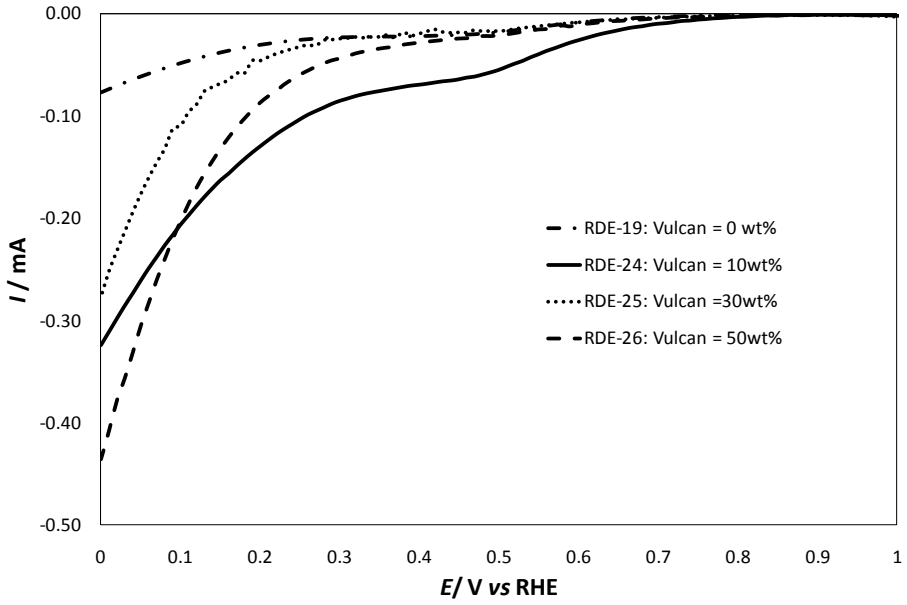

Figure 129: Effect of the Vulcan® loading on the polarization curves. Ir loading on the electrode: 0.3 mg cm^{-2} (powders n°6). Background electrolyte: 0.1 M $HClO_4$; scan rate: 10 mV s^{-1}; rotation rate 1600 rpm.

In the case of a RDE-24 (10wt% of Vulcan®) a significant increase of the polarization currents is observed in the ORR region. This result is in line with the CVs measurements reported in Section 3.1.3-II. RDE-26 shows highest cathodic current only at very low potentials in the region of the full

ORR. The better performance of RDE-24 is also confirmed i_k/Q values (Figure 131) and, to a less extent, by E_{ORR} values (Figure 130).

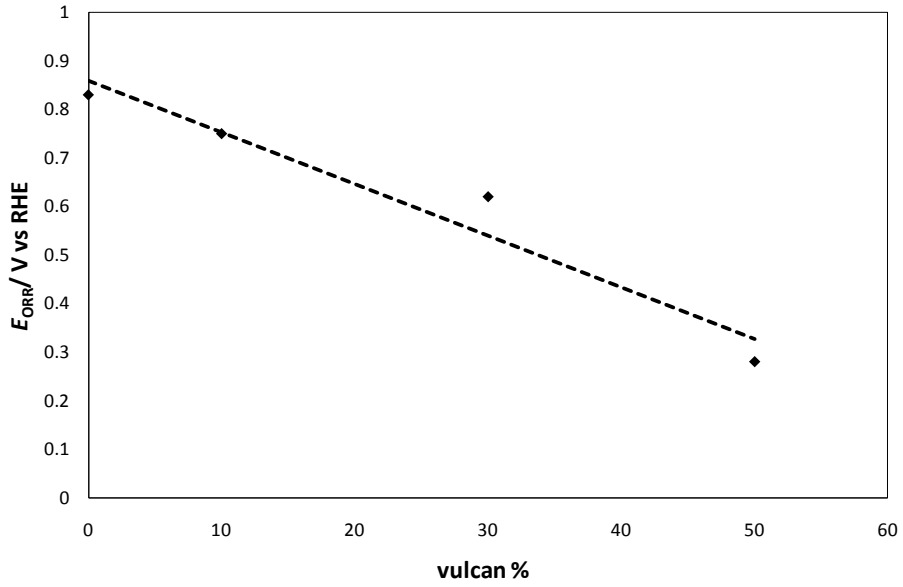

Figure 130: Effect of the Vulcan® loading on E_{ORR} values.

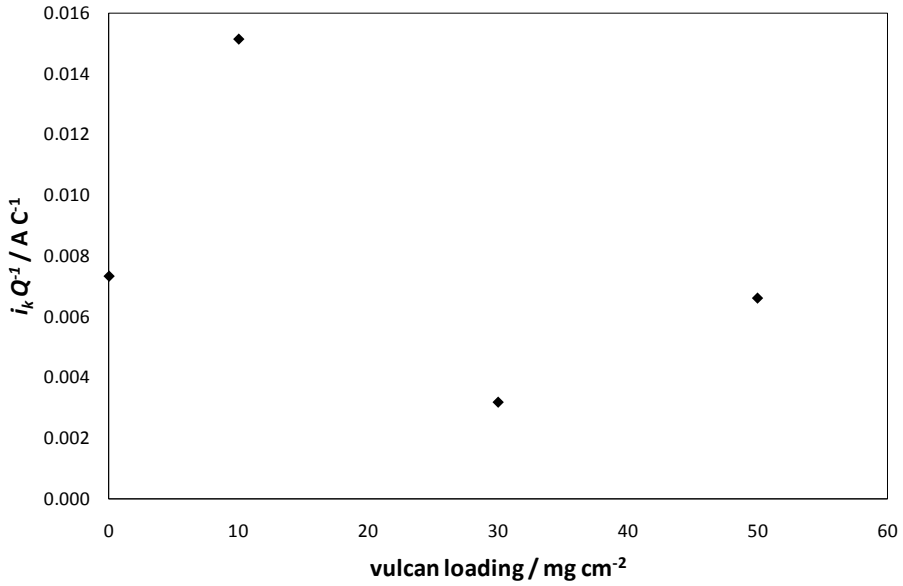

Figure 131: Effect of the Vulcan® loading on i_k/Q values.

RDE-24 presents the highest kinetic current, i_k/Q. Although the E_{ORR} decays with increasing Vulcan® loading, the shift toward less favourable values is more evident between 30% and 50% Vulcan®, thus substantiating that only a minimal Vulcan® amount is beneficial. Note that RDE-26 (50wt%) exhibits a potential value (0.3V *vs* RHE) identical to the one obtained with the bare

Vulcan® (see Section 3.3.2). Therefore 10%wt Vulcan® was used to prepare electrodes with different Ir loading on the electrode to verify a possible further improvement in the electrocatalytic properties of the material. Figure 132 shows the corresponding polarization curves.

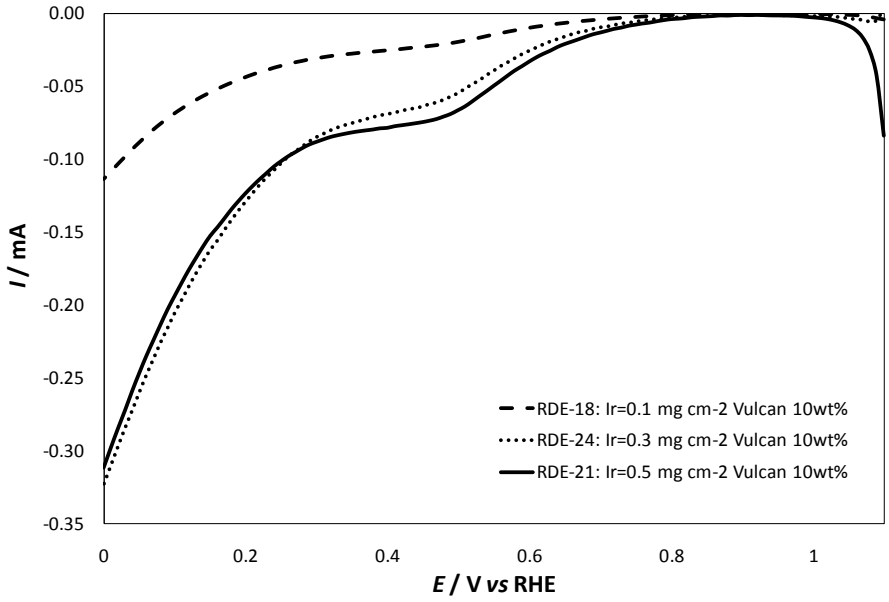

Figure 132: Effect of the Ir loading increase (Vulcan® loading 10wt%) on polarization curves. Background electrolyte: 0.1M $HClO_4$; scan rate 10 mV s^{-1}; rotating rate: 1600 rpm.

An increase of Ir loading above 0.3 mg cm^{-2} does not lead to any significant improvement of performances. This effect is more evident in CV measurements as the potential window is reduced between 0.4-1.4V (see Section 3.1.3-II). The results obtained allow affirming that electrodes prepared with 0.3 mg cm^{-2} of Ir and 10wt% of Vulcan® present the best performances. Since the carbon can easily degrade to CO_2 in presence of O_2, a test in order to verify the stability of the electrode was carried out. Different polarization curves were recorded consecutively (see Figure 133).

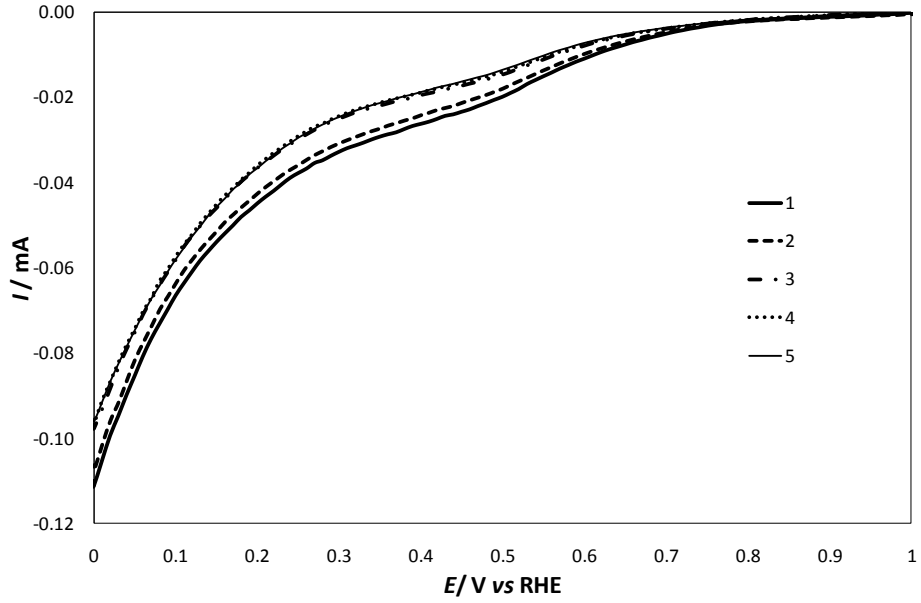

Figure 133: Consecutive polarization curves recorded on RDE-18. Ir loading on the electrode: 0.1 mg cm^{-2}; Vulcan® loading: 10wt%; background electrolyte: 0.1M $HClO_4$, scan rate: 10 mV s^{-1}; rotation rate 400 rpm.

It is clearly visible a small degradation of the performances after the second polarization curve, probably due to the degradation of the matrix; in any case, starting from the third cycle, the electrode behaviour remains constant with no further loss of activity.

3.3.6-Comparison of the tested electrocatalytic materials

In the next table E_{ORR} and normalized i_k values, obtained for the diluent matrices, the glassy carbon support and the most representative electrocatalytic materials characterized are reported.

N°RDE	Composition	E_{ORR}/ V *vs* RHE	$i_k Q^{-1}$ (A C^{-1})
RDE-9	SnO_2	0.30	----
RDE-10	Vulcan®	0.37	----
RDE-11	RDE glassy carbon	0.37	----
RDE-7	Pt/C Pt= 0.5 mg cm-2 Nafion=12 µm	0.97	0.34
RDE-13	Powder 5 Ir=0.5 mg cm-2 Nafion=20 µm	0.88	0.02
RDE-12	Powder 5 Ir=0.3 mg cm-2 Nafion=10 µm	0.89	0.02
RDE-19	Powder 6 Ir=0.3 mg cm-2 Nafion= 10 µm	0.83	0.01
RDE-24	Powder 6 Ir=0.3 mg cm-2 Nafion= 10µm Vulcan 10wt%	0.75	0.02

Table 29: E_{ORR} and i_k/Q values obtained with different compositions.

The support electrode and the diluent matrices are inert toward ORR as can be inferred from the E_{ORR} values, which are significantly lower than the other ones. Moreover, an evaluation of the kinetic current has not been carried out for these materials since the well known plateau, between 0.3-0.5V, is not visible in the polarization curves.

The Pt/C powder presents the best performance: most favourable E_{ORR} and i_k/Q values were obtained. It has to be underlined that Pt/C powder shows the highest surface area detected with BET technique ($160 m^2/g$). Even if the i_k were normalized, this high surface (which is 2-3 times higher than the IrO_2-based powders) can have synergistic effect on ORR. The IrO_2-based materials that show the best performance are: RDE-12, RDE-13 and RDE-24, even if they present kinetic current significantly lower than Pt/C.

Comparing the RDE-19 and RDE-24 it is possible to note the benefice effect of the Vulcan® loading in the catalytic layer. An evident doubling of i_k/Q values is obtained and only a slight E_{ORR} decrease is visible; this improvement is correlated to a better electric contact among electrocatalyst particles.

Considering these preliminary results and remembering that an optimization of the synthesis procedure has still to be carried out, it is possible to affirm that the IrO_2-based materials are very promising electrocatalysts in view of their application in URFC.

3.3.7-Conclusions

The activity of different IrO_2-based materials was investigated toward ORR. These materials are possible candidate for application in URFC due to their good behaviour for OER (see Section 3.2).

In order to evaluate the kinetic activity of the tested materials, the electrochemical characterization was carried out recording polarization curves with a Rotating Disk Electrode. In particular, electrodes having different composition were tested in order to evaluate the effect of:

- Nafion® loading;
- synthesis methods;
- Ir loading;
- Vulcan® loading.

The Nafion® improves the proton conduction in the catalytic layer, but high amounts introduce an electric resistance contribution which leads to a worsening of the electrochemical behaviour. The optimum Nafion® thickness values is 12 nm, which corresponds to a powder/Nafion® ratio of 0.03 mg/mg.

Powders synthesised by I method present, as already verified in Sections 3.1 and 3.2, the best performance. In particular powder n°5, having the lowest IrO_2 content, shown the best electrochemical response since the most promising E_{ORR} and i_k/Q values were obtained. This could seem a surprising results, due to the low IrO_2 loading, but it can be explained by XPS outcomes which show a significant enrichment of Ir species on the nanoparticle surface, due to the synthesis procedure. Increasing IrO_2 loading in the composite electrode a progressive decrease of electrochemical performance, correlated to a decrease of the active surface, was verified.

In any case, the CS-Cl method was revealed a more suitable synthesis method for high IrO_2 content.

A further improvement in the electrocatalytic behaviour can be obtained introducing a small Vulcan® amount in the catalytic layer. Vulcan® presents a high electronic conductivity therefore reduces the electric contact resistance among the electrocatalyst particles. The presence of carbon matrix, in fact, allowed obtaining a significant enhancement in the kinetic current (*ca* the double) and only a slight decrease in the potential values at which the oxygen reduction reaction starts.

The promising behaviour of these electrocatalysts toward ORR prompts further investigations, and their extension to other mixed oxide systems.

3.3.8-References

[1] Mitlitsky F, Myers B, Weisberg AH. *Energy Fuels* **1998**,12, 56.

[2] Smith W. *J. Power Sources* **2000**, 86, 74.

[3] Ioroi T, Kitazawa N, Yasuda K, Yamamoto Y, Takenaka H. *J. Electrochem. Soc*. **2000**;147, 6, 2018.

[4] Ioroi T, Kitazawa N, Yasuda K, Yamamoto Y, Takenaka H. *J. Appl. Electrochem*.**2001**, 31, 1179.

[5] Ioroi T,Yasuda K, Siroma Z, Fujiwara N, MiyazakiY. *J. Power Sources* **2002**, 112, 583.

[6] Chen G, Delafuente DA, Sarangapani S, Mallouk TE. *Catal Today* **2001**, 67, 341.

[7] Chen G, Bare SR, Mallouk TE. *J. Electrochem. Soc*. **2002**, 149, 8, A1092.

[8] Zhigang S, Baolian Y, Ming H. *J. Power Sources* **1999**, 79, 82.

[9] A. Minguzzi, M. A. Alpuche-Aviles, J. R. López, S. Rondinini, and A. J. Bard *Anal. Chem.* **2008,** 80, 4055.

[10] Takenaka, E. Torikai, Y. Kawami, and N. Wakabayashi. Int. J. Hydrogen Energy, 1982, 7, 397. T.

[11] J. Schmidt, H.A.Gasteiger *"Handbook of fuel cell-Fundamentals technology and applications"* Wolf Vielstich **2003** chapter 22.

[12] Silvia Ardizzone, Giuseppe Cappelletti, Mariana Ionita, Alessandro Minguzzi, Sandra Rondinini, Alberto Vertova Electrochimica Acta 2005, 50, 4419.

PART-2: DEVELOPMENT OF ELECTROCATALYSTS FOR VOH ELECTROREDUCTION

3.4- Investigation of silver-based electrodes for trichloromethane electroreduction.

3.4.1-Introduction

Volatile organic halides (VOH) are a large family of substances, among which the more ubiquitous compounds are chlorinated solvents like CH_2Cl_2 (pharmaceuticals, chemical processing, aerosols, etc.), $CHCl_3$, CCl_4, $Cl_2C=CCl_2$ (dry and metal cleaning), and $Cl_2C=CHCl$ (metal cleaning and specialty adhesives). Notwithstanding their relatively short atmospheric life-time [1] (*e.g.* 6–8 days for trichloroethylene and 5–6 months for tetrachloroethylene and dichloromethane), their toxicity together with the wide spectrum of waste types (from concentrated organic solutions/emulsions to very dilute aqueous phases, to airborne streams) constitute serious challenges in developing suitable treatment methodologies. Despite the several biological and physico-chemical methods proposed so far, none of them is free from some significant drawback, *e.g.* formation of undesirable by-products, excess of reagent, exhaustion of absorbing substrates, which require additional treatment steps. On account on their higher selectivity, milder reaction conditions and simpler process design and operation, electrochemical methods can play a key role in environmental protection and remediation. Although electrooxidative processes are more attractive, because they may lead to the complete mineralization of the substrate, and have been therefore more studied [2], their application to VOH degradation may produce undesired chlorinated compounds possibly even more toxic than the treated substrates. On the other hand, the electroreductive route, leading to hydrodehalogenated derivatives (*e.g.* CH_4, C_2H_6, C_2H_4), represents a convenient way of waste detoxification, provided that the dehalogenation is exhaustive. In this context the highly electrocatalytic properties of silver extensively demonstrated towards organic halide electroreductions [3]-[8] have been successfully applied to VOH degradations [9][10]. In particular the electroreduction of $CHCl_3$ in non-aqueous and aqueous media has been shown to give CH_4 as main product [9][10].

This remarkable behaviour of silver allows the development of low specific energy consumption processes, thanks to the concomitant reduction of cell voltage and increase in current efficiency and substrate conversion. It is assumed to be linked with the well-known specific interactions of silver

with halide anions [11]-[14], which, in turn, are governed by the Ag surface state and its modifications in dependence on the composition of the reaction medium (*i.e.* the halide leaving group, the structure of the organic moiety, the solvent and the supporting electrolyte). In particular, the electrocatalytic activity of silver was reported to increase with increasing surface roughness [15][16], thus prompting the research toward the development of micro- and nano-sized electrode materials, whose properties usually encompass the simple geometric effect on the real surface area.
Together with the accumulation of additional evidence of Ag electrocatalytic activity towards selected substrates of synthetic or environmental relevance [17], the research interests are now focusing on the preparation methodologies of the electrode material, both to improve the catalyst performance and reduce the silver content.
Although most of the reported applications are performed on massive Ag electrodes, there is evidence [18][19] that micro and nanostructured particles may exhibit similar or even better behaviour than massive silver, while allowing a substantial reduction of Ag loading. Moreover, as evidenced by [20] the Ag nanoparticle size deeply affects the dissociation of gaseous $CHCl_3$ on silver. In fact, this surface reaction shifts from weak on bulk Ag(111) to strong on 20–50 nm Ag particles, and medium Ag coverage, suggesting that the process is controlled by the number of surface defect sites.
In the present thesis three different Ag-based materials were characterized:

- silver electrodeposited on Pt disk (diameter 3mm) and on Pt wire (0.5mm diameter, 1 cm length);
- silver micro-sized powder commercially available;
- in home silver nanoparticles powders.

Silver electrodeposited electrodes were obtained using both $KAg(CN)_2$ and $AgNO_3$ baths. The principal electrodes characteristics are summarised in the Table 30.

Electrode name	Support	Bath	j_{app} (mA cm^{-2})	Electrodeposition time	Deposited thin (μm)
$AgNO_3$-high	Pt disk	$AgNO_3$ 0.1M	5	18 min	0.6
AgCN-high	Pt disk	$KAg(CN)_2$ 0.05M	5	18 min	0.6
AgCN-low	Pt wire	$KAg(CN)_2$ 0.05M	0.5	18 hours	20

Table 30: List of electrodeposition conditions of silver and respectively supports.

More detailed information about the electrodeposition procedure is reported in Section 2.2.5-V *"Electrode preparation"*.

Although it is well known that the silver deposit grown from silver nitrate bath tends to be dendritic, the replacement of the cyanide bath was prompted by both environmental considerations and the need of avoiding any cyanide contamination in the final deposit. In fact, studies on electrodeposited gold from cyanide baths showed that the cyanide can be inglobed within the deposit [21], and work is in progress to confirm possible similarities in the silver deposits. In the following, the electrochemical behaviour in non aqueous solution of silver electrodes electrodeposited at high current density, 5mA/cm^2, and of Ag-micro powder electrode will be compared to silver electrodes electrodeposited at low current density, 0.5mA/cm^2 [9][10].

Micro-sized silver powder commercially available was also characterized in order to obtain a comparison with silver electrodes.

Silver nanoparticles powders were synthesised by chemical-reduction method as describe in Section 2.1.2. The particle size, size distribution (polydispersity) as well as the stability of the system can also be modified by additional components such as surfactants (surface-active molecules) or polymers [22]-[24]. Novel pale-yellow silver sols, Ag_NP(0–5), composed by Ag(0) nanoparticles have been obtained by reduction of an $AgNO_3$ aqueous solution, under N_2 atmosphere, with $NaBH_4$ in the presence of six different ligands, acting as stabilisers reported in Table 31.

Compound	Ligand	Chemical formula
Ag_NP0	L(+)-glutamic acid M = 147 kg kmol^{-1}	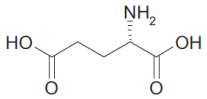
Ag_NP1	PVA Poly(vinyl alcohol) M = 13,000–23,000 kg kmol^{-1}	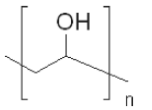
Ag_NP2	Igepal® CO-720 (branched) α-(nonylphenyl)-ω-hydroxypolyoxyethylene $M \approx$ 749 kg kmol^{-1} n ≈ 12	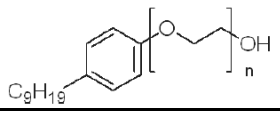
Ag_NP3	Brij 35® α -Dodecyl- ω-hydroxypolyoxyethylene $M \approx$ 1198 kg kmol^{-1} n ≥ 23	$CH_3(CH_2)_{10}CH_2(OCH_2CH_2)_nOH$
Ag_NP4	PEG-BDE Polyethyleneglycol bisphenol A epichlorohydrin copolymer M = 7000–9000 kg kmol^{-1}	$[C_{15}H_{16}O_2{\cdot}C_3H_5ClO{\cdot}(C_2H_4O)_n{\cdot}H_2O]_x$
Ag_NP5	PEG Poliethylene glycol $M \approx$ 200 kg kmol^{-1} n ≈ 4	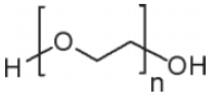

Table 31: Stabiliser compounds selected for the synthesis of silver nanoparticles. The numbering is used in the text to denote the corresponding Ag(0–5)/Vulcan®XC72R composite.

The electrochemical characterization by cyclic voltammetry were carried out supporting the powder materials by means of cavity micro-electrode (C-ME) a device especially developed for electrochemical studies of disperse systems (see Section 2.2.5-I). C-ME's are greatly attractive because of their low impact on the supported materials (neither special manipulations nor sticking agents are required) and of the offered possibility of quick and reliable renovation of the electrode surface by a rather simple operation of emptying-and-reloading with fresh material.

In particular the voltammetric investigations were carried out in two types of media: non aqueous and aqueous. The study of behaviour in aqueous solution is necessary since the relevance application of these materials in the detoxification of water.

A first study was carried out in organic solvent (acetonitrile containing tetraethylammonium tetrafluoborate 0.1 M, TEATFB, Aldrich ≥99.8%), in order to characterize, in the presence of the organic halide, the electrodeposited silver prepared using different electrolytic bath: $KAg(CN)_2$ and $AgNO_3$. CVs between -0.5 and -2.8 V *vs* SCE at scan rates between 100 and 5000 mV s^{-1} were recorded.

Commercially available silver micro-sized powder was also tested in the same organic solvent (acetonitrile) in order to compare the electrochemical behaviour, at the presence of the same organic

halide ($CHCl_3$), of the different Ag deposits and to determine the best electrodeposition parameters to obtain an active electrocatalyst.

The silver micro-sized powder was also characterized in aqueous solution ($KClO_4$, Fluka, 0.1 M in water) in the presence of the same organic halide ($CHCl_3$), and was compared with the silver nanoparticles prepared with chemical-reduction method. More detailed information about the experimental condition was reported in Section 2.2.5-I and 2.2.5-V.

A structural and morphological analysis silver nanoparticles powders were also characterised by UV-Vis, TEM, SEM and XRPD techniques.

3.4.2- Results of Ag electrocatalysts in non aqueous media

(I) Electrodeposited silver

In Figure 134 a comparison among Ag_CN_high and Ag_NO3_high (respectively obtained by electrodeposition at 5 mA cm^{-2} from cyanide and nitrate baths for 18 minutes) and on Ag_CN_low (obtained at 0.5 mA cm^{-2} from cyanide bath for 18 hours) is shown. In the case of Ag_NO3_high and Ag_CN_high the trichloromethane concentration is 1.3 mM, while in the case of Ag_CN_low the trichloromethane concentration is 2 mM. The CVs, recorded at the same scanning rate (500 mV s^{-1}), for sake of comparison were rescaled.

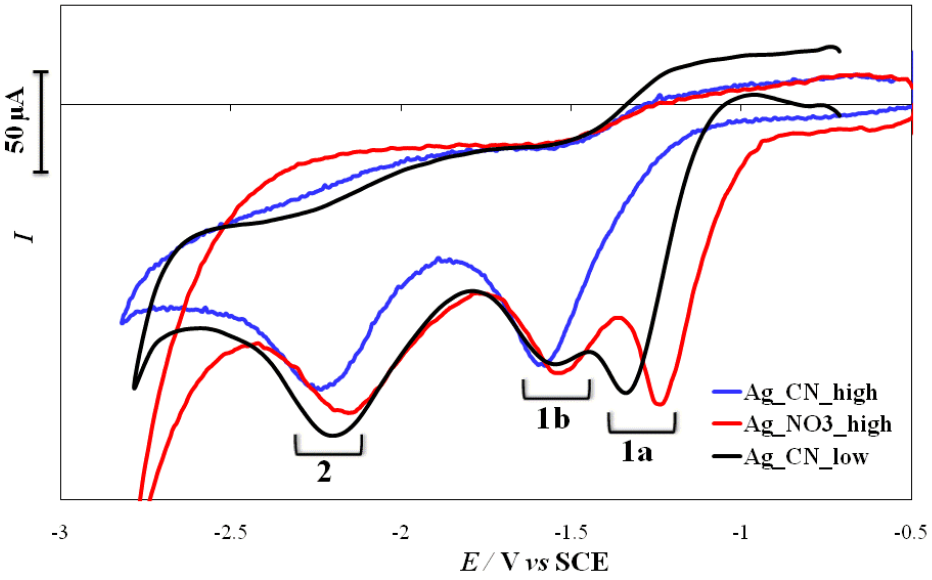

Figure 134: CV characteristics (1st cycle) on Pt electrode coated with Ag electrolytic deposit, in TEATFB 0.1 M in CH_3CN, scan rate = 500 mV s^{-1}: Ag_CN_high (blue line), c_{CHCl3} = 1.3 mM; Ag_NO3_high (red line), c_{CHCl3} = 1.3 mM; (c) Ag_CN_low (black line), c_{CHCl3} = 2mM.

Up to three peaks are observed, grouped in the -1.2/- 1.6V (group 1 in Figure 134) and in the -2.1/-2.3V (group 2 in Figure 134) ranges. The two groups are reasonably assigned to consecutive reactions, namely from $CHCl_3$ to CH_2Cl_2 and from CH_2Cl_2 to CH_3Cl, respectively, while the differences in peak number and position within each group highlight the critical role played by the silver surface and specifically interacting anions. In particular, curves red and black show one peak (indicated as 1a in Figure 134) at -1.2 and -1.3V, respectively, which is absent in curve blue. These features are further modified in the subsequent cycles, the more evident change being the disappearance of peak 1a in all CVs. This peak is linked with the most active silver surface sites which are easily saturated by competing adsorbing species like the leaving chlorides, possible reaction intermediates and/or residual cyanides [15].

For example, the adsorption of cyanides on the same $CHCl_3$ reacting sites could account for the striking difference in the behaviour of Ag_CN_high and Ag_CN_low (compare curves blue and black).

To demonstrate the presence of reaction sites having different electrocatalytic activity, the substrate concentration was progressively reduced. The evolution of CVs (first cycle) with $CHCl_3$ concentration on Ag_CN_high is shown in Figure 135.

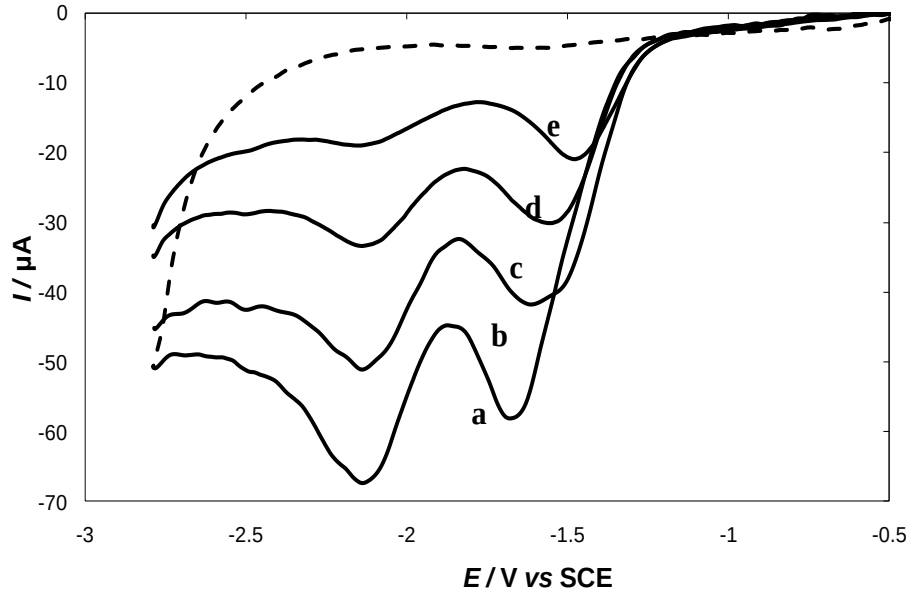

Figure 135: CV characteristics (1st cycle) of Ag_CN_high, in TEATFB 0.1 M in CH_3CN, scan rate = 100 mV s^{-1}, containing $CHCl_3$ at (a) 1.3 mM, (b) 1 mM, (c) 0.67 mM, (d) 0.33 mM. Line (e) represents background electrolyte. The reverse scan has been omitted for the sake of clarity.

All curves have two peak regions 1b and 2. For intermediate concentrations (0.67 and 1 mM), the peak 1b splits into two components at -1.5 and -1.7V. This phenomenon is even more evident in the subsequent cycles, as in the case of Figure 136 for the 0.67 mM $CHCl_3$ in the solution.

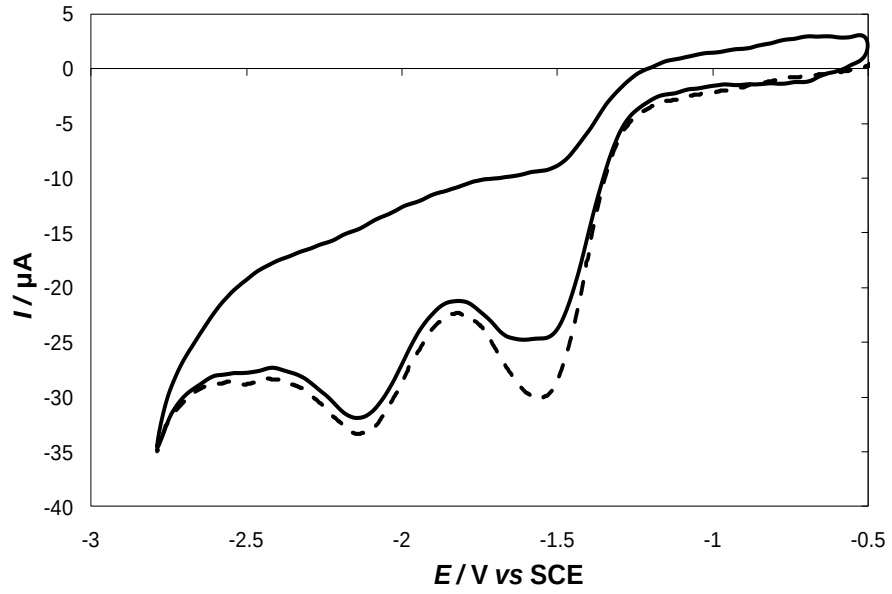

Figure 136: CV characteristics of Ag_CN_high, in TEATFB 0.1 M in CH_3CN, scan rate = 100 mV s^{-1}, containing 0.67 mM $CHCl_3$. First cycle (dashed line) and "steady-state" cycle (solid line).

At the lowest concentration (c_{CHCl3} = 0.33 mM), only the component at -1.5V is observed whereas at the highest concentration (c_{CHCl3} = 1.3 mM) only the component at -1.7V is visible.

The presence of a less negative peak at lower concentrations is consistent with the weak adsorption of reaction products/intermediates. The potential of the peak at around -2.1V is almost independent on $CHCl_3$ concentration. When considering the CV characteristics recorded on Ag_NO3_high (see Figure 137, 1st cycle) the three peaks 1a, 1b and 2 are observed for all $CHCl_3$ concentrations.

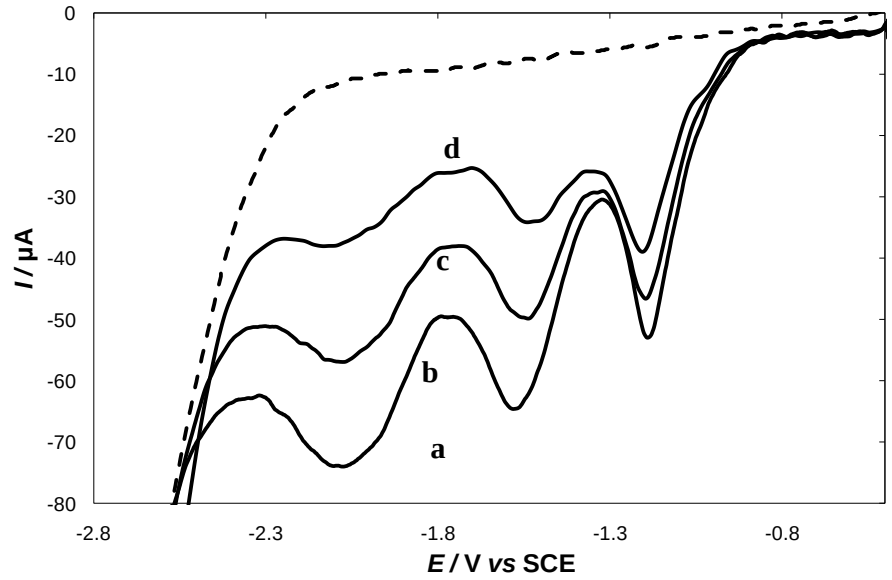

Figure 137: CV characteristics (1st cycle) of Ag_NO3_high, in TEATFB 0.1 M in CH_3CN, scan rate = 100 mV s^{-1}, containing $CHCl_3$ at (a) 1.3 mM, (b) 1 mM, (c) 0.67 mM. Line (d) represents background electrolyte. The reverse scan has been omitted for the sake of clarity.

All the peak currents vary linearly with substrate concentration. Beside the analytical implications, this represents an indirect proof of the stability of the deposit, which, due to the short deposition time, is far from being dendritic (see Figure 138), but rather appears as formed of compact and dispersed grains the sizes of which are between 10 and 30 µm.

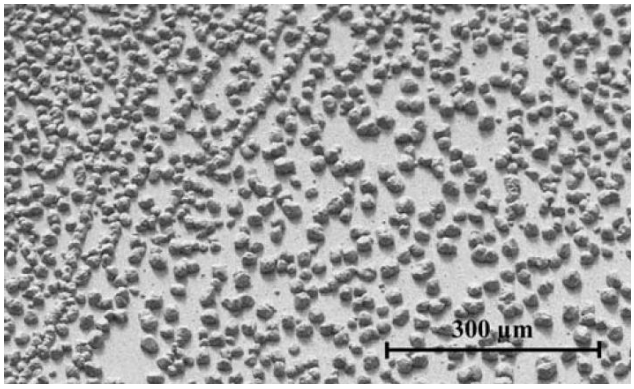

Figure 138: SEM image of the Ag_NO3_high electrode.

In terms of potentials, peak 1a is independent of concentration, while, again, peak 1b shifts and broadens as for the case of Ag_CN_high. Moreover, peak 1a disappears in the subsequent cycles and also in the case of consecutive recordings, unless the electrode is allowed to rest in the solution at open circuit potential, possibly denoting slow depoisoning of the silver surface. Figure 139 collects the curves obtained on the same electrode at first use and recorded immediately after.

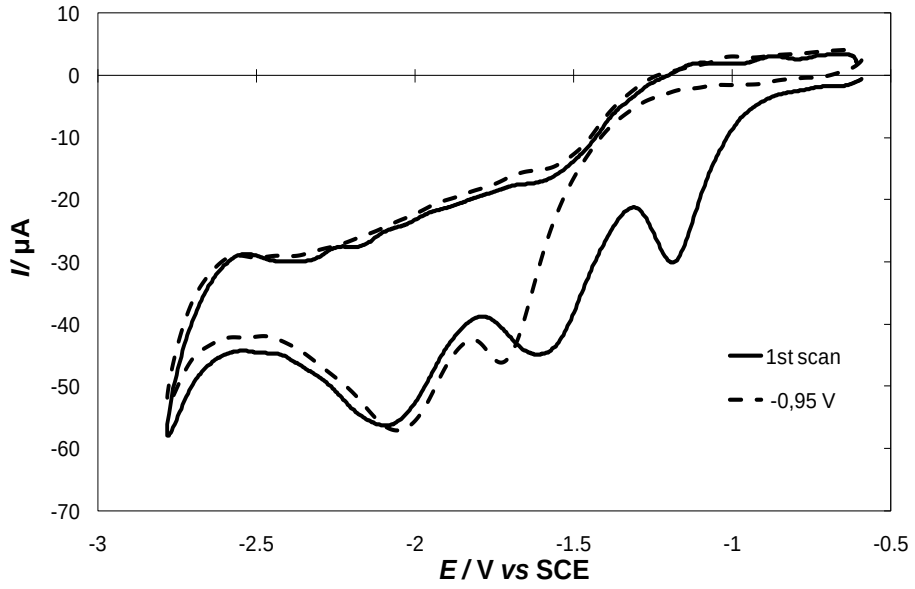

Figure 139: CV characteristics of Ag_NO3_high, in TEATFB 0.1 M in CH_3CN, scan rate = 100 mVs^{-1}, containing 2.5 mM $CHCl_3$. (a) First scan (solid line) after $CHCl_3$ addition (b) subsequent scans (dashed line).

In the case of curve (b) (for which an OCP value of -0.95V is observed), only the more negative component of peak 1b is still present showing that the reaction occurs through a modified surface layer (*e.g.* by adsorbates like possible reaction intermediates and/or chloride leaving groups).

Figure 140 collects the curves recorded after rest at open circuit, until specific open circuit potentials (OCP) are reached.

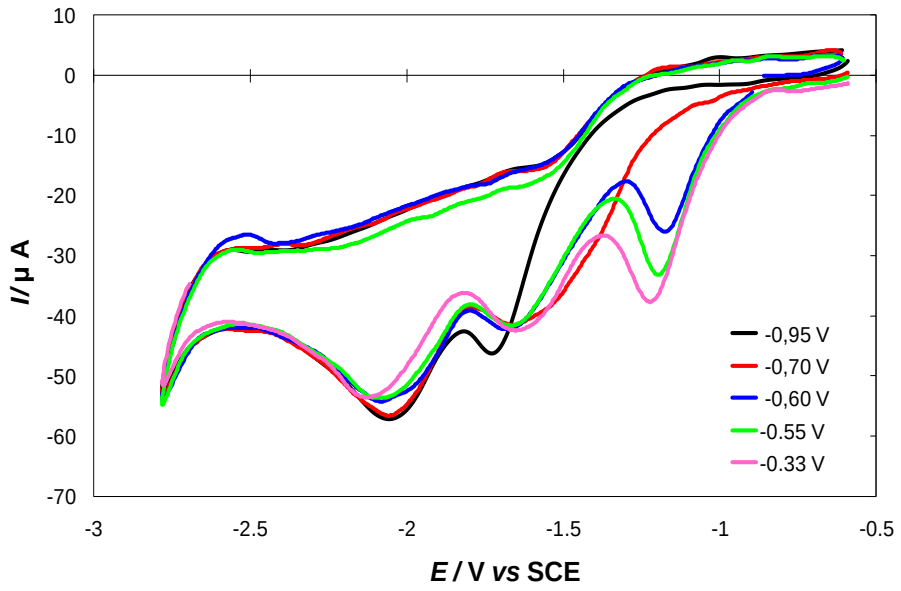

Figure 140: CV characteristics of Ag_NO3_high, in TEATFB 0.1 M in CH_3CN, scan rate = 100 mVs^{-1}, containing 2.5 mM $CHCl_3$. recorded after rest at open circuit condition, until the OCP reaches: (b) (black line) -0.95V; (c) (red line) -0.70V; (d) (blue line) -0.60V; (e) (green line) -0.55V; and (f) (pink line) -0.33V.

To follow the electrode depolarization and the surface depoisoning processes, OCPs are more reliable than resting times, which in turn ranged from few minutes to about 1 h. Peak 1a reappears when the OCP reaches a value around -0.6V, the peak current slowly increasing with increasing OCP values. This is consistent with the progressive restoring of free Ag sites by desorption of interacting species. Concomitantly, peak 1b broadens revealing the presence of a pre-peak as discussed in Figure 135 and Figure 136. Any subsequent cycle (reported for curve corresponding to -0.95V of OCP values only, see Figure 141) is independent on the rest period and is similar to curve (b) but with reduced current values.

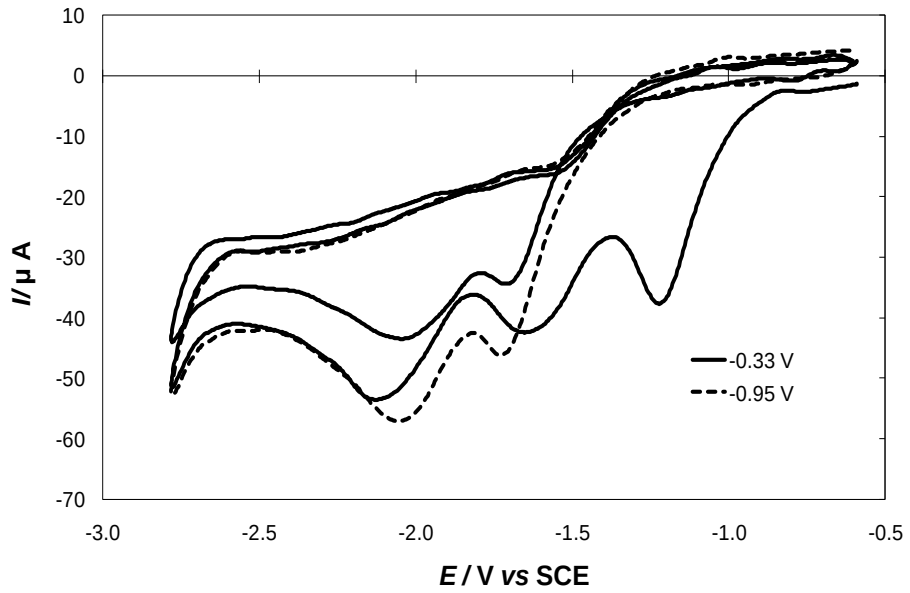

Figure 141: CV characteristics of Ag_NO3_high, in TEATFB 0.1 M in CH_3CN, scan rate = 100 mVs^{-1}, containing 2.5 mM $CHCl_3$. recorded after rest at open circuit condition, until the OCP reaches: (a) (full line) -0.33 V 1st and 2nd cycles; (b) (dashed line) -0.95 V 1st cycle.

Comparing the results obtained on Ag_CN_high and Ag_NO3_high, the superior performance of the latter kind of electrodes is evident, which shows the accessibility of very active surface sites and their possible restoration.

In view of the role played by the surface and its roughness, the CV analysis was extended to microcrystalline Ag powders, whose characterization required the use of C-ME as supporting electrodes, as described in the next section.

(II) Micro-sized silver (C-ME)

The use of C-ME required some preliminary experiments to establish the most effective operating procedure. The main problem encountered in using C-ME supported Ag powders is the presence of dissolved oxygen, which is hard to remove from the cavity. Simple N_2 bubbling, even for extended time, was unsuccessful. A polarization step at -2V for 5 min, before adding the substrate, allows eliminating the oxygen reduction peaks that are in the same range of substrate reduction peak (see Figure 142).

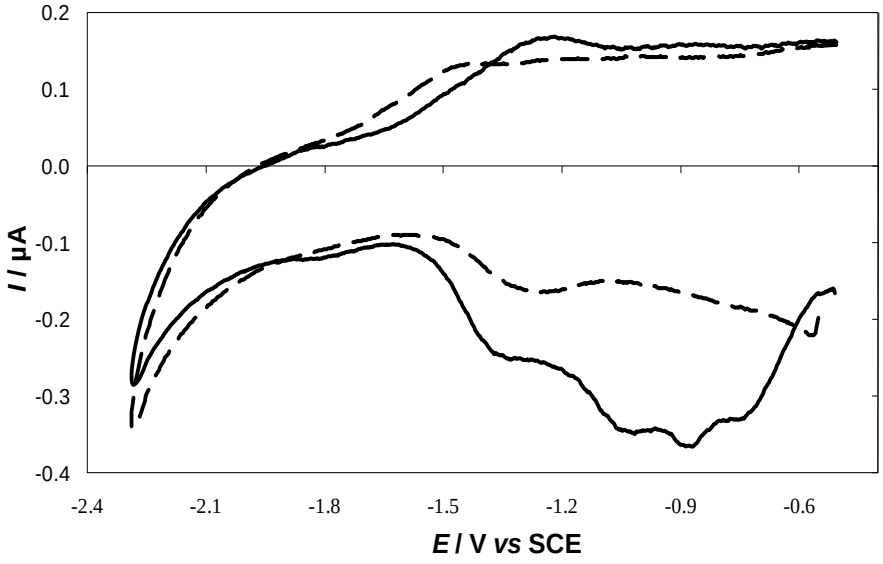

Figure 142: CV characteristics (1st cycle) of Ag_powder, in TEATFB 0.1 M in CH_3CN, scan rate = 2,000 mV s^{-1}: (solid line) after 30 min N_2 bubbling; (dashed line) after polarization at -2 V for 5 min.

Very likely, this procedure is also effective for the reduction of any possible form of surface silver oxide. The filling of the cavity was highly reproducible; a maximum difference of 9% was observed in the peak current for repeated electrode filling/emptying procedures.

To this end, the cavity size was tailored to the particle size of the commercial Ag powder (see Figure 143).

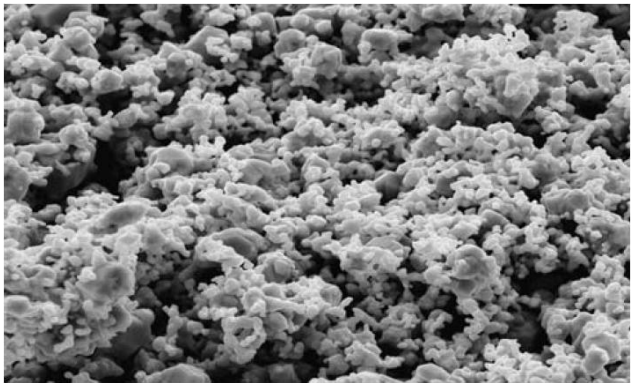

Figure 143: SEM image of the micro-sized Ag powder.

As predicted by the theory, the C-ME behaves as a microelectrode at low scanning rates (almost hemi-spherical diffusion layer) and as a macroelectrode at high scanning rates (planar semi-infinite diffusion layer), in the latter case shows a behaviour similar to that already discussed for electrodeposited Ag disks, although at far higher scan rate. Figure 144 presents the CVs recorded at 2000 mV s^{-1} at different trichloromethane concentrations. In this case the two groups of peaks, 1 and 2, are also clearly present.

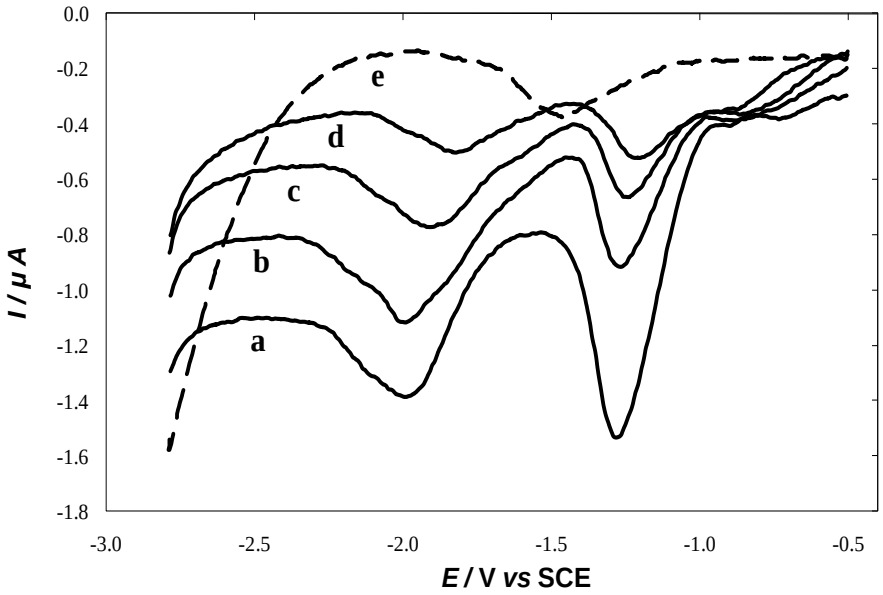

Figure 144: CV characteristics (1st cycle) of Ag_powder, in TEATFB 0.1 M in CH_3CN, scan rate = 2,000 mV s^{-1}, containing $CHCl_3$ at (a) 6.7 mM, (b) 4.2 mM, (c) 2.5 mM, (d) 1.3 mM. Line (e) represents background electrolyte. The reverse scan has been omitted for the sake of clarity.

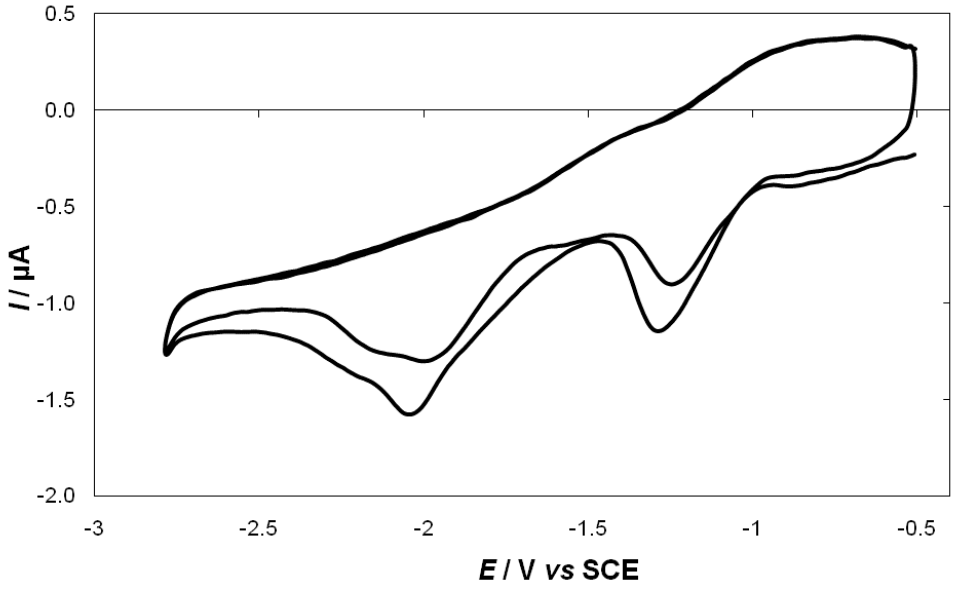

Figure 145: CV characteristics of Ag_powder, in TEATFB 0.1 M in CH_3CN, scan rate = 2,000 mV s^{-1}, containing $CHCl_3$ at 6.7 mM, 1st and 2nd cycle.

The more substantial differences with the electrodeposited Ag electrodes are:

- the general positive shift of peak potential;
- the contraction of group 1 into one large peak;
- the multiplicity of peaks observed for group 2 at increasing $CHCl_3$ concentration;
- the preservation of the whole characteristics with cycling (see Figure 145).

In particular, group 1 shifts negatively with increasing concentration. As already observed for Ag deposits on Pt, this is likely due to the coexistence of a multiplicity of reacting sites, and to the saturation of the more active ones, whose features are eventually masked by the increasing characteristics of the less accessible ones. Similar behaviour is observed for group 2. However, in this case two/three peaks are increasingly discernible at increasing $CHCl_3$ concentration. The contraction of group 1 suggests the presence of reactivity sites on the silver powder, whose activity is markedly higher than the 1b sites. Apparently sites 1a are absent, possibly because the powder is not freshly prepared. Nonetheless, the powder exhibits high electroreductive properties, very likely due to its morphology. As expected, lowering the scanning rate leads to a progressive modification of the CV shapes.

Figure 146 reports the CVs recorded at 100 mV s^{-1} for the same substrate concentrations presented in Figure 144.

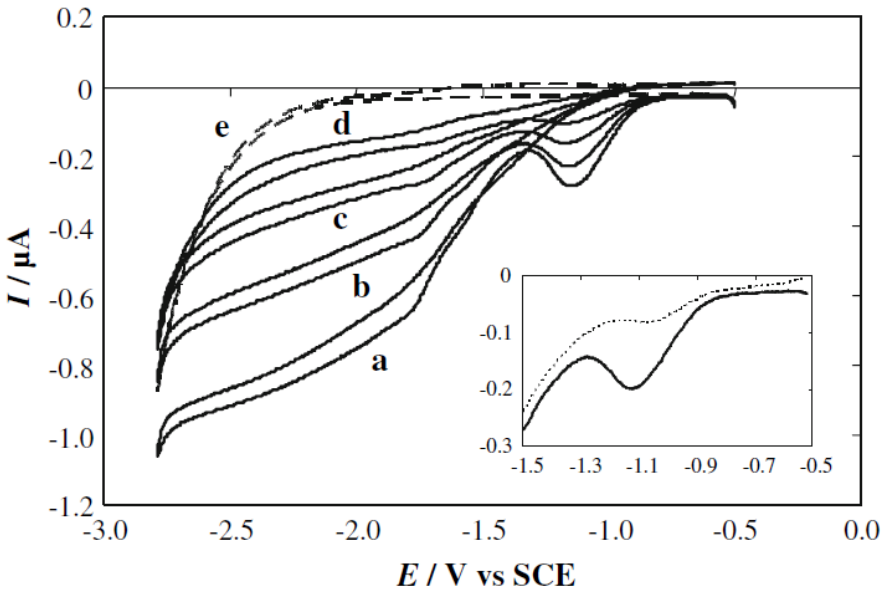

Figure 146: CV characteristics (1st cycle) of Ag_powder, in TEATFB 0.1 M in CH_3CN, scan rate = 100 mV s^{-1}, containing $CHCl_3$ at (a) 6.7 mM, (b) 4.2 mM, (c) 2.5 mM, (d) 1.3 mM. Line (e) represents background electrolyte. Inset: forward scan, 1st and 2nd cycle, 6.7 mM $CHCl_3$, the reverse scan has been omitted for the sake of clarity.

The overall characteristics resemble that predicted for a microelectrode, since the high electronic conductivity of the powder strongly reduces the current penetration depth.

Therefore, all the phenomena generate waves, with the exception of that giving rise to the first peak in the first cycle. This peak is due to reduction of trichloromethane present inside the cavity at the beginning of the experiment, an amount that is consumed during the first scan. In the subsequent cycles, when no trichloromethane (or a negligible quantity) is present inside the cavity, the electrode starts to behave as a silver microdisk of rather high surface roughness, and the peak is replaced by a small sigmoidal wave (see Figure 146 inset), so that at least three consecutive waves are discernible. The dependence on trichloromethane concentration is reported in Figure 147 for the I_{peak} at around -1.1V and for the I_{wave} at -1.8V.

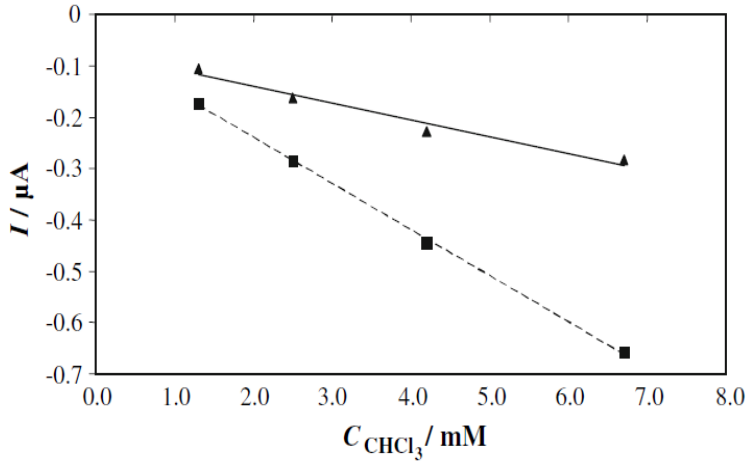

Figure 147: I_{peak} *vs* c_{CHCl3} characteristics from data in Figure 146: (triangles) I_{peak} at -1.1 V; (squares) I_{wave} at -1.8 V. Lines represent the interpolating linear regressions.

In both cases the observed excellent linear behaviour highlights the applicability of C-ME supported Ag powders to quantitative determinations of volatile halocompounds. In this context, the reproducibility limits observed in filling the cavity are more than balanced by the advantage of working with an easily and quickly refreshable electrode, thus overcoming the problem of the rapid aging of the sensing Ag surface.

(III) Comparison between silver electrodeposited and micro-sized silver powder

In Figure 148 is reported a comparison between the different Ag surfaces tested.

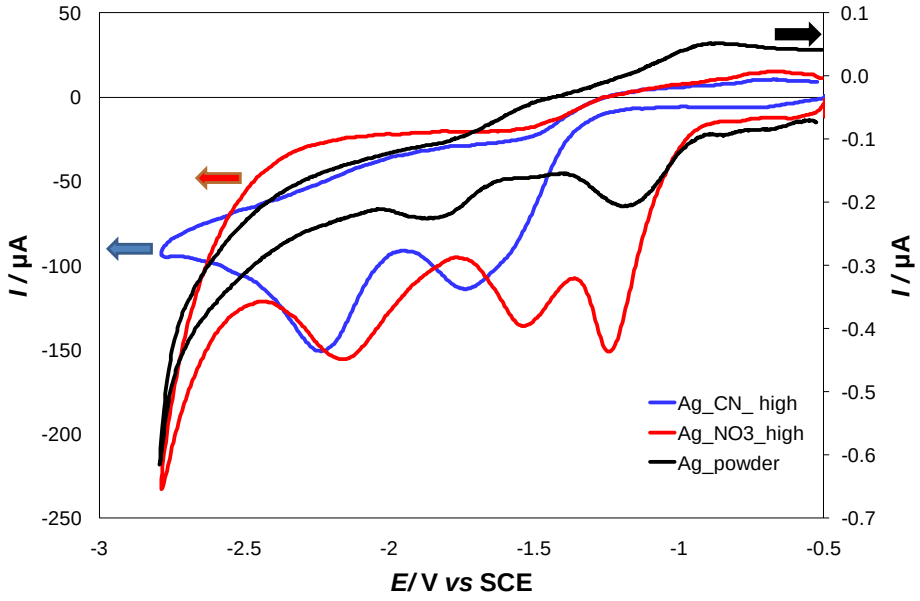

Figure 148: CV characteristics (1st cycle) in TEATFB 0.1M CH_3CN, scan rate = 500 mV s^{-1}, c_{CHCl3}=1.3 mM (a) Ag_CN high (blue line), (b) Ag_NO3 high (red line) (c) Ag_powder (black line).

It is possible to observe that the silver microcrystalline powder show both group of peaks shifted toward less negative potential values. Considering the peak potential values starting from the most favourable value the subsequent sequence is obtained: Ag_powder, Ag_NO3_high and Ag_CN_high.

The electro reductive hydrodehalogenation of organic halides follows the general stoichiometry [25]:

$$R\text{-}X + 2e^- + H^+ \rightarrow R\text{-}H + X^- \quad (87)$$

which applied to the trichloromethane case corresponds to:

$$CHCl_2Cl + 2e^- + H^+ \rightarrow CHCl_2H + Cl^- \quad (88)$$

with formation of dichloromethane. Reaction (88) can be repeated using di- or mono-chloromethane as reactant, ultimately leading to methane. On the whole, a separate voltammetric peak could be expected for each dechlorination step.

On this basis, as already observed in a previous work [9], the 1st group of peaks in the -1.2/-1.6V region (-1.1/-1.3V on silver powders) should be related to hydrodehalogenation of trichloromethane to dichloromethane, while the 2nd group of peaks around -2V should correspond to the formation of chloromethane, since the reduction of dichloromethane is observed in the same potential zone [9]. Nonetheless, preparative electrolysis experiments performed at controlled potentials between -1.2 and -1.6V [9][10] gave methane as final product, thus pointing to a possibly different reaction pathway. Consequently, the presence of a multiplicity of peaks could either suggest (as already assumed in [9][10]) the coexistence of sites of different activity, or the presence of multiple reaction steps. The use of the C-ME has disclosed the coexistence of at least three peaks (at high scanning rates) even for group 2, a feature not observed on the electrodeposited disk electrodes.

3.2-4- Results of Ag electrocatalysts in aqueous media

(I) Micro-sized silver (C-ME)

In Figure 149 is reported the behaviour corresponding to micro-sized silver powder.

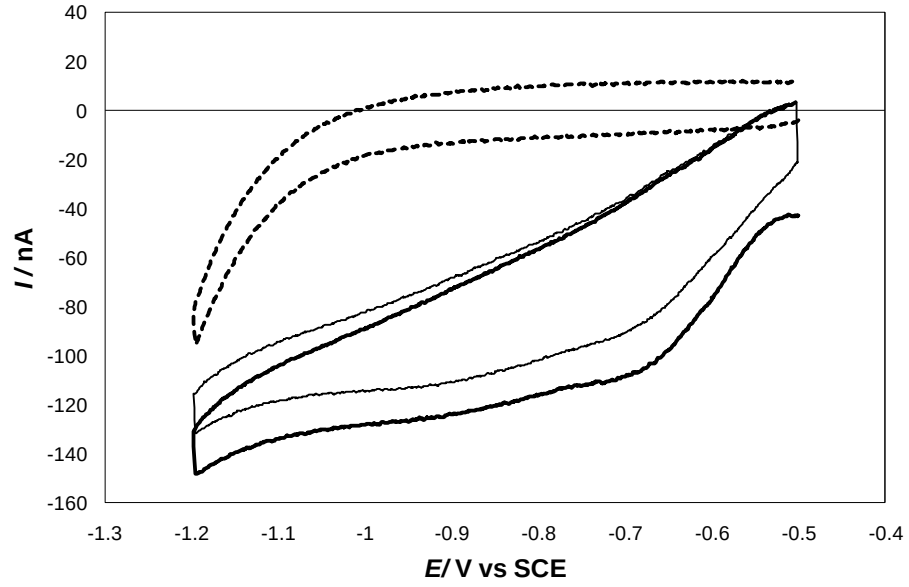

Figure 149: Cyclic voltammetry of 0.01 M $CHCl_3$ in 0.1 M $KClO_4$ background electrolyte, on C-ME with Ag microcrystalline powder, at room temperature. Full lines: heavy– first cycle; light– steady-state cycle; dashed line– only background electrolyte. *v*: 300 mV s^{-1}.

Between -0.6 and -1V, a large reduction current is obtained in 0.01 M $CHCl_3$, whose high $I_p/I_{background}$ ratio is only marginally reduced between the first and the subsequent cycles. Rather than separate reduction peaks, a large plateau is observed, which is attributed to the presence of multiple reaction sites on which the electron transfers relevant to the consecutive expulsion of the chloride groups take place.

(II) Ag_NP

PHYSICAL-CHEMICAL CHARACTERIZATION

The physical-chemical characterization was carried out using different analytical techniques such as: UV-vis, TEM and XRD. The UV–Vis spectra of Ag_NP (0–5) are collected in Figure 150.

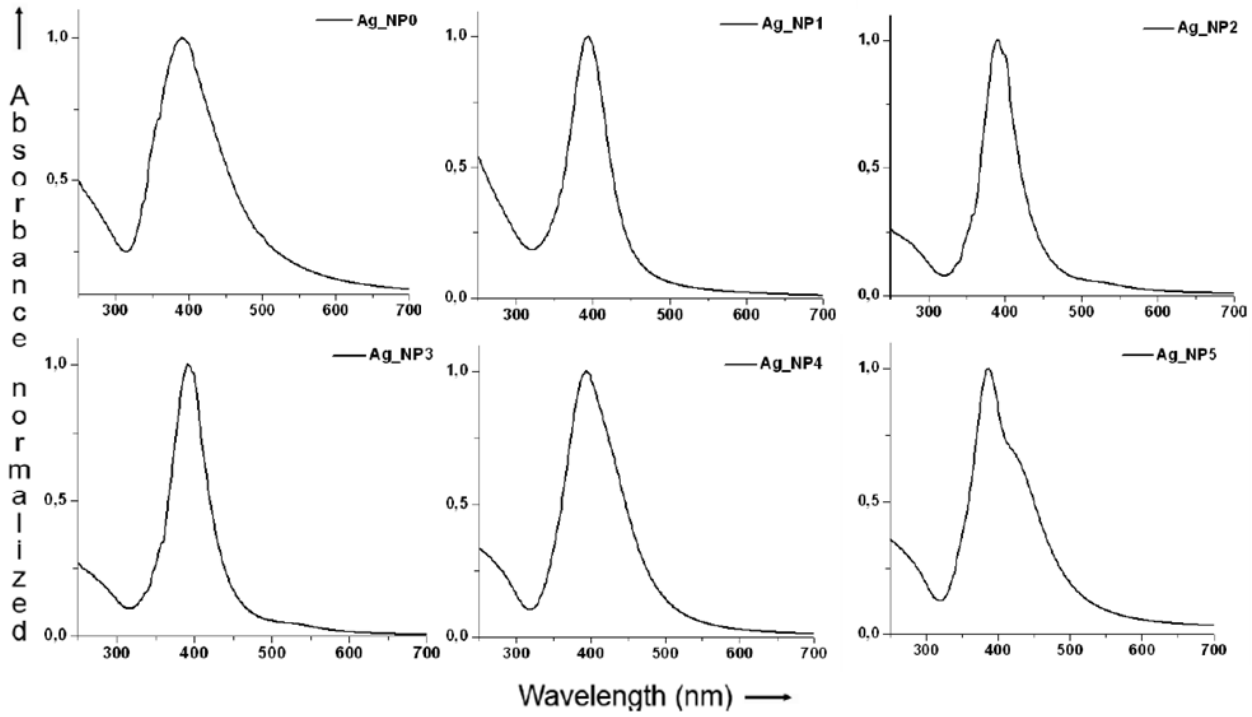

Figure 150: UV–vis spectra of Ag_NP(0–5).

Spectra present plasmon resonance peaks close to 390 nm (from 387 to 394 nm, see Table 2) in agreement with the yellow colouration of the sols.

Colloid	λ_{max} (nm)
Ag_NP0	390
Ag_NP1	393
Ag_NP2	390
Ag_NP3	392
Ag_NP4	394
Ag_NP5	387

Table 32: λ_{max} values of the plasmon resonance peaks of silver colloids Ag_NP(0–5).

The dimensional and morphological analyses of Ag_NP(0–5) colloids were performed by TEM. As an example, in Figure 151A a TEM micrograph of Ag_NP1, showing particles of 2.5 nm averaged mean diameter (see Figure 151B) is reported.

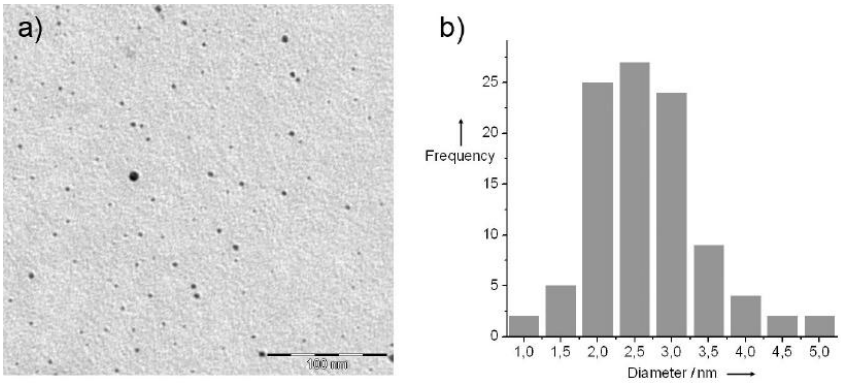

Figure 151: (a) TEM micrograph of Ag_NP1 and (b) the corresponding particle size distribution histogram.

The different stabilizers influence the particles size and polydispersity, varying particle mean diameters in a range of 2–15 nm.

The Ag_NP_C materials were characterized by XRPD analysis highlighting their crystallinity by showing the presence of one Ag(0) peak close to 38° (2 θ) for all samples, as shown in Figure 152 in the case of Ag_NP5_C.

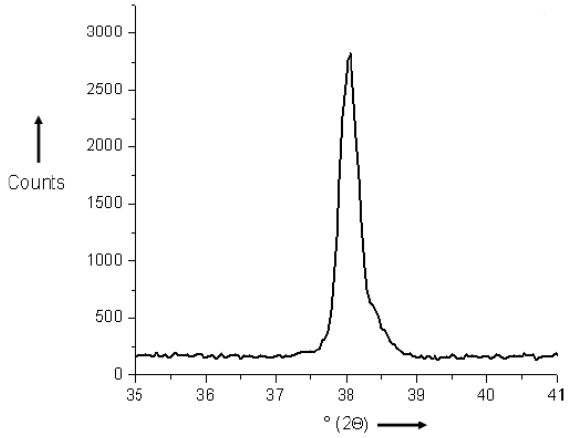

Figure 152: XRPD spectra of crystalline Ag_NP5_C, with the characteristic Ag(0) peak at 38.06 2θ.

The diameters of Ag_NP(0–5) nanoparticles on carbon support, calculated from the Scherrer equation, have been found in the range of 15–20 nm. As these values are larger than those measured by TEM, moderate agglomeration of the particles during the immobilization step is suggested.

ELECTROCHEMICAL CHARACTERIZATION

The electrochemical behaviour of the composite powders supported on C-ME, in aqueous 0.1 M $KClO_4$, for the six different electrode materials are reported in Figure 153. In each case the CV

recorded both in the absence and in the presence of 0.01 M $CHCl_3$ are shown. It possible to note that in [19] there is an error in the current values, in particular the current is ten times lower.

Here the corrected values are reported.

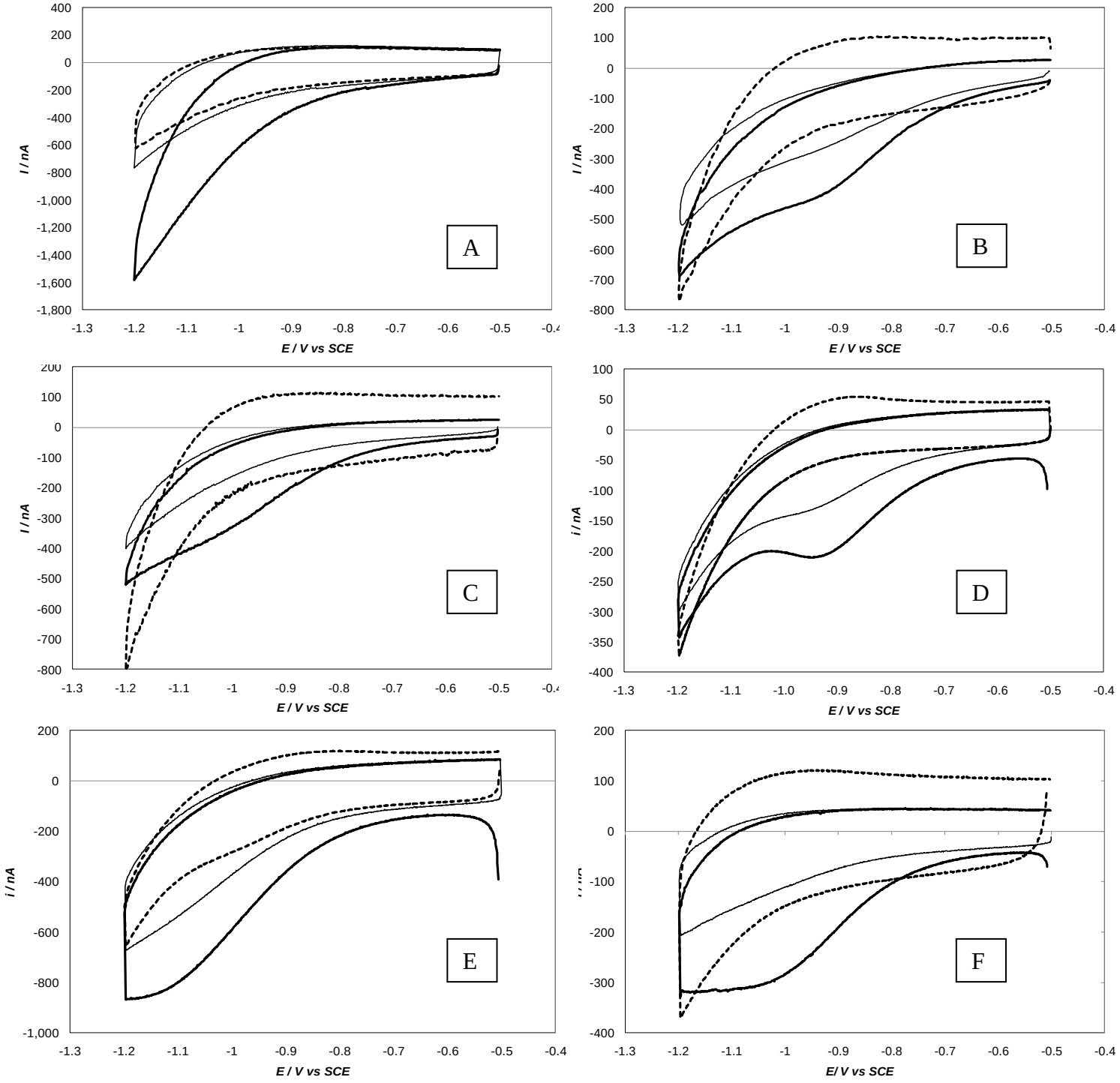

Figure 153: Cyclic voltammetry of 0.01 M $CHCl_3$ (full lines: heavy–first cycle; light–steady-state cycle), in aqueous 0.1 M $KClO_4$ background electrolyte, on C-ME supported composites, at room temperature. Dashed line: background electrolyte only. Scan rate: 300 mV s^{-1}. (A) Ag_NP0_C; (B) Ag_NP1_C; (C) Ag_NP2_C; (D) Ag_NP3_C; (E) Ag_NP4_C; (F) Ag_NP5_C.

As can be seen, all the background curves show the typical capacitive responses of silver in the supporting electrolyte, until for sufficiently negative potentials ($E \leq -0.9$ V) the onset of the hydrogen evolution reaction (HER) is observed. No signal can be attributed to the presence of the stabilizer molecules, which do not show any electroactivity in the relevant potential window, but for their possible role as proton source, the modification of the relative permittivity of the surface layer and the partial shielding of the silver sites. Note that, with the only exception of Ag_NP3_C whose features will be discussed below, the charging currents are quite similar for all composites, thus denoting a good homogeneity in silver loading, the small differences being easily attributed to the reproducibility of filling the cavity, which is ≥90%. In addition, the d.c. capacitances have comparable values with the ones recorded on carbon powder (Figure 154), which are about 10 times lower than ones recorded on Ag_powder (Figure 149).

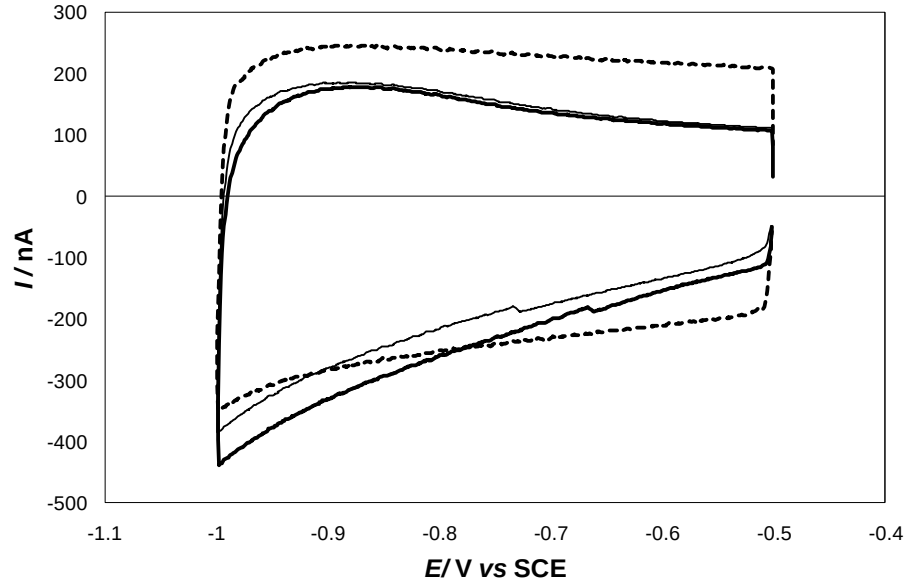

Figure 154: Cyclic voltammetry of 0.01 M $CHCl_3$ in 0.1 M $KClO_4$ background electrolyte, on C-ME with VulcanXC72R powder, at room temperature. Scan rate: 300 mV s^{-1}. Full lines: heavy–first cycle; light–steady-state cycle; dashed line: background electrolyte only.

This feature is connected with the high surface area provided by the carbon support in which silver nanoparticles is dispersed. The six composites show larger differences in the hydrogen evolving region, due to the superposition of different phenomena, like the reduction of carbon side groups, small changes in the surface acidity bound to the different properties of the six stabilizers, differences in the surface availability of Ag sites for Hydrogen evolution reaction (HER). Interestingly, the largest differences are observed between the composites based on Ag_NP2_C, Ag_NP3_C and Ag_NP5_C, whose ligands, in turn, differ for the presence of a branched nonylphenyl and a linear dodecyl group in **2** and **3**, respectively. Ag_NP3_C shows about one-half

the d.c. capacitance of the others. Since the good reproducibility of the recordings rules out effects bound to the cavity filling, the high HER/charging current ratio rules out a reduced silver loading and the well-shaped CV shape rules out a higher internal resistance of the material, the low capacitance could point to a larger shielding of the silver nanoparticles. This is very likely due to the presence of the highly hydrophobic dodecyl groups in the Ag(0)-stabiliser micelles, which can deeply modify the double-layer electric permittivity, while acting as good anchoring tools to the carbon support. However, the same does not apply to Ag_NP2_C, which does not show any reduction in capacitance, while exhibiting, as Ag_NP3_C, a high HER/background current ratio. It is probably due to the strong effect of the bulky branched nonylphenyl group together with a reduced polyoxyethylene chain ($n \approx 12$ *vs* $n \geq 23$) on the micelle structure, which in turn governs the carbon–nanoparticle interactions on one side, and the silver surface accessibility on the other. The small size of **5** could be, as well, at the base of the corresponding composite behaviour, which, at variance with the other two, shows a low activity for HER, thus evidencing a poor availability of silver active sites. In comparison with Ag_NP2 and Ag_NP3, a higher hydrophilic character of the micelle can be expected, which could be at the base of a more labile interaction with the carbon support, and hence of a reduced silver loading. A more complex hypothesis could involve the competition between the carbon–ligand and the Ag–ligand interactions, and the loss of silver. This picture could also explain the different behaviour of Ag_NP5_C and Ag_NP0_C, which present the lowest and the highest HER currents, respectively. In fact, thanks to the stronger interactions between silver and **0**, due to the presence of the amidic nitrogen, neither micelle destabilisation nor the loss of nanoparticles is observed for the corresponding composite, notwithstanding the small size of the ligand and its high hydrophilic character.

When considering the CV features in the presence of 0.01 M $CHCl_3$, a general electroactivity of the composites towards the trichloromethane reduction, in comparison with the bare carbon support (see Figure 154) was observed. In fact, in all cases, a more or less well-shaped peak located at potentials more negative than –0.8 V is observed, or at least, as in the case of Ag_NP0_C, a strong increase in the reduction current in comparison with the background. Nonetheless, the peak position together with the comparison between the first and the steady-state cycles shows how the Ag_NP properties do heavily affect the electrode performances in the presence of the probe reaction.

Although to a lesser extent, the behaviour of the six composites, for which the silver loading is only the 10 wt% of the total electrode material, reproduces the Ag_powder behaviour. The main differences being generally lower $I_p/I_{background}$ ratios and more negative and more localized reduction peaks. The remarkable reduction of the $I_{p,steady\text{-}state}$ in the case of Ag_NP0, Ag_NP2 and Ag_NP5

point to either a total deactivation or to the loss of silver. A strong deactivation is also observed for Ag_NP1 and Ag_NP4, which, nonetheless, may be considered for further investigation. In summary, considering the shape and the potential values of the reduction peak, together with the extent of current decrease between the first and the steady-state cycles the Ag_NP3 exhibits the most promising CV features.

(III) Comparison between silver nanoparticles and micro-sized silver

In Figure 155 the comparison between micro-sized silver with Ag_NP3, that shows the most selective behaviour between the reduction of trichloromethane and water in respect to the others composites, is reported.

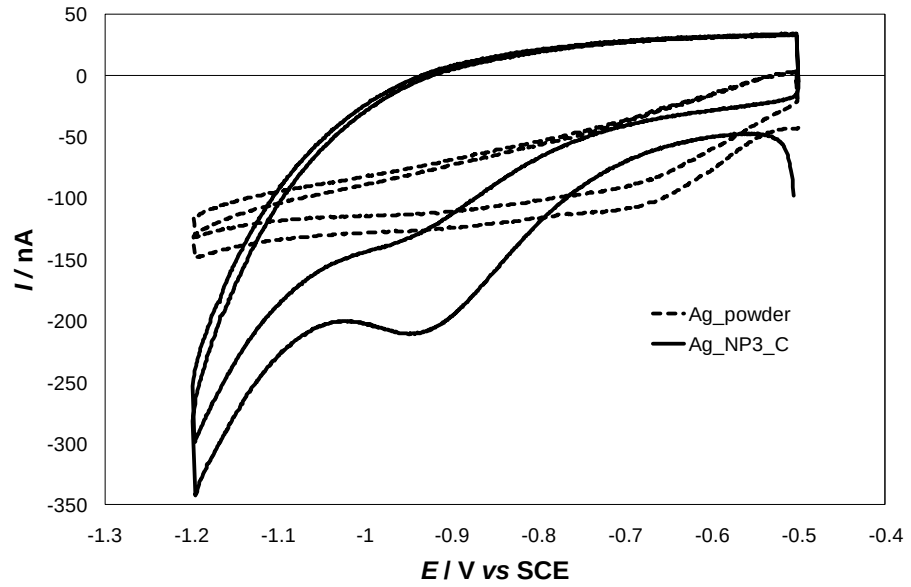

Figure 155: Cyclic voltammetry of 0.01 M $CHCl_3$ in 0.1 M $KClO_4$ background electrolyte, on C-ME supported materials, at room temperature. Scan rate: 300 mV s^{-1}. (dashed line) Ag microcrystalline powder; (Full line) Ag_NP3_C powder.

As just observed in the case of Ag_powder a large reduction current between –0.6 and –1V in 0.01 M $CHCl_3$ is obtained and the high $I_p/I_{background}$ ratio is only marginally reduced between the first and the subsequent cycles. Moreover a large plateau attributed to the presence of multiple reaction sites on which the electron transfers relevant to the consecutive expulsion of the chloride groups is observed.

Ag_NP3 presents a well-shaped peak at a rather less negative potential (–0.94V at 300 mV s^{-1}) and the steady-state current reduces to one-half with respect to the first cycle, thus denoting a low deactivation effect. In addition the presence of carbon, which increase the surface area, the capacitive behaviour is very pronounced causes an evident enhancement of d.c. capacitance.

This result is satisfying, considering that the Ag_NP3 contain only 10 wt% of the total electrode material.

3.2.4- Conclusions

VOH compounds represent a class of highly toxic pollutant both the environment and living beings. Among the different treatment methodologies the electrochemical ones (both oxidative and reductive) show the better conditions. In fact, the middle reaction conditions, the high selectivity and the simple process design give these processes very interesting in the environmental protection and remediation field. In particular the reduction method of VOH look at the substrates hydrodehalogenation producing the corresponding hydrocarbon more easily degradable.

The key element of the process is the electrode and among different materials the silver presents the best electrocatalytic properties that can be tuned modifying different parameters such as: superficial state, type of halogen, nature of organic residual, solvent and support electrolyte etc. In particular the preparation of the material determines both the nature and accessibility of active site and the life of the electrode.

The responses described in the previous sections on three different kind of electrodic materials highlight the dependence of the voltammetric behaviour and, in turn, of the electrocatalytic activity, on the silver surface.

In non-aqueous solution the micro-sized silver powders showing the highest performances, as inferred from the less negative potential values. This gain in the reduction potentials observed on the C-ME, and the multiplicity of peaks around -2V also suggest that the expulsion of the third Cl substituent becomes accessible. This result suggests the possibility that, on extremely active sites, the reduction of trichloromethane proceeds to complete hydrodehalogenation at potentials well above (less negative than) -2V.

The use of powders allows the setting up of three-dimensional electrodes, a feature especially interesting when treating large volume of dilute solutions. Gas diffusion electrodes could be applied to the treatment of low conducting media. In all cases, supporting silver micro- or nano-particles onto a dispersed matrix (*e.g.* carbon) would enable substantial saving in both energy and materials.

Silver nanoparticles were synthesised and successfully applied to the electroreductive dehalogenation of organic halides. The potentialities of the new electrocatalytic composite materials, obtained from colloidal Ag(0) nanoparticles stabilized by a selection of six different ligands and supported on carbon powder, were tested by cyclic voltammetry in aqueous medium, by

means of a cavity-microelectrode. In the supporting electrolyte, all the composites show a silver-like behaviour, only moderately modulated by the different ligands.

A preliminary ranking of the electrocatalyst activity was obtained using trichloromethane as a model probe, whose electroreduction is usually masked by the hydrogen evolution background current, but for the most active materials, as confirmed by parallel measurements performed on the microcrystalline silver and plain carbon support, taken as blank electrodes. On the basis of the evaluation criteria, *i.e.* the shape and the potential value of the reduction peak, together with the extent of current decrease between the first and the steady-state cycles, the most promising composite seems to be Ag_NP3_C, followed by Ag_NP1_C≥Ag_NP4_C≥Ag_NP2_C ≈ Ag_NP5_C ≈ Ag_NP0_ C. Note that by neglecting the deactivation of the material evidenced by the dramatic decrease in the $I_{p,steady\text{-}state}/I_{p,first}$ ratio, the simple, frequently used, peak potential (first cycle) criterion would have led to: Ag_NP3_C ≈ Ag_NP1_- C>Ag_NP5_C ≥ Ag_NP2_C>Ag_NP4_C>Ag_NP0_C.

The electrocatalytic activity of Ag_NP3_C, with only 10 wt% of silver loading, was then confirmed by the results of the electrolytic reduction of gaseous trichloromethane, performed in a two-compartment membrane cell, using gas-diffusion cathodes based on the new material.

3.2.5-References

[1] Papp R *Pure Appl. Chem.* **1996**, 68, 1801.

[2] Chen G *Sep. Purif. Techol.* **2004**, 38, 11.

[3] Rondinini S, Mussini PR, Sello G, Vismara E *J. Electrochem. Soc*. **1998**, 145, 1108.

[4] Rondinini S, Mussini PR, Crippa F, Sello G *Electrochem. Commun*. **2000**, 2, 491.

[5] Rondinini S, Mussini PR, Muttini P, Sello G *Electrochim. Acta.* **2001**, 46, 3245.

[6] Rondinini S, Mussini PR, Specchia M, Vertova A *J. Electrochem. Soc*. **2001**, 148, D102.

[7] Doherty AP, Koshechko V, Titov V, Mishura A *J. Electroanal. Chem.* **2007**, 602, 91.

[8] Isse AA, Ferlin MG, Gennaro A *J. Electroanal. Chem*. **2005**, 581, 38.

[9] Rondinini S, Vertova A *Electrochim. Acta* **2004**, 49, 4035.

[10] Fiori G, Rondinini S, Sello G, Vertova A, Cirja M, Conti L *J. Appl. Electrochem*. **2005**, 35, 363.

[11] Valette G, Hamelin A, Parsons R *Z. Phys. Chem. Neue. Fol*. **1978**, 113, 71.

[12] Foresti ML, Innocenti M, Forni F, Guidelli R *Langmuir* **1998**, 14, 70086.

[13] Mussini PR, Ardizzone S, Cappelletti G, Longhi M, Rondinini S, Doubova LM *J. Electroanal. Chem.* **2003**, 552, 213.

[14] Migani A, Illas F *J. Phys. Chem*. **2006**, 110,11894.

[15] Ardizzone S, Cappelletti G, Mussini PR, Rondinini S, Doubova LM *Russ J. Electrochem. (translation of Elektrokhimija)* **2003**, 39, 170.

[16] Miranda-Hernandez M, Gonzalez I, Batina N *J. Phys. Chem*. **2001** B 105, 4214.

[17] O. Scialdone, A. Galia, G. Errante, A. A. Isse, A. Gennaro, G. Filardo, Giuseppe, *Electrochim. Acta* **2008**, *53*, 2514.

[18] A. A. Isse, S. Gottardello, C. Maccato, A. Gennaro, *Electrochem. Commun.* **2006**, *8*, 1707.

[19] A. Vertova, R. Barhdadi, C. Cachet-Vivier, C. Locatelli, A. Minguzzi, J.-Y. Nedelec, S. Rondinini, *J. Appl. Electrochem.* **2008**, *38*, 965.

[20] H. Zhang, Q. Fu, Y. Yao, Z. Zhang, T. Ma, D. Tan, X. Bao, *Langmuir* **2008**, *24*, 10874.

[21] Costentin C, Robert M, Save´ant J-M *Chem Physics* **2006**, 324, 40.

[22] E. Matijevic, *Chem Mater*. **1993**, *5*, 412.

[23] Y.Saito, J. J. Wang, D. N. Batchelder, D. A. Smith, *Langmuir* **2003**, *19*, 6857.

[24] J. Soukupova, L. Kvitek, A. Panacek, T. Nevecna, R. Zboril, *Mater. Phys.* **2008**, *111*, 77.

[25] C. Costentin, M. Robert, J.-M. Savéant, *J. Am. Chem. Soc.*2003, *125*, 10729.

4-Conclusions

In the recent years the quality of life and a sustainable development have prompted several countries to adopt appropriate political resolutions. In particular Europe, in the fight against climate change, is committed to promoting a low carbon and resource-efficient economy and on June 2006 a strategy consisting of different objectives and concrete actions, for the coming period until 2010 is delineated. This thesis is in direct relation with some of the key subjects outlined: clean energy and sustainable consumption/production. In particular the development of new electrocatalytic materials for the exploitation of renewable energy sources (application in URFC systems) and the treatment of wastes (trichloromethane electroreduction) were considered.

At the moment fossil fuels (coal, oil and natural gas) are the principal primary energy sources. Beside their projected shortage, there are the environmental aspects associated with the combustion by-products (SO_x, NO_x, CO, CO_2, VOC, micro-pollutants, fine particulate, noise). Then a major attention is directed to the renewable energy sources. One of the main drawbacks of renewable energy sources is their intermittent availability and often their remote locations. This opens the question on energy storage and energy vectors. In this context H_2 is progressively considered as one of the most effective long-range and long term environmentally friendly vector. Among different method for hydrogen production the water electrolysis is the most environmentally friendly especially if the electric power is produced using renewable energy sources. Hydrogen produced can be successively oxidised in a fuel cell system for producing electric power, having heat and water as by-product. A Unitised Reversible Fuel Cell (URFC), combining both the water electrolysis and FC systems in a whole apparatus, has a high specific energy and allows the production and conservation of the fuel for a long time, so that it can be used on demand. The core of this technology is the electrode material that has to catalyse both the oxygen reduction reaction (ORR) and oxygen evolution reaction (OER). Since the cell design used in solid polymer electrolyte (SPE) water electrolysis is very similar with that used in PEMFC, the possibility of building-up a URFC device is very attractive. Then, as a further requirement, the electrocatalytic materials have not only to show high catalytic properties toward ORR and OER, but also have to be stable in acidic media.

In this thesis binary SnO_2-IrO_2 mixtures were synthesized by sol-gel technique and characterized in terms of both the bulk and surface compositions and morphologies and of their general electrochemical features and specific electrocatalytic activity as bifunctional material for OER and ORR. The new materials were synthesized as disperse phases and subsequently characterized as un-

supported and supported powders, as required by the electrochemical applications. Thanks to extreme flexibility of the synthetic methodology, the bulk and surface properties were finely tailored.

The synthesized materials were initially characterized by physico-chemical techniques (XRPD, SEM, XPS and BET) and by voltamperometric investigations using different supports (C-ME, RDE and Ti-plate), with and without the presence of a redox probe (Fe^{3+}/Fe^{2+}). The reactivity of powders toward OER and ORR was investigated recording *U vs I* using in-house designed electrolytic cells.

The characterization of the materials led to the selection of the most effective synthetic route (the Impregnation method) to produce powders with very interesting characteristics. More specifically, the powder with the lowest IrO_2 content exhibits the highest accessibility of active sites and the highest active area. This corresponds, in oxygen–saturated solution, to higher cathodic currents correlated to the oxygen reduction reaction.

These results are supported by physico-chemical characterizations which show round shape particles aggregates (20-40nm) with an evident enrichment of Ir species at the surface and a progressive increase of the surface area at decreasing IrO_2 content. *Vice versa* at high IrO_2 content the impregnation method does not leads to encouraging results due to the large crystalline IrO_2 aggregates that reduce the active surface, while the co-synthesis method starting from chlorinated salts (CS-Cl) seems more appropriate.

An improvement of the powders obtained with I method at high IrO_2 content was obtained dispersing the powder in an active carbon matrix (Vulcan®, optimal loading 10 wt%). The decrease of the electric contact resistance among catalyst particles allows improving the conductance within the catalytic layer and the electrochemical behaviour. The information obtained by electrochemical characterization was also confirmed in the case of reactivity study of the materials toward OER and ORR.

For OER, powders were directly supported on cationic membrane, the so-called membrane-electrode-assembly, MEA. The reactivity toward OER was evaluated using in-house designed and manufactured electrolytic cells. The contact resistance between MEA and the current collectors, the efficiencies of water supply and gas removal are key parameters. Notwithstanding the very promising results obtained especially in the case of the lowest IrO_2 content, the best performing flux cell requires further optimization. The ink composition also required specific optimization, leading to the optimal loading value of 0.6 mg cm^2 Nafion®, to obtain a good proton conductivity without the increase of the electronic resistance of the catalyst layer.

For ORR, the powders were supported on RDE, which allows the extrapolation of the kinetic information. Comparing the preliminary results of the synthesised powders with Pt/C (E-TEK)

catalyst, very promising values in terms of both E_{ORR} (the potential at which ORR begins) and kinetic currents were obtained. Also in this case the better behaviour was obtained with the lowest IrO_2/SnO_2 ratio.

In the second part of thesis the electrocatalytic materials for trichloromethane hydrodehalogenation were investigated. As previously mentioned, this theme is correlated to the sustainable development of human activities. Trichloromethane belongs to a category of very toxic substances: Volatile Organic Halides. VOHs are dangerous both to human health and environment, therefore treatment is required. Among different methods of degradation, the electrochemical reduction offers the better conditions. The mild reaction conditions (ambient temperature and pressure), the high selectivity, the absence of secondary pollution and the simple process design, that are characteristic of the electrochemical route, are highly valuable features in the field of environmental protection and remediation. Among the various electrode materials that can be adopted, silver presents the best electrocatalytic properties, thus substantially reducing the energy consumption of the process. The research goal is the decrease of the metal precious loading without compromising the electrocatalytic activity and the life-time of electrode.

Different types of silver electrodes, powder and electrodeposited electrode materials, were synthesized and electrochemically characterized into organic and aqueous media.

A first study was carried out in acetonitrile, to characterize the electrodeposited silver prepared using different electrolytic baths (aqueous 0.05 M $KAg(CN)_2$ and 0.1 M $AgNO_3$), by means of cyclic voltammetry, in the presence of the organic halide. Commercially available silver micro-sized powder was also tested in the same organic solvent in order to compare the electrochemical behaviour of the different Ag deposits and to determine the best electrodeposition conditions to obtain an active electrocatalyst.

The silver micro-sized powder was also characterized in aqueous solution, in the presence of the same organic halide, and was compared with the silver nanoparticles prepared with the chemical-reduction method.

Considering the peak multiplicity and position it is possible to affirm that between the $AgNO_3$ electrodeposition bath provides the more active surface. In particular the peak multiplicity suggests the presence of extremely active sites and the reduction of trichloromethane proceeds to complete hydrodehalogenation.

Silver nanoparticles supported on active carbon at low Ag content (10wt%) were successfully synthesized by chemical reduction in the presence of six different dispersing agents. The use of powders allows the setting up of tridimensional electrodes, a feature especially interesting when treating large volume of dilute solutions. Considering the shape and the potential value of the

reduction peak, together with the extent of current decrease between the first and the steady-state cycles it is possible to affirm that the use of α-Dodecyl-ω-hydroxypolyoxyethylene as dispersing agent allows obtaining an electrocatalytic powder with very interesting electrocatalytic properties.

5-List of Symbol

Symbol	Meaning	Usual Unit	Section References
a	activity of substance	none	2.2.2
A	Electrode area	cm^2	2.2.5-IV
A	Assorbance	none	2.3.2
b	Tafel slope	none	1.3
C	constant related to the adsorption heat for the first monolayer and to the gas liquefaction heat		2.3.1
c	concentration	mol cm^{-3}	2.3.2
C^*_0	bulk concentration of reactant	mol cm^{-3}	2.2.5-I
C_{dl}	double layer capacitance	F	2.2.1; 2.2.4
c_o	bulk concentration	mol cm^{-3}	2.2.5-IV
C_s	reagent concentration at the surface	mol cm^{-3}	2.2.5-IV
d	spacing between the planes of atoms,	Å	2.3.3
D_0	diffusion coefficient	cm^2 s	2.2.5-I; 2.2.5-IV
E	potential of an electrode versus a reference	V	2.2.1, 2.2.2,
$\boldsymbol{E}$	Potential vector	V	2.2.4
$E(t)$	a.c. applied potential	V	2.2.4
$E°$	Standard potential of the electrode	V	1.4.2, 2.2.2
$E_{1/2}$	Potential where i/i_d =1/2	V	2.2.5-I
$E_{1/4}$	Potential where i/i_d =1/4	V	2.2.5-I
$E_{3/4}$	Potential where i/i_d =3/4	V	2.2.5-I
E_a	activation energy of a reaction	kJ mol^{-1}	1.3
E_{app}	Potential electrode applied	V	2.2.5
E_b	binding energy of the electron	eV	2.3.4
E_{corr}	E_{SCE}-E_{RHE}	V	2.2.2
E_{eq}	equilibrium potential of an electrode	V	1.3
E_k	kinetic energy of electron emitted	eV	2.3.4
E_o	potential amplitude	V	2.2.4
$E_{p,a}$	anodic peak potential	V	2.2.1
$E_{p,c}$	cathodic peak potential	V	2.2.1

E_{RHE}	potential of an electrode versus RHE	V	2.2.2
E_{SCE}	potential of an electrode versus SCE	V	2.2.2
E_W	working electrode potential	V	1.3
F	Faraday constant	C mol^{-1}, Ah mol^{-1}	1.3; 2.2.2; 2.2.5-I; 2.2.5-IV
f	Frequency	s^{-1}	2.2.5-II; 2.2.4
h	Plank constant	eV s	2.3.4; 2.3.5
I	Current intensity	A	2.2.1
$\boldsymbol{I}$	Current vector	A	2.2.4
$I(t)$	a.c.current	A	2.2.4
I_0	current amplitude	A	2.2.4
I_C	Capacitive current	A	2.2.1
i_d	Diffusion limited current	A	2.2.5-I
I_F	Faradic current	A	2.2.1
i_k	kinetically limited current	A	2.2.5-IV
i_L	current due to diffusive flux	A	2.2.5-IV
$I_{p,a}$	anodic peak current	A	2.2.1
$I_{p,c}$	cathodic peak current	A	2.2.1
i_{ss}	Steady-state current	A	2.2.5-I
j	Current density	A cm^{-2}	1.3
j_0	exchange current density	A cm^{-2}	1.3
j_a	Anodic current density	A cm^{-2}	1.3
j_c	Cathodic current density	A cm^{-2}	1.3
k	Generic constant		2.2.1
k_0	standard heterogeneous rate constant for electron transfer	cm s^{-1}	2.2.5-I
k_h	heterogeneous rate constant for electron transfer	cm s^{-1}	2.2.5-IV
L	Depth electrode	cm	2.2.5-I
l	Length of the cell for UV measurements	cm	2.3.2
M	molar mass	g mol^{-1}	2.1.2
m	Angular coefficient		2.2.2
m_e	Electron mass	kg	2.3.5
M_p	molar mass of the product	g mol^{-1}	1.3
n	stoichiometric number of electrons involved in an electrode reaction	None	1.3; 2.2.5-I; 2.2.5-IV

n	Number of repetitive units	None	2.1.2
n	Integer number	None	2.3.3
N_A	Avogadro's number	mol^{-1}	2-3.1
P	Equilibrium pressure of the adsorbate	Pa	2.3.1
P_0	saturation pressure of the adsorbate	Pa	2.3.1
P_{atm}	atmospheric pressure	Pa	2.2.2
p_h	hydrostatic pressure	Pa	2.2.2
p_{H2}	Hydrogen partial pressures	Pa	2.2.2
p_{O2}	Oxygen partial pressures	Pa	2.2.2
p_{vap}	vapour pressure of the solution	Pa	2.2.2
Q	Voltammetric charge	C	2.2.1
q	Intercept of a straight line		2.2.2
q_e	Charge electron	C	2.3.5
Q_{in}	Inner voltammetric charge	C	2.2.1
Q_{out}	Outer voltammetric charge	C	2.2.1
Q_{tot}	Total voltammetric charge	C	2.2-1
R	Gas constant	$J\ mol^{-1}\ k^{-1}$	1.3, 2.2.2, 2.2.5-I
R	Pure resistance	Ω	2.2.4
r	Radius electrode	cm	2.2.5-I
r_0	equivalent radius of electrode	cm	2.2.5-I
R_e	electronic resistance	Ω	2.2.4
R_k	ionic resistance	Ω	2.2.4
r_p	Porous radius	cm	2.3.1
S	Specific area	cm	2.3.1
T	Temperature	K	1.3; 2.2.2; 2.2.5-I
t	Time	s	2.2.1, 2.2.4
v	Scan rate	$V\ s^{-1}$	2.2.1
V	adsorbed gas volume	cm^3	2.3.1
V_e	potential difference through which the electrons are accelerated	V	2.3.5
V_m	monolayer volume of adsorbed gas	cm^3	2.3.1
w	specific consumption of energy	Wh/kg	1.3
Z	impedance	Ω	2.2.4
$\boldsymbol{Z}$	Impedance vector	Ω	2.2.4
Z'	imaginary part of impedance	Ω	2.2.4
Z''	real part of impedance	Ω	2.2.4

Z_0	E_0/I_0	Ω	2.2.4
Z_{CPE}	Impedance of CPE	Ω	2.2.4
$Z_{f,k}$	faradaic impedance	Ω	2.2.4
α	Powder reflection width	None	2.3.3
β	transfer coefficient	None	1.3, 2.2.5-I
γ	liquid surface tension	Dyne cm^{1}	2.3.1
ΔG	Gibbs free energy change in a chemical process	kJ mol^{-1}	1.3
$\Delta G°$	standard Gibbs free energy change in a chemical process	kJ mol^{-1}	1.4.2; 1.4-3
$\Delta H°$	standard enthalpy change in a chemical process	kJ mol^{-1}	1.4.3
ε	molar absorptivity	cm^2 mol^{-1}	2.3.2
η	Overpotential, E-E_{eq}	V	1.3, 2.2.5
η_{ct}	charge-transfer overpotential	V	1.3
η_{mt}	Mass-transfer overpotential	V	1.3
η_{Ω}	Ohmic-drops overpotential	V	1.3
θ	fractional coverage of an interface	None	1.4.6
Θ	contact angle	degrees, radians	2.3.1
θ	incident angle	degrees, radians	2.3.3
λ	Wavelengths	Å	2.3.5
σ	area occupied by one adsorbate molecule	Å	2.3.1
υ	molar volume	cm^{-3} mol^{-1}	2.3.1
υ	Radiation frequency	s^{-1}	2.3.4
φ	phase angle between two sinusoidal signals	degrees, radians	2.2.4
Φ	spectrometer work function	None	2.3.4
χ_{ox}	Mulliken Electronegativity of metal oxide	eV, kJ mol^{-1}	1.4.6
ω	Angular frequency	s^{-1}	2.2.4
ω	rotation disk velocity	r s^{-1}	2.2.5-IV

6-List of acronyms

a.c	Alternate current
AFC	Alkaline Fuel Cell
BDDT	Brunauer, Deming, Deming and Teller
BE	Binding energy
BET	Brunauer –Emmett-Teller
BSE	*Backscattered Electrons*
C-ME	Cavity micro-electrode
CPE	Constant phase element
CV	Cyclic voltammetry
EC	European Community
EIS	Electrochemical Impedance Spectroscopy
EU	European Union
FC	Fuel cell
GC	Glassy carbon
GDE	Gas diffusion electrode
GDP	Gross Domestic Product
HALE	high altitude long endurance
HER	Hydrogen evolution reaction
HOMO	highest occupied molecular obital
HRTEM	*High resolution* Transmission Electron Microscopies
LUMO	lower unoccupied molecular orbital
MCFC	Molten Carbonate Fuel Cell
MEA	Membrane electrode assembly
NMVOCs	non-methane VOCs
OCP	Open circuit potential
OECD	Organization for the Economic Co-operation and development
OER	Oxygen evolution reaction
ORR	Oxygen reduction reaction
p.d.	Potential difference
PAFC	Phosphoric Acid Fuel Cell
PEG	Polyethylene glycol

PEG-BDE	Polyethylene glycol bisphenol A epichlorohydrin copolymer
PEM	proton exchange membrane
PEMFC	proton exchange membrane fuel cell
PVA	Poly(vinyl alcohol)
PZC	Point zero charge
RDE	Rotating disk electrode
rds	Rate determining step
RFC	Reversible fuel cell
RHE	Reversible hydrogen electrode
RS	Reference Scenario
SCE	calomel saturated electrode
SDS	Sustainable Development Strategy
SEM	Scanning Electron microscopy
SHE	Standard hydrogen electrode
SMES	Superconducting Magnetic Energy System
SOFC	Solide Oxide Fuel Cell
SRA	solar rechargeable aircraft
TEM	Transmission Electron Microscopies
TPES	Total Primary Energy Supply
URFC	Unitised Regenerative Fuel Cell
UV	Ultraviolet
VIS	Visible
VOC	Volatile Organic Compound
VOH	Halogenated VOC
WE	Working electrode
XPS	X-Ray Photoelectron Spectroscopy
XRPD	X-Ray Powder Diffraction
ZEV	zero-emission vehicles

7-Acknowledgements

Prima di tutto vorrei ringraziare la Prof.ssa Sandra Rondinini e il dott. Alberto Vertova sia per avermi dato la possibilità di raggiungere questo importante traguardo accogliendomi nel loro gruppo di ricerca. Vi ringrazio molto per avermi supportato non solo dal punto di vista scientifico ma anche umano con la vostra fiducia, pazienza, comprensione ed energia.

Vorrei ringraziare la De Nora Industrie, in particolar modo il Dott. Gian Nicola Martelli, per il materiale fornito: Nafion®, Pt/C powder, supporti per i GDE, PTFE, elettrodi DSA.

Ringrazio i miei compagni di laboratorio che mi hanno sopportato, specialmente nell'ultimo periodo di lavoro. In particolar modo ringrazio Gabriele Aricci e Alessandro Minguzzi: il primo per l'aiuto dato durante la realizzazione delle celle di elettrolisi e il secondo per l'aiuto dato durante la stesura della tesi.

Ringrazio sentitamente la mia famiglia che mi ha sempre supportato e incoraggiato. I vostri validi consigli e il vostro sostegno morale sono stati fondamentali. Senza di voi non ce l'avrei mai fatta.

In particolare ringrazio mio fratello Sergio che mi ha sempre sostenuto e aiutato nel momento del bisogno.

Per ultimo, ma non per questo meno importante, ringrazio con grande affetto il mio fidanzato Morgan. Grazie per essermi sempre stato vicino con grande amore e per avermi sempre dato una grande forza ad andare avanti.